

Subsurface ablation of tissue by ultrafast laser

THÈSE N° 7493 (2017)

PRÉSENTÉE LE 17 FÉVRIER 2017

À LA FACULTÉ DES SCIENCES ET TECHNIQUES DE L'INGÉNIEUR

LABORATOIRE D'OPTIQUE

PROGRAMME DOCTORAL EN PHOTONIQUE

ÉCOLE POLYTECHNIQUE FÉDÉRALE DE LAUSANNE

POUR L'OBTENTION DU GRADE DE DOCTEUR ÈS SCIENCES

PAR

Thomas Jean Victor Marie LANVIN

acceptée sur proposition du jury:

Prof. C. Moser, président du jury
Prof. D. Psaltis, directeur de thèse
Dr M.-N. Giraud, rapporteuse
Dr I. Papadopoulos, rapporteur
Prof. R. Grange, rapporteuse



ÉCOLE POLYTECHNIQUE
FÉDÉRALE DE LAUSANNE

Suisse
2017

Abstract

Laser-induced optical breakdown (LIOB) is a multiphoton process which can be used for selective removal of material. It revolves around the creation of a plasma in the focal volume of a beam, and requires very high peak intensities in the order of the GW.cm^{-2} . For this reason, ultrafast lasers sending high energy pulses with very short durations below 1 ps are favorite tools for triggering LIOB. The local creation of the plasma can induce a sharp rise in temperature and pressure over a few micrometers, which produce a cavitation bubble. The combined mechanical effects from the bubble creation and chemical effects from the free electrons in the plasma can induce dramatic changes in and around the focal volume.

This is particularly true in sensitive samples such as biological tissues, where cells can be selectively destroyed by LIOB. In this regard, the work presented in this thesis concerns the analysis of the effects of LIOB in soft biological tissues. More specifically, we investigate the case of arterial tissues and the opportunities this technique could offer in the treatment of atherosclerosis.

First, we present the current knowledge on the mechanism and impact of LIOB on the surrounding medium, and particularly in biological samples. We discuss their modeling, both via simulation and replication in organic and inorganic phantoms.

The following section of this thesis is devoted to investigating the effect of LIOB at the cellular level. We discuss an approach according to which LIOB may be of interest in the treatment of atherosclerosis or other pathologies which could benefit from the control of the population of cells undergoing controlled cell death (apoptosis). We then investigate the effect of LIOB on populations of epithelial cells in 2D and 3D cultures. We monitor the increase in the number of necrotic and apoptotic cells, in different regimes of ablation.

We then present the methods and results of subsurface ablation in arterial tissue, both healthy and atherosclerotic. On ex-vivo experiments, we focus on the observation of a bubble produced by LIOB, and the structural damage generated. On in-vivo experiments, we investigate the effect on necrosis and apoptosis of cells around the target area, and compare our findings with the results obtained in cell cultures and phantoms.

Finally, delivering the high intensities pulses to the target area in a minimally invasive way is essential in biomedical applications of LIOB, and we investigate this question in the final part of this thesis. We present two different approaches to answer this challenge: first by the use of transmission of pulses via a hollow-core photonic crystal fiber, and secondly by wavefront shaping of a pulse through a multicore fiber. Through both methods, we demonstrate subsurface ablation of biological tissue.

Keywords: *laser-induced optical breakdown, subsurface ablation, non-linear optics, microsurgery, plasma, atherosclerosis, apoptosis, endoscopy, wavefront shaping, multicore fibre.*

Résumé

La rupture optique induite par laser (LIOB) est un processus multiphoton peut être utilisé pour retirer de la matière de manière sélective. Ce processus découle de la création d'un plasma dans le volume focal d'un faisceau, et nécessite de très hautes intensités de l'ordre du GW.cm^{-2} . Pour cette raison, les lasers ultrarapides délivrant des pulses à très haute énergie avec une très courte durée (moins de 1 ps) sont un outil de choix pour générer des LIOB. La création d'un plasma peut induire une augmentation de température et de pression sur quelques micromètres, ce qui peut produire une bulle de cavitation. Les effets combinés de la création de cette bulle et des réactions chimiques des électrons libérés dans le plasma peuvent induire des changements dramatiques aux environs du volume focal.

Cela est particulièrement vrai dans des échantillons sensibles tels que les tissus biologiques, où les cellules peuvent être sélectivement détruites par LIOB. Le confinement axial et latéral de la création du plasma due à la nature multiphoton de la LIOB ouvre des perspectives intéressantes dans le domaine de la microchirurgie. En ligne avec cette idée, le travail présenté dans cette thèse s'attache à l'analyse des effets de la LIOB sur des tissus biologiques mous. Plus spécifiquement, nous étudions le cas des tissus artériels et les opportunités que cette technique pourrait apporter dans le traitement de l'athérosclérose.

Premièrement, nous présentons l'état de la connaissance sur les mécanismes et l'impact de la LIOB sur le milieu environnant, en particulier dans les tissus biologiques. Nous discutons de leur modélisation, par simulation et par reproduction dans des échantillons artificiels organiques et inorganiques.

La section suivante de cette thèse est dédiée à l'étude des effets de la LIOB au niveau cellulaire. Nous discutons d'une approche selon laquelle la LIOB pourrait être d'un certain intérêt dans le traitement de l'athérosclérose ou d'autres pathologies qui pourraient bénéficier d'un contrôle de la population de cellules encourant une mort cellulaire contrôlée (apoptose). Nous étudions par la suite les effets de la LIOB sur des populations de cellules épithéliales dans des gels 2D et 3D. Nous contrôlons l'augmentation du nombre de cellules nécrotiques et apoptotiques, dans différents régimes d'ablation.

Nous présentons alors les méthodes et résultats de notre ablation sous la surface de tissus artériels, dans des tissus sains et athérosclérotiques. Au cours d'expériences ex-vivo, nous nous concentrons sur l'observation de la bulle produite par LIOB et les dommages structurels subis par les tissus. Dans les expériences in-vivo, nous examinons les effets sur la nécrose et l'apoptose aux abords de la zone cible, et comparons nos résultats avec les expériences précédentes.

En dernier lieu, nous étudions la question de la transmission de pulse à haute intensité de manière non-invasive, point essentiel dans le développement d'applications biomédicales. Nous envisageons deux approches : par la transmission via une fibre optique à cœur vide, et par la modulation du front d'onde dans une fibre multi-cœurs. Nous démontrons l'ablation de tissu biologique en profondeur avec chacune de ces deux méthodes.

Mots-clef: *rupture optique induite par laser, ablation en profondeur, optique non-linéaire, microchirurgie, plasma, athérosclérose, apoptose, endoscopie, modulation de front d'onde, fibre multi-cœur.*

Acknowledgements

The main part of this work has been done in the Optics Laboratory of EPFL under the supervision of Professor D. Psaltis. I would like to express my gratitude to him for giving me the opportunity to work in such a great research environment and with a talented, friendly and dynamic team. I also would like to thank him for his ideas, advises, challenging questions and guidance without which the completion of this thesis would not have been possible. Also I would like to thank Marie-Noëlle Giraud from the University of Fribourg for her contribution to my PhD thesis and her availability to discuss the biological aspects.

I would like to address special thanks to Donald Conkey, for his patience and openness, as much as for his scientific qualities and wise advice. His impact on this work was essential in conducting this project to its conclusion, and his rigor was essential in dealing with many facets of this project.

My fellow members from the *Ablation Team*, Marilisa Romito and Eirini Kakkava are also deserving of all my appreciation, as a constant source of freshness and energy, on top of proving to be great assets in the laboratory. Nicolino Stasio, Alexandre Goy and Grégoire Laporte have also helped me more than shows in this final thesis, as they have always been available to share ideas about my project, science, and really any conversation researchers might have a fancy starting around the coffee machine. I would also like to thank the *Fribourg Team*, and in particular Aurélien Frobert and Jérémy Valentin for their expertise in the field of animal cardiology and great conversations to help Donald improve on his French, and Manish Jain for his readiness to help in experiments. Finally, a word of acknowledgement to Carole Berthet, who was always eager to share a smile and facilitate our everyday life by her motivation and efficiency.

Some images presented in this thesis have been acquired in the Bioimaging facility. I would like to thank all the BIOP team for their kindness and their expertise, especially Thierry Laroche for his help since the first days of the project. Fabien Kuttler and Benjamin Rappaz from the Biomolecular Screening Facility of EPFL also played a strong role in the later stages of this project, by providing training and advice on every topic related to cell culture. The members from the Histology Core Facility of EPFL, especially Jessica Dessimoz and Mancini Gianfillipo also showed great support and professionalism in providing training, advice and technical support regarding staining and histology. Also, the advice and explanations of Damien Lotterie were invaluable in the understanding, usage and modification of his Transmission Matrix code. Informal support and advice from my friends Nathalie Brandenburg and Kaspar Rothenfusser were also relevant to the shaping of this thesis, especially regarding the investigation of in-vitro experiments. I would also like to thank Pooria Hadikhani and Alexandre Goy for their help in the simulation of bubble expansion and BPM.

I would like to mention all the member of the Laboratory of Optics, past and present: Ye Pu, Rachel Grange (thank you for giving me the opportunity to discover Optics Laboratory during one of my Master projects), Chia-Lung Hsieh, Andreas Vasdekis, Wuzhu Song, Jae-Woo Choi, Xin Yang, Ioannis Papadopoulos, Salma Fahari, Laurent Decloux, Marcin Zielinski, Miguel Modestino, Sébastien Walpen, Mohammad Hashemi, Mortesa Hashani Shoreh, Alexandre Burnand, Joowon Lim, Fauzia Albertin. Finally, thanks to our neighbors from the LAPD team for their joy of living and the good atmosphere in the building, and being such good sport at laser tag.

And finally, a huge thank to my family and friends in and outside EPFL, in Switzerland and abroad, for their encouragements and unwavering support.

Contents

| | |
|---|-----------|
| Chapter I: Introduction | 1 |
| I.1.1 Technology and knowledge synergies..... | 2 |
| I.1.2 Overview of the Thesis | 2 |
| Chapter II: Introduction to Laser-Induced Optical Breakdown (LIOB) in tissue | 5 |
| Part 1: Background about laser-tissue interaction..... | 6 |
| II.1.1 One-photon energy exchange | 6 |
| II.1.2 Two-photon absorption | 7 |
| II.1.3 Multi-photon absorption and ionization..... | 7 |
| Part 2: Modeling Laser-Induced Optical Breakdown and its effects | 9 |
| II.2.1 From multiphoton ionization to plasma creation | 9 |
| II.2.2 Creation of a cavitation bubble | 11 |
| II.2.3 Focus-shift at high intensities | 16 |
| Part 3: Direct effects of LIOB on cells..... | 19 |
| II.3.1 Generation of reactive oxidizing species | 19 |
| II.3.2 Mechanical effect of LIOB at the cellular level | 21 |
| Part 4: Observation of LIOB in phantoms | 23 |
| II.4.1 Fiber laser set-up..... | 23 |
| II.4.1.1 Overview of the set-up..... | 23 |
| II.4.1.2 Scanning using 3D stage | 24 |
| II.4.1.3 Modification for high-speed imaging | 24 |
| II.4.2 Preparation on phantoms | 25 |
| II.4.2.1 Introduction to phantoms | 25 |
| II.4.2.2 Agar phantoms | 25 |
| II.4.2.3 PDMS phantoms | 25 |
| II.4.3 Observation of ablation in phantoms | 26 |
| II.4.3.1 Elongation in glass | 26 |
| II.4.3.2 Bubble size increase in Agar | 28 |

| | |
|--|-----------|
| II.4.3.3 Lateral shielding in PDMS | 29 |
| II.4.4 Conclusion | 32 |
| Chapter III: Apoptosis and Atherosclerosis | 33 |
| Part 1: Introduction to Apoptosis..... | 34 |
| III.1.1 Overview of the apoptotic pathways..... | 34 |
| III.1.2 Observation of apoptosis | 35 |
| Part 2: LIOB and Atherosclerosis | 37 |
| III.2.1 Atherosclerotic and the role of apoptosis..... | 37 |
| III.2.2 Atherosclerosis as a multi-facet pathology..... | 39 |
| III.2.3 A model of the impact of LIOB on atherosclerotic plaques..... | 40 |
| Part 3: Investigation of LIOB in-vitro | 42 |
| III.3.1 Materials and methods..... | 42 |
| III.3.1.1 Integration of an OCT to the fiber-laser set-up | 42 |
| III.3.1.2 Cell Cultures | 44 |
| III.3.1.2.1 Cell line : HCT116 | 44 |
| III.3.1.2.2 2D cell cultures | 44 |
| III.3.1.2.3 Agar gels..... | 45 |
| III.3.1.2.4 Paraffin sections of agar gels..... | 45 |
| III.3.1.2.5 PEG Hydrogel..... | 47 |
| III.3.1.2.6 Matrigel | 48 |
| III.3.1.3 Staining of cell cultures | 48 |
| III.3.1.3.1 Fluorescent signaling of the whole cellular population: Hoechst and DAPI 48 | |
| III.3.1.3.2 Fluorescent signaling of necrotic cells..... | 49 |
| III.3.1.3.3 Fluorescence signaling of apoptotic cells: TUNEL..... | 49 |
| III.3.1.3.4 Caspase 3 immunostaining..... | 49 |
| III.3.1.3.5 Annexin V staining | 50 |
| III.3.1.3.6 Signaling of ROS-induced cellular damage..... | 50 |
| III.3.1.3.7 3.3.1.4 Fluorescence evaluation setup..... | 51 |
| III.3.2 LIOB and range studies of Necrosis | 51 |
| III.3.3 Laser irradiance and apoptosis | 54 |
| Chapter IV: Subsurface ablation of arterial tissue | 61 |
| Part 1: Observation of LIOB in scattering media..... | 62 |

| | |
|---|-----------|
| IV.1.1 Simulation for scattering in turbid media | 62 |
| IV.1.1.1 Effect of scattering on intensity | 62 |
| IV.1.1.2 Monte Carlo simulation of scattering through turbid media..... | 63 |
| IV.1.2 Ex-vivo measurements of bubble size | 64 |
| IV.1.2.1 Materials and Methods | 64 |
| IV.1.2.1.1 Overview of the optical set-up..... | 64 |
| IV.1.2.1.2 Pulse duration selection..... | 66 |
| IV.1.2.1.3 Fourier filtering | 66 |
| IV.1.2.1.4 Focusing on the sample..... | 66 |
| IV.1.2.2 Preparation of samples..... | 67 |
| IV.1.2.2.1 Pig artery samples | 67 |
| IV.1.2.2.2 Mice arteries and abdominal fat..... | 67 |
| IV.1.2.3 Measurements of ablation bubbles | 68 |
| Part 2: Ex-vivo ablation in atherosclerotic plaque..... | 72 |
| IV.2.1 Materials and methods..... | 72 |
| IV.2.1.1 Animal and sample preparation | 72 |
| IV.2.1.2 Ablation Patterns | 72 |
| IV.2.1.3 Preparation for cryocutting | 73 |
| IV.2.1.4 Staining | 74 |
| IV.2.1.4.1 General morphology staining with H&E..... | 74 |
| IV.2.1.4.2 Oil Red O | 74 |
| IV.2.1.5 Ablation characterization metrics | 75 |
| IV.2.2 Ablation characterization results..... | 76 |
| IV.2.2.1 Overview of the structural damage induced..... | 76 |
| IV.2.2.2 OCT observation of ultrafast ablation | 77 |
| IV.2.3 Discussion | 80 |
| Part 3: In-vivo Ablation..... | 82 |
| IV.3.1 Materials and methods..... | 82 |
| IV.3.1.1 Modification of the optical system..... | 82 |
| IV.3.1.2 Preparation and surgery of rats..... | 83 |
| IV.3.1.3 Paraffin sectioning | 85 |
| IV.3.1.4 Timeline and Troubleshooting | 86 |
| IV.3.2 Bubble and structural damage..... | 87 |

| | |
|--|------------|
| IV.3.2.1 OCT images of LIOB cavitation bubbles | 87 |
| IV.3.2.2 Histology cuts and damage | 87 |
| IV.3.2.3 Biological effects of ablation | 88 |
| IV.3.2.3.1 4.3.1 TUNEL Staining results | 88 |
| IV.3.2.3.2 Caspase 3 staining results..... | 90 |
| IV.3.3 Discussion on success and shortcomings of the in-vivo experiments..... | 92 |
| IV.3.3.1 OCT as a good way to monitor in-vivo LIOB | 92 |
| IV.3.3.2 Difficulties in observing ablation on histology cuts | 92 |
| IV.3.3.3 Relevance of apoptosis observation and implications for plaque ablation..... | 93 |
| IV.3.3.4 Conclusion on in-vivo experiments | 93 |
| Chapter V: Delivery high energy pulses | 95 |
| Part 1: Introduction to high energy pulse delivery through fiber | 96 |
| V.1.1 Minimally invasive approach to the treatment of atherosclerosis..... | 96 |
| V.1.2 Optical fibers for high energy pulse delivery | 97 |
| Part 2: Design for ex-vivo ablation | 99 |
| V.2.1 Design of a simple catheter probe | 99 |
| V.2.2 Ex-vivo ablation..... | 99 |
| V.2.3 Toward future designs..... | 102 |
| Part 3: Wavefront shaping for light control through multi-core fiber for ex-vivo ablation | 105 |
| V.3.1 Materials and Methods | 105 |
| V.3.1.1 The optical setup | 105 |
| V.3.1.2 The metal samples | 108 |
| V.3.1.3 The biological sample | 108 |
| V.3.2 Introduction to Transmission Matrix and multicore fibers | 108 |
| V.3.2.1 The multicore fibers..... | 108 |
| V.3.2.2 Measurement of the TM for a MCF..... | 110 |
| V.3.2.3 Use the TM for focusing through a multicore fiber | 111 |
| V.3.3 Dependence of peak intensities at focus | 111 |
| V.3.3.1 Optimizing the reconstruction of a focus | 112 |
| V.3.3.2 Measurement of focusing efficiency | 112 |
| V.3.4 Amplitude Correction | 114 |
| V.3.4.1 Reconstructed focus intensity flatness across output field | 114 |

| | |
|---|------------|
| V.3.4.2 Amplitude homogenization | 115 |
| V.3.5 Metal and Ex-vivo ablation | 116 |
| V.3.5.1 Metal ablation | 116 |
| V.3.5.2 Ex-vivo ablation..... | 117 |
| V.3.6 Conclusion | 119 |
| Chapter VI: Conclusion..... | 121 |
| Appendix A: Making of the gels and phantoms..... | 130 |
| Appendix B: Monte Carlo simulation..... | 133 |
| Appendix C: Staining Protocols | 136 |
| Appendix D: Challenges in in-vivo manipulation experiments | 138 |
| Appendix E: Simultaneous control of ablation scan and OCT imaging..... | 140 |
| Appendix F: Complementary experiments in-vivo | 143 |
| Appendix G: Design of catheters | 147 |
| Appendix H: Autocorrelator for pulse duration measurement..... | 149 |

List of figures:

| | |
|---|----|
| Figure I-1 : <i>Diagrams representing the different phases of an LIOB event.</i> | 3 |
| Figure II-1: <i>Calculated optical breakdown threshold as a function of laser pulse duration for various laser wavelengths</i> | 11 |
| Figure II-2: <i>The pressure of liquid water along the bimodal, spinodal and kinetic spinodal as a function of temperatures.</i> | 12 |
| Figure II-3: <i>Simulation of light intensity I ($W.m^{-2}$), plasma density ρ ($.cm^{-3}$) and pressure around the cavitation bubble P (bar) around focus for two pulses close to LIOB threshold in water.</i> | 14 |
| Figure II-4: <i>initial processes of the decomposition of water by ionizing radiations.</i> | 20 |
| Figure II-5: <i>Diagram of the fiber-laser ablation set-up.</i> | 23 |
| Figure II-6: <i>Experiments on filament creation in glass, with different pulse energy and pulse overlap.</i> | 27 |
| Figure II-7: <i>Measurements of bubbles in Agar gels.</i> | 29 |
| Figure II-8: <i>Experiments on filament creation in PDMS,</i> | 31 |
| Figure II-9: <i>Impact of pulse energies on maximum focus shift</i> | 32 |
| Figure III-1 <i>Schematic representation of the apoptotic pathways.</i> | 35 |
| Figure III-2: <i>Schematic representation of the location of plaque in an artery, and the different parts of the artery</i> | 37 |
| Figure III-3. <i>Mechanisms regulating the recruitment and accumulation in mouse atherosclerotic plaque.</i> | 38 |
| Figure III-4: <i>Integration of the ablation beam in the OCT head</i> | 43 |
| Figure III-5: <i>Cell cultures for ablation and histology preparation for immunostaining.</i> | 46 |
| Figure III-6: <i>20 μL PEG hydrogel at the bottom of a 24 wells plate.</i> | 48 |
| Figure III-7: <i>Observation of bubbles in PEG hydrogel.</i> | 52 |
| Figure III-8: <i>Apoptosis signal in Agar gel cultures</i> | 53 |
| Figure III-9: <i>2D ablation and apoptosis measurement</i> | 54 |
| Figure III-10: <i>Hystology cut of Agar gel</i> | 55 |
| Figure III-11: <i>Apoptosis of HCT 116 in PEG Hydrogel, Caspase 3 staining</i> | 56 |
| Figure III-12: <i>Apoptosis of HCT 116 in matrigel, Caspase 3 staining</i> | 57 |
| Figure III-13: <i>Apoptosis of HCT in matrigel, Annexin V staining.</i> | 58 |

| | |
|---|-----|
| Figure IV-1: Calculation of the peak intensity in a focus at different depths in a scattering media | 63 |
| Figure IV-2: Diagram of the ablation setup based on a regenerative amplifier.. | 65 |
| Figure IV-3: Diagram explaining why we initially used coverwells on our samples. | 67 |
| Figure IV-4: Ex-vivo data measurements of LIOB-induced bubbles | 69 |
| Figure IV-5: Bubble diameter after single-shot ablation by pulses of 1 ps and various peak intensity in arteries | 71 |
| Figure IV-6: Representation of the ablation pattern | 73 |
| Figure IV-7: Image of a mouse artery placed vertically in a sample mold filled with OCT | 74 |
| Figure IV-8: Images of representative ablation holes from histological slice in arterial tissue..... | 75 |
| Figure IV-9: Characterization results of ultrafast ablation in arterial tissue and atherosclerotic plaque | 77 |
| Figure IV-10: Volume ablation in arterial wall. | 78 |
| Figure IV-11: Volume ablation of ApoE-KO mouse plaque with a 50x100 μm^2 pattern, stained with Oil red On. | 79 |
| Figure IV-12: Volume ablation of ApoE-KO mouse plaque with a 50x100 μm^2 pattern and bubble collapse timelapse | 80 |
| Figure IV-13: Optical set-up used for in-vivo ablation. | 83 |
| Figure IV-14: Protocol for the animal surgery in preparation the laser ablation ablation. | 84 |
| Figure IV-15: OCT images of the effects of LIOB triggered inside the artery in-vivo..... | 87 |
| Figure IV-16: Histological observation of ablation holes made in-vivo | 88 |
| Figure IV-17: Data from TUNELstaining of samples ablated in-vivo | 89 |
| Figure IV-18: Data from Caspase 3 immunostaining of samples ablated in-vivo | 91 |
| Figure V-1: Arterial wall ablated through a catheter prototype..... | 101 |
| Figure V-2: Plaque ablated through a catheter prototype. | 102 |
| Figure V-3: Use of a balloon catheter for use in human coronary arteries, inserted in a rabbit femoral artery. | 103 |
| Figure V-4: The Transmission Matrix measurement setup and concept. | 106 |
| Figure V-5: Picture of the distal facet of the multicore fiber | 107 |

| | |
|---|-----|
| Figure V-6: <i>Efficiency of focus creation for different output powers through the multicore fiber</i> | 113 |
| Figure V-7: <i>Pulse duration broadening for different initial pulse durations and measured values of power at the output of the fiber.</i> | 114 |
| Figure V-8: <i>Amplitude homogenization.</i> | 115 |
| Figure V-9: <i>ablation of gold through the multicore fiber</i> | 116 |
| Figure V-10: <i>Ablation of different material through a 4.5 cm long multicore fiber using wavefront shaping.</i> | 118 |

Chapter I: Introduction

As living beings, light impacts us directly and in many different ways. For example, light can stimulate the production of some proteins in our bodies, or activate photoreceptors which allow us to see what is around us. In summer, light can also burn our skin, or possibly damage our DNA with irreversible and dramatic consequences. On the surgery table, laser light can allow physicians to establish advanced diagnosis, remove tissues, or locally remodel organs or biological material.

The way light interacts with cells and tissues is indeed a complex process, with numerous different regimes depending on the type of light and what sample is considered. In its most basic form, light-tissue interaction is an extension of what we know about light-matter interaction. Part of the knowledge accumulated from models of physics or industry applications can be used for biological samples. Yet, the intricacies inherent to the behavior of organic tissues make it necessary to verify, and sometimes adapt, expectations to match practical usability.

The applications of lasers in the field of biology and medicine have followed this course, with, along the way; many hopes, successes, but also disappointment, and there are still many more ideas to be formulated and tested. If problems with charring and healing of tissues has significantly limited the use of high average power lasers for thermal ablation, more recent “cold ablation” has known some success and is actually becoming the benchmark treatment for some pathologies of the eye. Indeed, not every cell will react in the same way to being exposed to light, or to the side-effects of a neighboring cell being exposed.

When a new type of laser is developed, it usually does not take long before its effect on biological tissue is investigated in one way or another. But new, unexpected results can still be discovered decades after its usage has been established. More than 50 years of research on development of new lasers has led to a situation where the parameters defining lasers reach values spanning over several orders of magnitudes. Wavelength ranging from a few hundreds to tenths of thousands of nanometers, bursts of light with durations from the attosecond to continuous emission, repetition rate above the megahertz range, and peak energies up to TW.cm^{-2} have become common values in commercial laser systems. A wide variety of combinations of these parameters have found use in biomedical optics - some for observation purposes, others for triggering modifications of the target for instance- but the wealth of reactions from one tissue to the other adds to the complexity of establishing laser-tissue interactions.

1.1.1 Technology and knowledge synergies

Science and knowledge do not progress only by leaps or revolutions. Sometimes an *enabling* technology can lead to progress in a seemingly unrelated field because it made it possible for the right tools to be developed.

Ultrafast laser-matter interaction is a very active field with vast applications in industry, and comparatively limited impact in medical technologies to date. As we will see in Chapter 2, ultrafast ablation is a multi-photon process; hence the axial localization of the ablation is limited to the focal volume, which makes it an appropriate tool when high precision or subsurface ablation is desired. Ultrafast ablation has proven useful in high-precision manufacturing¹ and has a great potential for biomedical microsurgery². Of course, medical applications can take time to reach the market, if anything else because of the requirements on safety and biological tissues complexities. But another limitation is the difficulty of transmitting through an optical fiber a pulse of high peak powers (necessary to the triggering of LIOB) from the laser to a target area in a patient. Fiber technologies which can either withstand these high peak powers or lower them during transport have the potential to be one of these enabling technologies, bringing LIOB closer to biomedical applications.

But does LIOB have the potential to transform some medical treatments as it is transforming some segments of micromanufacturing? Here again, synergy between different research fields can prove to be valuable in determining the answer. As an example, our knowledge of atherosclerotic plaque genesis, growth, and rupture has developed significantly in the past 15 years, and we now know that regulated cell death (apoptosis) can play an important role in the development of the plaque.

Taking into account 1) the proven ability of LIOB to specifically target and destroy individual cells (see Chapters 2 and 3), 2) that destroying apoptotic cells could prove beneficial to stabilizing an atherosclerotic plaque (see Chapter 4), and that 3) development in optical fibers may make it possible to trigger LIOB in the plaque by using a catheter (see Chapter 5), we considered the possibility of using LIOB as the basis of a treatment for atherosclerosis. This approach implies studying the biological and structural response of cells and tissues subject to LIOB, but also investigating ways to deliver high peak powers to a target ablation area; both have the potential to provide benefits to the more general fields of cell reaction to LIOB and high peak power energy transfer.

1.1.2 Overview of the Thesis

Considering the recent developments in lasers able to produce ultrashort pulses, as much as progress made in delivering these pulses, ultrafast lasers are currently considered for many applications, from two-photon endomicroscopy to high precision cutting and ablation. The current thesis investigates this last approach, with a focus on the effect of ultrafast pulses with high peak energy on arterial tissues and possible impacts on atherosclerotic tissues.

In this ultrafast and high photon density regime, a destructive light-matter interaction called Laser-Induced Optical Breakdown (LIOB) takes place. The concept of LIOB is the following: the

intense optical field will create a plasma in the focal volume, which will quickly expand in a cavitation bubble (Figure I-1). The generation of quasi-free electrons in an aqueous medium can modify the ionization potential around the focus and lead to oxidation of surrounding material. We will review the generation of this process and its possible impact on tissues in Chapter 2.

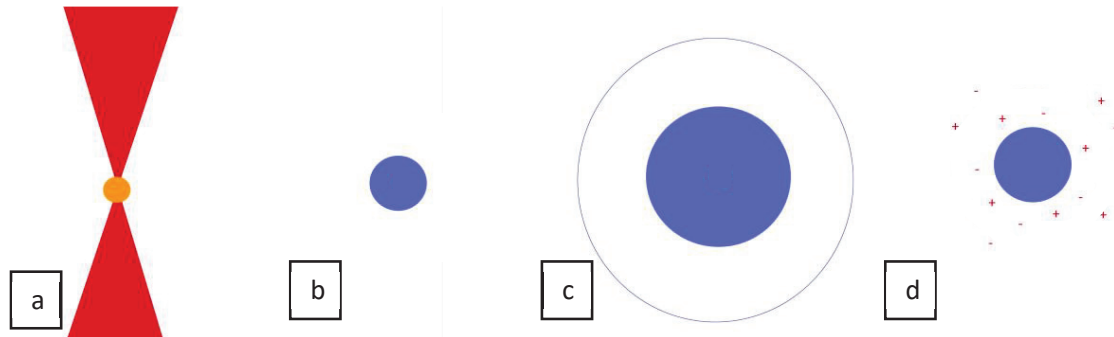


Figure I-1 : *Diagrams representing the different phases of an LIOB event, taking place from the left to the right. (a) exposure to a sample to high peak intensities, and creation of a short-lived, high electron density plasma. (b) creation of a cavitation bubble from the local increase of pressure at the plasma location. (c) fast increase in size of the bubble, driven by its internal pressure, and creation of a shockwave carried by the bubble expansion. (d) collapse of the bubble, and diffusion or recombination of ions and other reactive species created by reaction of the free electrons of plasma.*

The precise localization of structural damage due to the direct effects of LIOB can in theory allow for very precise biomedical applications. But the generation of oxidizing species is less controllable, and could have some specific impact in atherosclerotic plaques, as Chapter 3 will present. In-vitro experiments to evaluate these effects were conducted to help assert these risks.

If the cellular response to LIOB is critical in assessing potential uses of ultrafast pulses in treatment of atherosclerotic plaques, the way tissue behaves when subject to LIOB is also essential. Indeed, scattering of light by the tissue will set limits to the maximum depth of ablation, and the state of a sample of arterial wall will impact the bubble dynamics following LIOB. Chapter 4 introduces ex-vivo and in-vivo measurements and discussion on structural damage and apoptosis, for a more global picture of the reaction of arteries to LIOB.

In Chapter 5, we discuss the challenges of designing a catheter for biomedical applications in the artery or other cavities. After presenting a first prototype of catheter for ablation, we introduce the concept of multicore fibers for triggering LIOB, and demonstrate its feasibility.

The main results are summarized in Chapter 6, and followed by a discussion about the prospect of future developments in investigating the use of LIOB for biomedical applications.

Chapter II: Introduction to Laser-Induced Optical Breakdown (LIOB) in tissue

Laser-Induced Optical Breakdown (LIOB) is a complex process, whose understanding involves concepts of different fields of Physics, from optics to thermodynamics to plasma physics. The current chapter aims at providing an overview of the mechanism of LIOB and provide insights into the current knowledge in the domain. Since this Thesis is targeted at biomedical applications, we will relate simulations of this complex light-matter interaction to the effects of what should be expected in the biological samples considered in following chapters.

Hence, we will first describe some general concepts of laser-matter interaction, and how a high energy optical field can free large numbers of electrons from their atoms to create a plasma. Then, we will look into what happens when the plasma is created, and why it leads to a rise in temperature and pressure. And why this rise in pressure induces the creation of a cavitation bubble.

We will then discuss why the apparition of a plasma in a living organism can be detrimental to surrounding cells, both from a chemical and from a mechanical point of view.

Finally, we will go beyond the theoretical models to build an understanding of what could be the behavior of samples mimicking properties of tissue when they are subject to LIOB.

Part 1: Background about laser-tissue interaction

II.1.1 One-photon energy exchange

An initial way to look at laser-tissue interactions can be to consider tissue as a semi-conductor which is subjected to a flow of energy-packed photons. Some molecules in the tissue are more prone than others to absorb the energy photons, and can release it back in various forms. One of the most well-established use of this model is used to explain fluorescence of proteins, and its associated effects such as bleaching, quenching by triplet states or multi-photon fluorescence.

As a flux of photons with similar properties, one of the parameters defining a laser beam is the energy of its photons, defined by the Planck-Einstein relation:

$$E_p = h\nu \quad (\text{Eq. 1})$$

where ν is the wave frequency of the photon, and h is the Planck constant.

This energy defines how individual photons interact with molecules they come across. For the range of wavelengths between UV and NIR, this interaction can in theory range from not-being absorbed if the photon energy is not within the energy band of the molecule, to freeing an electron from a molecule orbital if the photon energy is above the ionization energy ΔE of the molecule, or induce vibrational transitions.

An example of linear low-energy laser-tissue interaction is fluorescence of proteins and other molecules. It takes place when a molecule has been excited to its first electronically excited state, S_1 , and relaxes to its ground state S_0 by emitting a photon. Competing relaxation mechanisms, such as vibrational or the conversion to a triplet state, can also happen and reduce the fluorescence efficiency.

However, most organic molecules constituting biological tissues are not inherently strongly fluorescent. In consequence, when they are excited by a laser beam, they mostly relax through dissipation of heat in the surrounding material by vibrational relaxation. This type of relaxation can cause a significant increase in temperature of a tissue or other sample, like when our skin warms up in the Sun. Lasers can induce this phenomenon in a confined area and to such high level as to induce thermal damage in a tissue.

From a historical perspective, thermal damage has been the first type of laser-tissue interaction to be used for surgical intervention. In 1972, M.D Geza J. Jako, by means of a system by Dr. Michael Polanyi from the American Optical Company, used a CO₂ laser for in-vivo ablation of vocal cord polyps in dogs, making it the first in-vivo use of tissue ablation using a laser. The device was a laryngoscope based on a mechanical arm comprising a set of mirrors to redirect light on a target area, and the choice of a CO₂ laser, whose wavelength is in the infrared at $\lambda=10600$ nm, was determined by the fact that water absorbs light strongly at this wavelength. Although more than 40 years old, their system already gave answers to some fundamental questions which every

future laser-ablation system would have to answer: how to direct the laser beam toward the target tissue? How to cope with the low absorption of light by tissue? How to give the surgeon a way to monitor the process of ablation? And finally, how to limit damage to surrounding tissues? Answers to these questions can vary a lot from one system to the next, depending on laser type and ablation target, and we will discuss some of these in the pages to come.

II.1.2 Two-photon absorption

When the density of photons reaching a target is sufficiently high, such as when a high-power laser is focused on a sample, several photons can interact with a molecule. In this process, their exciting effects on its electrons cumulate and the difference between the initial energy level of the molecule and its excited state is equal to the sum of the energy of the two photons. This process scales with the fluence of the two photon populations. In the case where we consider the interaction of two identical photons with a molecule, we talk about two-photon absorption and the process scales with the square of the fluence. Instead of considering the absorption coefficient, α , which defines linear absorption, we then consider the cross-section σ defined for a molecule in Goeppert-Mayer units (G.M). The two-photons nature of the process can be observed in the G.M unit itself, since 1 G.M is equal to $10^{-50} \text{ cm}^4 \text{ s photon}^{-1}$, which corresponds to the product of two areas (one for each of the two photons) multiplied by the duration within which the two photons can interact.

This cross-section can be related to the polarization reaction of the sample to an electric field, as it depends on the third order non-linear susceptibility $\chi^{(3)}$ used to define polarization reaction P of a medium to an electromagnetic field:

$$P = P_0 + \epsilon_0 \chi^{(1)} E + \epsilon_0 \chi^{(2)} E^2 + \epsilon_0 \chi^{(3)} E^3 + \dots \quad (\text{Eq. 2})$$

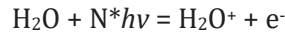
Where P_0 is the built-in polarization (equal to 0 except in ferroelectric materials), ϵ_0 is the electric permittivity of free space and E is the electric field. A particle which has been excited by two-photon absorption can relax in the same ways as any excited molecule.

II.1.3 Multi-photon absorption and ionization

In a similar way as two photons can interact together to excite a molecule to a higher energy level than their individual levels of energy, higher fluence can lead to more photons interacting to excite a molecule at even higher energy levels. Three-photon excitation, and the associated three-photon microscopy is an example of this, allowing for 3 photons in the NIR domain to trigger fluorescence in the ultra-violet. However, even higher levels of accumulated energies can lead a molecule to reach excitation levels where it is not stable anymore, and it has to release an electron. This is the basis of multi-photon ionization, a concept which can have dramatic implications when it happens on a large scale.

If a molecule is ionized by a very intense flux of photons, a free electron (in gases) or quasi-free electron (in liquids) is being released. Formally, quasi-free electrons are electrons which are unbound in at least one direction, accounting for their ability to travel freely despite the influence

of surrounding molecules³. The number of photons interacting together to ionize a molecule depends on the ionization potential of a molecule and the energy of the individual photons. For example, in a model (not taking into account subsequent recombination of molecules) treating water as an amorphous semiconductor⁴, the ionization energy of liquid water, ΔE_w , is 6.5 eV, and the energy of a photon at 1030 nm, E_p , is about 1.2 eV. We are thus considering the classical charge-separation process defined by:



Which can happen if

$$n^*E_p = \Delta E_w + E_k \quad (\text{Eq. 3})$$

Where n is the number of photons interacting simultaneously to excite the molecule, and E_k is the excess energy transmitted as kinetic energy to the electron. According to this model, 6 photons would be required to act simultaneously in exciting a water molecule to ionize it. In practice, the number of photons required for multiphoton ionization by ultrashort pulses is slightly above this value. For very short pulses (below the nanosecond regime) the ionization energy must be replaced by the effective ionization potential $\Delta E'$ that includes a factor to account for the energy of the oscillations of the electron because of the strong electrical field from the laser.

$$\Delta E' = \Delta E_w + e^2 F^2 / (4m\omega^2) \quad (\text{Eq. 4})$$

Where e is the charge of an electron, F is the frequency of the electrical field, F is its amplitude, and m is defined as:

$$1/m = 1/m_c + 1/m_v \quad (\text{Eq. 5})$$

Where m_c is the mass of the quasi-free electron in the conduction band, and m_v is the mass of the hole in the valence band. For the case of water (assimilated here to amorphous silicon for time frames below 1 ns), the authors find $\Delta E' = 7.4 \text{ eV}$, and the simultaneous interaction of 7 photons is in fact required for photoionization of water. In other words, the probability of a multiphoton ionization event in water is proportional to I^7 .

In water, the created electron would be solvated in the order of 200 fs⁵, but the time required for it to recombine with other molecules will strongly depend on the molecules population, and electron population, surrounding it.

Part 2: Modeling Laser-Induced Optical Breakdown and its effects

II.2.1 From multiphoton ionization to plasma creation

In practice, high laser fluence on a sample can trigger ionization on a significant number of molecules in the focal volume, and produce a population of quasi-free electrons high enough that they can be considered to form a plasma. A threshold value of electron density ρ_{crit} corresponding to the apparition of a plasma has been defined in different ways in literature. But in the field of laser-matter interactions, this threshold is typically linked to observable modifications of the sample: at minimum from changes in the reflectivity of the sample⁶, particularly for hard transparent samples, but more commonly from the apparition of a bubble⁷, marker of a laser-induced optical breakdown (LIOB). This threshold value of electron density ρ_{crit} was measured to be in the order of 10^{18} to 10^{20} cm⁻³ in water by several research groups studying the dynamics of plasma⁸⁻¹⁰. However, a sample will start exhibiting modification of some of its physical properties (among which temperature at focus, modification of absorption spectrum, and polarization of molecules) below this threshold, accounting for a *low-density plasma*, which can be important for biological or other sensitive samples.

Although investigation of the exact chemical effects is out of the frame from our work, understanding of the general concepts linking the ionization of material in focus to the apparition of a bubble is important for this project. We will thus present these concepts here.

Two competing ionization mechanisms can lead to the creation of a plasma in the focal volume of a sample: multiphoton ionization and cascade ionization. As we wrote earlier, multiphoton ionization can not only free an electron from a molecule, but can also imbue it with extra kinetic energy. A free or quasi-free electron in the focal volume can continue to absorb energy from photons, and thus further increase its kinetic energy, by a non-resonant process called inverse Bremsstrahlung¹¹ which requires the presence of a third particle, atom or ion.

The kinetic energy of the quasi-free electrons in the focal volume can thus continue to increase after the photoionization event, but the electrons can also transmit energy to other surrounding electrons by energy exchange during collisions. If the kinetic energy transferred to an electron in the valence band is above the effective ionization potential, it can tear the electron from the atom it is attached to, effectively increasing the quasi-electron population by one. As this population grows, the probability of impact ionization increases, which can effectively lead to a surge in electron density called *avalanche ionization*. As opposed to multiphoton ionization, avalanche ionization requires the presence of at least one initial quasi-free electron, referred to as seed electron. This seed electron can either be provided by photoionization or by electron tunneling from the valence to the conduction band.

The decrease of the electron density on the focal volume is governed by two phenomena: the diffusion of quasi-free electrons out of the focal volume, and the recombination of quasi-free electrons with molecules in the focal volume.

The evolution of the plasma density in the focal volume can be defined as follows:

$$\frac{d(\rho)}{dt} total = \frac{d(\rho)}{dt} mpi + \frac{d(\rho)}{dt} casc + \frac{d(\rho)}{dt} diff + \frac{d(\rho)}{dt} rec \quad (\text{Eq. 6})$$

where $\frac{d(\rho)}{dt} total$ is the change of whole quasi-free electrons population in the focal volume, $\frac{d(\rho)}{dt} mpi$ is the evolution of the population produced by multiphoton ionization, $\frac{d(\rho)}{dt} casc$ is the evolution of the population produced by avalanche ionization, $\frac{d(\rho)}{dt} diff$ is the evolution of the population diffusing out from the focal volume, and $\frac{d(\rho)}{dt} rec$ is the evolution of the population recombining in the focal volume.

Vogel et al. reviewed this process in details¹² and presented the following model for the evolution of plasma density for a light irradiance I at focus close to the optical breakdown threshold value I_{th} . $\frac{d(\rho)}{dt} mpi$ is independent from ρ and is proportional to I^n . This can be understood by analogy to 2-photon fluorescence with n photons interacting simultaneously with an electron. $\frac{d(\rho)}{dt} casc$ is equal to zero if there is no seed electron available to start the avalanche ionization process (which is assumed to be the case until the irradiance at focus reaches I_{th}). From the moment when a seed electron is available, $\frac{d(\rho)}{dt} casc$ is proportional to both ρ and I . $\frac{d(\rho)}{dt} diff$ is a function of the shape of the focal volume and of the electron diffusion rate in the sample, and is proportional to ρ and independent from I . $\frac{d(\rho)}{dt} rec$ is independent from I and proportional to ρ^2 according to an empirical model by Docchio et al.¹³

From this model, ultrashort pulses strongly favor MPI compared to longer pulses, because of their high peak irradiance. Their ability to tear electrons from their orbitals with several photons interacting simultaneously increases the chance of providing them with a high kinetic energy and trigger an avalanche ionization very early in the ionization process.

The effect of avalanche ionization is more dramatic for longer pulse duration (in the order of nanosecond) as opposed to ultrashort pulse (in the order of femtosecond or picosecond), for identical pulse energies, in a couple of aspects. First, quasi-free electrons can have a lifetime of several tens of picosecond or more before being retrapped¹⁴, during which they can accumulate energy via inverse Bremsstrahlung if they are irradiated by laser light for this duration. Secondly, MPI is less probable in longer pulses, and it is possible that the first seed electron only appears relatively late compared to the whole pulse duration. In this case, avalanche ionization will not “benefit” from the whole pulse energy, which can lead to strong pulse-to-pulse variations in intensities.

Another interesting conclusion from this model is that the radiant exposure threshold is lower for pulses shorter than 10ps. This is due to the duration of the pulse if shorter than the time of recombination of electrons in the focus, hence the maximum electron density corresponds to the total number of electrons excited by the pulse, and no electron has the time to go through several excitation-recombination cycles. In that sense, this makes pulses below 10 ps more efficient than longer pulses in triggering LIOB from an energy perspective (see Figure II-1).

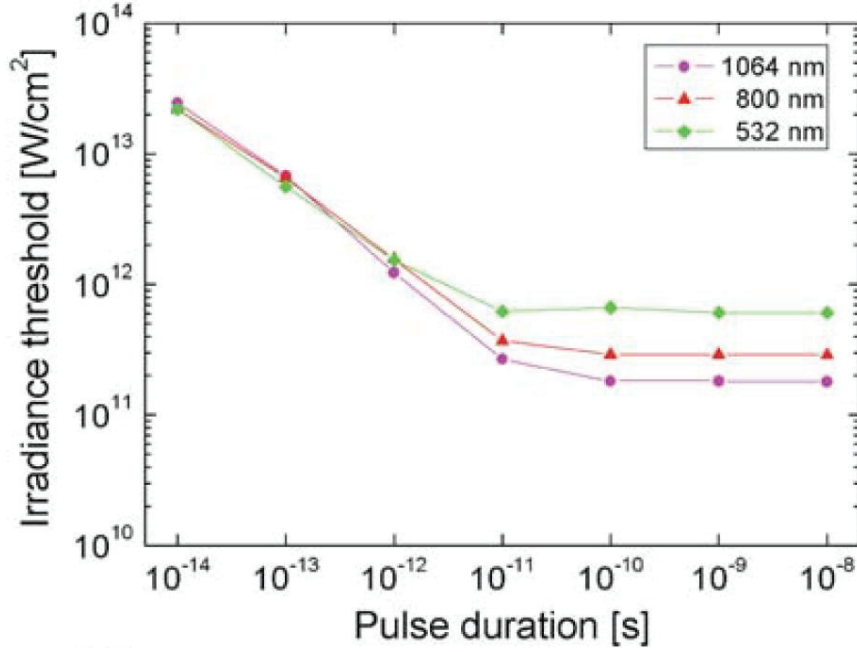


Figure II-1: Calculated optical breakdown threshold as a function of laser pulse duration for various laser wavelengths (considering a critical plasma density $\rho_{crit} = 10^{21} \text{ cm}^{-3}$). Reproduced from Mechanisms of femtosecond laser nanosurgery of cells and tissues, A. Vogel et al. 2005, Applied Physics B

II.2.2 Creation of a cavitation bubble

The production of a high density plasma in a confined volume of a few cubic micrometers happening in the timeframe of femtoseconds is an abrupt change from a thermodynamic point of view. The creation of quasi-free electrons with high kinetic energies within the lifetime of the plasma will induce a very local increase in temperature^{15,16}, of a few tens to thousands of degrees.

A simple model for pulses below 10 ps assumes that the maximum temperature ΔT increase in the focal volume depends on the maximum electron density ρ_{max} defined by $\rho_{max} = \omega^2 \frac{m_e \epsilon_0}{e^2}$ (with ω being the pulsation of the laser, m_e the mass of the quasi-electron and ϵ_0 the permittivity of free space), and that for such short pulses neither the recombination rate nor the diffusion rate of electrons out of the focal volume happen fast enough to decrease the electron density before it reaches ρ_{max} . A model for calculating ρ_{max} from the equation of $\frac{d(\rho)}{dt}$ defined above is presented in details in the paper of Noack et al.⁷. The energy density ϵ_p at the center of the plasma is given by $\epsilon_p = \rho_{max} \cdot \Delta E' \cdot K$ where K is a constant determined equal to 9/4 for ultrashort pulses around the plasma creation threshold. The definition of the heat energy gives us that $\Delta T = \epsilon_p / (\rho_0 \cdot C_p)$ where ρ_0 is the mass density of the medium, and C_p is its heat capacity. At the threshold plasma creation density of 10^{20} cm^{-3} typically used for water in the NIR, this model gives an increase of about 62°C, which would not be enough to trigger thermal evaporation at ambient temperature.

However, on a scale of just a few microns, even an increase by 20°C is going to put the matter in the focal volume in an unstable thermodynamic state. As the temperature increases, the medium is expected to undergo acoustic relaxation. However, considering the speed of sound in water of 1484 m.s⁻¹ and a radius of 1.1 μ m (waist of a Gaussian beam at $\lambda=1030$ nm focused by a 0.3NA objective), the acoustic transit time in water from the center to the edge of a focal volume is 0.74 ns. This is more than an order of magnitude longer than the time within which electron density and temperature increase in the focal volume, and thus no acoustic relaxation is possible, leading to a very strong and confined pressure rise^{17,18}. A tensile stress wave is generated, and can induce fracture of the material with creation of a cavitation bubble if no thermodynamic equilibrium can be reached in a solid or liquid sample. In other words, with the increase in temperature, the heated volume reaches a metastable state, and has two potential pathways to reach a new stable state: 1) if the relaxation time to thermal equilibrium τ_r is shorter than the metastable state lifetime τ_l , no cavitation is triggered and thermal energy diffuses away from focus. 2) in the case where the metastable state lifetime is the shorter one, thermodynamic rupture takes place in the form of a cavitation bubble. Vogel et al. define the critical pressure P_{crit} , at which τ_r is equal to τ_l . It varies with the temperature along a kinetic spinodal (line defining the limit between a stable and metastable states in a pressure vs temperature profile of a medium) in a model defined by Kiselev et al.¹⁹. For an ambient temperature of 20°C in water, an increase of temperature of 62°C (mentioned earlier as the temperature associated to the threshold for plasma creation) would require an increase in pressure of about 110 MPa for triggering cavitation (Figure II-2). Experimental pressure thresholds as low as 50 MPa have been reported¹⁷ for the creation of a cavitation bubble, which may be dependent on the purity and homogeneity inside the focal volume, as inhomogeneity can help nucleation of cavitation bubbles. On the other hand, experimental measurements using hydrophones to measure shockwaves induced by the pressure rise in the focal volume have estimated pressure increase above 200 MPa for temperature increase of 180°C¹².

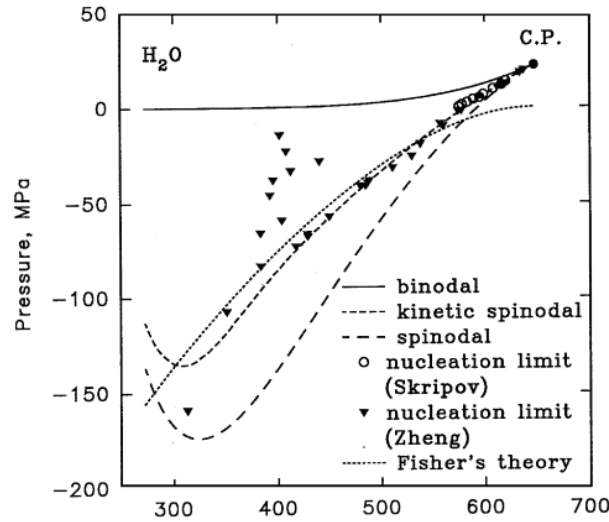


Figure II-2: The pressure of liquid water along the binodal, spinodal and kinetic spinodal as a function of temperatures. The circles and triangles correspond to experimental measurements, respectively from Skripov and Zheng. Figure reproduced from Kinetic boundary of metastable states in superheated and stretched liquids, S.Kiselev et al., 1999, *Physica A: Statistical Mechanics and its Applications*

The last step before investigating the dynamic of the bubble is to determine its initial volume and pressure. The initial volume of the bubble is defined as the volume for which the initial thermoelastic pressure $P_i > P_{crit}$, where P_i can be estimated by:

$$P_i(r) = \int_{T_1(r)}^{T_2(r)} \frac{\beta(T)}{K(T)} dT \quad (\text{Eq. 7})$$

with β is the thermal expansion coefficient of the sample and K is the compressibility of the sample²⁰, and T_1 and T_2 are respectively the initial temperature of the sample (typically ambient temperature) and T_2 is the temperature of the sample at the end of its thermalization. For the cases in which peak pressure was close to P_{crit} , the observed and simulated initial bubble diameters were as small as 90 nm for femtosecond pulses. Most of the experiments presented in the present thesis are conducted using pulse energies above the optical breakdown threshold, in a regime where the initial bubble size is comparable or larger than the focal volume.

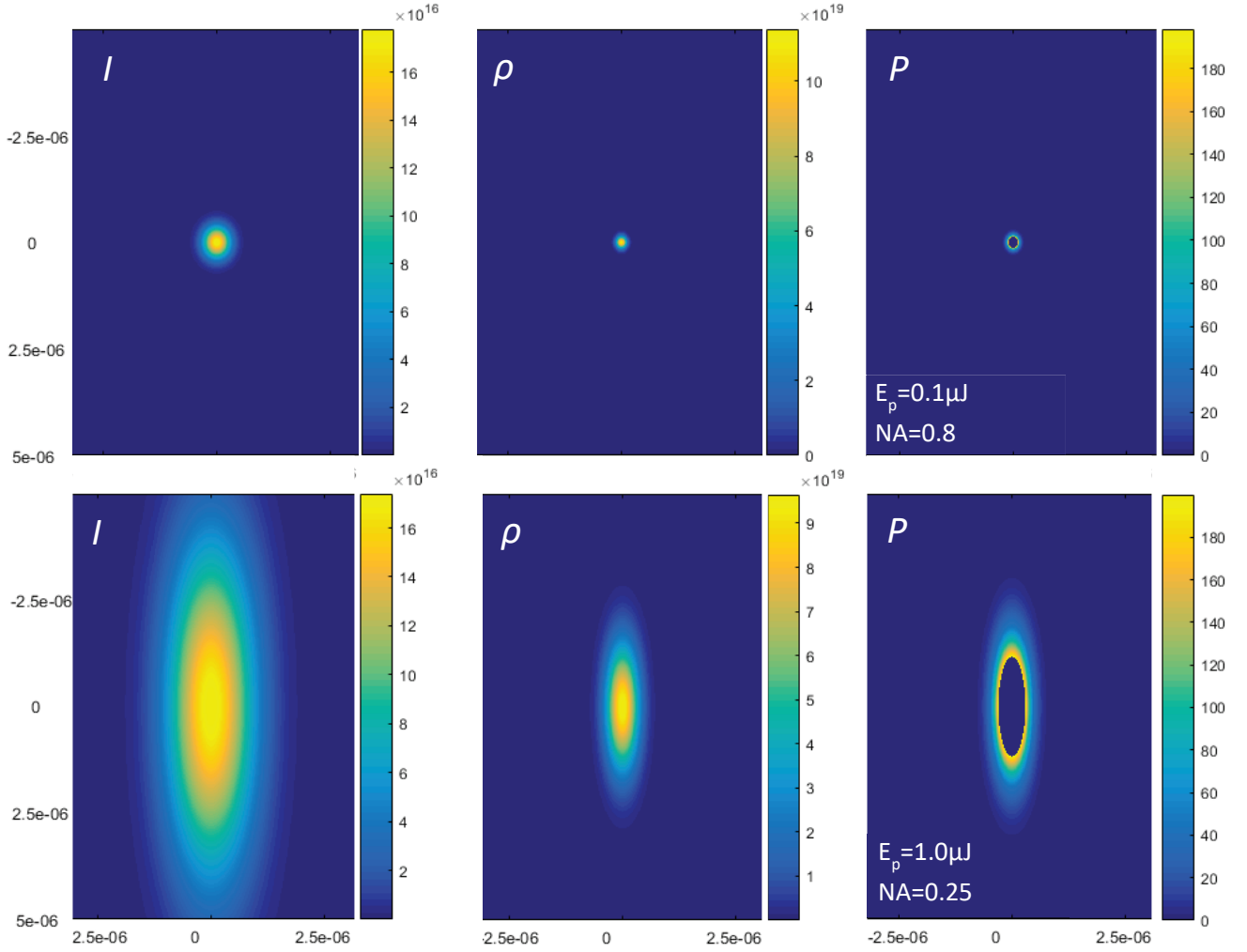


Figure II-3: Simulation of light intensity I (W.m^{-2}), plasma density ρ (.cm^{-3}) and pressure around the cavitation bubble P (bar) around focus for two pulses close to LIOB threshold in water. The blue area in the center of the pressure profile represents the cavitation bubble nucleus. The pulse comes from the top of each graph, and the graduations on the sides are the distance in m from the center of focus. (a,b,c) represent the results of simulations for a pulse of duration 1 ps, pulse energy $E_p = 0.1 \mu\text{J}$, focused with a NA0.8 objective. (d,e,f) represent the results of simulations for a pulse of duration 1 ps, pulse energy $E_p = 1 \mu\text{J}$, focused with a NA0.25 objective. The dimensions of these figures are given in m.

To illustrate this model, let us now consider an example corresponding to a set-up we used later in this thesis. Let us consider a pulse of light at 1030 nm, with a duration of 1 ps, and an energy of 0.1 μJ , focused by a 0.8 NA objective. The waist radius of the beam is 0.41 μm and the Rayleigh range is 0.21 μm . The model presented gives us $\rho_{\text{max}} = 1.14 \times 10^{20} \text{.cm}^{-3}$ (Figure II-3). This makes it barely above LIOB threshold, which is in good agreement with our own experimental observations.

The diffusion of heat out from the focal volume can be simulated with a finite element approach. This can be of interest to discuss pulse-to-pulse temperature increase, which can modify the required pressure to cross the kinetic spinodal or induce the creation of a vapor bubble at very high repetition rates. However, in all the experiments presented later, the repetition rate of the ablation pulses is below 10 kHz, which is far lower than the frequency at which

accumulation of heat would happen (estimated at 1 MHz for peak intensities around the threshold value for LIOB).

For a single pulse, defining the profile of $P_i(r)$ and comparing it to the kinetic spinodal defined by $P_{crit}(T(r))$ are essential steps in determining the initial bubble volume and its pressure. These two parameters will define the bubble dynamics. Figure II-3 shows the initial volume of the cavitation bubble in water, based on the thermodynamic properties of water measured by Rana A. Fine and Frank J. Millero²¹ for pulse near the plasma threshold value, for lasers with a wavelength of 800 nm and 1030 nm. Table 1 gives numerical values for some sets of parameters used in some of the experiments presented in this thesis.

From the values of the bubble pressure and volume, we can now use finite element methods to simulate the maximum expansion. We consider the pressure to be homogeneous in the bubble at the end of the cavitation process. For bubbles whose initial volume is in the order or bigger than the focal volume of the ablation beam, the heated liquid shell surrounding the bubble is already thin when the bubble appears, and get thinner as the bubble expands. The thermal energy is spread over a thin volume with a large surface, and dissipation of heat in the surrounding liquid happens quickly. Comparatively, the dissipation from the heated shell toward the gas of the bubble happens slowly because of the lower heat capacity and density of water vapor compared to liquid water. In consequence, most of the heat from the heated shell diffuses quickly into the surrounding medium, and the expansion of the bubble is considered adiabatic. We used a numerical volume simulation of the Navier-Stokes equation for two-phase flows to simulate the maximum diameter of the bubble for sets of parameters corresponding to some of our experiments (Table II-1).

| Pulse energy (μJ) | NA | Bubble Pressure (MPa) | Initial Bubble diameter (μm) | Max. bubble diameter (μm) |
|--------------------------------|-----|-----------------------|---|--|
| 0.089 | 0.8 | 21.7 | 0.064 | 0.6 |
| 0.1 | 0.8 | 35.7 | 0.2 | 3 |
| 0.5 | 0.8 | 407 | 0.6 | 26.8 |
| 5 | 0.2 | 365 | 2.6 | 128.789 |
| 1.5 | 0.2 | 27.9 | 0.4 | 16.3 |

Table II-1: *Properties of the bubbles created near the LIOB threshold by single pulses of 1 ps at $\lambda = 1030$ nm, for different pulse energies and focusing lens NA. The bubble pressure was simulated following model and based on spinodal values for water from R.A.Fine et al.²¹. The initial bubble diameter was calculated during the same step. The maximum bubble diameter was simulated using Navier-Stokes Equation in a 3D volume, considering the surrounding media to be water and the external pressure equal to the atmospheric pressure. These values of the maximum size of the bubble are in good agreement for bubble size measurements conducted in Agar 0.5% in Part 4 of the current Chapter.*

Although this model has been shown to be a good approximation of the plasma density and bubble dynamics at intensity slightly below or above the threshold value, it comes with some limitations. As the plasma density increases, a larger part of the total number of electrons which

are both in the ground state and available for ionization (by absorption of an energy of ΔE) are excited to become quasi-electrons in the plasma. An electron density ρ_{lim} corresponding to the saturation of the total number of these electrons available for ionization thus constitutes an upper limit for the density of the plasma. H.O. Jeschke et al.²² estimated this value for water to be $\rho_{lim}=6.68 \cdot 10^{23} \text{ cm}^{-3}$. For plasma density above this saturation value, multiphoton ionization is not possible and only cascade ionization can increase the overall energy in the plasma. However, the generation of new quasi-electrons can only happen outside of the focal volume, following diffusion, or if some electrons recombine within the duration of the pulse. Noack and Vogel models calculate the decay of the plasma based on a recombination model where recombination is assimilated to hydration of the electrons, which happens in the order of hundreds of femtoseconds. In this model, electrons have recombined before they leave the focal volume. However, electrons in a hydrated state can last up to 300 us, which is enough time for them to diffuse several hundreds of micrometers out of the focal volume before recombining. For one thing, this can be an explanation for some chemical impact of LIOB outside from the focal volume. On top of it, it could partially explain pulse-to-pulse cumulative effects for pulse with a repetition rate above 1 MHz: as a population of hydrated quasi-free electrons can still exist out of the focal volume defined for multiphoton ionization when a second pulse arrives on a sample, these quasi-free electrons can be used as seed electrons for starting an ionization avalanche out of the focal volume. Since avalanche ionization scales with I and not I^k , subsequent ionization events can happen closer to the laser input, and over a larger diameter, leading to a conical elongation of the ablated volume toward the laser.

II.2.3 Focus-shift at high intensities

For the high energies we will be considering later in this project, it will be important to consider that the plasma can also take place, or grow, outside from the focal volume. For one thing, we have already mentioned that electrons can diffuse out of the focal volume within their lifetime: this is particularly meaningful when we consider that some of them will diffuse along the axis of the beam, where they can significantly increase the local electron density to the point where the factor $\frac{d(\rho)}{dt}$ casc becomes significant. This is particularly true for focusing systems with a low numerical aperture for which intensity in a spot tenths of micrometers above the center of focus can be within an order of magnitude to the peak intensity.

Another effect which can lead to a shift of the plasma toward the laser is plasma shielding²³. High density plasma are highly absorbing in the visible and NIR. In consequence, a high density plasma initially located in the focal volume can make its interface highly absorbent and prone to inverse Bremsstrahlung interaction which will further increase its electron density where it interacts with the laser beam²⁴.

Single pulse elongation of the ablation pulse at high intensity has also been demonstrated in the past. Plasma shielding, or the increase in photon absorption of a high density plasma, happens in the frame of femtoseconds. In other words, any pulse longer than the time of the multi-photon ionization event (in the order of 10 attoseconds²⁵) can have its profile modified by plasma shielding. Since linear absorption of photons then happens through the plasma volume, the part of the plasma closer to the entry point of the laser will be subject to higher intensity, and in

consequence will become more absorbing to photons. D.X.Hammer et al. have measured absorption of more than 75% of the light going through a 3ps, 532 nm pulse at LIOB threshold, thus effectively preventing deep ablation below the plasma shield.

If plasma shielding can explain satisfactorily a “flattening” of the ablated volume in some cases, the shape of some ablation volumes is in fact way more elongated along the optical axis, in the form of filaments extending out from the focal volume. Plasma shielding does not provide a satisfactory explanation²⁶ for this filamentation which can sometimes be observed in high intensity LIOB. Earlier models proposed to explain filamentation by saying that the shockwave created by the cavitation compressed ionized medium around the focal volume, thus increasing its respective plasma density. This increase could favor a localized avalanche ionization close to the laser entry point, thus locally increasing the pressure of the shockwave, etc. However, experimental observations in water have shown that the growth speed of these filaments can be close to three times the speed of the shockwave in water, making this process impossible in water (but still considered in gas). Docchio et al. proposed a different model, called *moving breakdown model*, according to which LIOB can be triggered out of the focus on the optical axis, as soon as the irradiance breakdown threshold is crossed. Since in this model every point along the axis can undergo LIOB independently from each other, it naturally accounts for the high supersonic velocity of the filamentation creation²⁷. It defines the length of the filamentation toward the laser output z_{max} :

$$z_{max} = z_r * \sqrt{\frac{I}{I_{th}} - 1} \quad (\text{Eq. 8})$$

Finally, a last optical phenomenon can have an impact on the location of the ablated area: self-focusing through the optical²⁸. The Kerr effect is a non-linear change of the refractive index of material subject to a high amplitude electric field (for example, subject to a high optical peak irradiance). The non-linear term of its susceptibility, $\frac{3}{4}\chi^{(3)}*|E|^2$ becomes significant compared to $\chi^{(1)}$ at high intensities. The refractive index $n=\sqrt{1+\chi}$ can then be expressed as

$$n=\sqrt{1+\chi^{(1)}+\frac{3}{4}\chi^{(3)}*|E|^2} \quad (\text{Eq. 9})$$

or $n=n_0+n_2*I$ where E is the optical field, n_0 is the linear refractive index and n_2 is the second-order non-linear refractive index. For a positive value of $\chi^{(3)}$, the Kerr effect will increase the refractive index along the optical axis, and will thus induce focusing of the beam before it reaches the focal volume. In the case of laser ablation, it can thus trigger a light-absorbing plasma before the normal focal volume, effectively shifting the ablation process closer to the laser output. Kelley et al. presented a method to calculate the effective distance at which the beam would collapse in this way²⁹. Couairon et al. proposed a different model,³⁰ closer to experimental data for femtosecond high intensity beams in fused silica, according to which the self-focusing of the beam can strongly mitigated by the defocusing effect induced by the increase in electron density³¹. His model was shown to account for very elongated filaments of more than 100 μm in glass, created with a Gaussian profile beam, but cases of total collapse of beams above the focal volume for have also been reported³².

In the coming discussions, we will essentially consider the moving breakdown filamentation model proposed by Docchio, as it is a simple reference model in several publications for biomedical applications of LIOB. Also, the vast majority of our ablation are made using a NA0.8 objective which strongly mitigates self-focusing of the beam since the optical power is spread over a larger area out of the focal volume compared to smaller NA objectives.

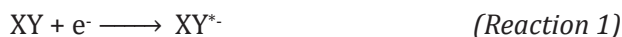
Part 3: Direct effects of LIOB on cells

II.3.1 Generation of reactive oxidizing species

We have seen that LIOB can lead to the vaporization of material in and around the focal volume, and trigger mechanical effects with longer ranges than the plasma volume itself. On top of these, the increase in quasi-electron density can have strong effect on the chemical composition of the sample. When an electron is detached from a molecule during ionization, both become highly reactive charge carriers (a negative charge for the electron, a positive charge for the newly-created ion). The two of them will recombine after some time, depending on their reactivity and the reactivity of molecules surrounding them. During this time between the ionization event and their recombination, the ions can travel a certain distance inside the medium, which will depend on their ability to diffuse inside a certain sample. Diffusivity depends on several aspects such as the size and charge of the ionized molecule, but also on the electromagnetic drag exerted by the charges on the surrounding medium³³.

The chemistry of quasi-free electrons in interaction with surrounding biological tissues and water molecules is very complex to simulate and very fast (the retrapping of the electron happens in the order of 300 fs¹⁴). Electrons are so reactive that a large part of the laws governing their recombination mechanism will be, at least in part, guided by the location and conformation of surrounding proteins when a new electron is created. This is particularly important when we consider some of the large organic molecules present in biological tissues. Among the ones which are very common in muscular tissues (such as arterial walls) are actin filaments, or DNA strands. These are two examples of molecules which can reach up to tens of micrometers (for actin filaments) or even 3m (for DNA strands) in length. If we consider that an electron recombines with a molecule after 1 ns (considering it stays in a non-hydrated state for 40 ps, and then enters a hydrated state for up to 1 ns before recombining with a molecule), it can travel a maximum of 5 nm before recombining³⁴ if we assume that its diffusion rate of $0.60 \text{ \AA}^2.\text{ps}^{-1}$ is the same for its hydrated and non-hydrated states. This can shift the location of the broken bond tens of amino acids away on a DNA strand, which can randomly impact the transcription of one protein or another which are coded by neighboring parts of a DNA strand.

This gives us an estimate that the creation of a plasma inside a biological volume can cause random individual modifications at the molecular level. Because the use of femtosecond lasers has been demonstrated to create plasma and cavitation bubbles in the orders of 100 nm, intracellular damage can be investigated. In the case of DNA, the molecular modification can be dramatic as it means the creation of a plasma in a cell nucleus can induce modification of DNA (and 3-20 eV electrons are enough to break these strands), which presents a risk of inducing cell death or cancerous modification³⁵ (p479). There are DNA repair processes which could limit this problem if it happened on a small scale, but for relatively high density plasma the damage to the nucleus may be too high³⁶. H.Hotop and L.G.Christophotrou discussed the process of direct ionization of organic molecules³⁷ and presents it as an example of a two-steps process of electron capture. In a first step, an electron is captured by an antibonding orbital of the molecule (XY), creating an anion according to reaction 1.



The negative charge induces a negative repulsion at the antibonding orbital, and the anion decays either by detachment of the electron or by dissociation of one or several bonds following reaction 2:



The case of intracellular cell damage to actin filaments was investigated in individual cells, and can have very strong, if not always fatal, consequences on the whole cells structure. Actin filaments are long chains of repeated polymer sequences G-actin sub-units sometimes considered to act as rigid “beams” providing an internal scaffold to the cell. For example, they can give their defining shape to non-spherical cells such as astrocytes, hair cells, or other highly differentiated cells. Actin filaments are dynamic molecules in that they grow or retract depending on the needs of the cell. This process revolves around the process of dynamic polymerization and depolymerization, addition or subtraction of additional G-actin units to the sequence. Polymerization and depolymerization happen by themselves in the cytoplasm, and are mediated by the presence of a capping protein stabilizing the filament. If an electron interacts with a strand of actin somewhere in its middle, it can potentially cut it and trigger depolarization toward both ends of the filament, effectively causing its self-destruction and weakening the cytoskeleton of the cell. This process has been demonstrated and quantified, and can lead to reduced functionality of muscular tissues despite limited effect on the local cell viability³⁸.

However, if direct modification of organic molecules is possible, the fact that most biological samples are mostly composed of water makes it more probable that the quasi-electrons created by LIOB will react with water molecules. Water molecules H_2O can indeed be ionized by LIOB, and electron-driven chemistry in water is an active field of research in itself. Extensive literature on the subject³⁹ tends to indicate that the most probable ionization pathways of water by a single electron are represented in Figure II-4.

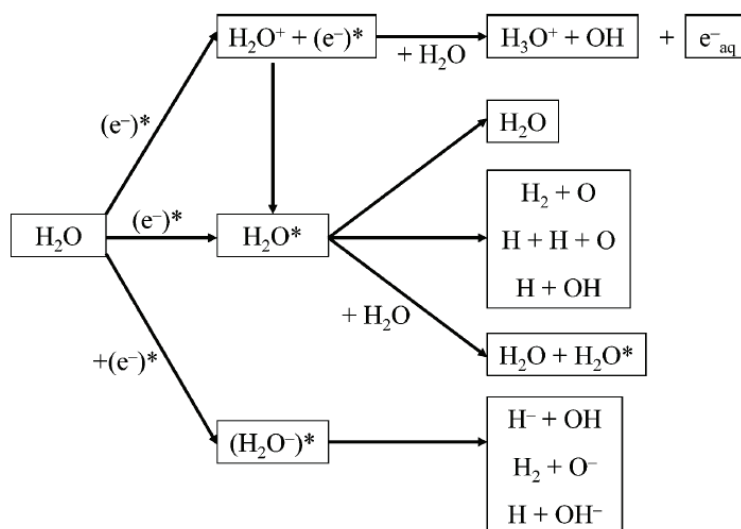


Figure II-4: *initial processes of the decomposition of water by ionizing radiations. Reproduced from The role of water in electron-initiated processes and radical chemistry: issues and scientific advances. C.Garrett et al Chemical Reviews, 2005.*

According to the same authors, the creation of new ions from hydration of electrons (generating H_3O^+ and HO^\bullet , for example) happens within 1 ps of the initial release of the quasi-free electron. However, the relaxation of excited states of these ions or their solvation can last up to nanoseconds. Within a time of 1 ns, an H^+ ion with a diffusion rate $D=9.31 \cdot 10^{-5} \text{ cm}^2 \cdot \text{s}^{-1}$ can travel a distance of only $4.3 \cdot 10^{-9} \text{ m}$ according to classical modeling of particle diffusion³³. In consequence, diffusion of ions is not going to trigger chemical damage to cells far from the plasma by itself. However, some of the most destructive reactive oxygen species (ROS, highly reactive charged molecules) can be produced by pathways initiated by the ionization of water and have way longer lifetimes: $^1\text{O}_2$ for example, is regarded as one of the most dangerous Reactive Oxygen Species (ROS) for cells, and it has been shown to be able to travel up to 4 μm in water and up to 100 μm in non-polar solvents⁴⁰.

Indeed, reactive oxygen species are known to be damaging to most cells⁴¹. Although they can damage the cell directly by inducing oxidative stress to proteins, lipids of the membrane, or DNA, some ROS are also important in messaging inside the cell, or have roles in other vital functions⁴². But even then, an over-expression of some functions of the cell can lead to it damaging itself or the cells around it.

II.3.2 Mechanical effect of LIOB at the cellular level

The cells of organic tissue, and particularly flexible tissues have an inherent resilience to mechanical stress exerted from outside the limits of their own cellular membrane, but are more susceptible to internal bubble growth. The cavitation bubble growing from inside can have a fatal impact because –aside from any chemical damage it can induce- the increase in volume of the cell stretches the bilipidic membrane of the cell, a process which can be reversible or not depending on its extent. If the stretching of the layer is under a certain threshold, the stretching of the membrane will induce a spreading of the amphiphile molecules constitutive of the membrane. This diminution of density can be more or less homogeneous depending on position of the bubble in the cell and the bubble lifetime compared to the time required for the bilipidic layer to spread more evenly (comparable to a drop of oil spreading over water). If the density of amphiphile molecules gets particularly low somewhere in the membrane, it can lead to the creation of ephemeral pores in the cell membrane. Apparition of such pores has been demonstrated by Tirlapur et al.⁴³, and they proved they could be used to increase the permeability of cells to various components to which cells are normally impermeable. More specifically, they and others have since demonstrated the usability of this method to selectively enhance the assimilation and integration of plasmids inside the DNA strands of in-vitro cells, thus proving the use of this laser-induced transient porosity for medical or research application, as well of the ability of cells to recover from the membrane damage.

For plasma defined by larger electron density and that trigger bubbles with diameters larger than a few micrometers, the damage to the cellular membrane can however be irreversible. P.A.Dayton et al.^{44,45} have shown that the apparition of cavitation bubbles inside a cell cytoplasm were enough to burst the cytoplasmic membrane by over-extension if the bubble growth was about 12% in neutrophils. In this case, the injury created to the cellular membrane is more akin

to forcefully separate a large pool of oil on the surface of water into separate smaller pools that might not merge into one large pool rapidly. While huge holes have been opened in the membrane, the mixing of the cytosol with the surrounding media can have dramatic effects on the functionality of the cell: organelles, vesicles, and other cellular components may flow away in the cell substrate, hindering some basic mechanisms necessary for basic cell functioning. This kind of damage is enough to induce cell-by-cell instantaneous cell death, where only the cells irradiated with a certain intensity above a threshold for large internal bubble creation will be fatally impacted. Following this idea, larger cells like macrophages or foam cells may require higher intensity pulses to create bubbles large enough to burst them this way.

Even if the sudden cellular death induced by the laser can be targeted very precisely, it does not mean that the surrounding cells may not be also affected by it. For one thing, the shockwave induced by the cavitation can be strong enough to damage particularly sensitive cells. For example, cells specifically differentiated to detect pressure waves, such as the hair-cells in the cochlea, can be particularly prone to functional damage induced by shockwave⁴⁶. More indirect damages are also possible. As part of the (or the whole) content has been released in the inter cellular matrix, it can come in contact with other cells and induce cellular damage. For instance, some cells (such as some immune cells or digestive cells in the liver and pancreas) produce and carry a number of vesicles whose content is highly acidic. The content of these vesicles is typically used to digest cells in the digestive track, or eliminate bacteria or other “enemies” of the organism. As can be expected, the release of this kind of cellular content onto surrounding cell can have far-reaching effects, and induce the inflammation or even cellular death of the neighboring cells. A more widespread, if less dramatic, risk comes from the fact that all cells also produce ROS in their mitochondria⁴⁷. These ROS and some of their precursors are acidic themselves, and are one of the reason why any small sudden cell death event can be a trauma to surrounding cells, and induce a local inflammation. An everyday life example of this is the irritation and inflammation of the tissue when one inadvertently cuts oneself: even an incision with a clean blade and direct damage to a limited number of cells, without exposure to air or other stress to the tissue is enough to trigger inflammation (with reddening and increase in temperature of the area around the wound).

Part 4: Observation of LIoB in phantoms

Experiments presented from literature and theoretical models provided us with an estimate of the type and range of damage we would encounter in tissue experiments, but the variability in reported biological experiments encouraged us to proceed with experiment in phantoms. These experiments would provide us with a way to estimate more appropriately what to expect from more complex tissue experiments performed in our laboratory.

II.4.1 Fiber laser set-up

II.4.1.1 Overview of the set-up

This set-up was used for ablation experiments, including all our in-vivo experiments, and was based on a Satsuma fiber laser (by Amplitude System), whose gain medium is an ytterbium doped fiber. This laser provided pulses with a central wavelength of 1030 nm, a wavelength that could be tuned between 350 fs and 5 ps, and a repetition rate that could be chosen anywhere between single shots and 2 MHz. The nominal pulse energy at the output of the laser was 40 uJ, although this value could only be obtained for repetition rate below 125 kHz for a maximum output power of 20 W. Control of both the output repetition rate and pulse duration were managed internally and could be set using the user interface by Amplitude System: the output repetition rate was controlled by Pockel cells, and the pulse duration is set by two pairs of grating similar to what has been described for set-up 1, but controlled electronically.

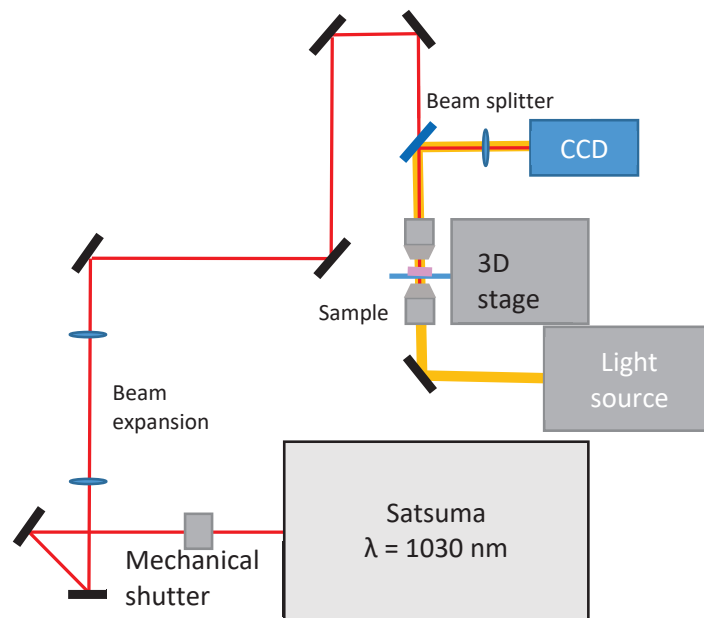


Figure II-5: Diagram of the fiber-laser ablation set-up.

At the output of the laser, a pair of lenses (of 50 mm and 150 mm focal length) were used to decrease the spot size from 1 mm to 3 mm in diameter. The laser at the output of the Satsuma laser had a beam quality of $M^2 < 1.3$, which we considered sufficient to not require the same

filtering we made for the regenerative amplifier set-up presented in Chapter 4. As the fiber laser set-up used here was primarily designed to trigger LIOB in tissues, immersed cell cultures, or with a water-immersion microscope objective, a set of gold mirrors were used to redirect the beam so it arrived from the top into a vertical microscope objective (a water-immersion 20x NA0.8 apochromatic NIR Nikon objective, unless specified otherwise). A beam splitter was placed before the microscope objective and a lens was used to create an imaging system in reflection through the objective, for imaging on a CCD camera. For observing bubbles without the background due to the laser itself, a high-pass filter was placed in front of the camera to block reflection of the ablation laser. A lamp was placed as to illuminate the sample, either in transmission from the bottom of the set-up for thin samples, or from the top (at a narrow angle with the objective) for thicker samples where imaging in reflection was more appropriate. We set up a mechanical shutter directly at the output of the ablation laser for convenience and safety.

II.4.1.2 Scanning using 3D stage

As this set-up was used to investigate ablation in inhomogeneous tissue, a 3D mechanical stages system was set-up to automate the motion of the sample relative to the ablation beam focal volume. For this purpose, we used three linear stages (VP25 Precision Compact Linear Stages, Newport) controlled by a controller (ESP3013 3-Axis DC, Newport). Information for ablation patterns (scanning trajectory, speed, maximum acceleration) were sent to the controller from a computer via RS232 protocol using the LabView programming software. Several patterns were used, but the most common one was a “stair-like” pattern: a raster scan in the horizontal X-Y where each line was deeper along the Z axis. This type of pattern was meant to produce recognizable pattern during histology, as slicing of the sample would result in ablation holes aligned with each other, and each point being deeper than the previous one.

Controlling the acceleration and deceleration of the stages proved to be important. The stages we used weighed 3.2 kg each, and their inertia during fast moves induced vibrations in the sample when they were suddenly starting or reaching a stopping position.

II.4.1.3 Modification for high-speed imaging

High-speed imaging with a high-speed camera (Fastcam Mini UX100, Photron) was accomplished in one of two ways. One option was to use the fiber-laser setup with a slightly modification: with the high-speed camera replacing the CCD for images from the top of the sample. A second option was to image the sample from the side. For this, we constructed a second imaging system of the sample, where a second microscope objective was used to image the focal volume of the ablation beam along its axis onto the high-speed camera. Because of difficulties to image a same area with two perpendicular microscope objectives, two objectives with relatively long working distance of 2 mm, a magnification of 10x, and a NA of 0.4 were used in this configuration. The relatively low amount of light reaching the camera in this configuration, for thick tissue samples, limited the number of frames per second on the camera to about 5,000 fps.

II.4.2 Preparation on phantoms

II.4.2.1 Introduction to phantoms

At several points during this project, there was a need to produce phantoms, typically to help characterizing an optical system or evaluate the aspect and effects of ablation for a set of parameters. As the goal of this whole project was application of LIOB in organic tissue, phantoms had to be produced to mimic the optical and mechanical properties of tissue, and preferably arterial tissues. Arterial tissue, as most smooth muscle tissues, has an absorption μ_a in the NIR, in the order of 0.1 cm^{-1} . In comparison to this, its scattering coefficient μ_s , in the order of 15 cm^{-1} at a wavelength of $\lambda=1030 \text{ nm}$, is going to dominate the penetration of light. Its anisotropy is in the order of 0.8. In terms of mechanical properties, a physiological elastic modulus in the order of 1MPa in human⁴⁸ and mouse artery⁴⁹ was considered.

In the following part, we will consider two types of phantom: Agar phantoms, which can be made more scattering by adding intralipid, and PDMS (polydimethylsiloxane) phantoms, to which titanium oxide can be added. Glass, in the form of untreated microscope glass slides, was used for investigating ablation with no effect on bubble growth.

II.4.2.2 Agar phantoms

Agar gels with intralipids have been widely used as phantoms for biological tissues. According to literature described previously^{50,51}, we need to have an agar concentration (in weight/volume) of about 7% and an intralipid concentration of about 4% to obtain the desired elasticity and scattering properties. However, our own experiments about bubble size measurements tended to show these phantoms were too stiff to mimic rodent arterial tissues, as we were initially aiming to do. For this reason, we decreased the agar concentration to about 4%, which should make the elasticity E_{agar} of the sample close to 200 kPa. This seemed to increase their resemblance to ex-vivo arterial tissue (our benchmark at the time we made of agar phantoms). Also, considering the elasticity modulus of plaque E_{plaque} was reported to be in the range of 5 kPa to 250 kPa⁵², agar phantoms may be good for modeling them. It later appeared to us, from observation of in-vivo ablation, that the mechanical properties of arteries were widely different between their in-vivo and ex-vivo states, and that the samples may have proved to be more accurate if they had been consistently made with a concentration of agar of 7%. A protocol for preparation of Agar gels can be found in Appendix A.

Since Agar gels is produced by algae and is very biocompatible (to the point of being widely used for cell cultures), it is also subject to contamination. The fact that more than 90% of the gel consists of water also makes it prone to drying. Both these factors make agar gels inappropriate for long term storage.

II.4.2.3 PDMS phantoms

Polydimethylsiloxane (PDMS) phantoms are very different from agar gels, and were not used for the same purpose during our research. Their synthetic nature makes them less prone (if not immune to) contamination, and their total optical transparency⁵³ in the NIR makes them very appropriate for observation of LIOB in a viscoelastic media. This proved useful in helping us evaluate certain aspects of LIOB-induced effects such as focus shift and filamentation with or without the effect of scattering, depending whether or not we added titanium oxide during curing

of PDMS. For an elastic modulus E_{PDMS} in the order of 1Mpa we used a ratio of curing agent of 20:1⁵⁴. For the samples when we wanted to reach a scattering coefficient μ_s of 200 cm⁻¹, we added 0.5 g of TiO₂ to 275 mL of PDMS⁵⁵.

II.4.3 Observation of ablation in phantoms

Several experiments have been conducted to build a practical know-how on sub-surface LIOB and its diverse range on impact on the surrounding media. Not all of them will be presented here, as many of them were mostly validation of established theory. We will thus focus on the investigation of one behavior we later replicated in tissue: measurement of the elongation and focus of the damage area for high energy pulses.

We triggered ablation in glass, agar and PDMS at different repetition rates and ablation speed. Using these three different phantoms allowed us to investigate a possible dependence of results on mechanical properties. We used the fiber laser set-up described in 4.1.1 with the mechanical stage and high-speed camera modifications presented in 4.1.2 and 4.1.3. Four objectives with NA of 0.1 (4x Plan N NA0.1, Olympus), 0.25 (10x Plan A NA0.25, Olympus), 0.5 (40 x EC Epiplan, Zeiss) and 0.8 (Nikon APO NIR 40x NA0.8 Water Immersion) were used for these experiments. All measurements were made with 1000 ps pulses.

II.4.3.1 Elongation in glass

We performed high power ablation in glass, about 600 μm under the surface, at repetition rates of 100 Hz and 10 kHz, and stage velocities of 0.16 mm.s⁻¹ and 1.6 mm.s⁻¹. The spacing between ablation holes is thus varied between 0.016 μm and 16 μm . Microscope objectives used were NA0.1 and NA0.5, and the results are reported in Figure II-6. The experiments at NA0.1 show a very low dependence on speed and spacing between ablation holes, but a strong shift depending on the pulse energy used. An elongated filament of ablation appears to go deeper into the sample from there. The length of this filament increases with the square root of I over the range of pulse energy tested, which corresponds qualitatively to the Docchio model for filamentation presented earlier with a large offset of 175 μm . However, none of the general models for focus shift at high intensities presented earlier accounted well for the very long filaments we observed (Table II-2). A notable exception to these are the models such as the one presented by Couairon et al.³⁰ which are complex and specific to the study of filament in glass and are thus not appropriate for further investigation for biological applications.

| Pulse Energy (μJ): | 1 | 2 | 5 | 9 |
|---------------------------------|--------------------|--------------------|--------------------|---------------------|
| Kerr effect (BPM): | 4 μm | 8 μm | 24 μm | 34 μm |
| Docchio model: | 14.5 μm | 38.4 μm | 72.7 μm | 101.9 μm |
| Measurement: | 180 μm | 220 μm | 250 μm | 335 μm |

Table II-2: *Focus shift observed in glass compared to simulation of the focus shift induced by the self-focusing due the Kerr Effect (simulated by Beam Propagation Method⁵⁶), and the moving focus model of Docchio et al.*

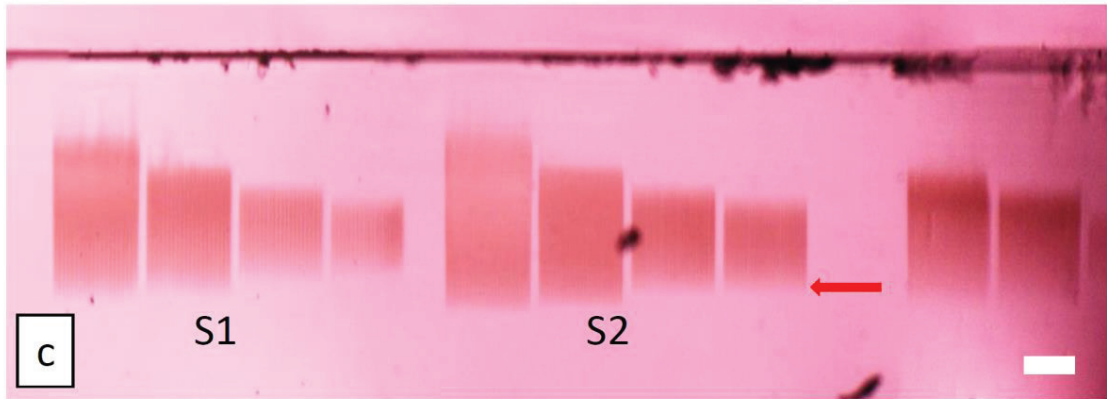
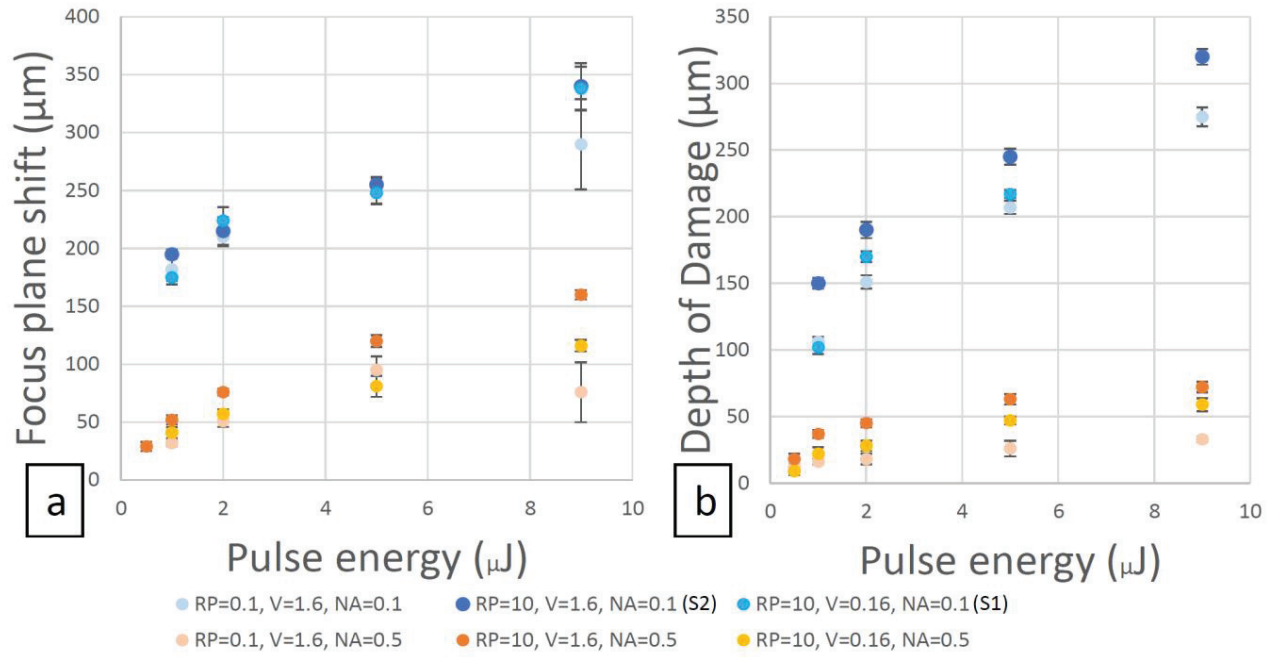


Figure II-6: Experiments on filament creation in glass, with different pulse energy and pulse overlap. The stage speed for the scanning of the beam is $V \text{ (mm.s}^{-1}\text{)}$, and the repetition rate of the laser is $RP \text{ (kHz)}$. (a) Focus shift, measurement from the line marked by the red arrow, to the point closest to the sample surface where the ablation could be observed. (b) Depth of damage, referring to the length of the filaments. (c) Picture of filaments from the side of a glass sample, after ablation coming from the top of the image. S1 is a series of four scans (at $RP=10 \text{ kHz}$, $V=0.16 \text{ mm.s}^{-1}$, $NA0.1$) made, from left to right, at pulse energies of 9 μJ , 5 μJ , 2 μJ and 1 μJ . S2 was made with the same parameters, except for a scan speed of $V=1.6 \text{ mm.s}^{-1}$. The scale bar is 50 μm .

Experiments at $NA0.5$ gave us significantly different results. We do find an increased presence of a filament depending on the pulse energy, but the focus shift as we initially defined it is more difficult to evaluate due to the presence of a first locus of ablation above, but separated from, the main damage area at some higher pulse energies. Although they were initially interpreted as the

result of Kerr effect self-focusing, these only appeared in the highest speed measurement. In consequence, the present of these specific areas of damage do present some level of time-dependence or deposited energy dependence incompatible with an explanation by Kerr Effect only. We propose to explain this behavior by the fact that the creation of a low-density plasma can permanently change the optical properties of glass, practically producing defects which could induce an early breakdown of the beam, but more experiments would be required to prove this. Similar behaviors have been reported in literature about ablation of glass by ultrafast laser⁵⁷. The overall decrease in the focus shift and filament length is coherent with the use of a higher NA.

II.4.3.2 Bubble size increase in Agar

At the other end of the spectrum of mechanical stiffness, ablation in Agar was measured with focus on the bubble size evolution, monitored with the high speed camera. We report an increase of bubble size from one pulse to the next. In proportion, this effect is stronger on bubbles produced at lower energy. We measure the impact of two pulses focused by a NA 0.25 objective, separated by 10 ms, in a 1% agar gel (Figure II-7 (d) and (e)). We observed an increase in volume by up to 150% for a 5 μm^3 bubbles induced by a 0.4 μJ pulse, but only up to 20% for a 500 μm^3 bubble induced by a 6 μJ pulse. If the bubble had the time to collapse between two pulses, no significant difference in diameter were measured. The measurements of the lifetime of bubbles in Agar gels show an increase of lifetime of the bubble corresponding directly to its increase in diameter (Figure II-7 (a) and (b)). Agar gels were also a practical model to evaluate if our theoretical models for bubble expansion in water were adapted to the behavior of Agar Gel: the maximum diameter

of bubbles in the 0.5% agar were about what our simulations predicted for water (bubble of 16.3 μm radius for pulses of 1.5 μJ focused with an NA0.2 objective).

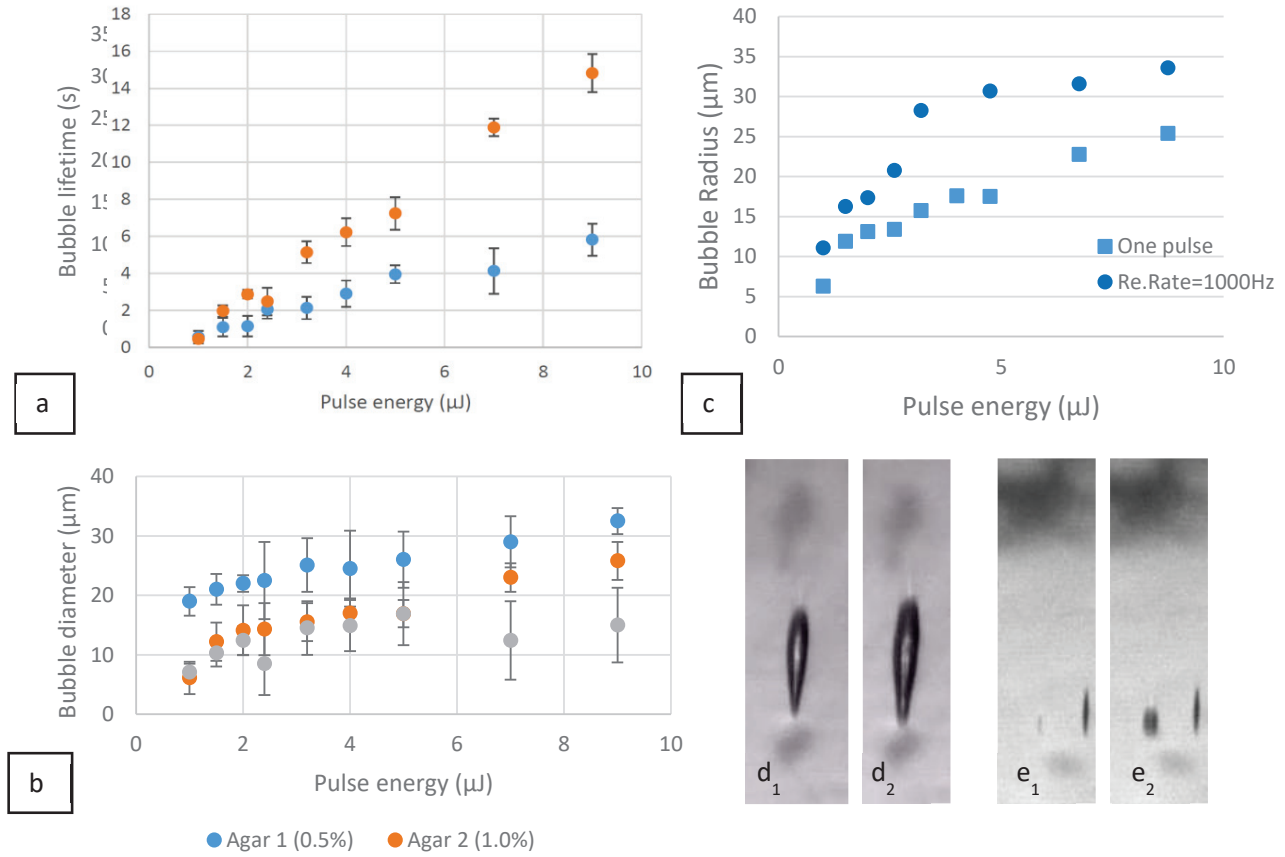


Figure II-7: Measurements of bubbles in Agar gels. (a) Measurement of the time between an LIOB event creating a bubble and this bubble collapse, for 0.5% and 1% Agar gels. (b) Measurements of the maximum bubble radius (defined as their maximum extension perpendicular to the laser beam axis). (c) Bubble radius in Agar 1.0% gel after one pulse and 100 pulse at 1 kHz. (d) Bubble created in Agar 1% with a NA0.25 objective after one 2 μJ pulse (d_1) and five 2 μJ pulse (d_2). (e) Bubble created in Agar 2% with a NA0.25 objective after one 0.2 μJ pulse (e_1) and five 0.2 μJ pulse (e_2). The width of these pictures is 10 μm .

II.4.3.3 Lateral shielding in PDMS

The ablation we conducted in PDMS was following a procedure identical to the one we presented for ablation in glass. The results are reported in Figure II-8 and show widely different behaviors, in between what we observed in glass and Agar. For low NA (0.1) ablation at low repetition rate (10 Hz, speed stage of 0.16 mm.s^{-1}), the behavior was similar to what was observed in glass: thin (less than 2 μm wide) filaments extending above the normal ablation focal plane. However, the filaments are longer where the pulse stayed for a longer duration, showing some cumulative effect. On pulses released at higher frequencies however, a shielding of the target focal area clearly appears: the ablation starts (from the right, on each ablation pattern) at the defined focal plane, but quickly accumulates so that subsequent damage happens a distance (from 50 μm to 500 μm) above the target area. As the scanning of the ablation line progresses, all ablation

happens at the same level, over a more or less elongated depth (from 40 μm to 200 μm) depending on pulse energy and repetition rate. In this case, the target focal plane below stays intact. In consequence, there is some lateral shielding of the ablation due to previous ablation events.

We observed that an increase of the repetition rate and a decrease in stage speed have a similar impact on the focus shift and shielding in PDMS, but for samples where the bubble collapse quickly, repetition rate may prove to have a stronger impact. Using a higher NA objective for targeting the ablation beam seems to mitigate this effect to some extent, but even the use of a NA0.8 objective can produce such cumulative filaments with lengths above 20 μm for pulse energy of only 2 μJ .

In the review from 2006, K. Itoh proposed that defects and easily ionized surface states near the interface may enhance the breakdown process⁵⁸. The results we show here tend to validate this concept, as the dependence on repetition rate more than on stage velocity could be explained by the fact that some of the microdefects induced can be partially recovered thanks to the elasticity of PDMS and Agar. The recovery from this defect would then increase the ionization threshold back to higher levels. Also, since charges accumulate at interfaces, ions with a long enough lifetime, created following the LIOB, could accumulate to the interface and thus further decrease the ionization threshold. This lowers the energy barrier for both MPI and avalanche. According to this model, this can only be triggered if LIOB was strong enough to create a bubble that lasted the time between two pulses, to provide an interface for defects and charges to

accumulate. This explains why no shielding was observed in glass using the same parameters as in glass.

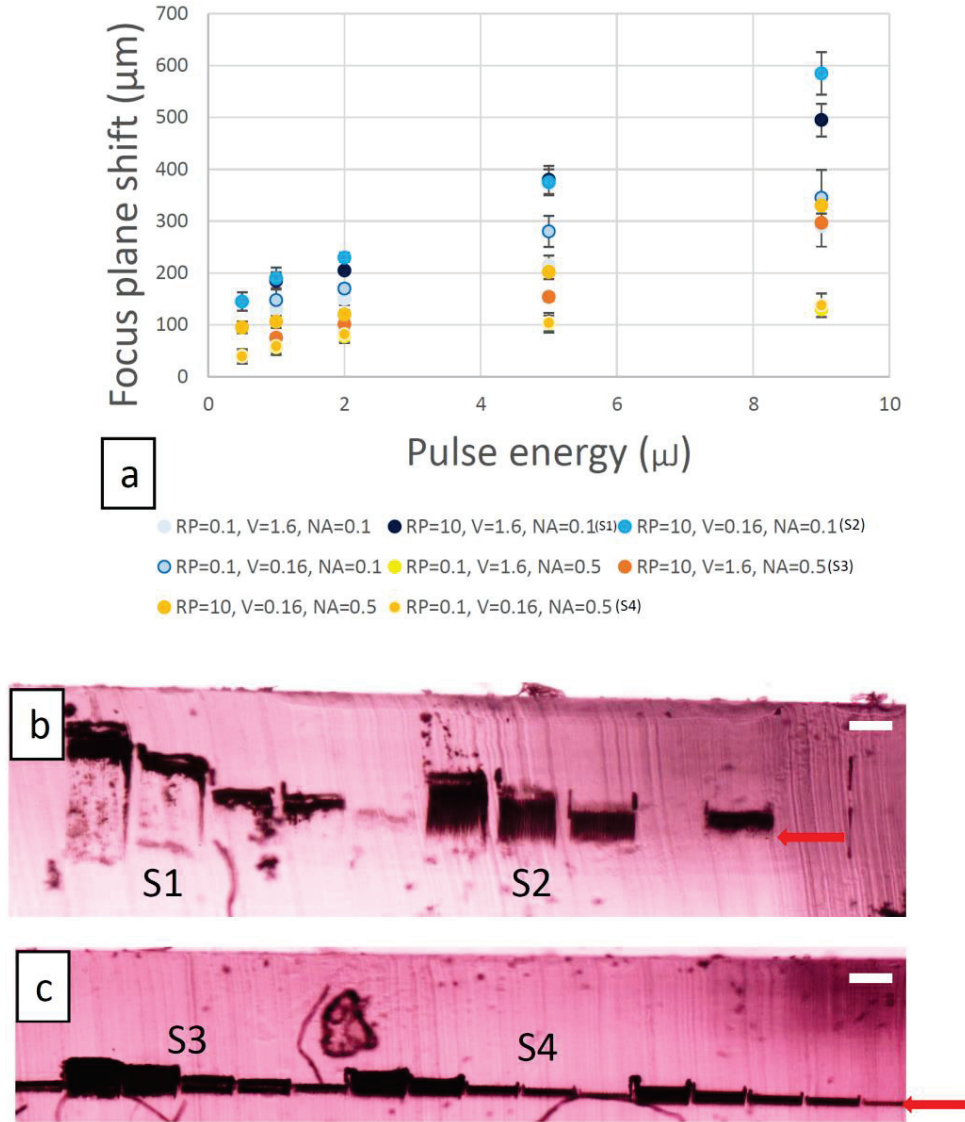


Figure II-8: Experiments on filament creation in PDMS, with different pulse energies and pulse overlap. The stage speed for the scanning of the beam is V (mm.s^{-1}), and the repetition rate of the laser is RP (kHz). (a) Focus shift, measurement from the line marked by the red arrow, to the point closest to the sample surface where the ablation could be observed. (b-c) Picture of filaments from the side of a glass sample, after ablation coming from the top of the image. (b) S1 is a series of four scans (at $RP=10$ kHz, $V=1.6$ mm.s^{-1} , $NA=0.1$) made, from left to right, at pulse energies of $9\text{ }\mu\text{J}$, $5\text{ }\mu\text{J}$, $2\text{ }\mu\text{J}$, $1\text{ }\mu\text{J}$ and $0.5\text{ }\mu\text{J}$. S2 was made with the same parameters, except for a scan speed of $V=0.16$ mm.s^{-1} and pulse energies of $9\text{ }\mu\text{J}$, $5\text{ }\mu\text{J}$, $2\text{ }\mu\text{J}$ and $1\text{ }\mu\text{J}$. The scale bars are $50\text{ }\mu\text{m}$. (c) S3 is a series of four scans (at $RP=10$ kHz, $V=1.6$ mm.s^{-1} , $NA=0.5$) made, from left to right, at pulse energies of $9\text{ }\mu\text{J}$, $5\text{ }\mu\text{J}$, $2\text{ }\mu\text{J}$, $1\text{ }\mu\text{J}$ and $0.5\text{ }\mu\text{J}$. S4 was made with the same parameters, except for a scan speed of $RP=0.1$ kHz and $V=0.16$ mm.s^{-1} . The scale bars are $50\text{ }\mu\text{m}$.

The focus shifts and increased depth of damage area presented in these phantoms can have dramatic effects on ablation. Particularly in inhomogeneous samples like tissue. Indeed, if it were possible to compensate for a well-defined focus shift by, for example, moving the objective away

from the sample to compensate, inhomogeneity in the sample properties make it more difficult to predict the appropriate correction. Figure II-9 shows an ablation line in 3.5% agar with 7% intralipid, following a line ablation at 0.2 kHz and 1 mm.s⁻¹ by 2 μ J pulses. Inhomogeneity in the medium induced an irregular “reset” of the ablation area down to the focal plane, and the filamentation and shielding start again from there up. However, there appears to be a threshold height dependent on the pulse spacing and pulse energy, above which the probability of the damage volume to expend up is very low. Tuning the repetition rate and energy down can thus allow a better control of the damage length is thus essential for ablation in-tissue at a well-controlled depth. On the other hand, one could imagine using the random reset of the ablation area down to the focal plane as a way to scan axially the ablation the ablation volume through inhomogeneous sample without any mechanical or optical modification.

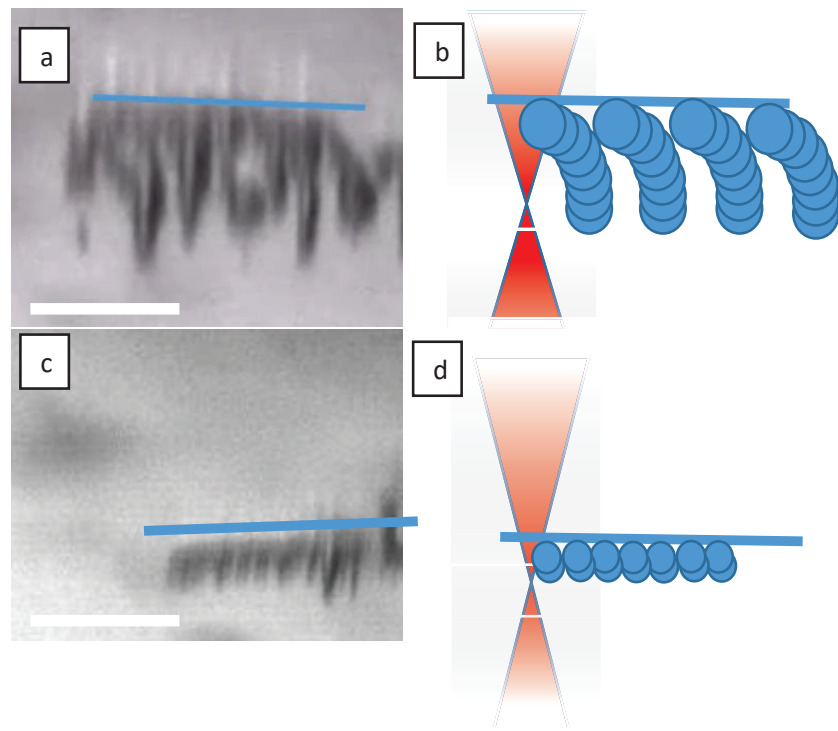


Figure II-9: (a) and (c): side pictures from the ablation as the focus is scanned from right to left at $V=1\text{mm.s}^{-1}$ for in an agar 3,5% with intralipid, for a distance between pulses of 5 μm . Scale bars are 50 μm . (a) $E_p = 2 \mu\text{J}$. (c) $E_p = 0.3 \mu\text{J}$. (b) and (d) simplified representation of (a) and (c), where each blue circle is the volume of a bubble. The blue bar indicates the maximum height above the focal volume at which LIOB can happen before “falling” down to the focal plane.

II.4.4 Conclusion

In conclusion, we presented results for cumulative effects of ablation even at low repetition rate compared to the plasma lifetime. Their precise modeling is beyond the scope of this thesis, but the possibility to replicate the results in phantoms, particularly in the field of scanned ablation in soft material, provides us with a better knowledge of what to expect during ablation in biological tissues.

Chapter III: Apoptosis and Atherosclerosis

We have seen a general presentation of the concept of LIOB and some of the direct damage it can induce to biological tissues. One important type of cellular reaction to injuries has however not been discussed, despite some literature linking it to the use of laser ablation: apoptosis. Apoptosis (from the Greek *apo*, off, and *ptosis*, falling) is often referred to as *clean, organized* or *programmed* cellular death, particularly as opposed to sudden cell death. Despite this positive image, apoptosis remains a complex process, which triggering can have effects on surrounding cells and tissue through different pathways; some of them highly detrimental to the organism. Recent research has linked local apoptosis to the increase of severity in atherosclerosis, an actively studied pathology in which a lipid-rich plaque accumulates inside an arterial wall. In this chapter, we will present apoptosis, its link to atherosclerosis, and how laser-induced optical breakdown could prove to be a potential tool to decrease the growth of atherosclerotic plaque, and eventually reduce their severity.

In this chapter, we will start by introducing the concepts of apoptosis and atherosclerosis, which will come frequently as we discuss biological effects of LIOB.

We will then present a series of in-vitro experiments whose aim was to investigate the range of effects induced by LIOB on cell lines, in preparation for in-vivo experiments to be discussed in Chapter 4.

Part 1: Introduction to Apoptosis

III.1.1 Overview of the apoptotic pathways

Cells are sometimes compared to small-scale factories, or even miniature cities, where various entities of different sizes (from individual molecules to organelles) have highly specialized tasks. Many of these tasks are vital to the proper functioning of the cell, and some can have terrible consequences if they are not executed properly. An error in copying the DNA of the cell, and it may not be able to produce the right type of protein required by the organ it is part of⁵⁹. Dysfunction of the mitochondria⁶⁰, and the cell might see its energy output decrease to a point where it may not be of any use to the organism. Improper synthesis of a hormone, and the behavior of the host of the cell can start to be erratic. To cope with these potential malfunctions, and many more, advanced organisms have developed complex pathways whose ultimate goal is the elimination of damaged, dysfunctional, or over numerous cells which have detrimental effects. Apoptosis is an essential part of this process⁶¹, as it essentially consists in the proper “packaging” stage before elimination.

Apoptosis is a complex process which can be triggered in different ways⁶¹, mostly starting from an internal signaling that the cell must be eliminated (internal pathway), or from an external source where a second cell signals to the first cell it should undergo apoptosis (external pathway and perforin/granzyme pathway). Once one of these two pathways has been activated, it triggers a chain signaling inside the cell, which will ultimately prepare the cell for elimination by the immune system. According to Calvino Fernández et al., oxidative stress on mitochondria is one of the major trigger of the internal pathway⁶². Figure III-1 *Schematic representation of the apoptotic pathways. Each of the three pathways, intrinsic, extrinsic and perforin/Granzyme pathways, initiates the activation of its own initiator Caspase protein (respectively 9, 8 and 10). Every one of this pathway will in turn activate the Caspase 3 protein initiating the execution pathway. Reproduced from Apoptosis: A Review of Programmed Cell Death by S.Elmore, Toxicologic Pathology, 2007* presents a general view of the principal steps of the apoptotic cascade of events. The general concept is that an initiator signaling protein will either penetrate the cellular membrane (external and perforin/granzyme pathways) or be synthesized inside the cell in reaction to some cellular injury (internal pathway). This signaling protein will enter the cell nucleus and bind to DNA to initiate the production of apoptotic-specific proteins.

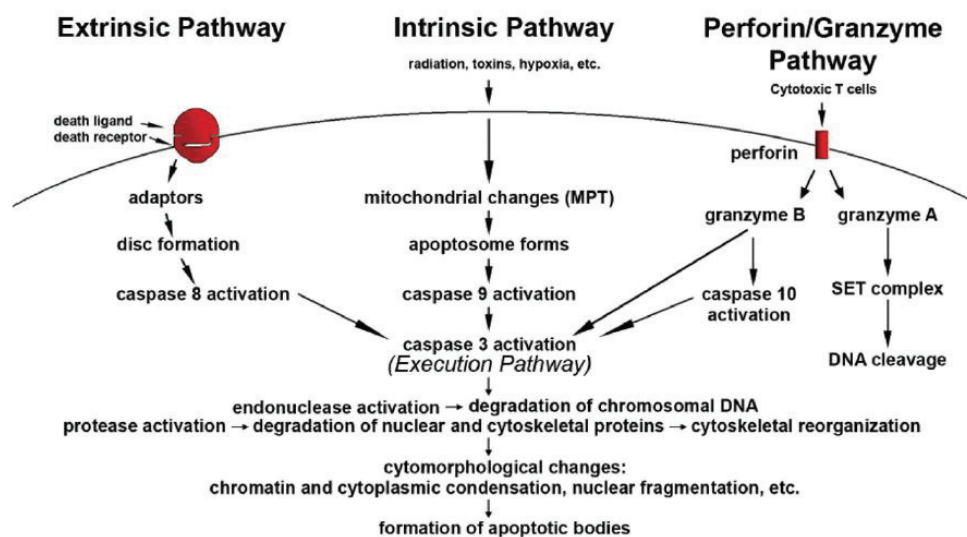


Figure III-1 Schematic representation of the apoptotic pathways. Each of the three pathways, intrinsic, extrinsic and perforin/Granzyme pathways, initiates the activation of its own initiator Caspase protein (respectively 9, 8 and 10). Every one of this pathway will in turn activate the Caspase 3 protein initiating the execution pathway. Reproduced from Apoptosis: A Review of Programmed Cell Death by S.Elmore, Toxicologic Pathology, 2007

The generated apoptotic proteins are going to consume the different part of the cell one after the other, and signal back to the nucleus for production of more apoptotic-specific proteins. Once the execution pathway of apoptosis has started, it is nearly impossible to stop it and allow the cell to heal⁶³. The different organelles are digested by enzymes, and ultimately, even the nucleus is destroyed. In the meantime, some specific inflammation signals are also produced and subject to exocytosis in the surrounding medium or expressed on the cellular membrane, essentially to attract cells which will phagocyte the apoptotic cell. The DNA in the nucleus is fragmented by DNAase produced by the cell itself. The overall apoptotic process takes several hours depending on the cell considered, and by the end of it the cell appearance will have changed significantly, including shrinkage of the cytoplasm and loss of asymmetry⁶⁴ (p637).

III.1.2 Observation of apoptosis

Here we present the concepts for three approaches to identification of apoptotic cells: TUNEL, Annexin V and Caspase 3 staining. We used TUNEL in tissue, Annexin V in cell cultures, and Caspase 3 immunostaining in both cell cultures and tissue.

The fragmentation of DNA has been identified as a marker of apoptosis since the process has been known. Apoptosis was in fact initially known as chromatolysis (whose modern meaning is different) due to the condensation of chromatin in apoptotic cells. One of the most widely used

method for staining apoptotic cells, Terminal deoxynucleotidyl transferase (TdT) dUTP Nick-End Labeling (or TUNEL) revolves around the ability of a fluorophore-conjugated complex to form specifically at the sites of DNA breaks typical of apoptotic auto-digestion⁶⁵.

A third known technique of observation and quantification of apoptosis use the anticoagulant Annexin V bound to a fluorophore. Annexin V binds to Phosphatidyl Serine (PS), which is normally expressed on the inner lining of a cellular membrane. Since Annexin V is membrane-impermeable, it does not stain cells in their normal state. However, during apoptosis, PS shifts from the inner lining to the outer lining of the membrane, and Annexin V can thus stain apoptotic cells specifically.

Among the proteins produced specifically during apoptosis, Caspase 3 is an interesting protein for two reasons: first, it is produced in the early stages of both internally and externally induced apoptosis. Secondly, it is a very well conserved protein from an evolutionary point of view, present in most mammals (including mice, rats, rabbits, pigs, and humans) and several antibodies are now commercially available which bind specifically to Caspase 3. These properties make it particularly well adapted to be a marker of early-stage apoptosis for samples where immunostaining is an option.

Part 2: LIoB and Atherosclerosis

III.2.1 Atherosclerosis and the role of apoptosis

From a very general physiological point of view, Atherosclerosis is a pathology which consists in the accumulation of cells and lipidic components inside the arterial wall (Figure III-2). The cause of atherosclerosis and the initial biological event which determines the start of an atherosclerotic plaque are still investigated, and constitute an active field of research⁶⁶⁻⁶⁸. From a process point of view however, the growth of the plaque is now known to be the result of an immune response anomaly⁶⁹.

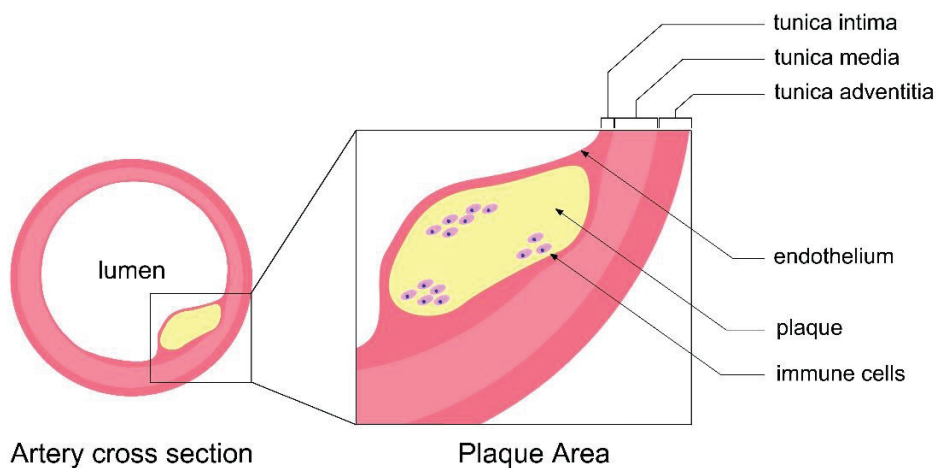


Figure III-2: *Schematic representation of the location of plaque in an artery, and the different parts of the artery. Together, the tunica intima, tunica media and tunica adventitia form the arterial wall. The plaque, represented in yellow, grows inside the intima media, below the endothelium (thin layer of cell separating the arterial wall tissue from the blood flow in the artery). Here, the term immune cells refers generally to monocytes and differentiated monocytes (dendritic cells, macrophages, foam cells) which accumulate into the plaque. A plaque can grow up to the point where it occludes the whole artery (total occlusion) or be separated from the lumen by a particularly thin layer (unstable plaque).*

Some of the latest hypothesis about the initial cause of the development of atherosclerotic plaque tend to show that mechanical damage to the endothelium⁷⁰ may be the initial cause of the atherosclerotic plaque, or that infiltration of oxidized LDL lipids⁷¹ through the endothelium will induce local inflammation. Inflammation of the endothelium attracts monocytes naturally flowing in the blood to attach to the endothelium. As the endothelium is damaged, lipoproteins may infiltrate the arterial wall, where they can be oxidized. Oxidized lipoproteins have been demonstrated to attract monocytes⁷², which will then cross the endothelium, transferring from the lumen of the artery to the arterial wall in between smooth muscle cells (SMCs), and effectively acting as the first brick in the building of the plaque.

From this point, the trapped monocyte can develop in different ways. Because of the change in environment and signaling perceived inside the arterial wall, the monocyte will either differentiate into a dendritic cell or into a foam cell. Both foam cells and dendritic cells can produce their own signaling proteins and release them in the surrounding tissue⁷³. Because of low access to nutrients and oxygen, as well as other factors whose discussion is out of the frame of this work, the cells trapped behind the endothelium will undergo apoptosis and send inflammation signaling that they have to be eliminated by the immune system. In consequence, new chemoattractant cytokines will either reach the blood flow by diffusion back through the endothelium, or the endothelial cells themselves will exhibit intramembrane chemoattractants to cells flowing in the blood flow⁶⁹ (Figure III-33). Monocytes will answer the call and bind to the endothelium, before transferring through it and joining the cells constituting the plaque, leading to its growth, one cell at a time.

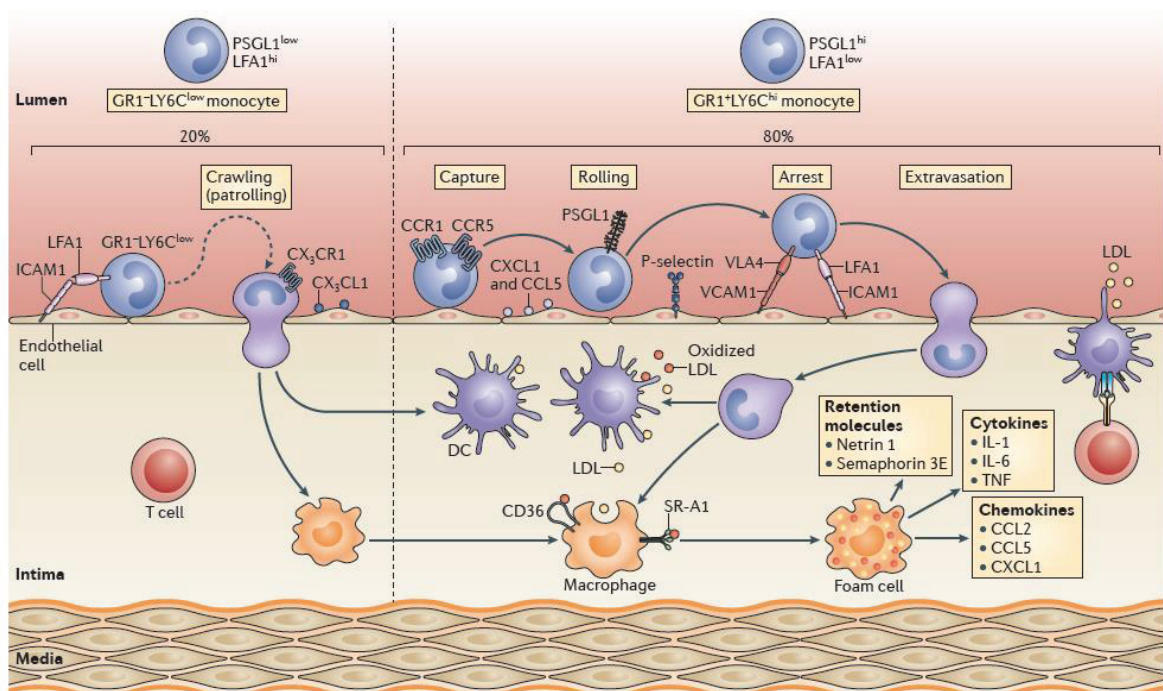


Figure III-3. Reproduced from *Macrophages in Atherosclerosis: a Dynamic Balance*, K.J.Moore et al. *Nature Reviews*, 2013. Mechanisms regulating the recruitment and accumulation in mouse atherosclerotic plaque. Intercellular Adhesion Molecules (ICAM1) and Vascular Adhesion Molecules (VCAM1) are expressed on inflamed endothelial cells, and facilitate the recruitment of new monocytes to the plaque. The recruited monocytes differentiate into Macrophages or Dendritic Cells (DC) and interact with lipoproteins. Macrophages phagocytose surrounding atherogenic lipids in large quantities for highly lipidic plaques, leading to their transformation into foam cells. Foam cells release inflammatory cytokines and Tumor Necrosis Factors (TNF, which will lead to the creation of a necrotic core).

In the meantime, cells which have been part of the plaque for a longer time continue to degenerate, typically through internal apoptotic pathway. In the later stages of apoptosis, these cells will have reached the stage when their DNA and various organelles have been entirely destroyed, and what is left is a set of vesicles stuck inside the arterial wall. At this point, it is important to consider that monocytes are initially relatively large cells (with of diameter of 15-30 μm) which are intrinsically rich in lipids, and that their concentration in lipid correlates with the

intake of LDL (low-density lipoproteins) by the organism⁶⁸. Monocytes which are particularly rich in lipids and accumulate inside the plaque will release LDL in the interstitial cellular matrix upon death. LDL are known to have an inflammatory effect on surrounding cells, and the amount of LDL released from a single monocyte will be more important for individual with a higher level of LDL in their blood. Also, cells with a higher LDL content have a higher chance of differentiating into foam cells when they reach the plaque⁷⁴, and foam cells have a lower chance of leaving the plaque and transferring back to the blood flow. Monocytes also have a higher probability to differentiate into foam cells if the plaque is already rich in lipids, and they will try to phagocytose them⁷⁵. Surprisingly, foam cells have also been reported to decrease the inflammatory response compared to other cells in the plaque⁷⁶. The lipids which are released from the cells ending their apoptotic process can either be taken up by surrounding foam cells (which size can reach several hundreds of micrometers in plaque⁷⁷) or aggregate into lipidic pools.

III.2.2 Atherosclerosis as a multi-facet pathology

Depending on the composition of cells joining the plaque, and other mechanisms leading the plaque dynamics, additional features can appear. Fibrosis (a local increase of density of collagen fibers) of the arterial walls around the plaque⁷⁸, and apparition of a fibrous cap between the plaque and the lumen, are defining features of atherosclerotic tissues. Jaeger et al. have hypothesized that the increase in collagen content is the result of inflammation of the smooth muscle cells around the plaque⁷⁹, but not of the cells constitutive of the plaque. Whether this process has a positive or negative effect on the tissue is subject to debate, as it both prevents the rupture of the plaque and enhances stenosis (which has been shown to attract pro-atherogenic proteins⁸⁰) of the plaque. Some of the larger plaques envelop a necrotic core, constituted of debris of cells which were not captured by phagocytosis. This happens essentially because the plaque surrounding it prevents access by macrophages, and the necrotic core becomes an area prone to development of infection. Other plaques are subject to accumulation of calcium deposit⁸¹. Although this process is not well understood (literature in the domain shows an ongoing debate about whether it is an active process of local cellular calcification, or passive accumulation of calcium phosphate crystals^{81,82}), it can induce the appearance of flat or needle-like rigid calcification inside atherosclerotic plaques. Under mechanical pressure or flexing, these sharp calcified protrusions can rip through the endothelium or fibrous cap, with dramatic consequences.

Considering these various potential features, and the fact that an atherosclerotic plaque can evolve over several tens of years, atherosclerotic plaques come in different forms, and different degrees of severity.

Some plaques develop in lower limbs, inducing partial or total occlusion of the artery. In this case, the plaque accumulates under the surface of the arterial wall, in a volume which can grow over several years. As this volume grows towards the lumen of the artery and occludes it, it can limit the blood flow locally. In the most severe cases, the blood flow is not enough to provide enough oxygen and nutrients to the tissues downstream from the plaque, and its cells start dying (case of *chronic total occlusion*). In the last 30 years, several technologies have been developed for

revascularization of limbs following total occlusion⁸³, including optical and mechanical drilling catheters.

Another type of plaque, for which treatments are making continuous progress, is the case of atherosclerosis in coronary arteries. This pathology can have particularly sudden and tragic consequences, as coronary artery atherosclerosis is the main cause of severe occlusive coronary lesions resulting in myocardial infarction that can lead to a lethal event. More than 7 million fatal cardiac deficiencies each year makes CHD the most common cause of death worldwide⁸⁴. As the plaque grows, the fibrous endothelium separating the plaque from the blood thins and becomes prone to rupture, and fibrous cap below 100 μm are what define *unstable plaques* to clinicians. The fibrous cap of these plaques is particularly prone to rupture, and if it happens to break, the lipidic content of the plaque is released into the blood flow. Part of this content, including the lipids, are thrombogenic⁸⁵. In consequence, a thrombosis forms, which can have particularly serious effect in coronary arteries or carotid arteries. A thrombus in the coronary arteries can induce a myocardial infarction by preventing part of the heart to receive a sufficient amount of oxygen. A similar situation can happen in the carotid where a thrombus can be formed and flow to the brain, causing irreversible or fatal damage by inducing an ischemic (due to lack of blood flow) stroke.

Various approaches have been investigated to fasten resorption, decrease the growth, or at least avoid breaking of plaques in the coronary arteries. Among them, metallic⁸⁶ and bioresorbable⁸⁷ stents are now used routinely in surgery rooms, and chemical approaches have also emerged in the recent years⁸⁸.

III.2.3 A model of the impact of LIOB on atherosclerotic plaques

Considering the process of LIOB in chapter 2, and the existing knowledge about the generation and growth of atherosclerotic plaques, we propose a model in which LIOB could prove to be a useful tool for surgery of fragile tissues, and more specifically in the case of atherosclerotic plaque.

A main concept of our approach is to consider that plaque growth is a slow process, where a strong continuous inflammation signal from the plaque makes it grow over years, and that a controlled destruction of some cellular components could diminish the signaling leading to its growth. In other words, we want to investigate the possibility of diminishing the overall population of pro-inflammatory cells inside a plaque.

We have presented that LIOB can vaporize small volumes, effectively triggering the death of cells if the precision of the laser is enough to allow targeting of specific cell components. But we have also discussed that creation of bubbles in the order of several tens of micrometers can be enough to induce sudden cellular death if they are created inside the cytoplasm. The literature is still lacking in in-vivo short-range effects investigation of LIOB, but in-vitro experiments have shown that laser irradiance can also damage cells by an apoptotic pathway if the oxidative stress is high enough.

Although this would rarely be the case in other situations, in the specific case of atherosclerosis, apoptosis may be as detrimental to healing, if not more, than sudden death: at the end, both types of cell death result in a necrotic phenotype (since apoptotic cells are not

eliminated from the plaque), but the apoptotic cell will have released inflammatory cytokines before decomposing to cell fragments. The idea that apoptosis could increase the speed of plaque development is supported in a review by Kock and Herman⁸⁹, but recent research⁹⁰ suggests the impact of necrotic cores in plaque has an even stronger atherogenic effect. T.Seimon also proposes a more nuanced approach⁹¹, indicating that macrophage apoptosis has a benefic effect in limiting lesion cellularity and in suppressing plaque progression in young plaques, while agreeing on the damaging effect of apoptosis on older plaques. However, if one short-term high intensity inflammation might not improve healing of the arterial wall by itself, it may be effectively coupled with a localized a temporary anti-inflammation treatment and medication to reduce the population of necrotic material⁹². Considering the impact LIOB-generated ROS could have on participating to the oxidation of lipids in the plaque and their effects⁹³, a complementary antioxidant treatment may also be preferably used.

Between the vaporization in the focal volume, and the possibility to trigger specifically apoptosis or sudden cellular death, LIOB in theory offers an array of effects at the cellular level which can be investigated in arterial tissue. And considering LIOB has a good axial sectioning due to being a multiphoton process, it could potentially reach target deep in tissue with minimal damage to material above it.

Part 3: Investigation of LIOB in-vitro

Experimenting on cell cultures (in-vitro) is often the best way to evaluate the impact of a process at the cellular level, besides in-vivo experiments. Recent publications in the domain⁹⁴ show that despite decades of research on light-matter interaction, in-vitro investigation of the impact of laser on cellular death is still an active field. Surprisingly, although some research groups have published on the impact of intra-cellular effects of ultrashort pulses, little has been formally investigated in the domain of longer-reach effects of LIOB. Although extensive literature exists in the mechanisms of light-tissue interaction, and the usability of laser radiation for biological and biomedical applications, the truth is the fields of biology and the field of laser-matter interactions are already so vast that many laser regimes, and many types of biological samples, have not been investigated in combination to each other. In preparation and in parallel to in-vivo and ex-vivo experiments, we thus decided to proceed with investigation on the nature, the severity, and the range of several laser-induced biological reactions in cell culture for the specific range of picosecond NIR low-repetition rate LIOB.

We have discussed previously that cellular death and oxidation of lipids are particularly sensitive issues in and around atherosclerotic plaque, hence evaluating the reach of effects of LIOB is important in determining its application. While acting on an atherosclerotic plaque, particular care must be taken in not damaging the healthy tissues (or the fibrous cap) separating the core of the plaque from the blood flow. Hence, since the multiphoton process nature of LIOB naturally grants it optical sectioning capabilities, we aim at developing a model where damages along the axis of the ablation beam can be evaluated.

For this purpose, a three-dimensional model seems particularly adapted. In the end of this chapter, we will thus evaluate three potential effects of LIOB (apoptosis, sudden death and ROS generation) in various 3D models.

III.3.1 Materials and methods

III.3.1.1 Integration of an OCT to the fiber-laser set-up

Optical coherence tomography (OCT) is an interferometric method which has been shown to be very valuable in observation of deep tissues⁹⁵. It has in particular been used for imaging and characterization of arteries and atherosclerotic plaque for years, to the point where it is now routinely used as a diagnostic tool for assessment of atherosclerosis⁹⁶. In this part we will describe the use of an OCT system as a scanning and imaging modification to the fiber-laser set-up presented in Chapter 2 (4.2). Integration of an OCT imaging system presented several promises as well as some limitations, for both in-vitro and in-vivo experiments. Most of all, real-time depth imaging and monitoring of the ablation process was of course very appealing for application and experiments where transmission imaging was too limited by the scattering of the tissue. We integrated a Ganymede II Spectral Domain OCT in our ablation system, with some slight modifications to it. In this modified version of the fiber-laser set-up, instead of sending the ablation beam toward the upright microscope system presented previously, the beam was sent inside the OCT head. The chosen entry point of the OCT head was located below the beamsplitter

separating the OCT beam between the sample arm and the reference arm, according to Figure III-4. To do so, two additional mirror were added to the OCT head to allow proper alignment of the ablation beam toward the reference arm. This way, the ablation beam was refracted toward the sample arm of the OCT. After the beamsplitter, both OCT beam and ablation beam reach a pair of galvanometric mirrors which redirect them toward the focusing objective at the output of the OCT sample beam. Both beams can then be scanned together on the sample by controlling the galvanometric mirrors inside the OCT head. The OCT Head also included a CCD camera providing a wide-field top view of the scanned area, which proved useful in helping us locate target ablation areas. It also was useful to quickly assess the effect of LIOB by allowing imaging of bubbles or large-size sample modifications.

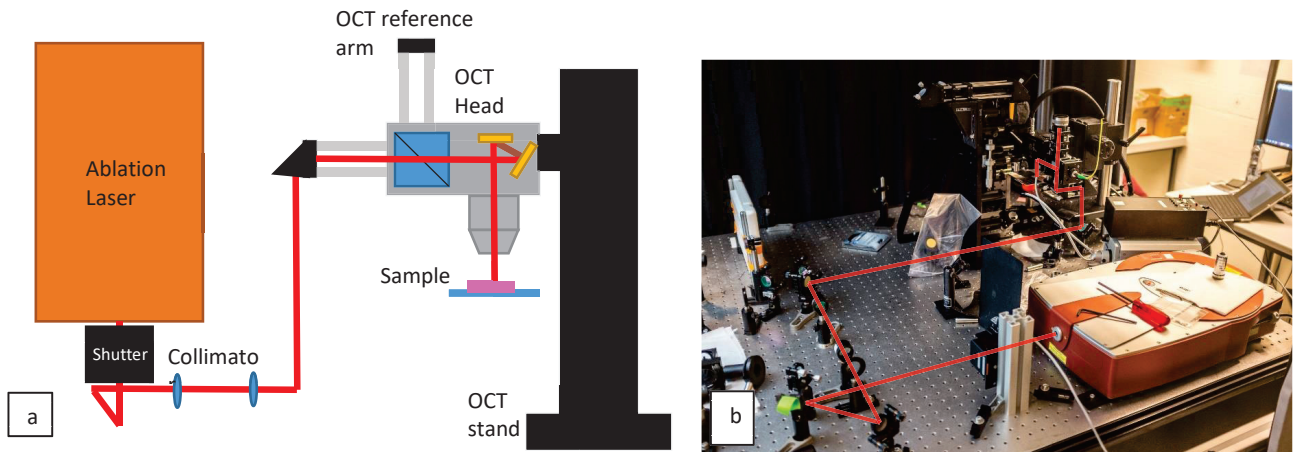


Figure III-4: (a) Diagram of the integration of the ablation beam in the OCT head via an added arm to access the beamsplitter facing the reference arm of the OCT. The ablation beam is represented in red, the OCT illumination beam is not represented. The galvanometric mirrors are represented as two yellow rectangles. (b) Picture of the set-up integrating the ablation beam in the OCT.

Another in-house Labview program (Documented in Appendix E) was used to control both the Satsuma laser and the Ganymede OCT in conjunction to one another. This proved very useful for increasing the speed at which we could set and control ablation parameters, particularly during in-vivo experiments where time constraints are particularly important. The following parameters could be controlled via this interface: Laser output repetition rate, power modulation of the laser (directly determining the pulse energy), size of the pattern in the horizontal plane (X-Y), offset of the laser in the horizontal plane (XY), scanning speed of the pattern, number of times the ablation pattern should be repeated in the same location, as well as the A-mode OCT scan plane (X-Z) to be imaged in real-time. The depth of ablation, being directly dependent on the focus of the objective, was set by manually moving the OCT head height above the sample. During all our experiments, our LabView program was used to achieve raster scanning of the target area. By default, it also took OCT images right before and right after an ablation sequence, to help in evaluating the effect of the ablation beam.

Two microscope objectives were used to focus light at the output of the OCT head. The first one was a Thorlabs objective designed primarily for OCT imaging, the other one was the water-immersion 20x NA0.8 apochromatic NIR Nikon objective mentioned earlier. The Thorlabs objective was characterized by a wide aperture of about 5mm, and was thus appropriate as a

wide-scanning pattern objective. Its numerical aperture was estimated to be 0.21 after characterization by a blade-edge measurement at 1030 nm. In consequence, it is more prone to non-linear effects such as self-focusing than the water-immersion objective. We thus used the OCT objective for cell ablation in gels, where deep ablation was easier to obtain due to the low scattering of gels, and used the water-immersion objective for most of our tissue ablation experiments.

Apart from our LabView software, we also used a proprietary software by Thorlabs, ThorImage OCT, to control our OCT. The images obtained using ThorImage OCT typically showed a higher contrast and better image processing corrections than our own software. However, communication conflicts between Labview and this program made it difficult for us to image a target area right after ablation using this software, so we mostly used our LabView software when several ablation experiments had to be made in a fast sequence (for example during in-vivo experiments). While we still used it in several instances, we did not use ThorImage OCT for ablation after we realized that the scanning mechanism induced by it was more complex than initially considered: during every scan, the focus point would regularly be redirected to a position far away from the target area. This process is due to the fact that the galvanometric mirrors are set to a default position while ThorImage OCT optimizes the apodization of the OCT beam; as it happens very fast we did not observe it right away, and it produced some issues in early experiments when we were using this OCT.

III.3.1.2 Cell Cultures

III.3.1.2.1 Cell line : HCT116

With the exception of 2D cell cultures for which we used C2C12 (mouse myoblasts) cells provided by the Université de Fribourg (UniFr), all our cell cultures experiments we made using HCT 116 cells. These cells are epithelial cells from human colon carcinoma. We continued to use them for the rest of our experiments as a readily available strand obtained from the Biomolecular Screening Facility (BSF) at EPFL, which had the advantage of being compatible with several staining methods for apoptosis.

The cells were cultured in McCoy 5A medium (from Sigma-Aldrich) with 10% Bovine Serum Albumine (BSA) containing growth factors and nutrients for the cells, and cell medium was changed about once every three days.

III.3.1.2.2 2D cell cultures

The first samples we investigated were 2D cell cultures of C2C12 (mouse myoblasts) cells. The cells were prepared by the team of Marie-Noëlle Giraud at UniFr, and transported to EPFL in transport-friendly sealed culture vials. When submitted to high power ablation though, the shockwave induced by the LIOB event was enough to detach cells from their anchor points. This protocols was still sporadically replicated at the Biomolecular Screening Facility (BSF) of EPFL with HeLa or HCT116 cells, for example when quick assessment of the functionality of a stain was needed.

III.3.1.2.3 Agar gels

When we realized the shortcomings of the 2D cell cultures, and wanted to investigate three-dimensional effects of ultrafast laser ablation such as the ones taking place around the focal volume of the ablation beam, or the diffusion of ROS, we decided to prepare 3D gels as scaffolds for cell culture. Agar gels were the first ones we tested because of the ease to prepare them, availability of agar, and the economical aspect of this type of scaffolds. Training, facilities and consumables were provided by the BSF. Being initially less concerned about the mechanical properties of the gels and more with their optical clarity as well as the quality of the cell culture itself, we produced gels with an agar concentration of 0.5%. Later tries were made with a concentration of up to 2% agar. Agar was added to PBS before being heated to 70°C in a microwave, mixed with cells (at a concentration between 50,000 and 500,000 cells per milliliter) before it had solidified, and dispersed at the bottom of 96-wells plate, in volumes ranging from 100 uL to 200 uL depending on the experiment. 100 uL of agar gel without embedded gels were placed at the bottom of each well, as a base layer, prior to adding the agar containing the cells. This is expected to help the formation of a more homogenous cell culture by allowing the cells at the bottom to have access to the culture medium from all sides. After the base layer and the cell-containing agar have solidified, we added 100 uL of McCoy 5A medium (from Sigma-Aldrich) with 10% Bovine Serum Albumin (BSA) containing growth factors and nutrients for the cells.

Some troubleshooting regarding the tendency of cells to grow more numerous toward the bottom of the wells was needed, and a significant improvement in the gels homogeneity was achieved by regularly turning the gel culture upside down during its cooling, and putting it in the fridge over a few minutes to let it cool faster. The attenuation coefficient of these gels, including the scattering from the embedded cells, was estimated to be in the order of 0.5 cm^{-1} by measurement of the ablation laser beam through the sample, hence the ablation beam will have lost about 5% of its ballistic photons population after going through 1mm of gel with embedded cells. Knowing this, we consider these gels to be appropriate for deep ablation experiments and subsequent fluorescence imaging, but the power loss will have to be accounted for.

III.3.1.2.4 Paraffin sections of agar gels

The protocol for agar gel manipulation had to be modified for experiments requiring embedding of gels in paraffin, because agar gels with a concentration below 2%, as we were using for cell cultures, would break to pieces during the many steps of the paraffin embedding protocol. A solution to that was to embed the agar gels containing the cells into a scaffold of higher concentration agar gel.

This corresponding protocol is presented in Figure III-5. First, a solution of PBS containing 5% agar was prepared and heated at 70°C and homogenized by shaking while it was still liquid. Wells of an empty 96 wells plate were each filled with 200 μ L of this 5% agar solution, and left for cooling and solidification of the gels (Figure II-5-a-1). The agar gels formed gel cylinders at the bottom of the wells with a diameter of about 6.5 mm, equal to the inner diameter of the wells. We then cut the thinner end of a 100 μ L pipetting tip for its diameter to be about 3 mm, and used it to suck out the center of the agar gel with a pipette tip. This left an empty cylinder in the middle of the 5% agar gel (Figure II-5-a-2). We then followed the protocol previously described for preparation of agar (see paragraph III.3.1.2.3) to this empty space with 50 μ L of 2% agar base layer containing no cell, 50 μ L of 0.5% agar gel, and add 100 μ L of cell culture medium (Figure II-5-a-3).

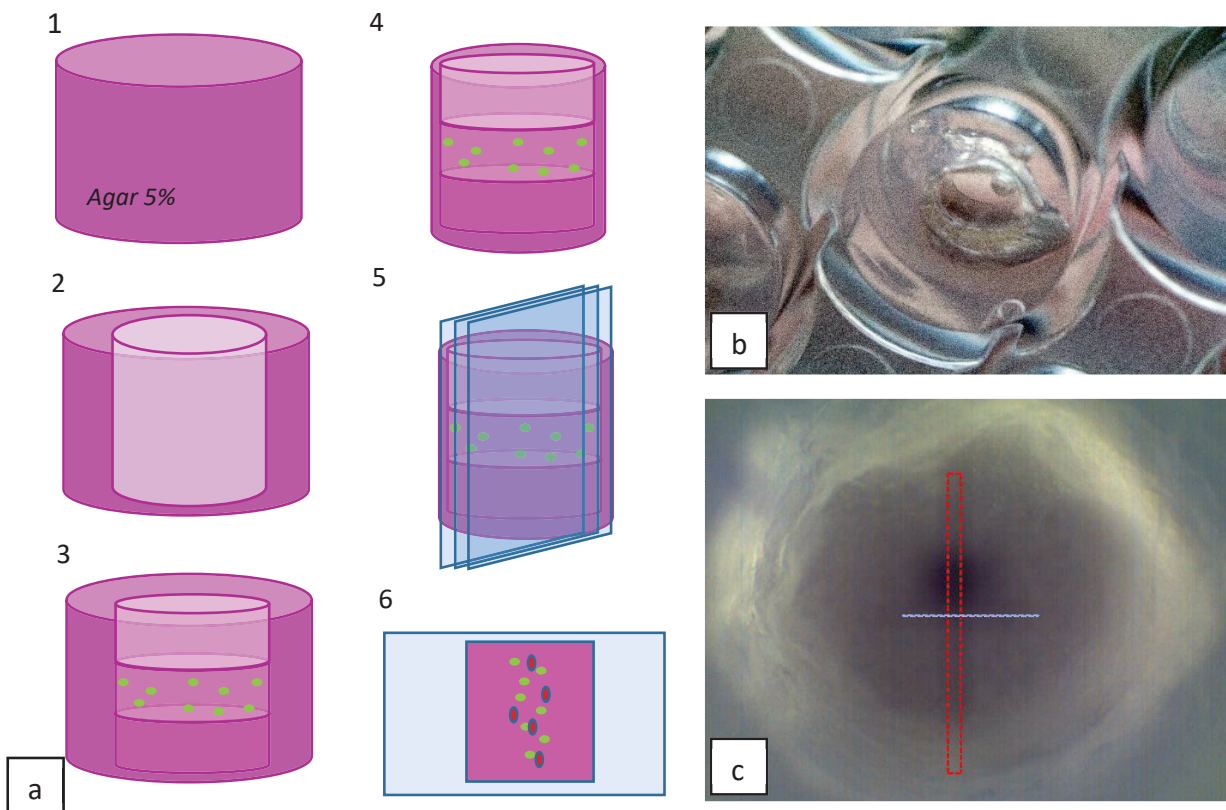


Figure III-5: (a) Diagrams of the different steps to prepare cell cultures for ablation and histology preparation for immunostaining. (b) Bottom view from a well containing a Agar 1% gel surrounded by an Agar 5% scaffold. (c) The gel of image (b) imaged with the OCT microscope. The red rectangle is the area to be ablated, and corresponds roughly to the diameter of the 1% Agar gel, which edge from the Agar 5% scaffold can be observed as it diffuses light projected on the sample.

After they have been illuminated by the ablation beam, the gels were fixed in PFA 4% (weight/volume) for 2h directly inside their wells. They were then washed with PBS and extracted from the well using a thin spatula: the high concentration agar scaffold gives more stiffness to the sample, and prevents its collapse or damaging by the spatula (Figure II-5-a-4).

The cylindrical gel extracted from the well was then placed in the center of a cubic plastic mold with a 10 mm edge. The mold was then filled with 4% Agar at 60°C until it covered the cylindrical gel entirely. This second layer of high density Agar presented two advantages: once removed from the plastic mold, the final gel had a cubic shape easier to manipulate, and this extra layer also

covered the upper surface of the cell-containing 0.5% gel. The side from which ablation had been conducted was marked on the cassette.

The cubic sample was then placed into a plastic cassette and embedded into paraffin. The protocol for paraffin embedding starts with a gradual replacement of water by ethanol for fixation, with the sample being immersed over a series of seven baths with increasing ethanol concentration (from 70% to 100%). The sample is then immersed in 3 baths of xylene, followed by 3 baths of paraffin at 60°C, and the whole process takes place overnight in a tissue processor (ASP200, Leica Microsystems) with about 1h per bath.

The samples were then embedded into paraffin scaffold in preparation for sectioning: they were placed in a metal mold and immersed in melted paraffin at 60°C, and quickly put on a cooling pad at -20°C for quick solidification of the paraffin blocks. These bloc were then unmolded and mounted on a microtome (HM 325 rotary microtome, Leica Biosystems, Germany) for cutting (Figure II-5-a-5).

Samples from 4 to 16 μm were cut by sliding the samples against the static blade of the microtome, and the sections were stretched on the surface of a demineralized water bath at 45°C. Microscope glass slides were then used to scoop them from below. 2 to 4 slices were collected on each slide and kept for staining or immunostaining (Figure II-5-a-6).

III.3.1.2.5 PEG Hydrogel

In order to increase the optical quality of the gels used for cell culture, particularly for stiffer ones, we investigated the option of using polyethylene glycol gels. These gels are more optically clear than agar gels at for a similar elastic modulus. As an example, an agar gel with an elastic modulus of 600 kPa require an agar concentration of 5.4%, which would increase its scattering coefficient. We produced gels with agar concentration of 5% and measured their attenuation coefficient to be about 3 cm^{-1} by measuring intensity before and after a 1 mm thick sample. As opposed to this, PEG hydrogels with an elastic modulus of 600 kPa were produced (for about 1.8% of PEG in the gel) which had near to no attenuation in the NIR (measurements before and after a 0.5 mm sample showed no change in intensity). PEG gels also presented the advantage of being highly reproducible and homogeneous even at these high concentration levels.

Considering the high cost of these gels and our desire to try different sets of parameters, we prepared 20 μL gels at the bottom of wells on a 48 our 24 wells plate.

III.3.1.2.6 Matrigel

As HCT116 cells did not seem to thrive in our high density Agar gels nor hydrogels (the apoptotic population in non-exposed samples amounting to up to 20% of the whole cellular population), we produced some matrigel cell cultures. These gels had relatively low stiffness, with an elastic modulus measured to be around 150 kPa (measurements done by Dr.Nathalie Brandenberg from the Laboratory of Stem Cells Biology of Prof.Lutolf at EPFL, by using a Bohlin C-VOR modular rheometer), but their optical attenuation coefficient was also very low (less than 1% decrease through 0.5 mm of matrigel at a laser wavelength of 1030 nm). A downside of matrigels as opposed to PEG hydrogel, and to some extent agar, is their batch-to-batch variability: as they are directly extracted from cancerous mice cells (Engelbreth-Holm-Swarm tumor), their optical and mechanical properties can vary significantly⁹⁷. Matrigel samples were prepared as 20 μ L gels at the bottom of glass-bottom 24 wells plates.



Figure III-6: 20 μ L PEG hydrogel at the bottom of a 24 wells plate.

III.3.1.3 Staining of cell cultures

III.3.1.3.1 Fluorescent signaling of the whole cellular population: Hoechst and DAPI

For every staining of a cell culture, it is important to have a counterstain which will mark every single cell in the sample. In that way, any other staining (for apoptosis, necrosis, etc) can be evaluated in regard to the whole population. Here we present the different stains used for this function, and the main differences between them.

Hoechst 33342 (#62249, ThermoFisher Scientific) is a fluorescent dye for DNA and nuclei that we used in several occasions as a general counterstain, it binds preferentially to adenine-thymine (A-T) regions of DNA. It can be used in fixed or living samples, from cell cultures or in tissue. Its maximum excitation wavelength is 361 nm, and its emission wavelength is maximum at 486 nm (according to the provider). Hoechst 33342 was bought in 20 mM solution, diluted in PBS and stored as a solution of 1 mg.mL⁻¹ at 4°C, and used for staining at a concentration of 0.1 μ g.mL⁻¹ further diluted in PBS.

DAPI (4',6-Diamidine-2'-phenylindole dihydrochloride, 98% purity, #D9542 from Sigma-Aldrich) is another fluorescent dye for DNA and nuclei which binds preferentially to adenine-

thymine (A-T) regions of DNA. It can be used in fixed or living samples, from cell cultures or in tissue. Its maximum excitation wavelength is 364 nm, and its emission wavelength is maximum at 454 nm. DAPI was purchased in 10 mg of powder, diluted in PBS and stored as a solution of 5 mg.mL⁻¹ at 4°C, and used for staining at a concentration of 1 ug.mL⁻¹ further diluted in PBS.

III.3.1.3.2 Fluorescent signaling of necrotic cells

Propidium iodide (PI, #81845 from Sigma-Aldrich) is a membrane impermeant marker of DNA. As such, it will not stain viable cells whose membrane integrity has not been compromised, and can be used as a marker necrotic cells in cell culture. When bound to DNA, its maximum excitation wavelength is 540 nm, and its emission wavelength is maximum at 608 nm. PI was purchased as 25 mg of powder, diluted in PBS and stored as a solution of 1 mg.mL⁻¹ at 4°C, and used for staining at a concentration of 0.5 ug.mL⁻¹ further diluted in PBS.

Positive control of apoptosis was obtained by heating control cell culture to 80°C and measuring their PI and counterstain levels.

III.3.1.3.3 Fluorescence signaling of apoptotic cells: TUNEL

Different approaches can be taken to imaging samples undergoing apoptosis: either by staining or immunostaining of proteins specific of apoptosis, or by staining of the cellular damage induced by apoptosis. Both methods are widely used in research for identifying, but they do not mark the same stages of apoptosis.

DNA fragmentation is one of the hallmarks of the later stages of apoptosis, when proteins produced by the cell itself proceed with self-destruction of the cell nucleus. Terminal deoxynucleotidyl transferase dUTP nick end labeling (TUNEL)⁹⁸ is a method to stain DNA fragmentation resulting from cascade apoptotic signaling cascade. It is based on the specific binding of terminal deoxynucleotidyl transferase (TdT) to the 3'-OH site of DNA. TdT is used to incorporate deoxyuridine triphosphate nucleotides (dUTPs) at sites of DNA breaks. These dUTPs are the molecules which can be visualized depending on the label used. Many types of dUTPs have been used after the original biotinylated dUTPs: fluorescently-labeled dUTPs, Bromine dUTPs (BrdUTP) or Alkalyne group dUTPs (EdUTP) to name some. In our case, the TUNEL staining was performed by J  r  my Valentin and Dr.Manish Jain from UniFr using Digoxigenin-11-UTP, stained by Anti-digoxigenin fluorescein. The protocol can be found in Appendix C. The fluorescent excitation of fluorescein is maximum at an excitation wavelength of 494 nm and a maximum emission wavelength at 512 nm.

Positive controls were obtained on tissue samples by use of DNAase to induce DNA breaks before TUNEL staining.

III.3.1.3.4 Caspase 3 immunostaining

Immunostaining of Caspase 3 was demonstrated to work in both tissue and cell cultures, and we thus used it in several occasions. It follows a typical immunostaining protocol: the sample is fixed in PFA 4%, then immersed in PBS containing 0.1% Triton X-100 (Sigma Aldrich), and 1% Bovine Serum Albumine (BSA, Sigma Aldrich). The role of Triton-X is to permeabilize the membrane and allow antibodies to access proteins in the cytoplasm, while the role of BSA is to block the epitopes on the tissue sample to prevent non-specific binding of the antibodies.

The primary antibody (Cleaved Caspase-3 (Asp175) Antibody, #9661S, *Cell signaling technology*) was kept at -20°C and used directly when it was taken out of the freezer. The antibodies were diluted to obtain 2 ug.mL⁻¹, and added to the sample.

After incubation of the first antibody and cleaning of the sample with a PBS 0.1% Triton-X, 1% BSA, a secondary antibody was diluted to 0.2 ug.mL⁻¹ and added to the sample. The choice of secondary antibody depended on which other fluorescent stain was being used, but was chosen among a set of three donkey anti-rabbit antibodies, conjugated to either Alexa 488, Alexa 568, or Alexa 647 (#A21206, #A10042, #A31573, *Molecular Probes - Invitrogen*). The name of these antibodies indicate their peak excitation wavelength in nanometer, and their respective peak emission wavelengths were 525 nm, 603 nm and 665 nm.

Alternatively, samples were marked with a secondary antibody for donkey anti-rabbit Horseradish Peroxydase (HRP) antibodies (#SA&-200, *Molecular Probes - Invitrogen*). HRP is an enzyme which catalyzes the oxidation of 3,3'-Diaminobenzidine (DAB)⁹⁹, forming a brown-colored precipitate on the sample. This method has the advantage of being compatible with H&E staining, and in the case of caspase 3 immunostaining, apoptotic cell nuclei marked by the primary and secondary antibodies will appear brown instead, giving a possibility for discriminating them from blue-colored non-apoptotic cell nuclei.

An image processing script programmed in the ImageJ software was then used to sort the cells between apoptotic and non-apoptotic cells, and classifying them between cells in the target area of the ablation beam, or outside of it. The main function of the algorithm was to threshold the minimum signal for considering a cell for counting in each color channel, and use a cell counting macro to evaluate their numbers.

III.3.1.3.5 Annexin V staining

Annexin V was used as another staining for apoptosis. We used an Annexin V – Alexa 488 kit with propidium iodide (#V13245, Invitrogen). The stain was diluted in an Annexin V binding buffer solution (essentially HEPES with additional ions), which was also used to wash the cultures from the culture medium prior to staining. An observation of the culture 2h after the start of the staining showed low penetration (about 50 µm deep) of Annexin V into the sample, so the incubation of the sample was extended to 12h before observation. This increase in incubation time allowed good penetration of the stain in the gel, but at the cost of a higher level of naturally happening apoptosis (from ischemia or lack of nutrients).

To verify the validity of our observation of apoptosis induced by exposure to the ablation beam in gels, we also carried out staining experiments on positive control samples for apoptosis. For this, we prepared gels with the same concentration as non-control gels, and identical protocols, with the exception that we added gambogic acid (#G8171, Sigma Aldrich) to the solution before solidification of the gel. Gambogic acid has been shown to be a particularly good initiator of apoptosis in HCT116 cells¹⁰⁰. The apoptosis of these controls was tested for cells embedded in matrigel, and observed via Capsase-3 immunostaining and Annexin V staining.

III.3.1.3.6 Signaling of ROS-induced cellular damage

Direct staining of ROS is difficult, and a more widely used approach is to investigate the population of cells which have undergone an oxidative stress from ROS¹⁰¹. DHE (Dihydroethidium 98%, Adipogen) is a superoxide indicator which exhibits a strong shift in its fluorescence

spectrum when it is oxidized (and is particularly reactive to 1O_2), its excitation peak changing from 350 nm to 518 nm and its emission peak from 400 nm to 605 nm, by the generation of 2-hydroxyethidium. However, it has been shown that the detection of O_2^- by DHE can be interfered by other oxidative reactions¹⁰², especially in living cells where two-electron oxidation of DHE can produce ethidium cation instead, another ion with a similar fluorescent spectrum to 2-hydroxyethidium. Although this may prove to be an issue in-vivo or in-vitro, it should not be problematic for ex vivo experiments.

III.3.1.3.7 3.3.1.4 Fluorescence evaluation setup

An inverted confocal microscope (LSM 700, *Zeiss Microscopy*) with a black and white CCD and various microscope objectives and mechanical stage for z-scan was used. Illumination was provided by a set of several lasers to provide a wide range of excitation wavelengths for fluorophores.

III.3.2 LIOB and range studies of Necrosis

Most of the ablation we carry on in this thesis was done with relatively high peak intensity pulses, reaching easily in the $GW.cm^{-2}$. According to both the simulations and phantom experiments presented in Chapter 1, we are expecting single pulses to trigger bubbles of several micrometers (about 20 μm for a 2 μJ pulse focused by a NA 0.2 objective). This is enough to destroy the cellular membrane of most middle-sized cells (10 to 20 μm) such as the ones we used in our models. In consequence, we were expecting to preferentially trigger necrosis in the focal volume, and this is the first process we investigated.

For this purpose, we used the fiber-based setup presented in Chapter 2 Part 4 with the NA 0.2 OCT. This objective was chosen over the NA0.8 objective for two main reasons: first, the fact it did not require immersion made it convenient to use for multiple wells ablation. Secondly, as an objective whose primary use is as part of an OCT with an imaging field of 2 mm x 2 mm, it was appropriate for scanning a gel with a diameter between 0.5 mm and 2 mm in one shot. Also, its long working distance was appropriate for ablating and imaging through the thick plastic bottom (0.5 mm) of some of the well plates we used. All ablation and observation was carried using our in-house Labview program to control the OCT and the laser.

The first cell cultures on which ablation was carried out were cultures of HCT116 cells in Agar gels; prepared as described in III.3.1.2.3. These were the largest gels we produced, and they filled the wells of 96 wells plates. The volume was about 50 μL of 3% Agar base layer and 100 μL of 2% Agar gel containing cells in a concentration of between $1 \cdot 10^6$ cells. mL^{-1} and $3 \cdot 10^6$ cells. mL^{-1} . Figure III-7 shows images of the A-scan of the OCT just before and after ablation with pulses ($E_p=3$ μJ , $T_p=1$ ps, $R_r=5$ kHz) focused 500 μm deep into the culture of the well with a 250 μm wide pattern of ablation, about 0.5 seconds before and after ablation. The reason we go so deep is to go past the base layer, whose thickness is about 300 μm in the center of the well (it forms a slight meniscus in the wells of a 96 wells plate). The cells can be observed on the OCT scan, helping us to target the ablation plane inside the cell-rich area of the gel. The recording on the OCT camera shows an average maximum size of bubbles of about 20 μm and a lifetime of about 8 minutes before collapse. Both these values are higher than the initial experiments in Agar we had

presented in Chapter 1, but we infer this is due to the ability of neighboring bubbles to fuse during scanning, thus extending their diameter and lifetime.

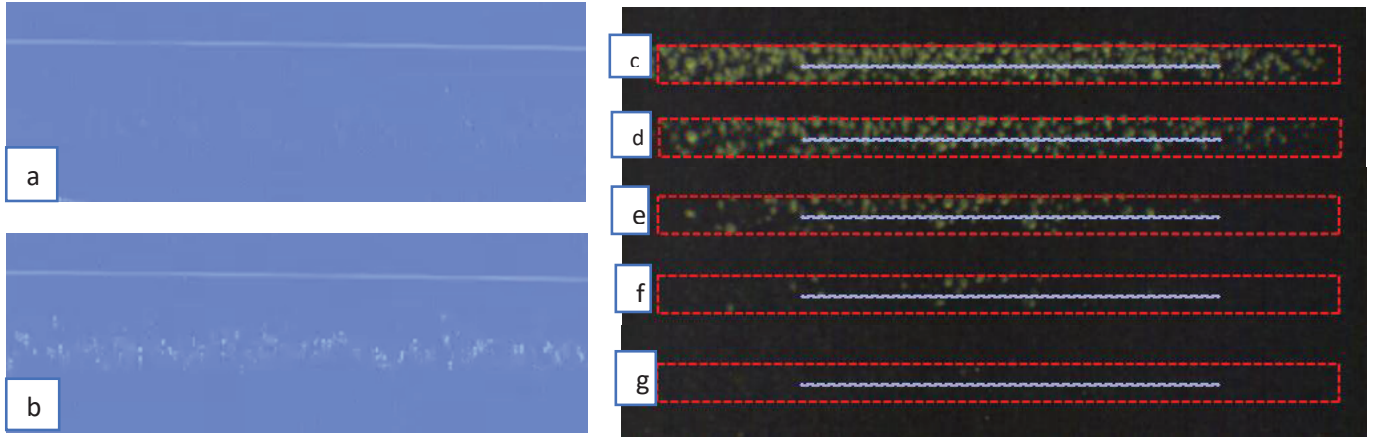


Figure III-7: (a-b) A-scan from the OCT of a PEG hydrogel, before (a) and after (b) exposure by a serie of $3 \mu\text{J}$. Bubbles can be observed on (b), centered about $250 \mu\text{m}$ deep. (c-g) timelapse of the collapse of bubbles after ablation, viewed from the top, at times of 2, 6, 10, 15 and 20 minutes after ablation. The red rectangle indications the ablation pattern, and the blue line is the plane where the OCT A-scan was made.

We triggered ablation with pulses at different energies ($2 \mu\text{J}$, $3 \mu\text{J}$, $5 \mu\text{J}$), a pulse duration of 1 ps, a repetition rate of 1 kHz and through the NA0.2 OCT objective. The results are presented in Figure III-8.

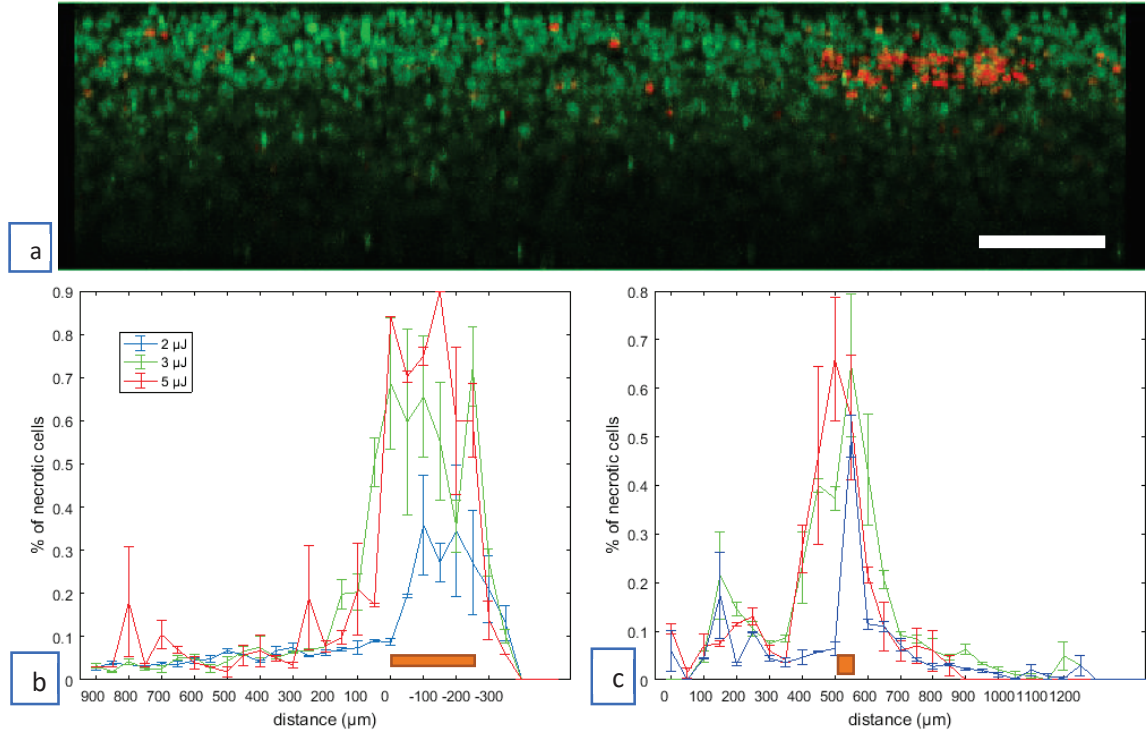


Figure III-8: (a) reconstructed cut (from a confocal microscope z-scan) in an Agar 2% gel containing cells, perpendicular to the axis of the ablation pattern. The samples was stained with Hoechst 33342 (green, all cells) and PI (red, necrotic cells). The ablation and confocal imaging were made from the top of the image, and the area highly stained with PI in the top right corner is where ablation took place. The scale bar represents 200 μm. (b) Data of the percentage of necrotic cells measured at different positions in the plane of ablation in an Agar 2% gel. The orange rectangle above the horizontal axis indicates the target area of ablation. (c) Data of the percentage of necrotic cells measured at different depths along the center of the ablation pattern in the Agar 2% gel analyzed in (b). The orange rectangle above the horizontal axis indicates the target depth of ablation (around 550 μm).

Considering the low presence of necrotic markers (less than 5% of cells marked with PI) far away from the ablation area, we considered that cells more than 600 μm of the ablation could be used as a negative control. Positive control of necrosis was obtained by heating a gel which had not been exposed to the ablation beam to a temperature of 80°C. Staining on one such sample with both Hoechst and PI returned a necrosis of more than 95% of the cells, showing the PI staining to work appropriately.

From these experiments, it appears that necrotic phenotype is strongly limited to the scanned volume, where the vast majority of cells is killed. At pulse energies from 3 μJ, the scanned volume is filled with necrotic cells clearly marked with PI (about 70% of the population), with few marked cells out of it in the plane of ablation. However, damage along the axis of the ablation beam extends further away for higher energy pulses. The overall confinement of damage concurs well with the hypothesis that necrosis of cells in the scanned volume is mainly due to mechanical overstressing of the cellular membrane. The axial extension seems to happen mainly toward the laser entry point I the gel, which may be due to the focus shift and partial lateral shielding discussed and demonstrated in PDMS in Chapter 2 Part 4.

We replicated triggering of necrosis by exposure to identical high energy pulses in both PEG hydrogel and matrigel for qualitative evaluation as we were testing for induced apoptosis. Both

gels provided similar results. The response of all three types of gels seemed to be similar, although it was only quantified in Agar gels.

III.3.3 Laser irradiance and apoptosis

Literature makes several mentions of femtosecond pulses triggering single-cell apoptosis at relatively low peak irradiance¹⁰³. As this is a low energy multiphoton process, we were expecting cell damaging effects to be observable without the need of a 3D model to observe out-of-focus effects. Hence, we only investigated it in 2D cell cultures. We thus illuminated a 2D cultures of C2C12 cells in a pattern of parallel ablation lines separated by 100 μm , at intensities of 0.2 μJ and 1.5 μJ at 100 Hz and a stage speed of 1mm.s⁻¹ with a 10x NA0.2 objective and a pulse duration of 1 ps. TUNEL staining was made 3 hours after ablation, to let time for fragmentation of DNA to take place. The staining revealed that about 70% of the cells which had been exposed to the 0.2 μJ pulses were showing fragmented DNA, while less than 5% of surrounding cells showed a similar phenotype (Figure III-9). As opposed to it, exposure of samples with 3 μJ pulses displayed different results, with the vast majority of cells being detached from the culture substrate, making them inappropriate for analysis. It is probable that the cells got detached because of the shockwave and bubble expansion produced by LIQB, as we had seen a similar behavior in earlier experiments, where the pressure from bubble expansion was strong enough to cleanly remove dye from the surface of a glass slide. These experiments encouraged us in proceeding toward 3D experiments, where these kind of 2D effects (happening here at a fluence of 15.6 GW.cm⁻², relatively low compared to some other of our experiments) should not be present.

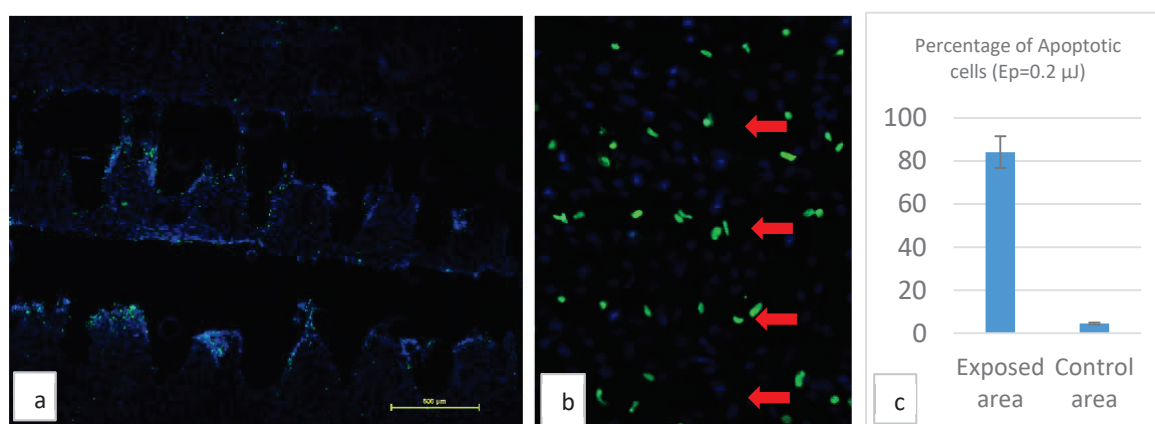


Figure III-9: (a) wide field image of a C2C12 2D cell culture ablated with 1.5 μJ pulses, and stained with TUNEL and DAPI. The black areas are empty due to detachment of the cells from the bottom of the substrate. The scale bar is 500 μm . (b) image of a C2C12 2D cell culture ablated with 0.2 μJ pulses along the direction indicated by the red arrows. The culture was stained by TUNEL and DAPI, so the green cells are the apoptotic cells, and other cells appear in blue. The width of the image measures about 200 μm . (c) Percentage of apoptotic cells on 5 samples prepared identically to the ones in (b), where the exposed area comprised all the cells which had been at least partially scanned by the ablation beam, and the control area were parts of the same sample imaged at least 200 μm away from the ablated area.

We tried to replicate the protocol for evaluating the range of laser ablation effects on surrounding cells we had used to assess necrosis, this time with immunostaining of the apoptotic marker Caspase 3. Unfortunately, immunostaining in-situ in Agar gels resulted in an inhomogeneous binding of the antibodies depending of depth, and negative controls (non-exposed agar gels) reported a high rate of false positives. Lowering the concentration of Agar to 1% did not address this issue.

For this reason, we developed the approach for immunostaining on paraffin cuts of the agar gels, developed in paragraph III.3.1.2.4. We carried it out on 3 agar gels prepared and exposed with the same parameters as the ones tested for necrosis, coupled with a DAB staining of the paraffin slices. The slices were cut to 20 μ m thickness to guarantee to depth-dependent inhomogeneity in the staining. This approach returned some preliminary results showing a low apoptotic signal over the whole gel (less than 5% of the cells counted on 10 slides exposed to 2 μ J pulses). However, this approach proved rather unpractical. The low amount of apoptotic signal overall, coupled with the low thickness of the histology slices made it difficult and costly to reproduce this protocol on large cell population for different sets of parameters. This approach did not provide enough information for a valid quantitative approach, but it was a first qualitative approach to the fact that apoptosis did not seem to be very strong on the cell population tested. This method is by essence independent from limitations due to reagent penetration, and the apparent homogeneity of the apoptotic population, although relatively low, is not an artefact due to the observation method.

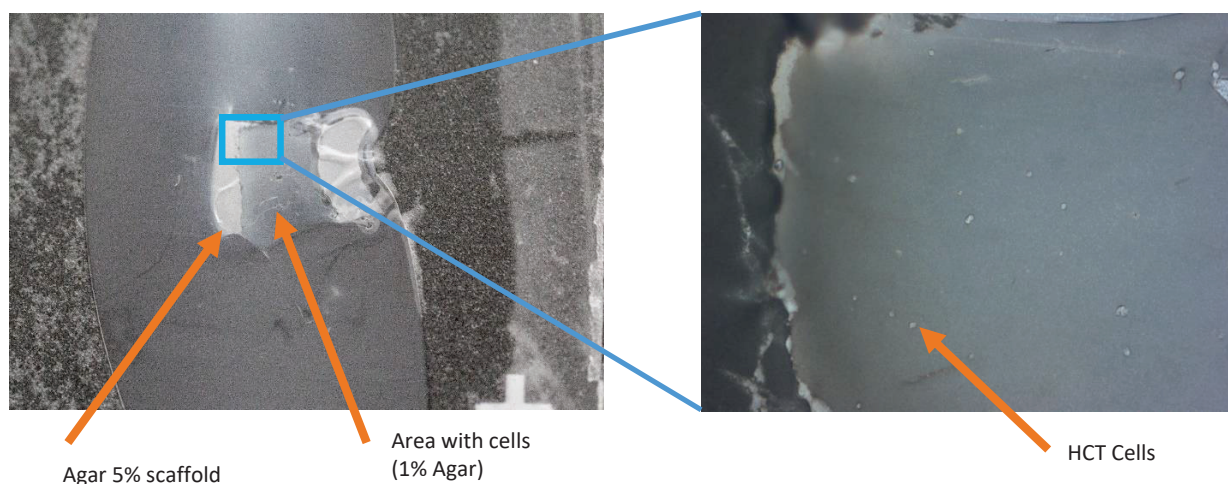


Figure III-10: (left) widefield transmission light picture of a sample of Agar 2% containing HCT116 cells prepared for paraffin slicing. The lighter white areas on the side and in the bottom are the 5% Agar scaffold holding the gel intact during dehydration and paraffin embedding. (right) Close-up of the sample, where unstained HCT116 cells can be observed.

The initial in-situ protocol for immunostaining of apoptotic cells was then replicated in PEG hydrogels with 1.5% of polymer instead of Agar, with the hope of better penetration of the antibodies. The apoptosis assessment of paragraph III.3.1.3.4 was properly replicated and quantitatively evaluated using an ImageJ cell-counting macro.

Immunostaining of the expression of the Caspase 3 protein in the hydrogel was done on a total of 30 hydrogels (12 for each pulse energy and 6 controls), with fixation of the cells happening 1h30 and 2h after ablation. Negative controls (non-exposed to the ablation beam) show a relatively high level of apoptosis (around 25%), but do not appear to strongly depend on depth (apoptosis level stayed within 5% of the 25% average over the whole thickness of the gel) showing good penetration of the reagents. The results only show a limited increase of apoptosis cells in the hydrogel (Figure III-11), and a relatively strong level of apoptosis in non-exposed control samples. Considering the variations in apoptotic signal between control samples and exposed samples are close to the range of error, we considered an evaluation of dependence between rate of apoptosis and distance from ablation spot was not appropriate. At this point we considered either changing the type of cells we were using in hope of finding some which may grow more favorably in PEG hydrogels, tune the gel recipe, or switch to another type of gel.

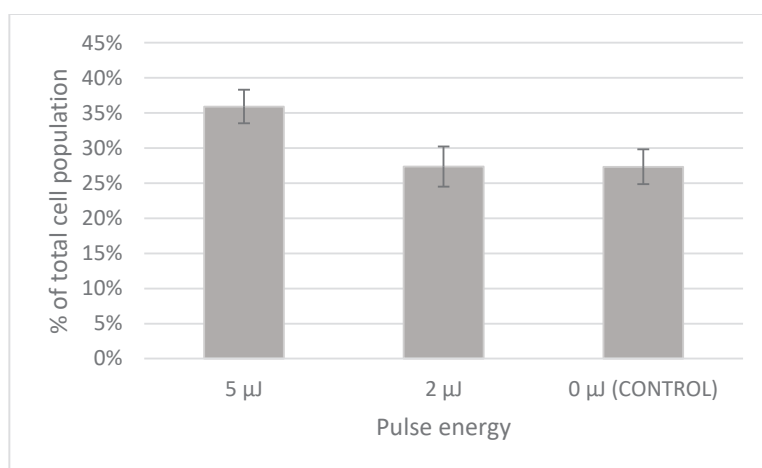


Figure III-11: Data from HCT116 cell cultures in 1.5% PEG hydrogels. Percentage of the cellular population exhibiting Caspase 3 activation in a $500 \times 500 \times 300 \mu\text{m}^3$ volume around the ablated area, after irradiation by 1 ps pulses of 2 μ J or 5 μ J energies, at a repetition rate of 1 kHz and focused by an NA0.2 OCT objective. Samples were stained using a Caspase 3 immunostaining method, and cells were counted using ImageJ. The control was a separate gel prepared in an identical way to the ablated samples.

We chose the latter option and reproduced the same ablation procedure on cellular cultures prepared in matrigel according to the method presented in III.3.1.2.6. Gels of only 20 μ L containing a concentration of 2×10^6 cells/mL prepared at the bottom of 24 well plates. Necrotic cell evaluation experiments were reproduced on a single gel, and reported cell less than 5% necrotic phenotype 24h after embedding the HCT116 cells in matrigel. No positive control was produced, but the presence of necrotic cells did not seem to depend on depth.

Here again, immunostaining of the expression of the Caspase 3 in the matrigel was done on a total of 48 gels (20 for each pulse energy and 8 controls), and the results are reported in Figure III-12. A significantly lower overall population of apoptotic cell was reported. Apoptotic on average exhibit about 20% fluorescence if they were located on the side of the gel than in the middle of the bulk, which we think is due to limited penetration of the secondary antibodies into

the matrigel. However, since we only evaluate a volume of about $500 \times 500 \times 400 \mu\text{m}^3$ in the bulk of the gel, we do not estimate this to have a significant impact on our measurements.

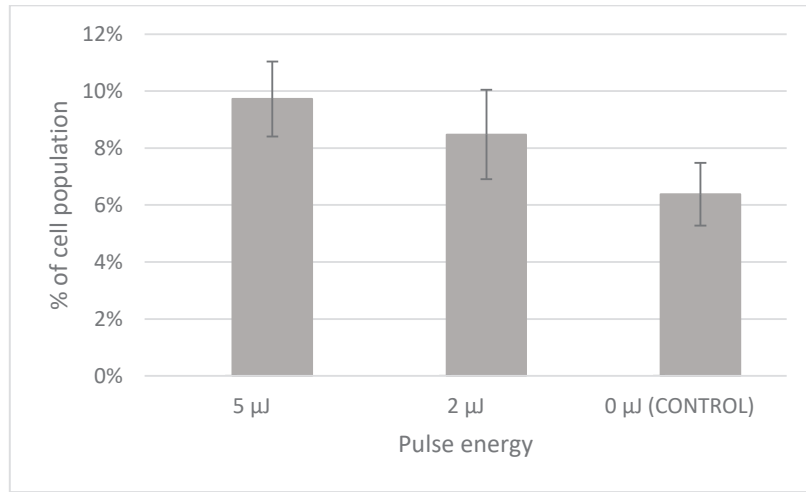


Figure III-12: Data from HCT116 cell cultures in matrigel. Percentage of the cellular population exhibiting Caspase 3 activation in a $500 \times 500 \times 300 \mu\text{m}^3$ volume around the ablated area, after irradiation by 1 ps pulses of 2 μJ or 5 μJ energies, at a repetition rate of 1 kHz and focused by an NA0.2 OCT objective. Samples were stained using a Caspase 3 immunostaining method, and cells were counted using ImageJ. The control was a separate gel prepared in an identical way to the ablated samples.

Our results indicate that even for relatively high energies up to 5 μJ (peak irradiance of 52 GW.cm^{-2}), the increase in apoptotic cells is very limited for a “low” repetition rate of 5 kHz. Our results should be put in perspective to the one of Q.Zuoniming et al.⁹⁴ where they conducted a similar experiment using burst of high frequency (80 MHz) of 30 μJ for a peak intensity at focus of 150 GW.cm^{-2} . They could not measure an increase in apoptosis despite higher peak intensity and overall energy deposited, but their sample of study (3 biopsies) was smaller than ours.

To rule out the possibility of a deficiency in the staining, we repeated this last experiment with Annexin V as the staining agent for Apoptosis. Repetition rate of laser was varied between 5 kHz to 100 kHz to evaluate if it increased the detection of apoptosis, and eventually decreased the prevalence necrosis in the focal volume. The pulse energy was set to 5 μJ , and the ablation pattern was an elongated rectangle (2 mm by 40 μm) parallel to the well bottom. The experiments were conducted and data analyzed for 8 gels (3 at 5 kHz, 3 at 100 kHz, 1 positive and one negative controls). As opposed to the immunostaining protocol of Caspase 3, staining with Annexin V does not require fixation of the culture, which makes it compatible with a staining of necrotic cells using PI. Figure III-13 present the results of this experiment.

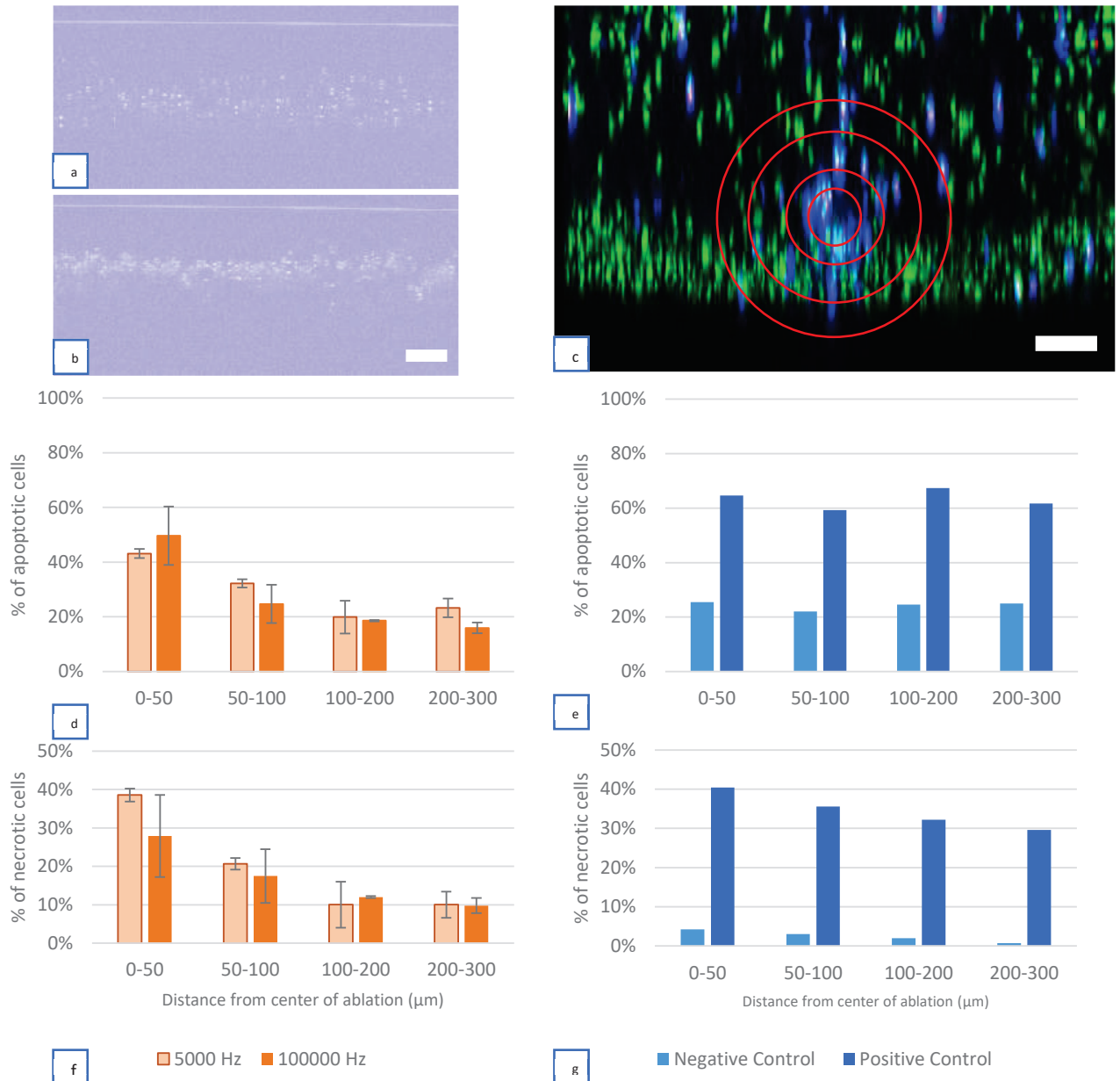


Figure III-13: Data from ablation made with 1 ps, 5 μl pulses focused with a NAO.2 OCT objective, in matrigel, stained with PI and Annexin V. (a) OCT A-scan of the ablated area after 5 kHz scanning. (b) OCT A-scan of the ablated area after 100 kHz scanning. The scale bar for both images is 200 μm . (c) reconstructed cut (from a confocal microscope z-scan) of a sample scanned at 100 kHz. The concentric red circles have radius corresponding to 50 μm , 100 μm , 200 μm and 300 μm , and the scale bar is 100 μm . Cells appear in green (Hoechst staining), red (PI Staining), blue (Annexin V staining) (d) Percentage of apoptotic cells stained with Annexin V in different ranges of distance from the center of ablation, 12h after ablation. (e) The positive and negative controls on apoptosis for the data presented in (d). (f) Percentage of necrotic cells stained with PI in different ranges of distance from the center of ablation, 12h after ablation. (g) The positive and negative controls on necrosis for the data presented in (f).

We see on the OCT images taken for repetition rates of 5 kHz and 100 kHz that we can recognize the ablation focus shift presented in Chapter 2 part 4, with a smaller depth of damage in the sample ablated at 100 kHz (about 80 μm for 100 kHz compared to of 200 μm for 5 kHz). The staining itself proved to be more problematic than expected, as despite the use of a buffer binding solution and the small size of Annexin V proteins ($\sim 36\text{kDa}$), the penetration of Annexin V was significantly lower than the antibodies for Caspase 3 immunostaining. In consequence, the samples had to be kept overnight in the solution of buffer and Annexin V, during which more cells underwent apoptosis presumably because of ischemia and lack of extracellular nutrients. This induces a relatively strong, but homogeneous, background signal on our measurements (about 20% of cells were apoptotic in the negative control and away from ablation).

The necrotic cells signal was strong (about 35% of signals showed strong PI fluorescence) in the ablated area, and a bit higher than in negative controls away from the ablation area, for both repetition rates. This was all-in-all coherent with our previous observations of necrosis.

The apoptotic signal was however significantly stronger and more localized than in the Caspase 3 immunostaining experiments, and were able to quantify apoptosis relative to distance from the ablation spot as we had done for necrosis. With about 50% percent of apoptotic cells in close vicinity of the ablation area, and up to 10% increase compared to the apoptotic background signal between 50 μm and 100 μm , there is a significant local effect on apoptosis.

Nevertheless, this local increase in apoptosis may not be directly due to LIOB itself. The Caspase 3 immunostaining was made between 1h30 and 2h after ablation, compared to the Annexin V and PI staining which lasted overnight, and this can make a difference in which effects have the time to develop. We have discussed in III.2.3 that necrosis could be the cause of inflammation, and it is possible that the products of the necrotic cell death (acidic content, signaling proteins, ROS, etc) in the focal volume diffused slowly in the surrounding matrigel. This would explain a delayed expression of apoptosis, not due to the LIOB event itself, but to the necrotic cell death it has induced. This would require more detailed investigation at the protein level to investigate which pathway was activated, and a timelapse experiment could also help in defining the dynamic more precisely.

In conclusion to this chapter, we have discussed the risk and benefits LIOB could induce on neighboring cells, and why it is relevant to research on atherectomy and other laser surgery applications. We have then developed a series of HCT116 cell culture models to monitor this impact, and the induction of either sudden cell death or necrosis in an around the target area. For the range of parameters tested, we could either trigger apoptosis or necrosis in the focal volume, with minimal direct out of focus damage, but a risk of secondarily-induced apoptosis in the surrounding tissues. We hope this finding will nourish discussions and research in the field of laser-cells interactions, and expect these experiments to be of use in interpreting our own experiments in tissue.

Chapter IV: Subsurface ablation of arterial tissue

In previous chapters, we presented the incidence of LIOB in the context of general light-matter and more specific laser-tissue interactions. In the present chapter, we will investigate the structural and biological impact of LIOB on ex-vivo and in-vivo arterial tissue, with or without atherosclerotic plaque.

First we will evaluate the bubble induce by the LIOB event. Not only because we have seen that creation of a bubble in a cell can lead to its sudden death, but also as a proof that we can induce ablation through thick samples. Other behaviors taking place in the tissue will also be considered, as well as the use of Optical Coherence Tomography (OCT) to observe these bubbles.

Secondly we will investigate the same phenomenon with the added challenge of proceeding in-vivo. Despite presenting technical difficulties, this approach also some insights in the reaction of tissue at the cellular level.

Part 1: Observation of LIOB in scattering media

IV.1.1 Simulation for scattering in turbid media

IV.1.1.1 Effect of scattering on intensity

Until now, we have considered ablation in transparent tissue, by making ablation in transparent or lowly scattering media. In biological tissue however, scattering is a significant barrier to the use of optical tools, from microscopy to laser surgery.

Light absorption in biological tissue is typically low compared to scattering. Arterial tissue are no exceptions, and literature reports reduced scattering coefficients μ_s' around 15 cm^{-1} for both arterial tissues of human coronary arteries^{104,105} and mouse aorta. The reported absorption coefficients μ_a for these tissues are in the order of 0.1 cm^{-1} . Our own measurements of the attenuation coefficient through a sample of pig artery are in this regime, giving us a scattering coefficient μ_s of 250 cm^{-1} , which we will be using in the following simulations.

For a first estimate of the impact that scattering will have on the peak intensity of the pulse, a simple model calculating the decrease in the intensity of ballistic photons (photons which are not scattered before reaching the focus) I_b was computed using the Beer-Lambert law according to which:

$$I_b = I_{surf} \exp[-\mu_s \mu_a d] \quad (\text{Eq. 10})$$

where I_{surf} is the intensity at focus without accounting for scattering, and d is the thickness of scattering media.

Figure IV-1 presents the results: the intensity at the center of focus for varying thicknesses of arterial tissue between the objective and the focal spot, for different NA. The threshold intensities for different materials (gold¹⁰⁶, muscular tissue and glass) are also represented. According to this model, a microscope objective with a NA of 0.45 focusing picosecond pulses of $1 \mu\text{J}$ would be enough to trigger LIOB in $50 \mu\text{m}$ of tissues. Considering the intima media of a mouse arterial wall is $50 \mu\text{m}$, this would be enough to conduct initial experiments of ablation in arterial wall. However, the same set-up could hardly reach more than $150 \mu\text{m}$ deep with pulse of $10 \mu\text{J}$, without considering the filamentation and focus-shift problematics presented in Chapter 1. The in-vitro and in-vivo ablation experiments were nearly all made using high NA (>0.65) objectives to increase the probability of deep ablation despite scattering, and these simulations are an indication that deep ablation will be challenging to pursue with low NA objectives transmitting pulses in the μJ range.

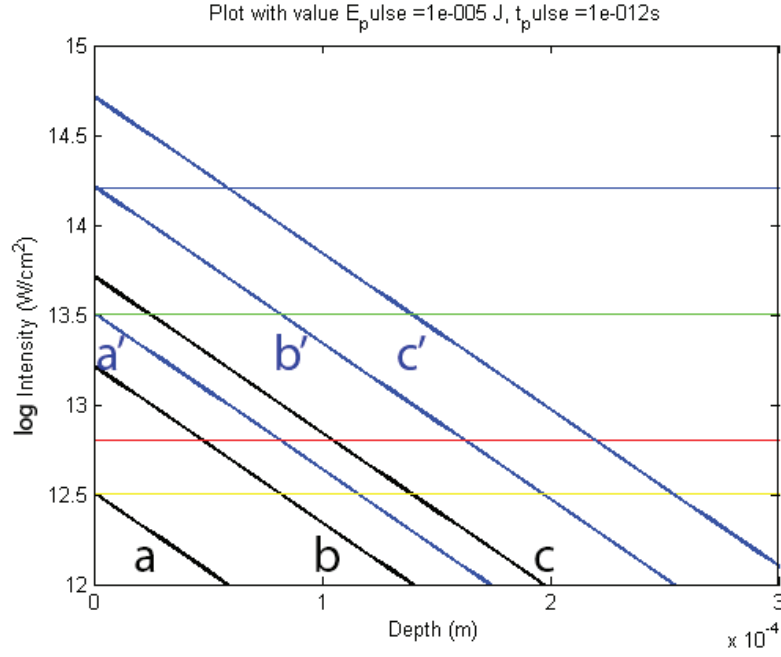


Figure IV-1: Calculation of the peak intensity in a focus at different depths in a scattering media (μ_s of 250 cm^{-1} , μ_a of 0.1 cm^{-1}) and for different focusing NA and pulse energy, compared to the LIOB threshold intensity of different materials. Lines a, b and c are the line representing peak intensity at focus for pulse of energy 1 μJ , with respective NA of 0.2, 0.45 and 0.8. Lines a', b' and c' are the equivalent lines for pulse energies of 10 μJ . The horizontal lines represent the LIOB threshold intensities found in literature for the following material (from highest to lowest): air (blue), SiO_2 (green), tissue (red), gold (yellow).

IV.1.1.2 Monte Carlo simulation of scattering through turbid media

Phantoms presented in Chapter 2 were meant to help us study ablation in a relatively well-controlled environment, as opposed to the random inhomogeneous properties of tissues. Simulations of light penetration could give us complementary information on values which are difficult to measure directly inside a sample, such as pulse profile at focus, or the proportion of ballistic photons at different depths. For this reason, we wrote a MATLAB program for Monte Carlo simulation to investigate the spatial and time-domain dispersion of a Gaussian beam through a 3D multi-layers scattering medium. The objective was to investigate the maximum depth of ablation, as well as the area around the ablation volume where photo-chemical effects could take place and potentially damage the sample. Description of the concepts behind the code of these simulations and some example of results can be found in Appendix B.

| Parameters | | | | | |
|--------------------|----------|----------|----------|----------|----------|
| NA | 0.8 | 0.8 | 0.8 | 0.25 | 0.25 |
| Focus depth (um) | 200 | 100 | 50 | 200 | 100 |
| | | | | | |
| Results | | | | | |
| Width FWHM (fs) | 420 | 290 | 280 | 290 | 260 |
| % focus 10 ps | 0.755443 | 9.453069 | 30.23225 | 0.866457 | 8.563046 |
| % ballistic photon | 0.673795 | 8.2085 | 28.65048 | 0.673795 | 8.2085 |

Table IV-1: Comparison of the results of the Beer-Lambert law for determining the number of ballistic photons reaching a target, and the effect of scattering on the pulse dispersion modelled by Monte Carlo simulation. These simulation were computed for 1000000 photons launched simultaneously toward a target at a certain focus depth, with a gaussian intensity profile corresponding to an objective with a NA 0.25 or 0.8. Photons were considered to have reached the focus when they reached a 2 μm diameter disk at the target depth. All simulations were made considering $\mu_s'=250\text{cm}^{-1}$, $\mu_a=0.1\text{ cm}^{-1}$. "Width FWHM" corresponds to the measured pulse duration at focus from the results of the simulation. "% focus 10 ps" is the percentage of the light exiting the objective which reaches the focus within 10 ps. "% ballistic photon" is the percentage of ballistic photons reaching the focus according to the model following Beer-Lambert law.

We considered the quantity of photons reaching the focus within 10 ps as an estimate of the lifetime of a quasi-free electron in water, as discussed in Chapter 2, to estimate the validity of a model considering on ballistic photons in the generation and growth of a plasma. According to these simulations, between 85% and 90% percent of the light reaching the focus within 10 ps is made of ballistic photons. We thus consider the Beer-Lambert model for acoustic photon to be appropriate to give us an estimate of the population of photons that will play a role in the plasma dynamics in tissue.

IV.1.2 Ex-vivo measurements of bubble size

In Chapter 2, we discussed that the observation of the creation of a bubble was recognized as a criterion of LIOB in aqueous media, and we have seen that the evolution of the size of a bubble could have an impact on the evolution on subsequent pulses. We will thus evaluate bubble size and its dynamics to assess our ability to control LIOB in tissue. We initially measure the size of bubbles created during ablation of pig arteries (to evaluate ablation in thick samples) before moving to mice samples. Adipose fat from the abdomen, being very rich in foam cells, was used as model for a lipidic atherosclerotic plaque.

IV.1.2.1 Materials and Methods

IV.1.2.1.1 Overview of the optical set-up

During the early stages of this thesis, the main optical set-up used revolved around a regenerative amplified laser (Spitfire F, Spectra-Physics) with a central wavelength of 800 nm. It was seeded by a Ti:Sapphire laser (Mira 9000, Coherent Inc.) which was itself pumped by a diode laser (Verdi G8, Coherent Inc.). The pump of the amplifier was a flash-lamp laser (Quanta-Ray, Spectra-Physics). Despite lacking the stability and high repetition rate of the more recent fiber-

laser, this system allowed us to obtain reliable bubble measurements, as well as the first ablation holes that we were able to observe ex-vivo.

The parameters of the amplifier, its seed laser, its pump laser, and the pump of the seed laser are presented in Table IV-1.

| | | | | |
|-----------------|-------------------|-------------------|-------------------|------------------------|
| Laser: | Verdi G8 | Mira 900 | Quanta-Ray | Spitfire F |
| Role: | Pump for Verdi G8 | Seed for Spitfire | Pump for Spitfire | Regenerative Amplifier |
| Wavelength | 532 nm | 800 nm | 532 nm | 800 nm |
| Pulse energy | 8W (continuous) | 3 nJ | 200 mJ | 2 mJ |
| Repetition Rate | continuous | 80 MHz | 10 Hz | 10 Hz |
| Pulse duration | continuous | 200 fs | 10 ns | 0.2-2 ps |

Table IV-2: Parameters of the 4 lasers part of the regenerative amplifier ablation system.

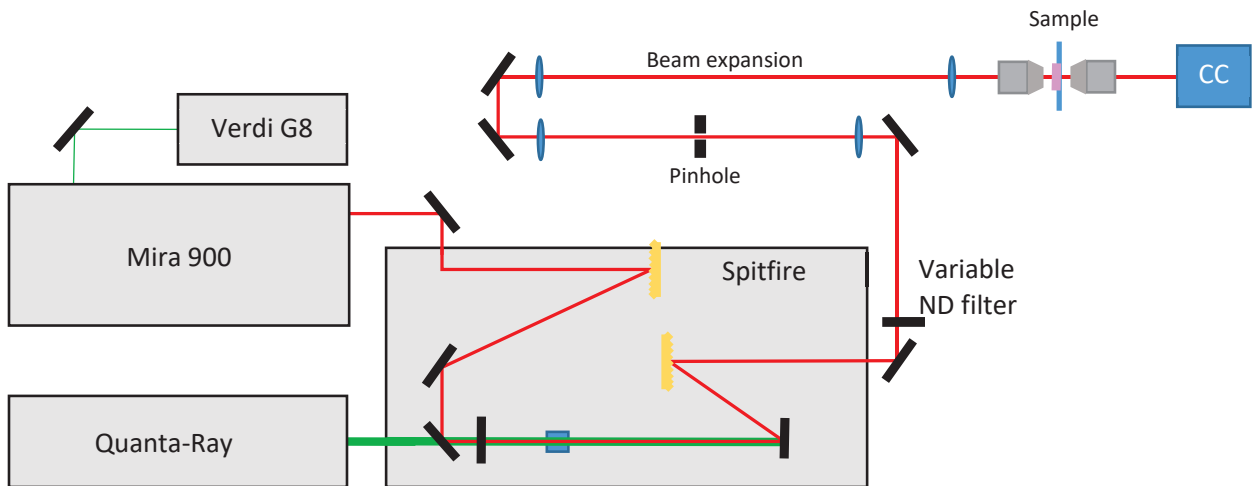


Figure IV-2: Diagram of the ablation setup based on a regenerative amplifier. The two yellow gratings represent the decompressive and compressive gratings in the regenerative amplifier cavity. Their placement represents their general location in the beam path.

The repetition rate of the pump was a limiting factor for the repetition rate of the whole laser system, and it was set to 10 Hz at the output to match the frequency of the pump. Pulse energy could reach very high levels of about 500 μ J, for an output power in the order of 5 mJ. Unfortunately, the output pulse energy was very unstable, its pulse to pulse repeatability varying from 3% to 10% depending on daily realignment quality or room temperature. This made it difficult to run iterative beam optimization algorithms, or, to some extent, ensure continuous ablation in tissue. A variable ND filter at the output of the amplifier was used to tune the pulse energy.

IV.1.2.1.2 Pulse duration selection

Apart from the very high pulse energies provided by this system, the possibility to use a pair of gratings in the cavity of the amplifier for adjustment to the beam duration proved valuable for some of our early experiments. The general concept is that a pulse of 150 fs emitted by the seed laser is spread by up to 10^4 by a pair of gratings in a parallel arrangement (to avoid photodamage to components of the laser), before being redirected to the cavity of the amplified laser where it goes through the amplification process itself. That is, the expanded seed beam interacts with a Ti:Sapphire amplifier crystal in the cavity which has previously been excited to a higher level of energy by pulses of the pump laser. Stimulated emission of the seed laser pulse takes place, with the generation of new photons adding coherently to the photon bundle traveling inside the cavity with a wavelength of 800 nm. The intensity of this pulse consequently grows each time it passes through the amplification crystal, as long as the population of excited particles is high enough to allow stimulated emission of photons. After several amplification back-and-forth through the amplification crystal, a Pockel cell located inside the cavity deflects the pulse out of the cavity onto a second pair of antiparallel gratings for time compression. By modifying the angle between these two gratings, we could choose the pulse duration at the output, by not completely correcting the chirp induced by the first grating stretching the pulse before the cavity with the second grating. The duration of the output pulse was thus set between 200 fs and 2 ps depending upon the experiments that we were conducting. A Frequency-Resolved Optical Gating (FROG) system was used to measure the pulse duration after the position of gratings had been modified. A mechanical stage was used to move the sample relatively to the focal volume.

IV.1.2.1.3 Fourier filtering

In order to improve the quality of the beam, whose intensity profile at the output of the amplifier was strongly dependent on the calibration and alignment of the system, and make it closer to a Gaussian beam, we filtered out the higher frequencies in the spectral domain. For this, we added a $2f$ system at the output of the laser, and added a pinhole in the central plane. Considering the very high intensities (in the order of the gigawatt), we decided to use a pinhole of 200 μm in diameter and two 50 cm focal length lenses, in order to limit the non-linear effects in the focus of the $2f$ system as they could induce a breakdown of the beam at the focus of the $2f$ system. With this system, the peak intensity was at maximum $3 \times 10^{-12} \text{ W.cm}^{-2}$, about one order of magnitude below the threshold for breakdown in air. A set of two lenses (50 cm and 75 cm) was then used to increase the beam diameter from 2 to 3 mm.

IV.1.2.1.4 Focusing on the sample

The beam was then focused on a sample by use of a 40x objective microscope with a numerical aperture of 0.65 with a working distance of 650 μm (Olympus) and a back aperture of about 3mm in diameter.

Depending on the thickness of the samples and the set depth of ablation, the focal plane of this objective was imaged either in reflection or transmission with a CCD camera (TM-7CN, Pulnix). A thicker scattering sample would typically be imaged in reflection, to mitigate the distortion due to the scattering taking place between the focal plane and the camera. This would for example be the case for the pig or lamb aorta samples whose thickness (above 1 mm) would result in a highly speckled image in transmission.

IV.1.2.2 Preparation of samples

IV.1.2.2.1 Pig artery samples

The first ex vivo samples we have been using to study the impact of LIOB in arterial walls were pig arteries. These were collected in the local slaughterhouse in Lausanne, on the day they were extracted (once a week). The collected arteries were pig abdominal arteries, and were thus the thickest samples we came to use in our studies. The arterial wall thickness (from the endothelium to the beginning of the adventitia) was measured to be about 0.6 mm.

This relatively high thickness and the natural stiffness of the aorta made it so that they tended to keep their curvature when they were placed on a microscope slide for ablation. This made it difficult to use a coverslide, but the exposition of the artery to air would lead to its drying. To prevent this from happening, we used 500 μ m coverwells imaging chambers (from Grace Bio Labs, USA) to keep the samples immersed in PBS, and slightly compressed by the coverslip polymer window. This slight compression diminished the roughness of the endothelium and allowed for a more homogeneous intensity when to focus was scanned laterally on the sample. Indeed, all points are covered by about the same thickness of tissue, and the beam profile was less strongly distorted by the air-sample interface when flat.

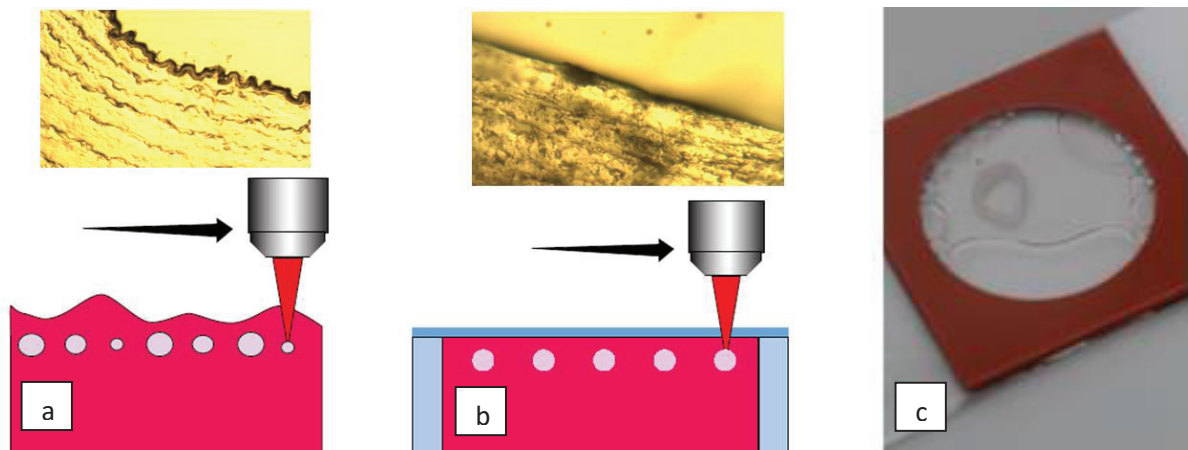


Figure IV-3: Diagram explaining why we initially used coverwells on our samples. (a-b) these two set of images represent ablation and sample cutting without (a) and with (b) a coverwell. Without a coverwell, the toughness of the sample creates aberrations: this is even more true on ex-vivo arterial tissue which will have a tendency to collapse inwards, increasing the roughness of the endothelium (upper images). This makes it difficult to have homogeneous ablation, and thus makes it difficult to discern ablation patterns in histology. (c) Picture of a piece of artery under a coverwell filled with PBS.

IV.1.2.2.2 Mice arteries and abdominal fat

Mice arteries and fat were initially provided to us by the laboratory Hemodynamics and Cardiovascular Technologies of Prof. Stergiopoulos at EPFL, and later by the Laboratory of Cardiology of the Université de Fribourg (UniFr, Fribourg, Switzerland) of Prof. Stéphane Cook. Both types of samples were harvested after the animal had been sacrificed, and were kept in PBS until the start of the histology or staining protocol, after ablation, to avoid drying. Before the

ablation, the arteries were cut open with a scalpel along the longitudinal axis, put on a microscope slide with the endothelium facing up, and a coverwell was used to keep them immersed in PBS. This way, the sample could be manipulated and put inside our ablation setup, with an easy access to the endothelium through the coverwell transparent polymer window.

The mice artery samples were from the aortic cross and ascending aorta: the lower part (toward the abdominal aorta) was straight, while the upper part (the aortic cross itself, leading to the heart) had a curvature of about 2 mm. This curvature made it more difficult to cut the sample in a straight line to get access to the endothelium, and to ablate in a straight line along the artery using the mechanical stages.

For experiments of ablation of abdominal fat, there was no problem for specific cutting or orientation issues, and volumes of about 2 mm³ samples were put directly under a coverwell filled with PBS. We tried to spread the volume evenly under the coverwell, to keep it evenly dense despite the pressure exerted by the polymer window: since the sample was soft and somehow compressible, this was a way to limit uneven optical properties within the sample.

The samples were extracted from adult C57BL-6J mice between 10 and 25 weeks old, and the arterial wall thickness was between 50 μm and 80 μm depending on the age of the animal and the location along the artery. After extraction, arteries collected from UniFr had to be maintained in PBS on ice from 2h to 5h before being cut open and placed under a coverwell.

IV.1.2.3 Measurements of ablation bubbles

Using the optical ablation system presented in IV.1.2.1.1, we proceeded with deep triggering subsurface LIOB and monitored the maximum bubble diameter depending on depth and pulse energy. Pulse duration was set to 1.5 ps, and we used a mechanical shutter to evaluate single-shot effects of ablation.

We first triggered ablation inside the arterial wall of a pig arteries, from the endothelium side. Our simulations presented at the beginning of this chapter show that we should be able to trigger ablation down to 45 μm for pulse of 0.5 μJ , and 160 μm with pulses of 5 μJ . Figure IV-4 presents the results of our measurements. Since the diameter of the bubble was measured from the camera imaging in reflection, we only recorded the maximum radial diameter value, and thus do not report elongation of the focus here. The indicated value reported as depth of ablation is in fact the distance the mechanical stage holding the sample was moved toward the objective, compared to its position for surface damage (measured for pulses at 0.5 μJ to avoid too much elongation of the beam). The coverglass window induced limited aberrations (estimated at 3 μm shift for focusing through the 170 μm of polymer of the coverwell itself). We repeated the same experiment on mouse arterial tissue, from the endothelium side, and mouse adipose tissue. The experiments are presented respectively in figures Figure IV-4 (c) and (d). The thickness of the arterial wall of the aorta in mice is about 60 μm , so no ablation was reported deeper than that value.

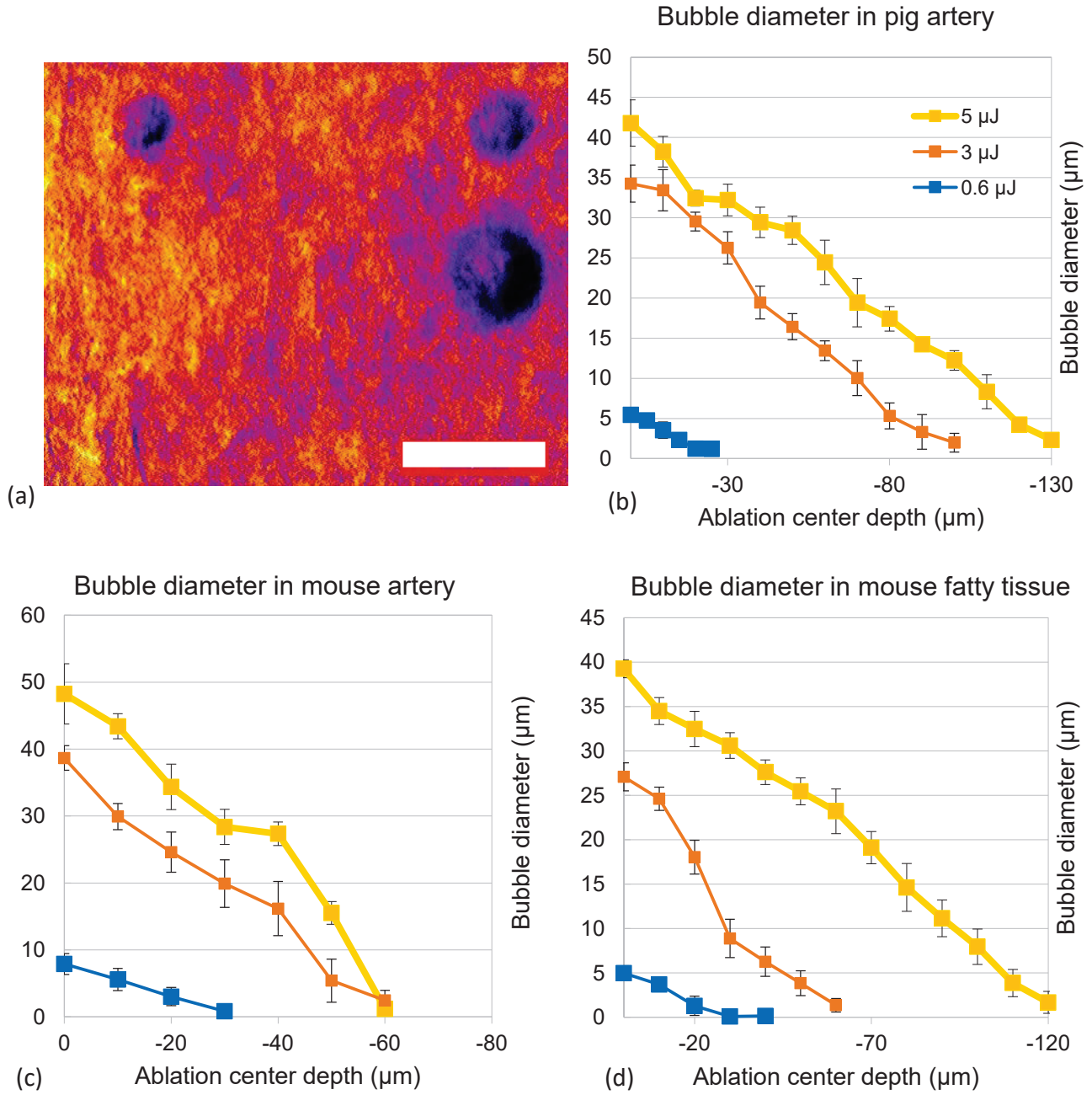


Figure IV-4: Ex-vivo data measurements. (a) Widefield image from LIOB-induced cavitation in pig artery. Scale bar is 50 μm . (b) Measurement of the maximum diameter of bubbles created by focusing the laser at different depths, inside pig arterial tissue. (c) Measurement of the maximum diameter of bubbles created by focusing the laser at different depths, inside mouse arterial tissue. (d) Measurement of the maximum diameter of bubbles created by focusing the laser at different depths, inside pig arterial tissue. All experiments were made with a NA0.65 objective on samples under a glass coverslide. Each point and its error bars are from measurements of at least 20 bubbles created in samples from two different animals.

The results obtained for the threshold of apparition of bubble created by LIOB are in line with the model presented at the beginning of this chapter for deep ablation; a comparison is summarized in table IV-2. The fact that the maximum depth of ablation for is slightly below the simulated values (especially for pulses of 0.6 μJ) may be explained by the inhomogeneity of the sample and its natural roughness which may induce aberrations. Additionally, the set-up we were

using only allowed us to measure bubbles whose lifetime is above 30 ms, so we are not able to image bubbles just above LIOB threshold, and whose lifetime can be in the order of μs .

| Parameters | | | |
|--------------------------------------|------|------|------|
| NA | 0.65 | 0.65 | 0.65 |
| E_p (μJ) | 0.6 | 3 | 5 |
| T_p (ps) | 1 | 1 | 1 |
| | | | |
| Measured | | | |
| Max ablation depth (μm) | 28 | 110 | 130 |
| | | | |
| Simulated | | | |
| Max ablation depth (μm) | 47 | 118 | 132 |

Table IV-2: Comparison between the measured maximum depth of ablation in pig artery measured in IV.1.2.3 and the simulation of maximum depth ablation in IV.1.1.1.

The bubble diameters just below the surface of the sample, where scattering is negligible, are also worth comparing with the results obtained from the phantoms in Chapter 2. In the range of pulse energy considered, single-shot LIOB in artery and in adipose tissue creates bubbles with very similar maximum diameter (within 10% difference). However, the bubble collapse in adipose tissue is significantly shorter than in arterial tissue. Although the focusing objectives and laser wavelengths were different between these ex-vivo experiments and the ones conducted in Agar and presented in Chapter 2, it is interesting to compare the two. The peak intensity from the NA0.65 is 4.07 times higher than the peak intensity from the NA0.25 objective used for agar gels ablation. Figure IV-5 represents the maximum bubble diameter in Agar 1% gel (Agar 2), Agar 3.5% gel (Agar 3) from Chapter 2, and in mouse artery, relative to peak intensity.

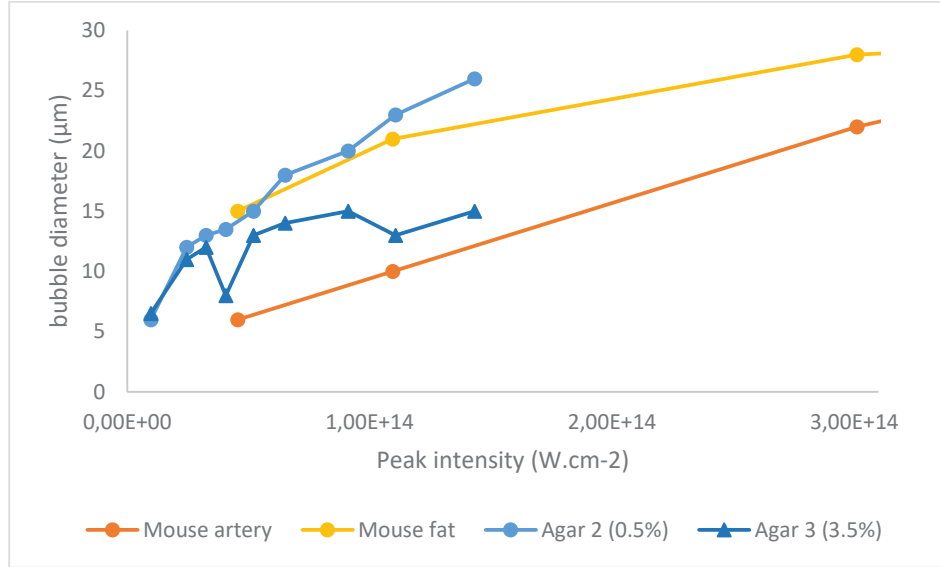


Figure IV-5: Bubble diameter after single-shot ablation by pulses of 1 ps and various peak intensity. The results for mouse tissue are the averages from 20 ablation events each, while the results for Agar are averages from 5 points in one Agar gel each.

Although none of these two gels seemed ideal to replicate the mechanical properties of tissue, the sample with Agar 3.5% gel (labeled Agar 3) is a good phantom to replicate bubble dynamics between fatty tissue and arterial tissue, despite having an elastic modulus about 3 times lower than the values reported for arterial tissue in literature. Our understanding of this situation is that: 1) the mechanical properties of the arterial wall are very directional because of the actin and collagen filaments aligned along its axis, and 2) the low thickness of the arterial wall limits its ability to apply pressure against the bubble. Although this partially validates the choice of our Agar gels as phantoms in Chapter 2, it indicates the 2% Agar gels we used for in-vitro studies were closer to fatty tissue than to arterial wall tissues.

The study of the bubble diameter (and more specifically its radial measurement) and collapse time provides more than an estimate of a mechanical effect of LIOB on a sample. It also provides two important benefits for ex-vivo and in-vitro measurements. Firstly, it allows us to estimate the minimum spacing we must maintain in an ablation scan, to avoid sending several pulses in one same location (which would probably only increase the size of the bubble, as described in the agar experiments in Chapter 2). Secondly, the size and lifetime of an LIOB-generated bubble are going to determine what kind of bubble (our threshold event for detection LIOB) we can observe in the following part of this chapter, where ablation bubbles are monitored in tissue using an OCT and histological methods.

Part 2: Ex-vivo ablation in atherosclerotic plaque.

We demonstrate sub-surface ablation of atherosclerotic plaque in harvested ApoE-KO mice aortas using ultrafast pulses. Femtosecond near-infrared (NIR) light pulses were focused into mouse arterial plaque and tunica media. Optical coherence tomography (OCT) was used to observe the ablation result, while the physical damage was inspected with histological slices of the ablated tissue. We characterize the effects of incident pulse energy on surface damage, ablated holes diameter, and filament propagation. We find that with appropriate pulse energy selection, subsurface ablation can be performed at 50 μm or deeper with minimal risk of surface damage.

IV.2.1 Materials and methods

IV.2.1.1 Animal and sample preparation

The ultrafast ablation experiments were performed using a genetically engineered mouse model that lacks apolipoprotein E gene. The ApoE knock-out (ApoE-KO) mice developed atherosclerotic plaques, particularly in the ascending aorta and the aortic arch when fed with lipid-rich (“western type”) diet¹⁰⁷. The plaque typically develops a few microns below the endothelium and grow to a couple hundred microns thick above the 70 micron thick tunica. In contrast, a plaque in an adult human coronary artery can be located a few hundred microns deep and be several millimeters thick. However, the chemical composition and growth mechanism of ApoE plaques are comparable to human plaque.

All animals received humane care in compliance with the European Convention on Animal Care and in accordance with the Swiss Animal Protection Law after permission was obtained from the State Veterinary Office, approved by the Swiss Federal Veterinary Office, Switzerland (FR 2013/35). Animals were fed for 12 to 16 weeks with a “western type” (lipid-rich) diet. The mice were anesthetized and sacrificed prior to aorta harvesting and kept in phosphate buffer saline (PBS) solution on ice. From 2 to 5 hours after harvesting, the arteries were cut open along the longitudinal axis, immersed in, PBS and mounted on a microscope slide with a cover slide. These tissues were then subjected to laser ablation with illumination from the endothelial side.

Control animals C57BL-6J of the same age were cared for and prepared in the same way as the ApoE-KO mice, except that they were not fed a lipid-rich diet, but standard mice food.

IV.2.1.2 Ablation Patterns

These ex-vivo experiments were performed on the fiber-laser set-up presented in Chapter 2, part 4, with the mechanical 3D stage. The OCT was not mounted on the set-up, and only used for observation of the sample before and after ablation. For analysis of the ultrafast ablation in atherosclerotic plaque, a specific ablation pattern was implemented by movement of the mechanical stage in conjunction with the selection of laser parameters. With the laser pulse repetition rate fixed to 1 kHz, the stage speed was adjusted to provide up to 5 overlapping pulses per focal volume. The ablation pattern routine created 8 or 10 ablation lines, each line separated

in the transverse (x) direction by $\delta_x=30\ \mu\text{m}$ and in the transverse (z) direction by $\delta_z=10$ or $\delta_z=15\ \mu\text{m}$ (Figure IV-6) The number of lines and δ_z were selected to allow for ablation from the endothelium, through the plaque, and into the tunica media. The focusing range was within the photon scattering mean free path in plaque, whose measured values ranged from 50 to 200 μm in the near infrared (NIR)¹⁰⁸⁻¹¹⁰. Thus, a majority of the incident photons did not undergo scattering in the tissue and the effect of depth on pulse intensity in the focal volume was limited in the depth range considered. Consequently, this analysis concentrated on the pulse energy and material type dependence of the ablation rather than on depth, with the exception being depth dependence on surface damage.

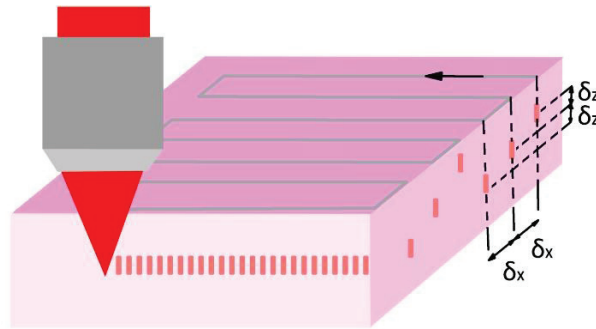


Figure IV-6: Representation of the ablation pattern and the arterial wall structure. A serpentine pattern is used for the ablation, with each line going a distance $\delta_z=10\ \mu\text{m}$ deeper than the previous one, and separated by a distance $\delta_x=30\ \mu\text{m}$. The right side of the diagram shows how the ablation pattern appearing on a transversal histological cut. The tunica media is the part of the arterial wall closest to the blood flow, its cells directly in contact with the blood flow are endothelial cells, forming the endothelium. This endothelium is what we refer to as the surface of the artery.

IV.2.1.3 Preparation for cryocutting

To preserve the ablation holes for analysis, the ablated tissue samples were frozen and prepared for histological sectioning. To ensure that the analysis accounted for ablation hole size and not gas bubble size, the time between ablation and freezing of the sample was greater than the observed diffusion time of the gas bubble ($\sim 30\ \text{min}$). The first step was to embed the sample in a matrix, optimal cryocutting temperature compound (Cryomatrix, Thermo Scientific), which would allow its freezing to take place in a homogeneous step removing the risk of ice crystal formation (Figure IV-7). Indeed, the formation of ice crystals in a sample before cutting would translate into cutting artifacts looking like empty areas on the final histological slice, and could be mistaken for an ablation hole. We hence filled a small plastic embedding mold (about 3 times the length of the sample) with OCT, and immersed the sample in it. We labeled the exact location of the sample on the sides of the mold to help finding its location during cryocutting. The sample was slowly frozen to -20°C in the fumes of isopentane cooled by dry ice. Later, the samples were cut orthogonal to the ablation lines 8 μm to 25 μm thick slices using a cryostat (Leica 3050S, Leica Biosystems, Germany) at the Histology Core Facility (HCF) of EPFL, and stained with haematoxylin and eosin (H&E). The main drawback of H&E was that the lipidic pools present in the plaque were

removed by the alcohol involved in the staining process, resulting in empty lipidic vacuoles on the histological slices.

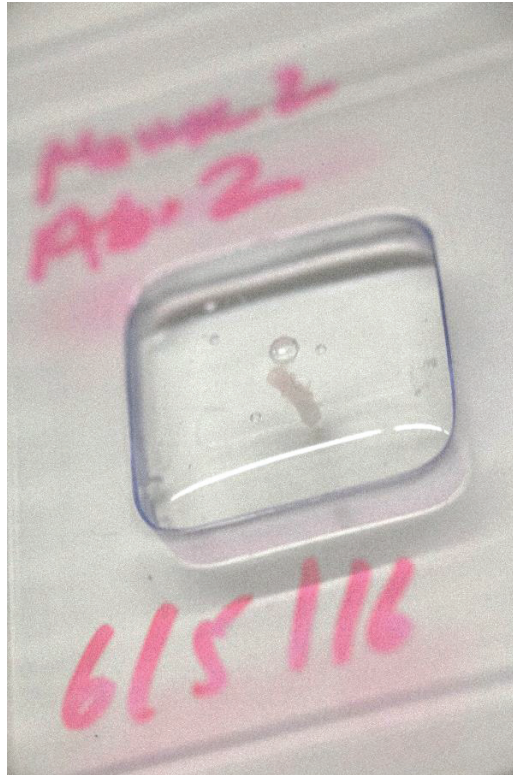


Figure IV-7: Image of a mouse artery placed vertically in a sample mold filled with OCT (Optical Cryocutting Temperature compound), prior to freezing for cryocutting.

IV.2.1.4 Staining

IV.2.1.4.1 General morphology staining with H&E

To observe the general morphology of a sample, we generally relied on a staining protocol very widely used in histology: hematoxylin and eosin (H&E). Hematoxylin is an organic molecule that binds to DNA in the cell nuclei via dye-metal complex, while eosin is an acidic compound that binds to basic compounds such as the cytoplasm. These two stains are widely used together as they provide a good set of information about the morphology of a sample: hematoxylin provides a good way to image the individual cell nuclei and thus estimate the whole cellular population, while eosin gives an idea of the size, individual morphologies, and connections of cells forming the tissue. In the case of the staining of arterial walls (and muscles in general), eosin also stains actin filaments and collagen strongly, thus providing extra information about the whole fibrous scaffold. H&E staining was performed by either Dr. Jessica Dessimoz and her staff of the HCF at EPFL or J  r  my Valentin at UniFr, and was compatible with both cryocut slices and paraffin sections.

IV.2.1.4.2 Oil Red O

When confirmation of whether a hole on a H&E slide was the result of a lipidic vacuole or a cut artifact was needed, Red Oil staining was used on an adjacent histological slice, as neither of these stains structurally modifies the lipid pools. Oil Red O (Sigma-Aldrich) is a fat-soluble dye (or

lysochrome) that we used to stain lipidic atherosclerotic plaques¹¹¹ in mice arteries. 25 mg of Oil Red O was diluted in 500 mL of isopropanol to create a stock solution. This stain is not compatible with protocols using clearing solvents (such as paraffin embedding) as these would remove the lipids to be observed, and we thus only used Oil Red O on cryocut slices. Before staining, 30 mL of the stock solution were mixed with deionized water for immediate use. Samples to be stained were fixed in PFA4% before freshly made Oil Red O was used to stain them.

Samples stained with Oil Red O would exhibit a strong red coloration in areas of high lipid concentration. Samples could then be mounted in Glycerine Jelly Mounting Medium to prevent diffusion of Oil Red O.

IV.2.1.5 Ablation characterization metrics

The H&E stained histological sections were evaluated under a transmission widefield microscope with a 40x objective (NA 0.7). Figure IV-8 (a-e) portray a variety of holes created with the ultrafast laser ablation, from well-defined symmetric holes of about 5 μm diameter (Figure IV-8 (a)) to elongated structural damage up to 100 μm in length (Figure IV-8 (d)) depending on the pulse energy used. Figure IV-8 (f) illustrates the metrics used during the quantitative characterization of the holes: the depth of ablation, D , the transverse and axial extent of the ablation hole, R_b and L_b , and the total length of ablation including the “tail,” L_r . The “tail” is the result of some sort of filamentation, as discussed in Chapter 2 Part 3, and could be found throughout the sample (Figure IV-8 (b-d)). Figure IV-8 (g) shows a representative tissue sample which includes the ablation pattern illustrated in Figure IV-6 (b).

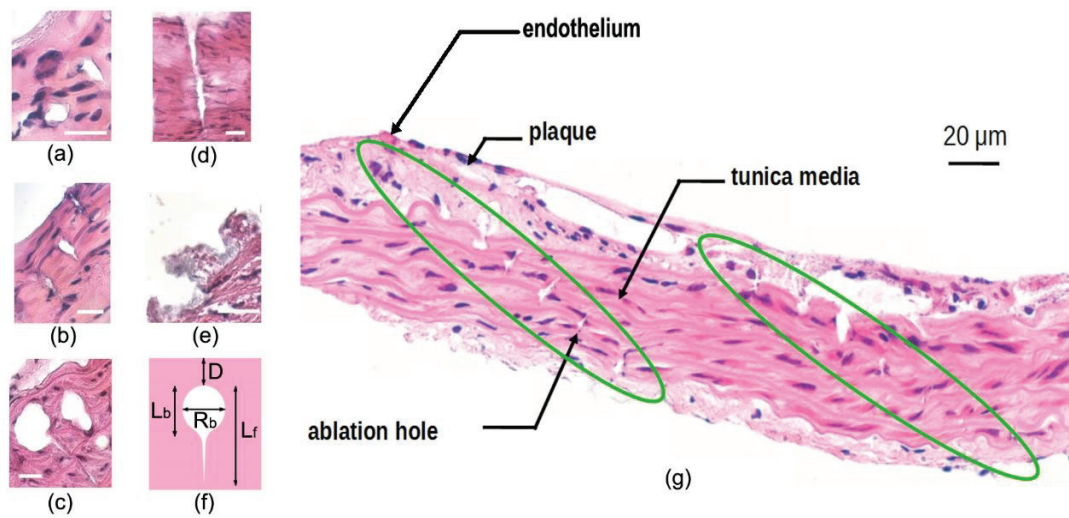


Figure IV-8: Images of representative ablation holes from histological slices. (a) Nearly symmetric 5 μm ablation spot ($E=0.6 \mu\text{J}$), (b) 5 μm ablation spot with short filamentation ($E=0.6 \mu\text{J}$), (c) ablation spot with elongated filamentation tail ($E=4 \mu\text{J}$), (d) pure filamentation ($E=10 \mu\text{J}$), (e) surface damage ($E=4 \mu\text{J}$), (f) diagram describing how the different holes were characterized, (g) representative ablation pattern (green oval) reconstructed from several images. Scale bar is 10 μm in (a-e).

The medical application of ultrafast ablation of atherosclerotic plaques requires that the fibrous cap, or endothelium, remain undamaged during the operation. For an accurate assessment of sub-surface ablation diameter, it was necessary to filter out results from scenarios in which the

laser was focused on the surface of the tissue and caused significant surface damage. Thus, only ablation holes that were further than 10 μm from the surface were considered in the analysis of ablation diameter, as the axial length of the ablation damage is around 10 μm .

Due to its extensive occurrence, filamentation was analyzed in further detail. We initially thought this filament propagation to be a nonlinear optical side effect of the high-energy pulses used for ultrafast ablation¹¹², but the experiments on tissue phantoms in Chapter 2 lead us to believe it could more probably be the result of some local pulse-to-pulse cumulative effects. Filamentation was considered to be present in either of two cases: (1) a “tail” of structural damage was apparent in the sample which continued from the ablated volume deeper into the tissue (Figure IV-8 (b and c)), or (2) the aspect ratio of the ablation hole was 0.2 or less (Figure IV-8 (d)), corresponding to an axial dimension greater than five times its transverse diameter. In the second case, the filamentation length, L_r , was set to the axial dimension of the hole, L_b , to be consistent with the measurement method presented in Figure IV-8 (f).

IV.2.2 Ablation characterization results

IV.2.2.1 Overview of the structural damage induced

The structural damage which resulted from ultrafast ablation in both plaque and the neighboring tunica media were characterized. Several criteria of the ablation holes were assessed: surface damage, ablation diameter, difference between ablation in plaque and tunica media tissue, and filament propagation. All these were analyzed in relation to incident pulse energy. No significant difference was seen within the range of pulse overlap values (5 or fewer pulses per focal volume). 2106 holes were characterized individually from the atherosclerotic aortas of 6 different ApoE-KO mice.

The surface damage risk dependence on ablation depth in plaque was analyzed. Figure IV-9 (a) plots the surface damage probability dependence on pulse energy and ablation depth. The existence of surface damage was evaluated on whether any structural modification above an ablation hole and near the surface of the tissue sample ($<10\text{ }\mu\text{m}$) existed. This could be manifested by a physical distortion of the tissue (scrambling) or an ablation hole which extended from the surface. As expected, the likelihood of surface damage decreases with increasing depth and decreasing energy. The data indicate that the risk to damage the surface remains minimal when focusing deeper than 15 μm under the surface with pulse energies below 4 μJ . Importantly, this suggests the possibility of ablating unstable plaques without damaging even the thinnest of fibrous caps.

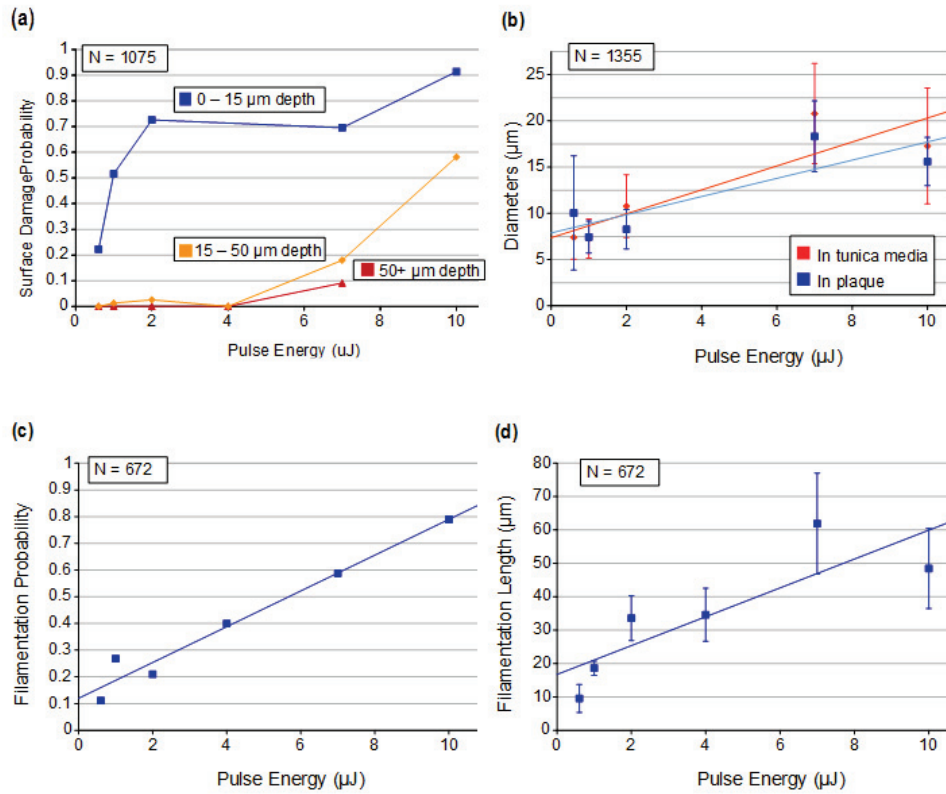


Figure IV-9: *Characterization results of ultrafast ablation. N is the number of holes characterized. (a) Surface damage probability in different depth ranges dependence on pulse energy. (b) Ablation diameter measured in plaque and tunica media versus pulse energy. (c) Filamentation probability for different pulse energies. (d) Filament propagation length versus pulse energy.*

The ablation diameter measured transversal to the laser propagation was also evaluated and compared based on the ablated material (Figure IV-9(b)). As described previously, the diameter measured corresponds to the material vaporized rather than the gas bubble size. Not surprisingly, the ablation diameter increased with increasing energy. The ablation diameters in plaque and tunica media tissue were not significantly different and offered cell-sized ablation diameters (10 μm) with 4 μJ pulses. By increasing the energy to 10 μJ per pulse, the ablation enters into a regime with extra-cellular ablation sizes ($\sim 18 \mu\text{m}$).

The filament propagation in plaque was characterized in two ways: (1) the filamentation probability (Figure IV-9 (c)) and (2) the filament propagation length (Figure IV-9 (d)). As expected, increasing the pulse energy increased the likelihood and length of filamentation. Ablation with pulses of 10 μJ posed a high risk of creating uncontrolled damage beyond the cellular range with filamentation extending on average 45 μm in length with a variability above 50%. The results also indicate that with pulse energy of 4 μJ the filamentation length is similar to the ablation hole size, despite the filamentation index remaining high (0.35).

IV.2.2.2 OCT observation of ultrafast ablation

The objective of a second experiment was to ablate an extended volume, and to image it with OCT to mimic a likely ablation scenario if applied medically. As an established tool for arterial

plaque imaging, OCT is a natural tool for use with arterial plaque ablation. OCT provides an ideal means to monitor the gas bubbles resulting from ablation because its contrast mechanism comes from index of refraction differences. The high index difference between gas and tissue would be clearly visible with OCT, in fact it has previously been used to observe subsurface ablation bubbles¹¹³. In the case of atherosclerotic plaque, it could be used to initially locate the plaque and to monitor the ablation¹¹⁴. For OCT imaging, an ablation pattern similar to Figure IV-6 (b) was implemented with the distinct difference that the parallel ablation lines were separated less ($\delta_x = 5 \mu\text{m}$) and all in the same axial plane ($\delta_z = 0 \mu\text{m}$). The resulting ablation pattern is a plane of $100 \times 200 \mu\text{m}^2$, as opposed to the discrete lines of the first experiment. Using a 5 pulse overlap for stage speed, this pattern could be scanned in 280 ms. In this implementation, however, time delays from a low x-axis step velocity, used to minimize stage vibration, slightly increased this time. This pattern was ablated in a healthy mouse aorta (from a C57BL-6J mouse) with the beam targeted in the middle of the tunica media and imaged before and after with OCT. The OCT images were compared to H&E stained histological slices prepared following the procedure described previously. The ablation was conducted with pulses of $1 \mu\text{J}$ energy. During the course of the ablation, the OCT image showed that the ablation gas bubbles merged. In the ablated region, the hole has partially closed down in both the OCT image (Figure IV-10 (a)) and histological slice (Fig. 5(b)). As expected from the results of the first experiment, there was no observable surface damage or filamentation at this pulse energy. Furthermore, the ablation area appears clearly defined, without detectable structural damage near the target area.

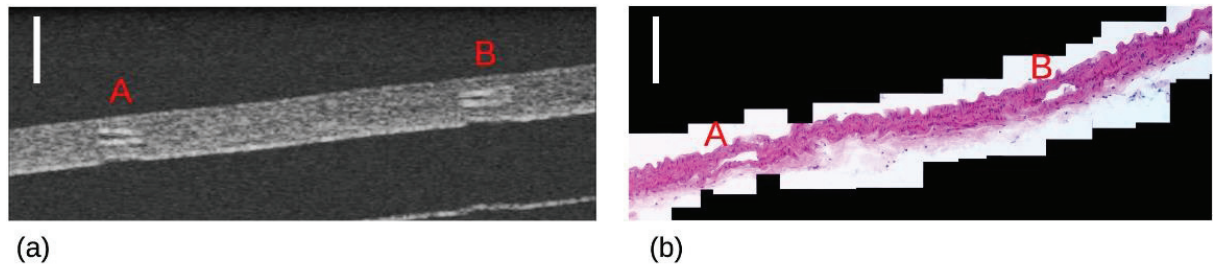


Figure IV-10: *Healthy mouse arterial wall ablated with two $100 \times 200 \mu\text{m}^2$ plane separated by $500 \mu\text{m}$. (a) Transverse OCT image of the ablation area. (b) Transverse of the histological cut of the ablation area, from a series of microscope transmission images reassembled with ImageJ. The letters A and B are indicative of which hole is which. Scale bars indicate $100 \mu\text{m}$.*

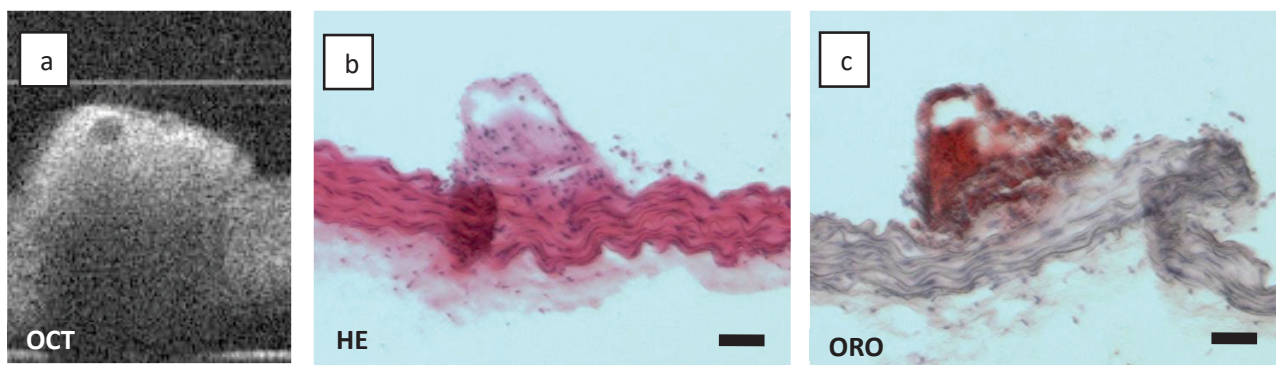


Figure IV-11: *ApoE-KO mouse plaque ablated with a 50x100 μm^2 plane. (a) OCT image of the plaque. (b) H&E staining of the same area, where the area corresponding to the bubble seen on the OCT image appears to be ablated. (c) Oil Red O staining of the next slide of the ablated volume, where an empty space appears to correspond well to the bubble on the OCT image.*

A final ablation experiment was pursued to observe volumetric plaque ablation via OCT. The plaque was clearly discernible with OCT and was specifically targeted in this experiment in which five planes were ablated consecutively above one another, starting with the deepest plane and moving towards the endothelium. By using 1 μJ pulse energy and selecting a separation of 10 μm between each plane, an ablation volume of 100x200x50 μm^3 was created. The target sample (a 25 week old ApoE-KO mouse) provided significantly thicker plaque (about 400 μm), with more lipidic pools (see figure Figure IV-12), than the previous samples. Due to the plaque thickness, it was mounted in a microscope slide well. The thickness of the sample required that the tissue sample be flipped over for OCT observation following the ablation procedure. Transversal OCT images of the ablation area at 1, 3, and 5 minutes after ablation were obtained and the corresponding histological slice was stained with H&E for comparison (Figure IV-11 and Figure IV-12). Despite the relatively large volume ablated, no bubble could be observed on the OCT 5 minutes after ablation in the sample of Figure IV-12, but staining of the sample of Figure IV-11 with ORO shows lack of lipid precisely in the area of ablation. The corresponding histological slice shows that the area corresponding to the ablated volume is empty after H&E staining. A possible explanation is that lipids filled in the space left after ablation and were later removed during the staining process.

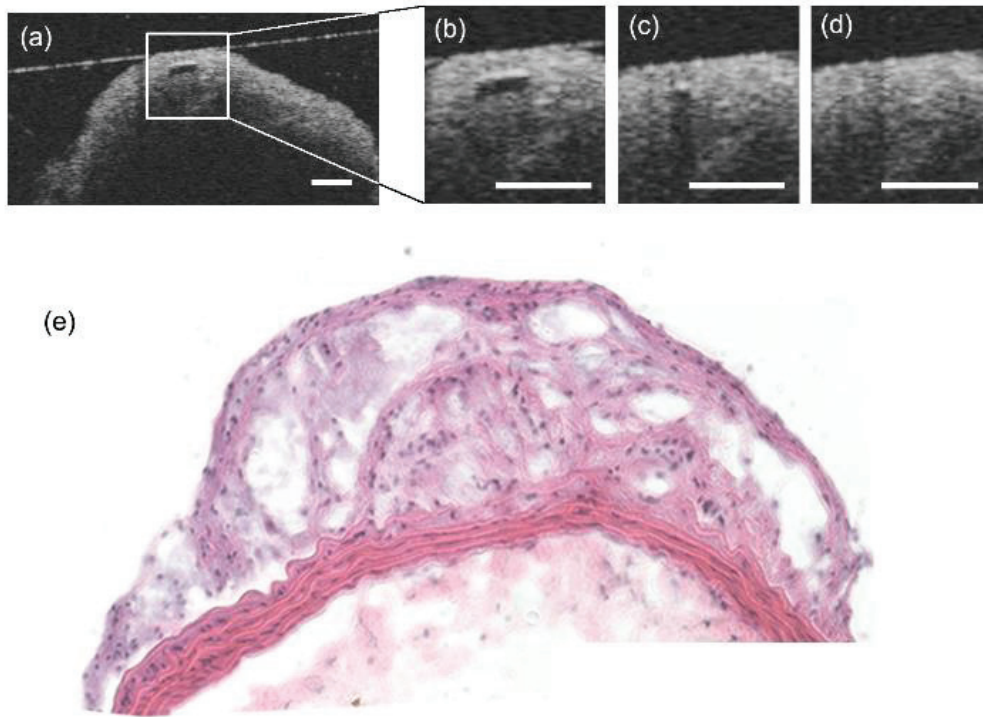


Figure IV-12: *ApoE-KO mouse plaque ablated with a $100 \times 200 \times 50 \mu\text{m}^3$ volume. (a) Transverse OCT image of the ablation area. (b-d) Time evolution of the ablated volume after the ablation ($t = 0 \text{ min}$). (b) $t = 1 \text{ min}$, (c) $t = 3 \text{ min}$, (d) $t = 5 \text{ min}$. (e) Transverse of the histological cut of the ablation area.*

IV.2.3 Discussion

We have observed and characterized ultrafast ablation in atherosclerotic plaque and tunica tissue. OCT images clearly showed the gas bubble resulting from ablation, which demonstrates the utility of this imaging technique for ablation observation. IV-OCT devices already exist and provide clinicians with a valuable, high-resolution tool for plaque recognition and characterization¹¹⁵. The ablation characterization experiments provide useful insights into the physical effects of ultrafast ablation in atherosclerotic plaque and neighboring tissue. The study indicates that ultrafast ablation in plaque and the tunica media have similar ablation characteristics regardless of the energy levels experimented with. The results further indicate that pulse energies below $4 \mu\text{J}$ provided axially isolated ablation volumes, such that ablation targeted below $15 \mu\text{m}$ deep rarely induced surface damage. These results suggest the possibility of fine ablation of unstable plaques only a few tens of microns beneath the endothelium. The experiment also has revealed that filament propagation plays an important role in ultrafast ablation in plaques at the studied energy levels. Balancing the effects of filamentation with subsurface ablation in plaques will be an important task in the design to any catheter device, depending on its designed focusing NA and pulse energy levels.

The applicability of these results in the context of a lowly-invasive catheter approach also depends on the ability to transfer the laser pulses through optical fibers. Fortunately, in the last decade there has been consistent progress in the maximum peak power which can propagate

through prototype and commercial single-mode hollow core photonic crystal fibers (HC-PCF)¹¹⁶. Picosecond pulses with energies of several tens of microjoules have been transmitted through HC-PCF with cores up to 70 μm in diameter¹¹⁷. Ultrafast ablation has recently been demonstrated through HC-PCFs with similar pulse properties in a catheter prototype¹¹⁸. In the experiments presented here, the pulse duration was fixed to 1.5 ps, rather than the femtosecond range, as pulses in the picosecond range experience a smaller change in their pulsewidth due to dispersion and, consequently, smaller reduction in peak intensity, while having similar ablation threshold values¹¹⁹.

Part 3: In-vivo Ablation

From our in-vitro and ex-vivo experiments, we had developed a good basis for a general vision of LIoB in arterial tissue. The next step was to repeat ablation in a sample where the optical, mechanical, and biochemical effects could be studied in the most realistic way. The best answer to this, obviously, was to proceed with ablation experiments in-vivo. We thus decided to pursue our experiments in the arterial wall of wistar rats, as a reasonable step-up from the mice experiments. Four reasons made rats an appropriate model: 1) the arterial wall of rats are similar to the ones of mice but thicker (around 100 μm instead of 60 μm for mice), 2) the internal diameter of rat aortic arteries is significantly larger (around 1.2 mm instead of 0.7 mm), 3) surgery on rats is well established and the races used in research can be quite resilient to post-surgery infections, making them a practical model 4) The abdominal cage is large enough the we can lower the imaging objective of the OCT close enough to the abdominal aorta for imaging and ablation. We want to mention that the results presented in this part are from a small set of 2 rats. 8 other rats had previously been used following a protocol similar to what is presented here, but with use of the NA 0.2 objective. This choice was guided by the hope of getting better OCT images, but the control in depth ablation proved very challenging and several other technical issues arose due to use a non-immersion objective. We decided not to include the corresponding results in this discussion, as none of them were subsurface and they all came with different problems during manipulations, but more detail is given in Appendix D for helping anybody who would be interested in trying to replicate these experiments. One of the two animals for which we analyzed the artery was also subject to a functionality test by use of a myograph which we discuss in Appendix F.

IV.3.1 Materials and methods

IV.3.1.1 Modification of the optical system

For the in-vivo experiments, we used the fiber-laser ablation system (Chapter 2 paragraph 4.1.1) with the integrated OCT (Chapter 3 paragraph 3.1.1) as the basis of the experimental set-up for the animal experiments we conducted at UniFr (Figure IV-13). The whole system was rendered more compact to hold on a 100x60 cm optical table to be transported inside the animal surgery room, and we designed a simple 3D stage to carry the weight of the animal, provide easy access to the animal for the surgeon and operators, as well as easily allow to tilt the animal in case the angle between the target sample and the OCT objective needed to be adjusted. A simple solution was the use of an aluminum stage of 30x20 cm (to accommodate an adult rat) fixed on a photography ball-head attached to the optical table. The aluminum stage was pierced with 6 holes to allow attachment of the animal on the table, or attach a heating pad for the duration of the experiment.

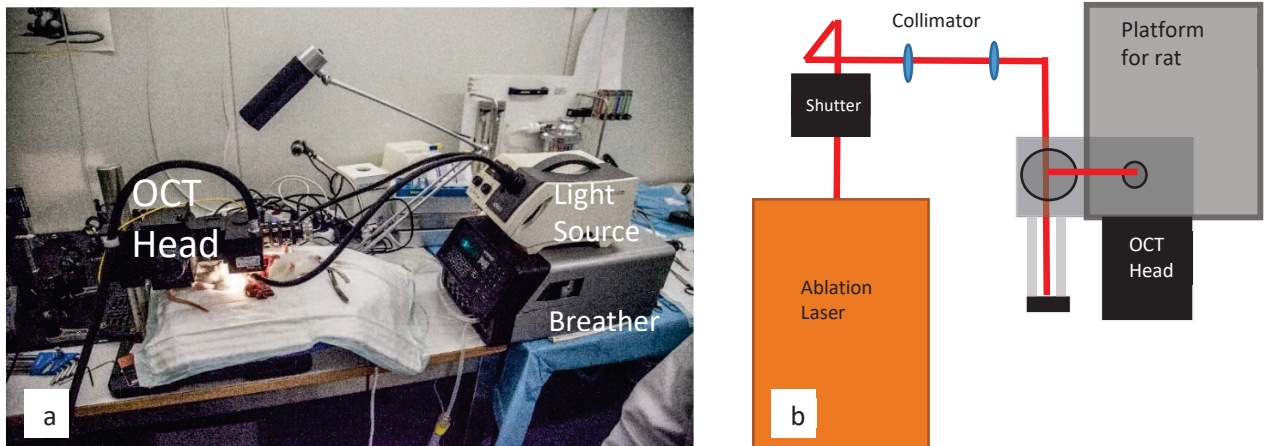


Figure IV-13: Optical set-up used for in-vivo ablation. (a) The set-up mounted in the surgery room in Fribourg. (b) Design of the optical set-up including the laser and OCT head, both controlled via a Labview program, the platform holding the animal and a mechanical shutter.

IV.3.1.2 Preparation and surgery of rats

The animals, wistar rats aged 3 to 5 months and weighing between 350 and 510 g, were anesthetized via injection of temgesic anesthetic, and laid down on a surgery blanket. Breathing was maintained and inhalation anesthesia was conducted using endotracheal intubation to deliver oxygen and isoflurane to the animal to increase the duration of the anesthesia. Surgery was conducted by Aurélien Frobert, expert in animal cardiology from UniFr by first cutting an opening in the outer abdominal tissues, which allowed for the removal of the intestines and other organs covering the abdominal aorta away from the beam path, without damaging any vital organ (Figure IV-14 (a-c)). This did not induce fatal injuries as it only required cutting through connective tissues, but allowed us to get a clear access to about 2 cm length of abdominal aorta. Two markings were then made by the animal surgeon using a fine-tip cautery to differentiate the target ablation area and separate it from the control area (Figure IV-14.d), which was located upstream from the branching between the abdominal aorta and the renal artery. The artery was also surgically cleaned of most of the connective tissues directly attached to it (Figure IV-14.e). The rat was then moved to a platform covered with a heating pad at 37°C to maintain the body temperature of the animal and prevent hypothermia, and was set on a mechanical stage so that the desired target area of the rat could be placed appropriately in the optical path of our ablation system by moving the animal platform. The respiratory device was kept next to the animal and active to help maintain its breathing capacities and ensure it remained anaesthetized during the ablation experiment.

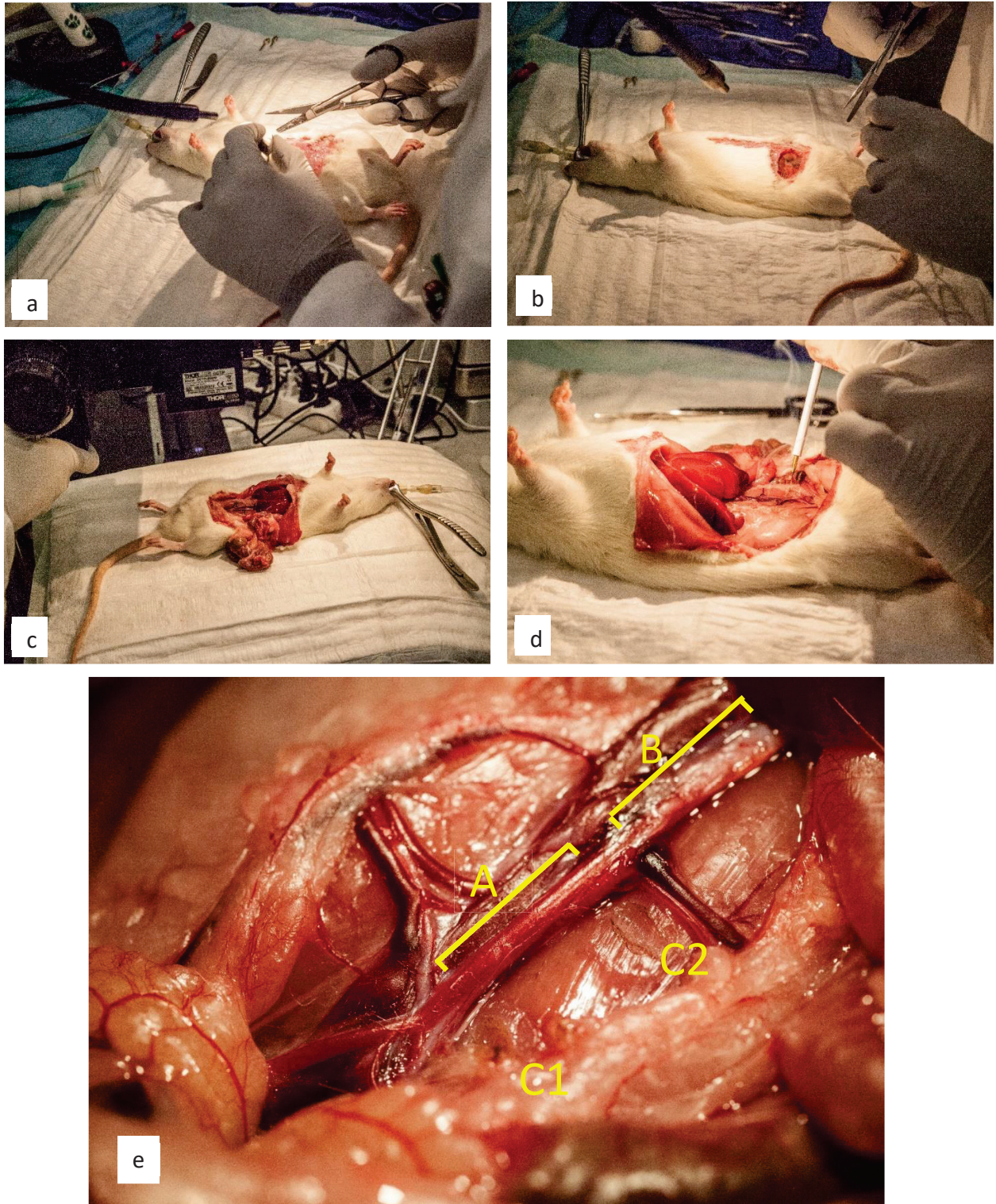


Figure IV-14: Protocol for the animal surgery in preparation the laser ablation ablation. (a) The anaesthetized rat on the surgery blanket. The surgeon is cutting through the outer layer of skin attached to the fur. (b) Opening in the abdominal wall to get access to the abdominal cavity. (c) The various organs of the abdominal cavity covering the aortic artery are taken out of the abdominal cavity and put aside on the surgery blanket to provide an access to the abdominal aorta. (d) A fine-tip cautery is used to help visualize the start and end of the target area along the artery during ablation. (e) The abdominal cavity cleared out of organs. A marks the target area of the artery, B marks the control area, C1 and C2 indicate the marks made with the fine-tip cautery. The dark vessel next to C2 is the renal artery, which also provided information to the focal volume location during the ablation.

In the case where ablation was performed using an air objective, we noted that for certain animals, a strong fogging of the objective outer lens would appear in less than a minute. For these experiments, we had to raise the microscope objective for about 30 seconds for the humidity on the objective to disappear, which prevented having a continuous ablation and increased our ablation time by a few minutes.

In the case when ablation was performed using an immersion-objective, we maintained the objective immersed in Phosphate Buffer Saline (PBS) by filling the abdominal cavity. The index of PBS is 0.002 higher than that of water, which was not enough to induce strong aberration during OCT imaging, while its osmotic saline concentration helped avoiding bloating of the organs. This worked well despite the fact that some leaking could not be avoided and PBS had to be added under the objective about every minute, due to its long working distance.

After ablation was performed, the surgeon would sacrifice the rat by exsanguination and harvest its abdominal artery. It was cut according to the markings previously made to separate the ablated area from the control area, and samples were either put in immersion in PBS for later staining or paraffin histology preparation, or prepared for cryocutting histology right after extraction. In both cases, keeping the right orientation of the artery to later help in recognizing the ablated area was essential. Samples to be stained for detection of apoptosis were stained for over 8 hours to guarantee the activation of apoptosis-specific proteins and DNA fragmentation.

IV.3.1.3 Paraffin sectioning

In Paraffin-embedding of tissue, keeping track of the orientation of the sample can be challenging. As opposed to sample preparation for cryocutting, where the OCT compound used to embed the sample is gel-like enough to prevent movement of the sample, preparation for paraffin sectioning requires several steps where the sample is immersed in liquid. As the sample is then moved in successive baths, its orientation can easily be lost. Considering how important it is for our experiments to be able to track the area of the sample which has been subject to laser ablation, we used a protocol to prevent the samples from moving freely in liquid. Straight after ablation (for ex vivo experiments) or after harvesting (for in vivo experiments), the samples were encased in plastic cassettes where they were held static between two rectangular foam spacers. Because of the slight pressure exerted by the foam, the arteries being maintained this way had a tendency to collapse inward to a more flat shape (as can be seen from histology cuts) because of the slight pressure exerted by the foam, this did not seem to induce any damage.

The samples were then fixed by immersion in 4% paraformaldehyde (PFA) for a period ranging between 1 and 2 hours, depending on their size. They were then placed in a tissue-processing apparatus (ASP200,) at the EPFL HCF for overnight treatment according to the protocol defined in Chapter III.3.1.2.4.

The samples were then embedded into paraffin in preparation for sectioning: they were placed in a metal mold and immersed in melted paraffin at 60°C, and quickly put on a cooling pad at -20°C for quick solidification of the paraffin blocks. These blocks were then unmolded and mounted on a microtome (HM 325 rotary microtome, Leica Biosystems, Germany) for cutting.

Samples from 4 to 16 µm thick were cut by sliding the samples against the static blade of the microtome, and the sections were stretched on the surface of a demineralized water bath at 45°C.

Microscope glass slides were then used to scoop them from below. 3 to 4 slices were collected on each slide.

Since the samples had been fixed prior to cutting, sections could be kept at ambient temperature for several weeks before staining and analysis.

IV.3.1.4 Timeline and Troubleshooting

Based on previous experiments of ex vivo ablation of mouse arteries presented in Chapter 4 Part 3, we decided to pursue ablation of arterial walls with pulse energies between 0.6 μJ and 10 μJ . Considering the risk of having cumulative pulse-to-pulse effects when using repetition rate of the laser higher than 10 kHz, ablation was performed with a repetition rate of 1 kHz and an energy of 9.5 μJ per pulse. The corresponding peak power in the center of focus was about 2.5 $\text{TW}\cdot\text{cm}^{-2}$ when focused on the surface of the sample, and about 0.5 $\text{TW}\cdot\text{cm}^{-2}$ when focused under 100 μm of rat artery, assuming an attenuation coefficient of 15 cm^{-1} typical of soft tissues at a wavelength of 1030 nm.

The galvanometric mirrors in the OCT head and the laser shutter were controlled using an in-house Labview program, allowing us to trigger ablation in patterned series and switch between an OCT imaging scan and an ablation scan modes. It allowed us to set and monitor the depth of focus, scanning pattern, and speed of the galvanometric mirrors, both for use in the OCT imaging and during the ablation process. It was also our interface to define the repetition rate and pulse energy at the laser output. A complementary shutter in the pathway of the laser was set-up as a security shut-off option.

The ablation pattern was 200 μm wide and 500 μm along the axis of the artery which allowed our focus to stay within the optimal area of the objective field of view and to be relatively thin with respect to the curvature of the artery, which had an inner diameter of about 1.5 mm. The beam was scanned in a raster pattern with ablation spots separated by about 1.5 μm . The ablation pattern was repeated 5 times along the artery, going upstream of the blood flow. As we were interested in subsurface ablation, we targeted areas of the intima media between 30 μm to 100 μm below the surface of the artery.

Once the animal was set on the platform, we lowered the microscope objective and moved the platform to have the exposed artery in the field of view and in the focal plane of the OCT objective. We then recorded a scan of the artery with the OCT, moving the animal by using the mechanical stage to go through the length of the artery by repeating the pattern several times.

The ablation along the artery lasted between 8 and 10 minutes. To estimate the duration of the full experiment, one has to add the time required for the surgery and the removal of connective tissue on the artery (15 to 25 minutes) as well as the time for extraction of the artery (5 minutes).

All experiments were always performed on both an ablated sample and a negative control located next to it, upstream, on the same animal.

IV.3.2 Bubble and structural damage

IV.3.2.1 OCT images of LIOB cavitation bubbles

As LIOB in water is known to trigger the apparition of a cavitation bubble, we were able to observe similar bubbles in the OCT images taken just after exposition of a target area to the ablation laser. The upper and lower interfaces showed as high contrast areas on the OCT images, as the local difference in refractive index is particularly sharp there. Individual bubbles in artery appeared to be in the order of $20\text{ }\mu\text{m}$, significantly larger than the separation between spots when the ablation pattern was scanned. Hence neighboring cavitation bubbles created by the scanned ablation pattern in liquid or soft tissue fused together to create larger bubbles with a lifetime before collapse of several minutes. Most of these large bubbles could be observed in reflection with the camera mounted on the OCT head, but the OCT also gave us information about the depth of the bubbles (Figure IV-15).

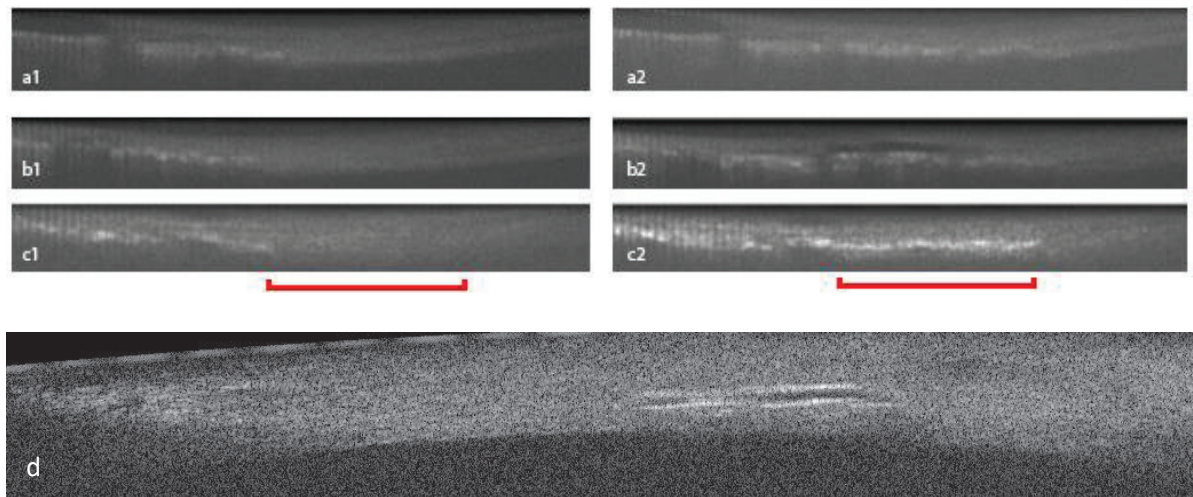


Figure IV-15: OCT images of the effects of LIOB triggered inside the artery (thickness about $100\text{ }\mu\text{m}$). (a1-c2) are depth profiles (A-scan) taken along the main axis of the artery with our in-house Labview program, where the surface of the artery (adventitia side) is at the top of the image, and the inside of the artery (epithelium) is at the bottom of the images. a1, b1, c1 were taken before the target area indicated by the red line ($300\text{ }\mu\text{m}$) was subject to ablation; a2, b2, c2 are images of the same areas right after ablation. The a1,a2 pair of image shows an increase in scattering in the target area after it was scanned by our ablation beam, about $50\text{ }\mu\text{m}$ below the surface. The b1, b2 pair of image shows a similar scattering inside the arterial wall, but also the appearance of an elongated bubble (black area) in a part of the sample which appears to be connective tissue, after ablation about $30\text{ }\mu\text{m}$ below the surface. The c1, c2 pair of images shows a strong increase in scattering, and possibly appearance of bubbles, very close to the epithelium, about $70\text{ }\mu\text{m}$ below the surface. (d) A-scan of a deep cavitation bubble observed, perpendicular to the artery main axis, with ThorImage (Thorlabs) for a higher resolution image, taken about 2 minutes after ablation; its collapse has started and it is only about $120\text{ }\mu\text{m}$ wide.

IV.3.2.2 Histology cuts and damage

In several locations corresponding to areas exposed to our ablation laser, histology cuts showed damage patterns appearing to correspond to ablation patterns (Figure IV-16): lines of holes, at an angle between 5° and 30° from the lining of the arterial wall. This angle could be

explained by breathing and heartbeat-induced movements of the artery while the ablation pattern was being scanned. However, these patterns were not repeated consistently along the whole ablated areas, and could only be observed in the intima media, not in the adventitia. The adventitia is particularly prone to histology cutting artifacts, hence we were not expecting to be able to identify ablation patterns reliably there.

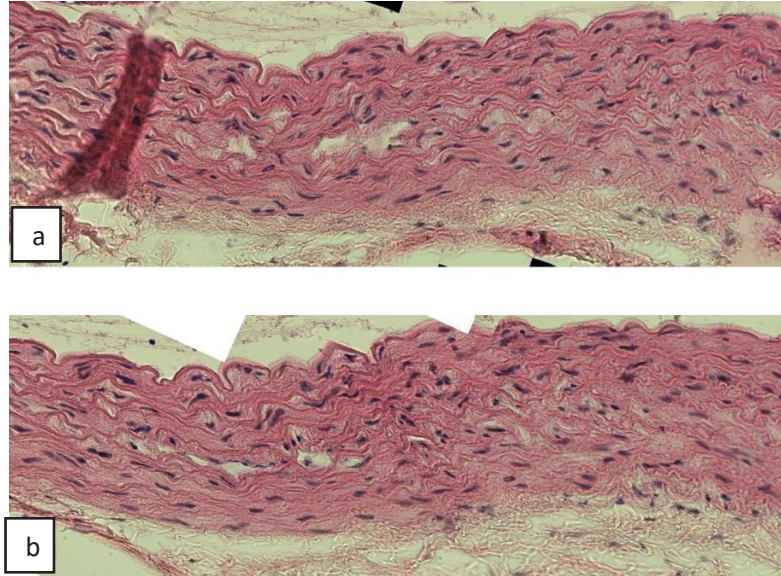


Figure IV-16: (a,b) 10 µm paraffin embedded slices of rat arteries stained with H&E, in locations exposed to the ablation laser. The slightly oblique white areas in the middle of the arterial wall are similar to some LIOB marks in mice¹²⁰. However, it proved difficult to reproduce them consistently from one sample to the next, and we cannot rule out that they may have been induced by the histology cutting.

IV.3.2.3 Biological effects of ablation

IV.3.2.3.1 4.3.1 TUNEL Staining results

In parallel to our search for structural damage using H&E staining, some slices were stained using the TUNEL protocol to observe marks of apoptosis in cells surrounding areas exposed to the ablation scanner focus. We alternated slices stained with H&E and slices stained with TUNEL, so as to corroborate structural damage with local apoptosis signaling. Slices stained with TUNEL and DAPI were one positive control (from rat A) obtained via DNA strand breaks by treating positive control sections with DNAase, 4 negative controls (1 from rat A, 3 from rat B) which were non-exposed parts of the artery located upstream from the exposed region, 3 slices from the ablated area of rat A, 3 slices from the ablated area of rat B.

Both the positive and negative controls of the TUNEL seemed to work properly from looking at their fluorescence signal, so we considered that the staining went well. Taking advantage of the co-staining of apoptotic cells with TUNEL and the whole cell population with DAPI, we used an automated cell-counting ImageJ algorithm whose purpose was to compare the ratio of apoptotic cells (exhibiting both DAPI and TUNEL signaling) over the whole cellular population (exhibiting only DAPI signaling) in the target ablation area as opposed to the whole surface of the stained slice. We applied this approach to the sample artery of rats A and B, where we considered the

target area to be a rectangle covering the whole depth of the artery intima media (roughly 100 μm) and a 300 μm wide area. This defined target area covers roughly 1/8 (or 12.5%) of the whole intima media surface (and thus not taking into account apoptosis in the adventitia).

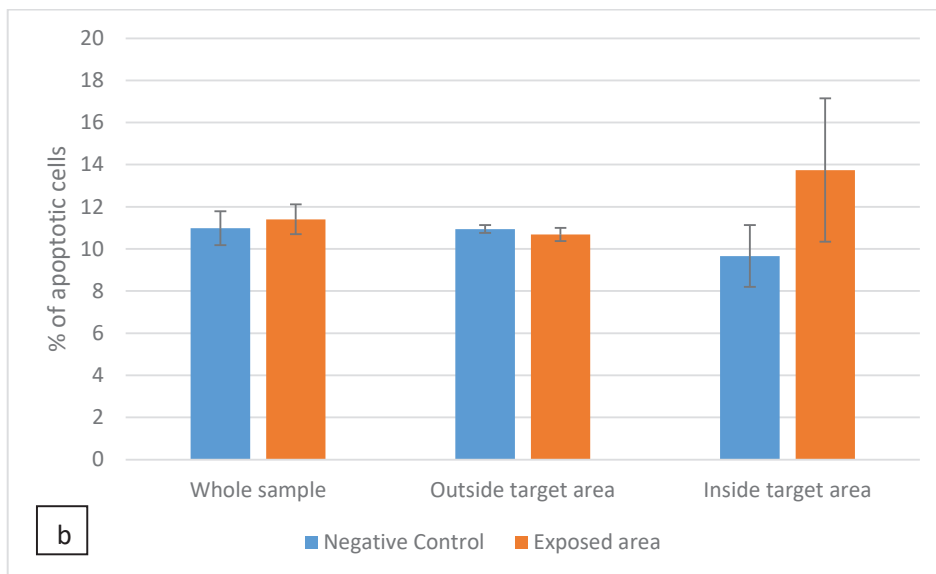
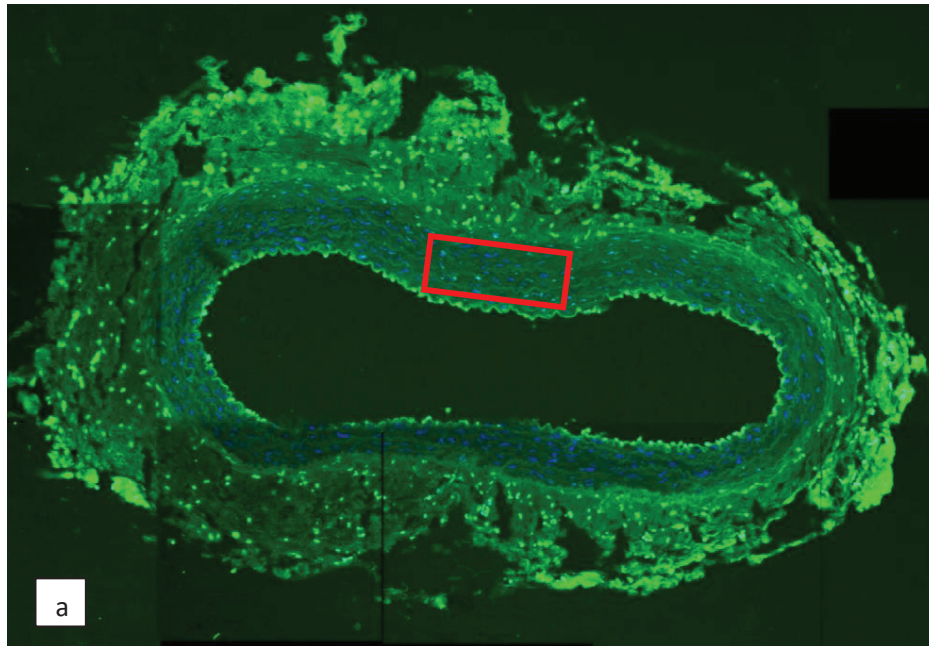


Figure IV-17: (a) Fluorescent image of a sample stained with TUNEL. Cell nucleus, stained with Hoechst, appear in blue. Apoptotic cells, stained in green, and actin fibers appear in green. The red square indicate the target area of ablation. (b) Results of an image processing analysis of the apoptotic and non-apoptotic populations inside and outside of the exposed area, and in control samples not exposed to the ablation beam, based on TUNEL staining.

The results of this TUNEL staining showed a limited but quantifiable increase in apoptosis in the target area as we identified it from keeping track of the orientation constant in the cassette it had been put into after harvesting (Figure IV-17). The relatively high standard deviation in the percentage of apoptotic cells in the target area might be due to identifying a non-ablated area as an ablated area, if the sample was not exactly laid in the right position in the cassette. Another

possible explanation might be that the number and intensity of LIOB events produced in the sample varies with the effective depth of ablation, which is dependent on the animal movements (breathing and heartbeat).

Since TUNEL stains DNA fragmentation, which is a marker of apoptosis happening late in the apoptotic pathway, some apoptotic cells in relatively early stages of apoptosis may not have been marked. For this reason, and to verify our observation with a second marker, we stained other slices from the same animal with a marker of Caspase 3.

IV.3.2.3.2 Caspase 3 staining results

Some of the paraffin-embedded slices were stained using the immunostaining protocol with HRP described in III.3.1.3.4. The considered dataset comprised the slices that were stained with both H&E and immunostaining together and had not be significantly damaged during histology: 4 slices from control samples (2 from rat A, 2 from rat B), and 15 slices from areas subject to ablation (6 from rat A, 9 from rat B).

A second ImageJ program very similar to the one used for counting eosin and HRP stained cells was devised for counting eosin and caspase-3 stained cells. The percentage of cells stained with HRP appeared high on control and non-control samples, compared to results from TUNEL staining and from what could be expected from normal tissue apoptosis stained about 5h after extraction. We thus used our ImageJ program to count only cells whose HRP signal was above a relatively high threshold.

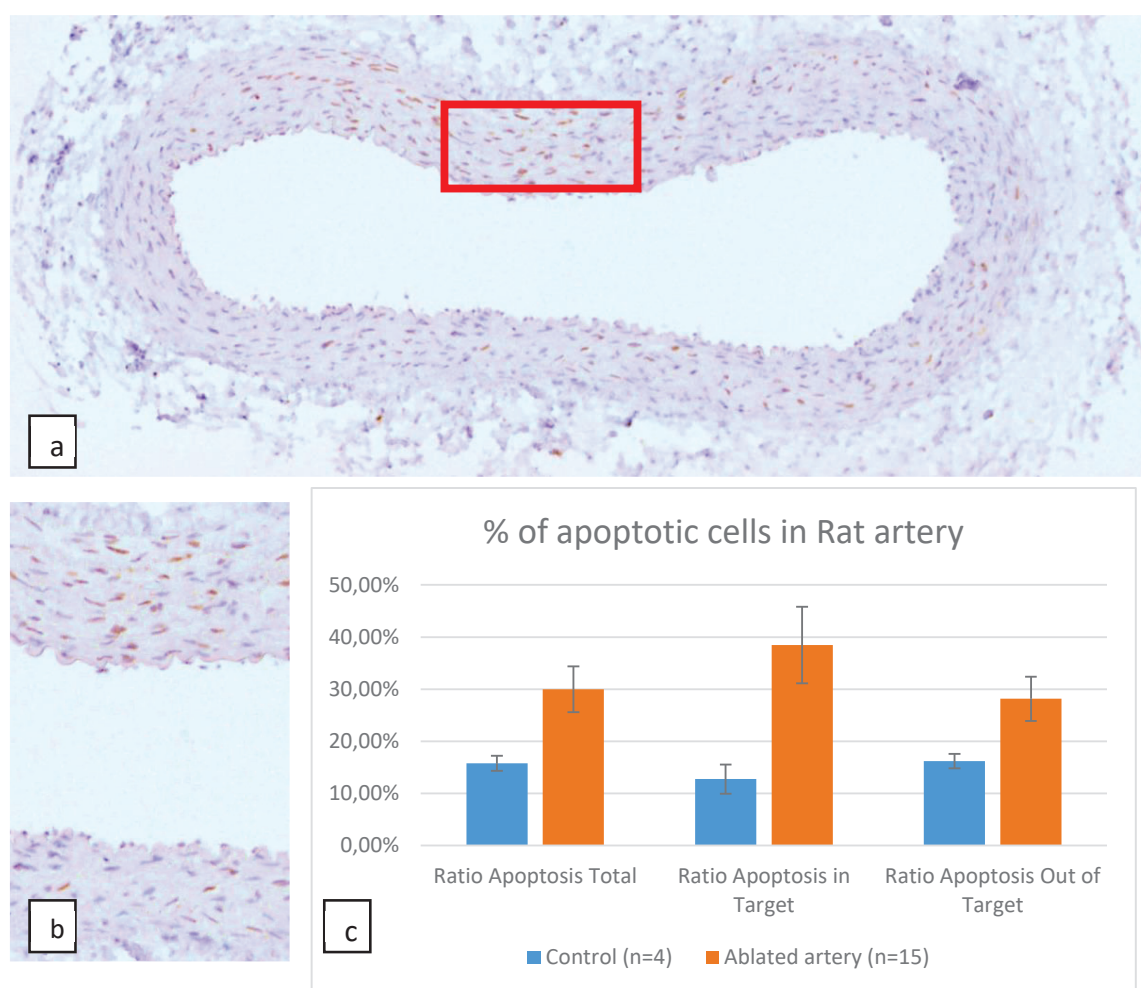


Figure IV-18: (a) 10 μm paraffin embedded slice of rat artery stained with H&E, and immunostaining of Caspase 3 antigen with DAB. Blue signal is hematoxylin (staining nucleus); brown corresponds to DAB (staining cells where Caspase 3 was expressed) and pink is the eosin (staining cell cytoplasm and collagen fibers). The area exposed to the ablation laser is located at the lower and central part of the image, where Caspase 3 immunostaining is stronger, indicating more apoptosis in this area. The red square indicates the target area. (b) close-up of the center of the image, where we can observe that the top part of the image, which was directly exposed to the ablation beam, shows proportionally more DAB signal than the bottom part of the image which was not directly exposed. (c) Results of an image processing analysis of the apoptotic and non-apoptotic populations inside and outside of the exposed area, and in control samples not exposed to the ablation beam, based on immunostaining of Caspase 3.

The samples showed a small local increase in the percentage of apoptotic cells in the area which had been exposed to our ablation beam, and a smaller, but significant, increase in the apoptotic population in the whole sample (Figure IV-18). This is rather consistent with the in-vitro tests made on matrigel with overnight Annexin V staining, although considering the small sampling size, we cannot rule out a potential statistical effect. The increase in apoptosis at the location of ablation can be explained by the local direct inflammation from necrotic cells, but a longer range effect in a compact muscular tissue like arterial tissue is more difficult to address. A more detailed

analysis, like a time-lapse on the apoptotic proteins activation, could help in understanding the mechanism of diffusion of the apoptotic signal out of the ablated area.

IV.3.3 Discussion on success and shortcomings of the in-vivo experiments

IV.3.3.1 OCT as a good way to monitor in-vivo LIOB

Considering the density of the intima media and the size of the bubbles, in the order of tens of micrometers, we assume that the effect of gravity and local pressure does not impact significantly their location, and that the depth at which the bubbles can be observed corresponds to the depth at which cavitation occurred. Observation of the bubble population after an ablation event along the set pattern thus indicates the depth at which LIOB was triggered.

Ablation performed in connective tissues which were left around the artery seemed to consistently induce the appearance of a large bubble with a well-defined interface. In contrast, ablation deeper in the tissue, in the intima media, mostly induced a diffuse scattering area on the OCT images. This effect would disappear a few minutes after ablation most of the time, and we make the hypothesis that it is due to a dense population of small bubbles created during the scanning of the focus in the target area. Since our OCT has a lateral resolution in the order of 5 μm , it may not be able to discriminate individual bubbles, but the local inhomogeneities (fiber, lipidic areas, etc) in refractive index would still show as an area of high contrast on the OCT images.

The OCT images corresponding to deeper ablation present bubbles that have been produced on the inside of the arterial wall, next to the endothelium. This confirms that we have been able to trigger LIOB through the whole thickness of the artery, and monitor it using the OCT system.

IV.3.3.2 Difficulties in observing ablation on histology cuts

While we were initially hoping to replicate histological observation of ablation holes with a similar success to the one we encountered when investigating ex vivo ablation in mouse arteries, the results obtained in both rat A and rat B were less conclusive. Although we believe that we have actually observed ablation patterns corresponding to our scanned patterns, this was only the case for a low number of slices (about 4 out of 50 slices) while OCT and wide field cam recordings showed a nearly continuous presence of bubbles over the length of the target area. Although we cannot rule out a possible mistake during the sample manipulation, some differences between the two sets of experiments could help in explaining the difference in results. For instance, comparing mouse and rat arteries, a higher arterial stiffness would make it more difficult for bubbles to expand, and their lifetime could be expected to be shorter. The pulse wave velocity, a usual evaluation of arterial stiffness, are different for APOE mice¹²¹ (PWV = 2.8 m.s⁻¹) and rats¹²² (PWV = 3.7 m.s⁻¹), and we could expect the extracted mouse arteries used for the ex vivo experiments to have even lower arterial stiffness since they are not held in extension by neighboring tissues anymore. Another effect leading to less easily observable bubbles could be the arterial pressure exerted by the blood flowing through the artery, which could also play a role in accelerating the

collapse of bubbles in surrounding arterial walls. SEM imaging may be an option to investigate tissue damage more precisely in future works.

IV.3.3.3 Relevance of apoptosis observation and implications for plaque ablation

The results we obtained from TUNEL and Caspase 3 immunostaining are relevant for biomedical applications in the field of laser surgery of arteries, but even more specifically for plaque ablation. Apoptosis and its associated signaling cytokines have been shown to play a role in attracting macrophages to accumulate through the arterial wall, into the plaque, thus leading to its growth¹²³. The present results show an increase between 40% and 200% in the apoptotic population of areas exposed to the ablation laser as opposed to unexposed control samples. For atherosclerotic tissues, that local increase in apoptotic cells could potentially lead to an increase in the plaque activity if the healthy smooth muscle cells surrounding the plaque were impacted by the neighboring LIOB events and underwent apoptosis. In the experiments presented here, we only investigated apoptosis induced by relatively high energy pulses as opposed to non-exposed control samples. However, considering the in-vitro results presented in Chapter 3, the apparition of apoptosis in and around exposed tissues is not a binary phenomenon. It could be interesting to investigate LIOB effects in arterial walls at lower pulse energy and fluence, where a lower level of induced apoptosis may be triggered.

There may be other applications where a regime like the one we have shown (in which ablation bubbles can be monitored by OCT and where LIOB events induce limited local apoptosis) could be of interest to the medical community. Apoptosis is often considered to be a “clean death” of cells, which can then be eliminated by the immune system with less damaging effects than other types of cellular deaths¹²⁴.

IV.3.3.4 Conclusion on in-vivo experiments

We have presented an in-vivo protocol allowing the targeting of cells through the whole arterial wall of a rat abdominal aorta (100 μm), and the triggering of LIOB in the target area with pulse of 9.5 μJ . These were performed in real-time monitoring with an OCT, and their effects were evaluated using histology techniques. We had initially designed this a set of preliminary experiments to establish a new in-vivo protocol for laser ablation, and it allowed us to verify that our set-up could be used to proceed with in-vivo ablation on the aortic artery of mice and rats in a limited time (down to less than 10 minutes for about 6 mm ablation length during our last experiments), while identifying and coping with experimental limitations (fogging, animal movements, access to sample, water immersion, etc). We were also able to validate our OCT and interface software as appropriate tools for monitoring, but also for targeting areas to be ablated. After some testing, we also identified ranges of parameters which allowed us to trigger deep LIOB, even through the whole artery thickness to reach the endothelium, without creating hemorrhage.

To go further than the evaluation of the OCT-monitored in-vivo ablation protocol itself, we proceeded with a battery of preliminary tests to investigate some effects of in-vivo LIOB in rat arteries, although the limited number of proper samples limits our ability to reach conclusions. Structural damage to the tissues were difficult to evaluate properly and no definitive conclusion could be reached about the identification of ablation holes, despite our previous success with the same method during ex-vivo experiments. The exposure to our laser ablation beam slightly

increased the population of apoptotic smooth muscle cells around the target area. Further investigation in this direction may be of particular interest for research on the potential of LIOB for atherosclerosis treatment, and for assessing the role of ultrafast laser for microsurgery applications in other tissues. For instance, replicating these experiments in the plaque of ApoE K/O mice might provide a more direct way to evaluate ultrafast NIR lasers as an appropriate tool for atherosclerotic plaque removal in itself, or if apoptosis regulators should be considered for simultaneous use. But in terms of developing catheter devices and trying them for treatment of atherosclerotic plaque, it would be significantly more beneficial to move to other animals¹²⁵, in particular, rabbit models (where mechanical damage can be used to induce plaque¹²⁶), or even larger animals where the constraints on catheter design may be closer to those found in human surgery and treatment.

Chapter V: Delivery high energy pulses

The applicability of ultrafast ablation of atherosclerotic plaque, as for many other internal applications, depends on the ability to deliver the laser pulses to a target area. Using optical fibers to transfer light a catheter device with the ability to focus it is an approach already used extensively for other light-based biomedical applications, and which is also becoming an option for high energy ultrafast pulses. In this chapter we will present two approaches to produce LIOB through a catheter for non-invasive biomedical applications.

First, we will be discussing the importance and challenges of delivering high power pulses through an optical fiber, and why this challenge is particularly relevant in the field of biomedical applications.

Secondly, we will present an approach for transmission and focusing through a single mode fiber and a lens in a first prototype used for ex-vivo ablation.

Finally, we will investigate the potential offered by wavefront shaping through multicore fibers, specifically in the domain of ultrafast laser ablation.

Part 1: Introduction to high energy pulse delivery through fiber

V.1.1 Minimally invasive approach to the treatment of atherosclerosis

Minimally-invasive treatments (in the sense of not requiring large incisions in the body) are nearly always preferable compared to direct surgeries which require extensive cutting of biological tissue and sometimes induce long and problematic healing processes. This is particularly true in the case of treatment of atherosclerosis in coronary arteries. A surgical approach to plaque in coronary arteries requires surgery through the pectoral tissues, access through the sternum and ribs, and the blood pressure inside the arteries themselves requires techniques such as temporary ligation¹²⁷. In practice, such direct surgery is still used by surgeons for medical interventions on coronary arteries due to relatively low mortality compared to other methods¹²⁸. Minimally-invasive approaches have proven particularly well suited for the diagnostics and treatments of coronary arteries¹²⁹. Due to the fact that all arteries lead back to the heart, it is possible for an experienced surgeon to guide a fiber (called guide wire) from easily accessible arteries body to coronary arteries of the heart¹³⁰. This is typically made possible with the injection of a contrast agent and X-ray real-time imaging¹³¹ (angiography) to allow the surgeon to see the guide wire and guide it to a desired location. Once a guide wire is in place, for example at the site of an atherosclerotic plaque, various tools can be led to a desired location by sliding along the guide. This method is routinely used for placement of stents¹³², but also for positioning tools for atherectomy¹³³ (for example mechanical atherectomy¹³⁴). Another type of tool which relies on the presence of a guide wire are OCT catheters¹¹⁵ for evaluation of atherosclerosis. In other words, the large majority of recently developed techniques which have been used to impact the medical treatment of atherosclerosis are made to be compatible in minimally-invasive approaches. Designing a deep-ablation system with a small catheter format would make it compatible with an array of existing tools. Maybe as importantly, it could broaden the use of our device to other uses requiring minimally-invasive approaches, as are most of the ones also requiring the use of an endoscope.

In the beginning of Chapter 2, we mentioned that during the early years of laser applications research, delivery of light was a significant challenge to in-vivo research, let alone design medical devices. The development of glass optical fibers as a way to transmit single-mode light¹³⁵ gave a lot of flexibility to applying optical discoveries to biomedical samples in-vivo. However, the high fluence required by LIOB and the relatively low damage threshold of the early fibers prevented their use in the field of ultrafast laser ablation in the early days of laser atherectomy. The first laser atherectomy procedures date back to the 1970s with the use of continuous lasers relying solely on the thermal effects of linear absorption¹³⁶. The ablation was clean and controlled, but it charred surrounding tissue and complicated healing with restenosis (re-narrowing of artery)¹³⁷. These results led to the abandonment of continuous laser use for atherectomy, and the pursuit of research with pulsed lasers, particularly in the 1990s¹³⁸. The laser atherectomy methods commercialized in the last 10 years are based on the ultraviolet excimer laser with nanosecond

pulses. These lasers also rely on linear absorption, and thus lack the good inerrant axial sectioning of multi-photon process, and are thus not fit for subsurface ablation. However, the short duration of the pulses prevent long-range thermal effects¹³⁹ and saw some success in the field of atherectomy. In particular, they have been successfully used for atherectomy in the lower limbs¹⁴⁰, where the risk of creating a thrombosis is less dramatic and better managed by embolic protection filters¹⁴¹. As opposed to these, ultrafast ablation is distinguished from linear absorption ablation by its higher precision and subsurface ablation capability¹⁴², but is not yet applied for medical ablation via catheters.

V.1.2 Optical fibers for high energy pulse delivery

We have seen in the previous chapters that LIOB has some properties which could make it an attractive technology for deep atherectomy or other biomedical applications, provided we are able to deliver high peak energy pulses to the plaque location by a minimally-invasive approach.

Fortunately, the last 15 years have seen continuous progress in the maximum peak power which can propagate through single-mode fibers, with the introduction of hollow core photonic crystal fibers (HC-PCF)¹¹⁶. These fibers work on the concept of a periodic lattice surrounding an empty core (filled with air, gas, or vacuum depending on the application). The periodic lattice prevents modes from traveling in the area surrounding the empty core, and in consequence the light stays confined inside it. These fibers are appropriate for transmitting high energy pulses for several reasons: 1) the laser-induced optical breakdown threshold of air is about 5 times higher than the threshold in SiO_2 ¹⁰⁶, and 20 times higher than the threshold in tissue¹²; 2) the concept of HC-PCF forbidding transmission of high order modes inside the core makes it possible to have relatively large cores, thus diminishing the peak intensity in the fiber and the risk of LIOB inside it; 3) the dispersion of light in air is low, as is its non-linear coefficient, which limits the pulse broadening and self-phase modulation in the fiber. The benefits 1) and 3) could actually be even more pronounced if the air in the hollow-core fiber is replaced by vacuum or by a gas with higher ionization potential or lower non-linear properties¹⁴³.

On the other hand, the fact that single-mode fibers can only transmit one mode makes them incompatible with wavefront-shaping methods to control the light field through the fiber. This prevents useful techniques for controlling light propagation through scattering media, such as holographic techniques, although pulse compression is still possible¹⁴⁴. In consequence, a focusing system has to be added at the output of the fiber to create the peak intensities necessary for ablation.

In practice, the field of hollow-core fiber is still quite explorative, and there have been improvements over some of the initial designs. Kagome type fibers are currently among the most promising designs for high energy ultrashort pulse delivery, because of their large mode size and minimal mode overlap with the cladding¹⁴⁵. It seems reasonable to hope that as more in-depth knowledge is gained of the guiding mechanism in some of the more advanced photonic crystal fibers, more efficient designs will be made commercially available.

In the meantime, hollow-core fibers have already found applications in the transmission of pulses for delivering LIOB for micro manufacturing¹⁴⁶. The ability of high energy ultrafast lasers to trigger LIOB independently from the absorption coefficient makes it an appealing option to trigger ablation deep inside transparent samples, or when a good control of ablation depth is essential. In these cases, the possibility to send high energy pulses through a fiber allows for more compact and adaptable devices. In some cases, adding a MEMS-based scanning system at the output of the fiber is a conceivable solutions. In the case of devices for atherectomy or more-generally minimally-invasive ablation device, the need for extreme miniaturization and compliance with requirements for use in sensitive biological environment (such as avoiding sharp angles, choice on biocompatible materials, etc) make the design on a catheter significantly more challenging¹⁴⁷.

Part 2: Design for ex-vivo ablation

V.2.1 Design of a simple catheter probe

To demonstrate LIOB through a hollow-core fiber, we designed a simple catheter with dimensions which would make it appropriate for use in human coronary arteries which has a diameter ranging from 1 mm to 4 mm (see Table V-1 and Figure V-3). Such a catheter was considered for use in aortic arteries of mice to try to replicate in-vivo ablation at atherosclerotic locations, but the surgery for insertion of the catheter would have been fatal to the animal.

| Artery type/ Animal | Mouse | Rat | Rabbit | Human |
|------------------------|-------------------------------|---------------------------|---------------------------|---------------------------|
| Aorta | 1.2+-0.5 ¹⁴⁸ | 1.7 - 2.2 ¹⁴⁹ | 5+-1 ¹⁴⁸ | 17 +- 1 ¹⁴⁸ |
| Femoral | <0.2 ¹⁵⁰ | 0.9+-0.1 ¹⁵¹ | 1.2+-0.1 ¹⁵² | 7+-1 ¹⁵² |
| Coronary | 0.16+- 0.01 ¹⁵³ | 0.51+-0.02 ¹⁵³ | 0.99+-0.06 ¹⁵³ | 1-4 ¹⁵⁴ |

Table V-1: Artery lumen diameter (in mm) for different animal models considered for ablation and testing of our catheter prototypes, and human. In grey, the arteries for which there exist established methods for generating atherosclerotic plaque with a combination of a fatty diet and either mechanical injury or genetic properties.

As a means to transmit pulses of light over a long distance in our first prototype catheter probe, we used a 1 cell Kagome type, hollow-core PCF (single cell kagome fiber from GLO Photonics, France), optimized for transmission for light centered at 800 nm. The numerical aperture of the fiber was 0.02, and its length was 1 m. To focus the light on the sample, we used a miniature lens with a moderately high numerical aperture of 0.6 (LightPath Technologies, 355070) and a diameter of 0.8 mm. To make the best use of the lens NA, the lens was located 3 cm away from the output of the fiber. An aluminum housing with an outer diameter of 1.2 mm held them in their relative positions, and epoxy glue was used to make the whole system rigid and convenient to manipulate.

V.2.2 Ex-vivo ablation

We first demonstrated the usability of our catheter for ablation by targeting a glass slide moved by a 3D stage. The setup was in fact the fiber-based ablation set-up presented in Chapter 2, with the fiber and catheter placed between the focusing objective (replaced by a 100 mm focal length lens to couple light into the fiber core) and the sample. The minimum pulse energy for which ablation spots could be observed was 1 uJ, and yielded apparent defects in glass with diameter down to 1.5 μ m. We replicated this experiment with pulses at the entrance of the fiber up to 4 μ J,

but did not push it further from fear of damaging the fiber. About 30% of the input power was transmitted through 1 m fiber.

For this initial demonstration of subsurface damage to tissue, we decided to replicate the ex-vivo ablation in the arterial wall of adult C57BL-6J mice. The sample was prepared in exactly the same way as the controls for the experiments in Chapter 4 Part 2. The slide supporting the sample was placed on the translation stage, while the catheter probe was stationary. Ablation was conducted through the fiber and catheter, with output power of 1 μ J, at a repetition rate of 1 kHz. The tissue was scanned to target seven successive layer separated by 5 μ m from each other, 20 μ m to 50 μ m deep, 70x70 μ m² as defined by the movements of the 3D stage. The scanning lasted about 40 seconds, starting from deeper in the tissue, and going back to the surface of the tissue one plane after the other, as to avoid distortion from bubbles above focus. Following ablation, we could observe a bubble by transmission microscope and waited 40 minutes for its collapse. After that time, its size stabilized, so we proceeded with preparation for histology. Following ablation the sample was prepared for paraffin-embedding and histological sectioning following the method described previously in Chapter 4 Part 4 to slices of 10 μ m.

Figure V-1: *Cryocut slices of volume ablation stained with H&E.* shows the H&E stained slice of ablated tissue, where a large volume without tissue can be seen which corresponds to the ablated region of tissue. Sharp walls can be seen on this image, cutting through several layers of actin and collagen. The third picture taken on the edge of the ablated region shows damage in the same area, but with less distinct holes. Although we had aimed at ablating a 70x70x30 μ m³ volume, the lateral damage did not extend further than 50 μ m in the two directions parallel to the artery plane on the slides, which may be due to shrinkage of the tissue during fixation with PFA 4%. The length of one axis was measured directly on H&E slices. For estimating the axial depth of damage produced in the arterial wall, we considered that a direct measurement of the area missing tissue would not be appropriate because the thin layers of tissue above and below the void could easily be distorted during histology. We rather compared the amount of tissue remaining above and below the damage area, and compared it to the full thickness of the arterial wall near to, but away from the damaged area. This method gave us an estimate of the range of missing tissue to be between 20 μ m and 35 μ m.

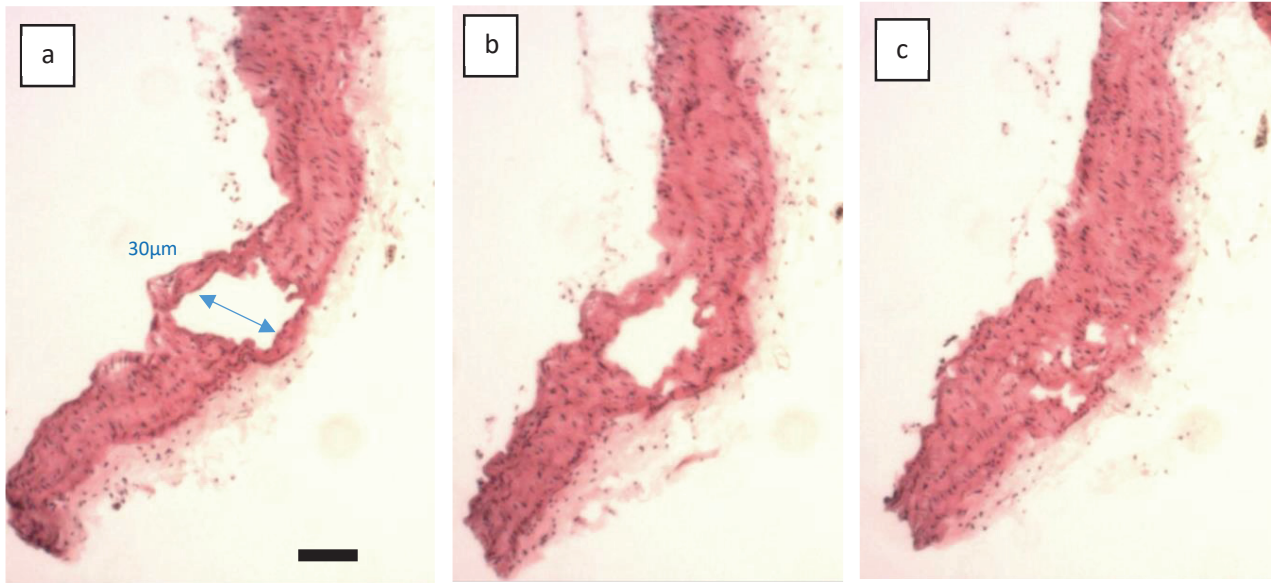


Figure V-1: Cryocut slices of volume ablation stained with H&E. The scanned pattern was a $70 \times 70 \mu\text{m}^2$ pattern ablated from the endothelium side (from the left of the pictures), into the intima media. The slices are $9 \mu\text{m}$ thick, and the three images are separated by $18 \mu\text{m}$ from each other. (a) and (b) show a clear ablation volume, while (c) (the last slide of the series where damage could be observed) shows a more fragmented damage. The blue marking on (a) measures $60 \mu\text{m}$ on the picture, but corresponds to a void of $30 \mu\text{m}$ if we measure the thickness of the tissue above and below it and compare it to the thickness of tissue in non-ablated areas of the artery. The Scale bar indicates $50 \mu\text{m}$.

We proceeded with repeating this experiment in an atherosclerotic plaque on an extracted ApoE-KO mouse aortic artery. Using the exact same parameters, we ablated on one sample in two locations: one at the surface of the arterial wall in a non-atherosclerotic area, and one below the surface of plaque, $250 \mu\text{m}$ away from the first location. Figure V-2 shows the result of this ablation on a cryocut slice stained with H&E. The damage in the arterial wall is obvious and its size fits the ablation pattern very well. The damage on the plaque is in exactly the right location and is only slightly smaller ($50 \mu\text{m}$ instead of $70 \mu\text{m}$ for the pattern) than what we were expecting, and its depth is only about $20 \mu\text{m}$. This last point may be due to lipids in the plaque partially filling the damaged area, as has been already discussed in Chapter 4 Part 2. We were not able to apply an Oil Red O staining to this sample because of difficulties during the histology cutting, and it is possible that this damage may have been induced by cutting artifacts, although the high degree of correlation to the ablation pattern suggests that these marks were created by ablation.

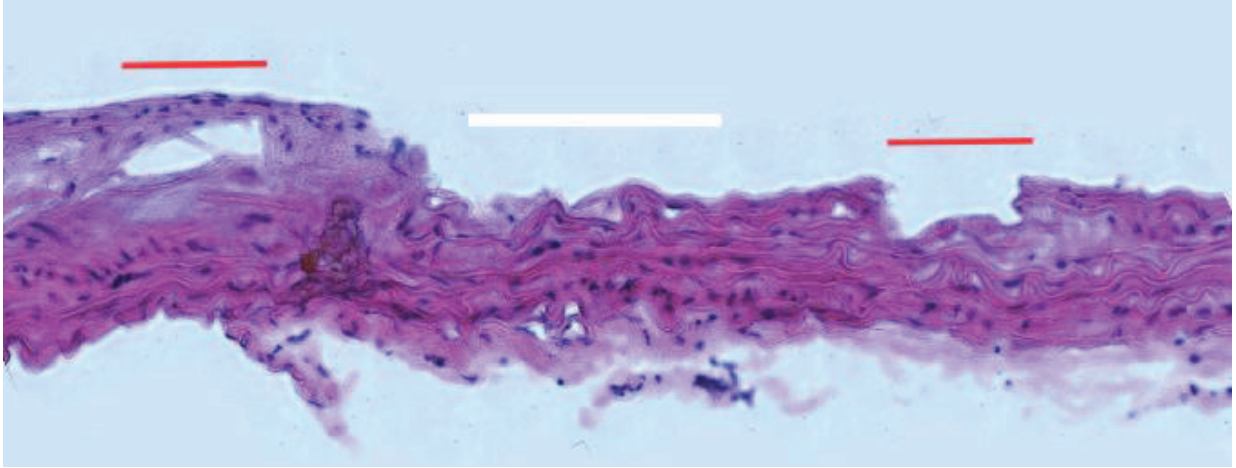


Figure V-2: Cryocut section stained with H&E on the aortic arch of an ApoE-KO mouse. The red line on the left indicates a 70 μm ablation at the surface of the arterial wall, and the red line on the right indicates the same pattern repeated 250 μm away inside an atherosclerotic plaque. The white scale bar measures 100 μm .

V.2.3 Toward future designs

In the previous section we demonstrated the use of a simple catheter for triggering LIOB ex-vivo. The prototype was initially meant to be the first of a series of hollow-core fiber-based catheter designs. This in part explains why few animals were tested: we wanted to prove the concept of ablating tissue through the fiber before moving to more advanced designs. Another prototype for ablation was created and is presented in Appendix G. The main limitation for any future design is the need to implement a scanning mechanism, since our single-spot ablation volume is so small.

One option would be to replicate the type of rotary scanner used in OCT catheters, where the scanning happens by moving the whole probe in a spiraling movement. This system has the advantage of having a very limited impact on the dimensions of the catheter itself, since the motor guiding the scanning is located outside from the patient, toward the proximal side of the fiber. On the other hand, it presents two strong issues: each scan can requires extensive movement of the catheter and could induce repeated damage when several scans are need, and this system does not integrate a method for scanning the beam axially.

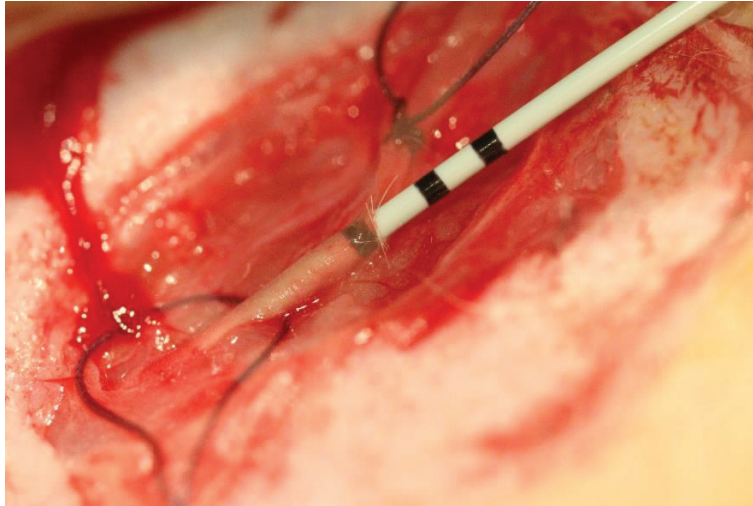


Figure V-3: Use of a balloon catheter for use in human coronary arteries, inserted in a rabbit femoral artery. Although the mechanical elasticity of the artery offers some leeway, this illustrates the difficulty to find appropriate laboratory animal models for trying prototypes designed for use in human.

Another approach is to develop a scanning mechanism at the output of the fiber. Progress in MEMS technology have made this approach viable for endoscopes aimed at entering cavities more than a few millimeters wide. The group of Prof. Ben-Yakar at the University of Texas is for example investigating the design of a catheter for delivery high pulses for LIOB, scanned by a MEMS-based system^{118,155}. At the time of finishing the present thesis, they are about to publish an article¹⁵⁶ presenting state of the art design for LIOB pulses delivery with a scanning mechanism at the output, for use in ablation and remodeling of vocal cords. However, their system has a diameter of 5 mm and a rigid length of more than 3 cm, which would make such a system entirely incompatible with lowly invasive approaches for treatment of the coronary arteries. The challenge of miniaturization of fibers with high numerical aperture and small form factors is a strong limitation for biomedical applications of LIOB, and in the next part, we will consider a significantly different approach, highly beneficial in terms of reducing the dimensions of the catheter.

Part 3: Wavefront shaping for light control through multi-core fiber for ex-vivo ablation

In this part, we continue to investigate design of catheter for ablation of biological tissues, but with a radically different approach for pulse transmission and scanning of the ablation beam. We will introduce a method for transmitting light through a multi-core fiber and focusing it at the distal end without use of a lens. Our approach is based on the measurement of the transmission matrix through the fiber to enable control of the field at the output of the fiber. We will begin by an introduction to the setup we used, before presenting how we measure the transmission matrix and how it is used it to shape the wavefront at the output of a multicore fiber.

V.3.1 Materials and Methods

V.3.1.1 The optical setup

For these wavefront shaping experiments, we used the same fiber-laser as in previous experiments (Satsuma, Amplitude System, France), and the whole system is presented in Figure V-4. The laser beam was split by a polarized beamsplitter between a reference arm and a sample arm. A half-waveplate before the beamsplitter allowed for adjusting the balance of optical power between the two arms.

The reference arm contained of a pair of mirrors on a mechanical stage forming a delay line to tune the optical path length in the reference arm. The beam was then deflected toward a second beamsplitter to combine the signals from the reference arm and the sample arm on a CCD camera for creation of an off-axis hologram.

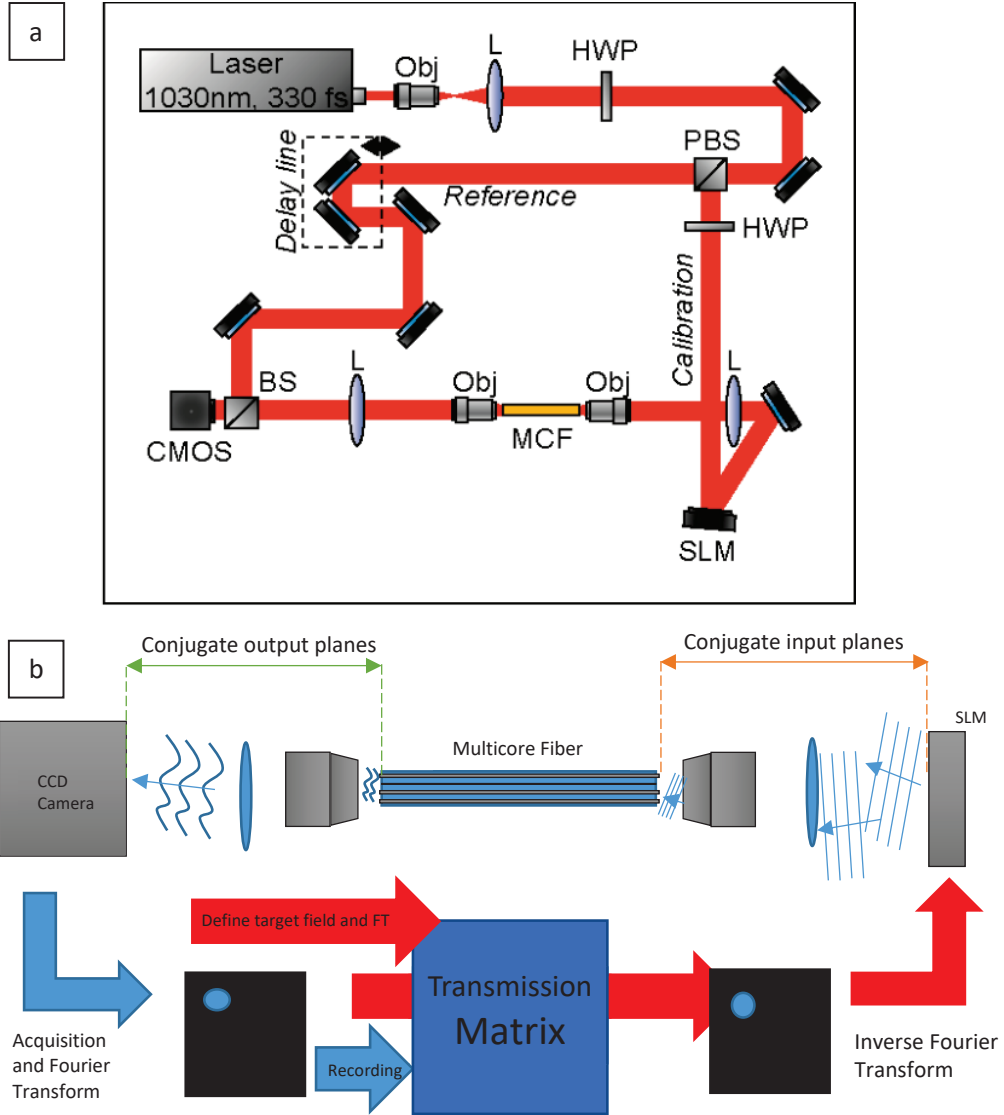


Figure V-4: (a) The Transmission Matrix measurement setup. (b) Diagram of the recording of the transmission matrix. The path for recording the TM is in blue (the reference arm is not represented but is still required to record the field on the CCD). The path for using the TM is in red.

The sample arm (or calibration arm) was where the multicore fiber (MCF, Fujikura, FIGH-10-500N) and the wavefront shaping system were located. The MCF diameter was $470\mu\text{m}$ and contains 10000 cores. Each individual core had a diameter of $2.9\mu\text{m}$ on average, the mean separation between neighboring cores was $4.5\mu\text{m}$, and their NA was 0.34. As can be seen from the fiber facet on Figure V-5, the cores were placed in a quasi-periodic arrangement, and their diameter and spacing had slight variations, which limited core-to-core coupling¹⁵⁷. At the exit of the polarized beamsplitter which separated the reference and the sample arms, the beam in the sample arm was directed toward a phase-only spatial light modulator (SLM, PLUTO Holo-Eye, Germany). A lens with a 125 mm focal length and a focusing objective (20x, NA0.4, Olympus) were placed between the SLM and the fiber, so that the SLM was imaged onto the fiber proximal facet. The zero-order diffraction from the SLM was blocked at the back aperture of the objective. In

practice, the objective focused the light slightly behind the proximal surface of the multicore fiber for reasons we will discuss in paragraph V.3.2.2. On the other side of the fiber, an imaging objective (20x, NA0.4, Olympus) and a lens of 150 mm focal length captured the light coming out from the distal end of the fiber and imaged a plane P_{obs} (located a distance d_{im} from the distal facet) onto the CMOS (MV1, Photon Focus) through the second beamsplitter. There, the signal interferes with the reference beam for creation of a hologram. In this initial setup, we only used 6000 cores of the fiber to limit memory load on the computer running the TM measurement algorithm.

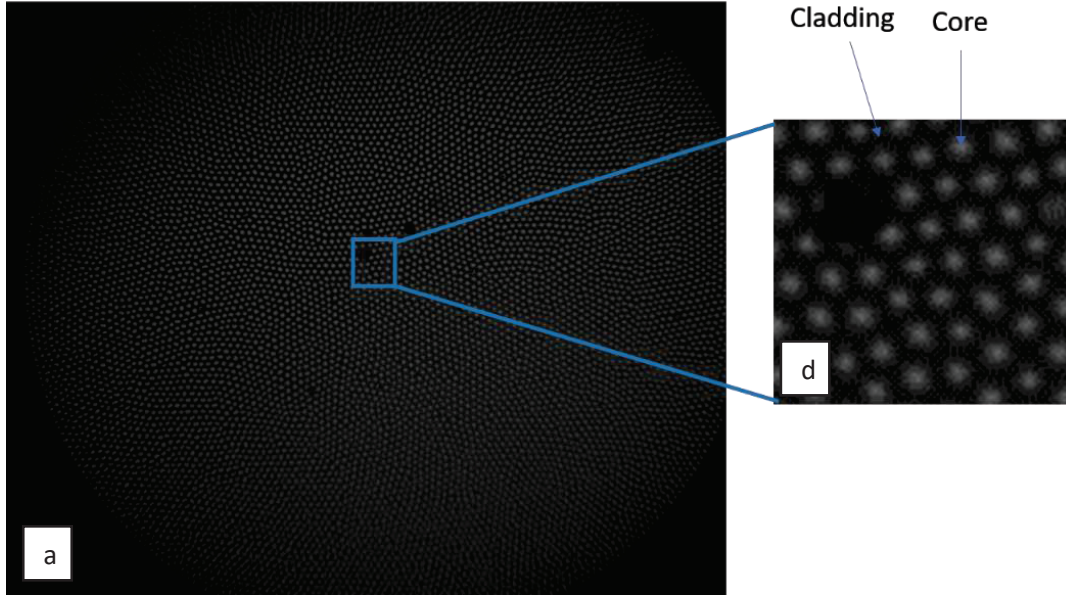


Figure V-5: (a) Picture of the distal facet of the FIGH-10-500N fiber. (b) close-up on cores at the center of the fiber. The inhomogeneity in the placement of the cores is more evident of the large-field image, because short-distance alignment of fibers was not entirely prevented during fabrication.

To modulate the illumination to optimize recording of the hologram or tune the ablation energy, a half-wave plate is located between the first beamsplitter and the SLM.

For measuring the transmission matrix, a single computer was used to synchronously provide the inputs for the SLM to modulate the wavefront of the beam, and to record and analyze images of the hologram on the CCD camera. The SLM was used to display different wavefronts to be evaluated during the transmission matrix recording, and the transmission matrix was computed as described in V.3.2.2. The software used for this purpose was a modified version of the MATLAB software from Damien Lotterie, used successfully for measurement and use of TM through a multimode fiber^{158,159}. We recorded the transmission matrix with a pulse energy of 0.5 μJ on the proximal facet of the multimode fiber, and a repetition rate of the laser of 125 kHz to avoid any variation of intensity of the CCD during the recording of the TM.

After recording of the transmission matrix, the reference beam path was blocked, and a wavefront for creating a single focus spot in the center in front of the fiber, at a desired distance d_{foc} , was set as an input for the SLM. The imaging objective was then moved to allow the imaging of the focal spot onto the CCD camera. Several images were taken and combined to create a high dynamic range image of the field in the focal plane of the imaging objective, and we defined the efficiency of the focusing by dividing the intensity in the focal spot compared to the background signal. The

power transmitted through the multicore fiber is measured by a power meter placed between the imaging objective and the second beamsplitter when measurement of power was needed.

For any ablation experiments, we used a mechanical stage to slide a sample between the output of the fiber and the imaging objective. This objective then had to be moved to correct the aberrations due to the sample and the sample holder (typically a microscope glass slide) and allow proper imaging of the ablation event.

The pulse duration at the output of the fiber was measured using a two photon autocorrelator (presented in Appendix H) positioned between the imaging objective and the second beamsplitter when needed.

V.3.1.2 The metal samples

Samples for metal ablation were 800 μm thick glass substrates on which about 10 μm of gold was deposited by chemical vapor deposition in clean room.

V.3.1.3 The biological sample

The biological samples were samples of commercial chicken breast embedded in 3% Agar and cut in slices using a vibratome (VTS1200, Leica Microsystem) from the HCF at EPFL. I was held between a 170 μm thick glass coverslide and a 50 μm polymer membrane separated by a 200 μm spacer, and immersed in PBS to prevent drying.

Observation of the cavitation bubble was made in real-time using the CCD on the set-up, and further imaging was made using an OCT from the BIOP at EPFL.

V.3.2 Introduction to Transmission Matrix and multicore fibers

V.3.2.1 The multicore fibers

Multicore fibers are a type of optical fibers which present some interesting features of both single mode and multi-mode fibers. They have been used with success in transmitting light for endoscopy, and their field of use is expanding. Essentially, a multicore fiber is a set of single-mode fiber cores bundled together. Individual cores will thus transmit light with the benefits and limitations of single-mode fibers, among which the absence of modal dispersion and the very small diameter of the cores. This last point is what allows MCFs to bundle several thousands of cores within a diameter below 1 mm. Although each core carries a single mode along the fiber, different cores carry waves with relative phase delays when they enter the fiber: when they exit the fiber, on the distal side, the optical signal from these cores will interact differently depending on their relative phase delay. This is the basis for wavefront-shaping through optical fibers: essentially considering different cores as carrying spatially located modes which can be controlled individually. This provides the degrees of freedom needed for wavefront-shaping at the output of the fiber, and it has been demonstrated to allow lens-less focusing and imaging through MCFs^{160,161}. On top of this option, the use of multicore fiber for transmission of high energy ultrashort pulses implies spreading the optical power over several cores. This not only leads to a decrease in the risk of damaging the fiber, but also in the non-linear effects which appear at high

peak intensities and could modify the profile of the beam. Kerr effects and self-phase modulation happen at lower peak intensities than LIOB, and are problematic phenomenon which can potentially lead to deterioration of high-energy transfer in fibers. It can lead to temporal dispersion of the pulse, and lowering of the peak intensity at the output of the cores.

First, let us consider the Kerr effect. The most damaging potential effect of Kerr-effect is self-focusing, which can lead to a collapse of the beam in the cores of a fiber. The collapse happens when the peak power gets higher than a critical power value P_{crit} . Its lower bound is defined¹⁶² as follows:

$$P_{crit,min} = \alpha \frac{\lambda^2}{4\pi n_0 n_2} \quad (\text{Eq. 11})$$

A numerical application of this formula for glass ($n_0=1.52$, $n_2=2.7 \times 10^{-17}$ for glass¹⁶³) and $\alpha=1.86225$ (for a Townes profile¹⁶²) returns a lower bound of the critical power in cores of 38.3MW.

In comparison to this, we can express the peak power P_{peak} in cores of a homogeneously illuminated MCF by:

$$P_{peak} = 0.88 \frac{T_{system} E_p}{\tau_p N_{cores}} \quad (\text{Eq. 12})$$

Where T_{system} is the measured transmission of power between the laser output and the proximal facet of the multicore fiber, and N_{cores} is the number of illuminated cores. As usual, E_p and τ_p are respectively the energy and duration of one pulse. A numerical application for our system ($T_{system}=0.018$) considering the highest energy and shortest duration possible pulse from the Satsuma ($E_p=40\mu\text{J}$, $\tau_p=400\text{ fs}$), and only 6000 cores illuminated on the Fujikura fiber returns $P_{peak}=264\text{ W}$. In consequence, the peak intensity in the cores is well below the threshold for self-focusing, and Kerr effect should not induce beam collapse in the fiber.

Self-phase modulation is the generation of a non-linear phase-delay parameter γ_{SPM} depending on the optical field own intensity. It is expressed in $\text{rad.W}^{-1}.\text{m}^{-1}$ and is defined by:

$$\gamma_{SPM} = \frac{2\pi n_2}{\lambda A_{eff}} \quad (\text{Eq. 13})$$

Where A_{eff} is the effective area of the mode in the core. The corresponding phase delay after a distance of fiber L at the peak power P_{peak} in each core is thus:

$$\Delta\phi = \gamma_{SPM} P_{peak} L = \frac{2\pi n_2}{\lambda A_{eff}} 0.88 \frac{T_{system} E_p L}{\tau_p N_{cores}} \quad (\text{Eq. 14})$$

Assuming the mode in the core is a Gaussian mode whose radius was imaged at $1.4 \mu\text{m}$ on the distal facet. The numerical applications with the same parameters as before was that of a phase delay of 4.67 radians, or about one wave. Empirical observations show that a self-phase modulation coefficient above 0.2 waves induces a strong frequency broadening and diminishes the measured peak intensity at the output of a core significantly. According to equation Eq. V-4, increasing the number of illuminated cores, increasing the pulse duration, diminishing the intensity at the entrance of the core, and eventually diminishing the length of the fiber, are ways to mitigate this effect.

V.3.2.2 Measurement of the TM for a MCF

The name of transmission matrix itself conveys well what the method is about: we want to establish a linear system linking the input field on a sample to be modeled to the output field after transmission through a medium. This method has been used for wavefront shaping through different randomizing medium, among which scattering phantoms and multi-mode fibers¹⁶⁴, and we will show how we used it for wavefront-shaping through a MCF to create focus fluences useful for ablation.

The use of TM to optimize the transmission of light through a randomized media is one of several wavefront-shaping methods^{165–167} which have been developed in the last decade. Since it relies on direct transmission measurements and treats the medium as a black box, it presents the advantage of correcting for all types of aberrations which can be modelled linearly. S.M Popoff et al. developed on the concept of the use of TM in optics¹⁶⁸, and the measurement and wavefront-shaping program we used is based on the model they developed, adapted to calculation in Fourier domain. The detailed analysis and optimization of TM is out of the frame from this thesis, but the introduction of the general concepts for its measurement and usage is important for the upcoming discussion.

We consider that the optical field on an input plane S_{src} , divided in N individual sources without overlap. The light from the input goes through the linear medium for which we consider the transmission matrix K , and is detected on the output plane S_{obs} , divided in M non-overlapping individual detectors. For a linear optical system, K is the matrix of $k_{m,n}$ of complex coefficients relating the optical field on a m -th detector to the n -th source. The relationship between the average fields on the input E^i and on the output E^o , is the following:

$$E_m^o = \sum_{n=1}^N k_{m,n} * E_n^i \quad (\text{Eq. 15})$$

In the computation method we have used however, we did the calculations of the TM in the Fourier space. This allowed us to use the full size of both the SLM and the CCD, while keeping the dimensions of the TM sufficiently low to keep the measurement time and amount of data manageable. By transferring Equation V-5 to the spectral domain, we can define a second transmission matrix \tilde{K} composed of vectors $\tilde{k}_{m,n}$ defined by:

$$\mathcal{F}(E_m^o) = \sum_{n=1}^N \tilde{k}_{m,n} * \mathcal{F}(E_n^i) \quad (\text{Eq. 16})$$

In the case we consider, the objective was to evaluate the $\tilde{k}_{m,n}$ coefficients linking the n k-vectors projected by gratings displayed on the SLM to the m pixels on a camera imaging a specific plane P_{obs} a distance d_{im} after the output (distal) facet of the fiber. By inputting different phase gratings to the SLM, the 1st order diffraction of the collimated beam can be angularly scanned, which equals scanning the angle of the k -vector of the diffracted beam. Considering the focusing system used on our setup, the gratings were repeated with a 3 times higher spatial frequency on the proximal facet of the fiber. This way, the surface S_{src} of the proximal facet can effectively be scanned. At the wavelength of 1030 nm, the MCF propagates two modes, LP₀₁ and LP₁₁. Also, the display of gratings on the facet during TM recording limited the risk of damaging the fiber compared to a point-by-point scan.

For each grating n on the SLM, the CCD records a hologram from the interaction of a reference beam and the optical field in the plane P_{obs} . From this hologram, both the amplitude and phase of the field in the plane P_{obs} can be computed for each pixel on the surface of interest S_{obs} of P_{obs} . This effectively gives the information needed to extract the values $\tilde{k}_{m,n}$ for all values of m in one measurement.

V.3.2.3 Use the TM for focusing through a multicore fiber

Once the TM has been recorded, it is possible to use it to generate a focus within the field of view of the MCF, at the desired plane P_{foc} . To do this, we must proceed in three steps:

- 1) Select the point in the output plan to focus to in the plane P_{obs} for which the TM was calculated.
- 2) Once we have generated the desired field in the plane P_{obs} , we generate its Fourier transform $\mathcal{F}(E^o)$ and use the inversed transmission matrix \tilde{K}^i to calculate the Fourier Transform of the corresponding field E_n^i on the SLM.

$$\mathcal{F}(E_n^i) = \sum_{m=1}^M \tilde{k}_{m,n}^i * \mathcal{F}(E_m^o) \quad (\text{Eq. 17})$$

- 3) Calculation of the field on the SLM by application of the inverse Fourier Transform to recover the values of E_n^i for each scanned angle n . E^i is then the sum of all fields E_n^i .

V.3.3 Dependence of peak intensities at focus

V.3.3.1 Optimizing the reconstruction of a focus

Using the TM to create a focus in front of the center of the fiber is more or less efficient depending on the distance d_{foc} between the distal facet of the fiber and the desired plane of focus. Two opposing effects factor in defining the distance for which the efficiency of the focusing will be highest. On the one hand, considering the MCF output facet as a lens with a variable focal length $f = d_{foc}$, a long focal length comes down to using a lens with a low numerical aperture, hence the focal spot size decreases with distance from the distal facet¹⁶⁹. On the other hand, a short focal length is challenging to create with a MCF, and imperfections in this simulation induce a decrease in the efficiency of the reconstruction of a focal spot. Indeed, creating a lens with a small focal length comes down to simulating a lens with a strong curvature by inducing stronger phase delays between the cores than for a longer focal length lens. On the outsides of the lens, this comes down to generating larger phase shifts between a finite number of neighboring cores, which induces stronger aliasing for shorter focal lengths, and decrease in the efficiency with which light is focused on the desired focal spot.

In practice, this leads to finding the location of a focal plane for which the best compromise can be found between spot size increase and focus efficiency. For the setup used, a good compromise was found for $d_{foc} = 700 \mu\text{m}$, and this is where we defined the focal plane for the following experiments. This setup was able to generate focal volume whose transverse FWHM was $2.9 \mu\text{m}$, and the measured peak intensities at this distance was measured to be an optimal compromise compared to other focusing distances obtained with this set-up.

We defined at the beginning of Part 3 that we were expecting self-phase modulation to appear for higher pulse energies transmitted through the MCF. This is particularly problematic because it means a phase-delay will appear between the different cores depending on the fluence transmitted by each core, which will add with the phase delay voluntarily set by wavefront-shaping. In other words, increasing self-phase modulation decreases the usability of the measured TM, which translates into a decreasing efficiency of the focus reconstruction. Since self-phase modulation depends on peak intensity, its effect in the MCF is expected to vary with pulse duration and not only on pulse energy.

V.3.3.2 Measurement of focusing efficiency

Considering the high intensities which propagate in the cores, we expected to see the effects of nonlinearities in the fiber. Since the TM model we use is based on the assumption that the optical system is linear, this should lead to a decrease in the efficiency of the focus made with the TM. To better understand the effects of self-phase modulation, we measured the efficiency of the reconstruction of a focal spot $700 \mu\text{m}$ from the distal facet of the MCF for varying pulse durations and laser powers. The results of our measurements can be found in Figure V-8, for pulse durations from 500 fs to 3 ps, repetition rate of the laser was 125 kHz, and powers at the distal end between 10 mW and 500 mW.

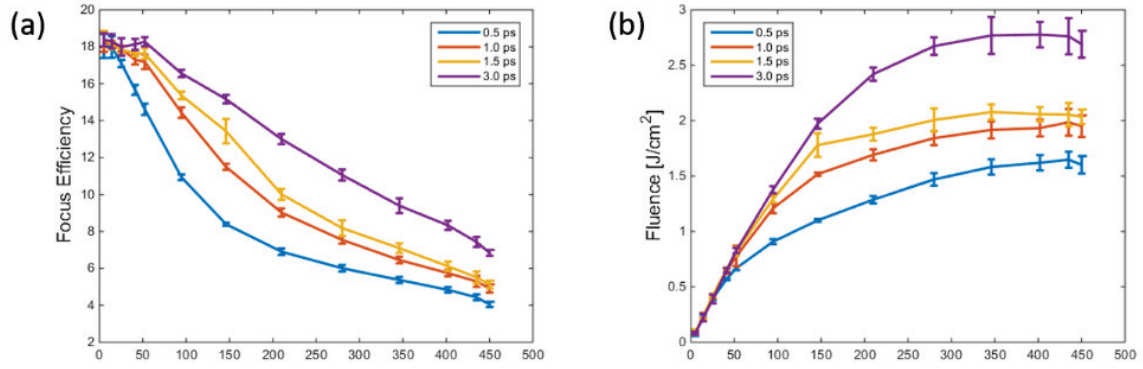


Figure V-6: (a) Focus creation efficiency for different measured values of power at the output of the fiber. (b) Peak fluence for different measured values of power at the output of the fiber (in mW, on the horizontal axis). Each spot was measured for 5 different TM measurements.

These measurements agreed qualitatively well with the behavior we were expecting: for low peak intensities, there was no impact of the laser power on the efficiency of the TM for reconstructing the focus, as the peak intensity in the cores was not high enough to induce significant self-phase modulation. Above a certain threshold value, between 15 mW and 60 mW depending on the duration of the pulse, the efficiency of the focus reconstruction started to decrease to a few percent of power inside the focal volume. The dependence of the efficiency decrease of the pulse duration is also well explained by nonlinear effects, as a shorter pulse induces a higher peak intensity compared to a longer pulse with an identical pulse energy.

Measurements of the pulse broadening in time were made using the autocorrelator, and the results are presented of pulse broadening are presented in Table 7, making the choice of 500 fs pulse less favorable than could be expected. Since this broadening increases at high pulse energies, we considered it to be another evidence of self-phase modulation. Taking this modification of the pulse profile in time, and according to the adjuted peak power presented in figure V-8, the peak intensity is optimal for a 1.5 pulse is around $0.58 \text{ GW}\cdot\text{cm}^{-2}$, for an average power at the proximal end between 150 mW and 200 mW at 125 kHz.

| Expected | No MCF | 50 mW | 205 mW | 405 mW |
|----------|---------|---------|---------|---------|
| 0.5 ps | 0.53 ps | 0.84 ps | 1.37 ps | 1.68 ps |
| 1.0 ps | 0.96 ps | 0.99 ps | 1.68 ps | 2.29 ps |
| 1.5 ps | 1.37 ps | 1.37 ps | 1.53 ps | 2.29 ps |
| 3.0 ps | 2.60 ps | 2.67 ps | 2.67 ps | 3.20 ps |

Table V-2: Pulse duration measured using the autocorrelator for different pulse duration expected according to the controlling software of the laser, and average energy at 62.5 kHz measured at the output of the fiber.

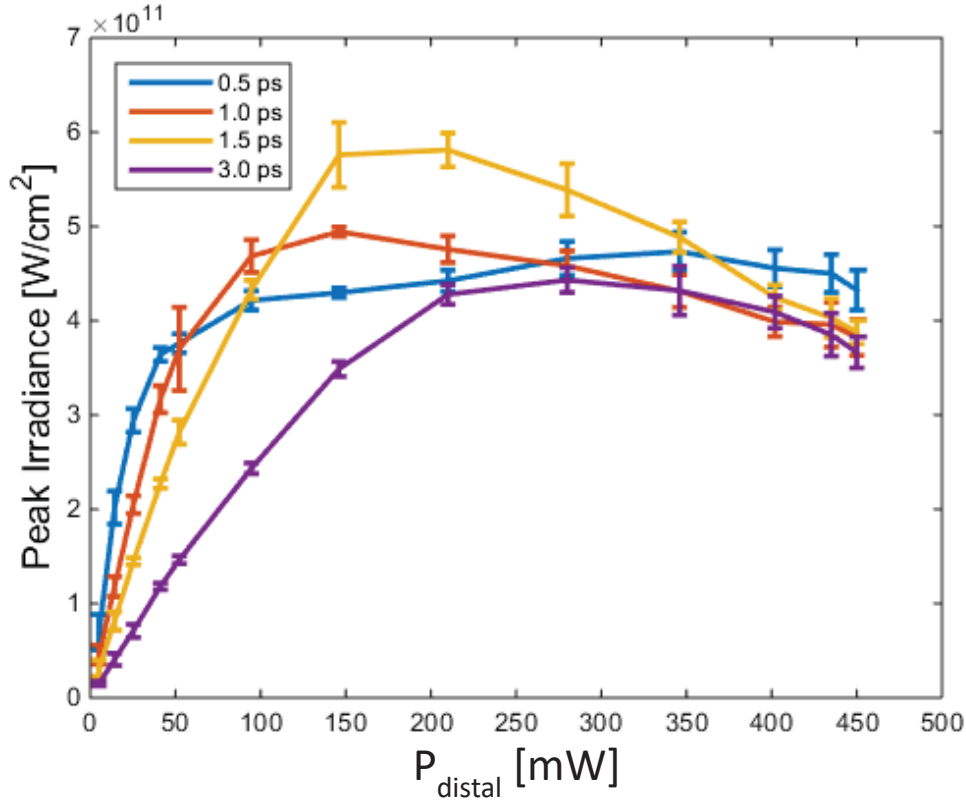


Figure V-7: Pulse duration broadening for different initial pulse durations and measured values of power at the output of the fiber.

V.3.4 Amplitude Correction

V.3.4.1 Reconstructed focus intensity flatness across output field

One of the great benefits of using a TM with a MCF, is that intensity control across the output field is possible – or a focus can be scanned across the measured output field. It can also allow the creation of multiple focal spots but in the frame of LIOB generation, we concentrate on optimizing the peak intensity in a single spot. We have already discussed the importance of scanning an ablation beam for minimally-invasive catheter approaches, and the upcoming experiment will demonstrate ablation over a scanning range of 120 μm by 120 μm .

When using the TM to generate a focal spot away from the main optical axis in our setup, it is important to remember that the amplitude of the modulated field reaching the proximal facet of the fiber was a Gaussian beam centered on the center of the fiber. Since there was low coupling between the cores of the MCF, this implies that the amplitude profile at the distal facet were also close to a Gaussian beam centered on the center of the fiber. To come back to the consideration we wrote earlier about the decrease in efficiency due to aliasing, the light coming out from the cores facing the desired focal spot directly were the ones less prone to aliasing. In consequence,

their light was proportionally better coupled into the focus compared to the light from “far away” cores. In consequence, the intensity of a focal spot directly on the optical axis was higher than the one of an off-axis focal spot. This can be a problem in the case of ablation, and particularly of tissue ablation where we have seen several intensity-dependent behaviors can arise.

V.3.4.2 Amplitude homogenization

To cope with this, we proposed a practical approach for allowing a scan of an ablation pattern with a constant intensity. In essence, we decreased the intensity focused in spots closer to the main optical axis by decreasing the coupling efficiency into the focusing objective.

We used the TM to generate focal spots one after the other, in the equivalent of a raster scan of a 30x30 pattern. The scanned area corresponded to a 120 μm by 120 μm , with focal spots separated by 4 μm in both directions. As individual spots were scanned, we recorded the corresponding maximum intensity in a 30x30 matrix, and normalized it to obtain an amplitude matrix M_A . The resulting matrix was used to generate a correction matrix M_C .

$$M_C = 1 - (M_A - \min(M_A)) \quad (\text{Eq. 18})$$

M_C was then used for modification of the wavefront used as input for each individual spot of the scanning pattern as follows: for spot k , each pixel on the SLM had a probability $M_C(k)$ to be replaced by a random value. In essence, we added noise to the calculated wavefront for generating a focal spot with too high intensity.

For example, a focal spot whose measured intensity was double the intensity of the spot with the lowest measured intensity, half the pixels on the SLM would be set to a random value. This method could be problematic for cases where the discrepancy of measured intensity would be high as it could induce a majority of random pixels on the SLM. But for the range of variations we were measuring, corrections of the intensity was made within 50% of the initial intensities, and the correction approach worked well as can be seen from Figure V-8.

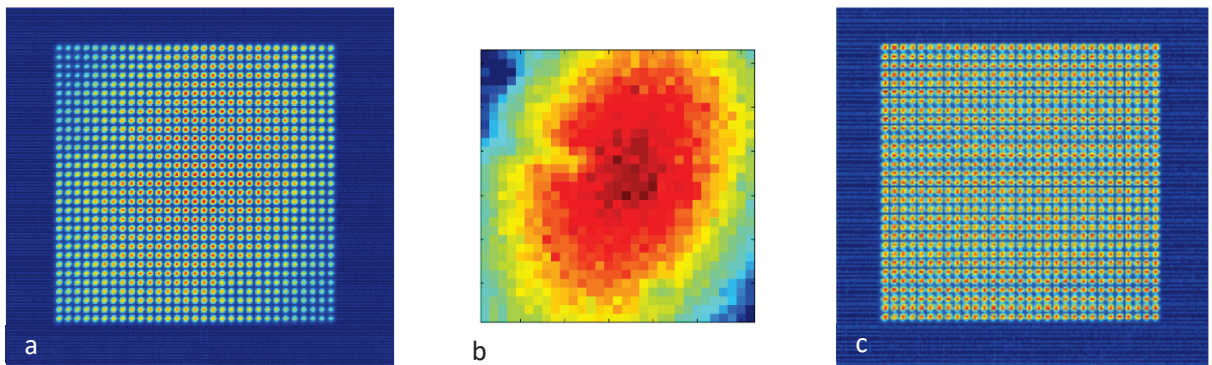


Figure V-8: (a) The 30x30 scanned pattern before correction of amplitude (camera integration time: 300 μs), normalized. (b) The normalized matrix of noise to be added for the creation of each individual focus. (c) The same 30x30 pattern after correction of amplitude inhomogeneity using matrix (b)(camera integration time: 300 μs , but noise appears from normalization). The minimum spot intensity on image (a) is 40% of the maximum value. Images were recorded with pulses of 1 ps and 1 μJ .

V.3.5 Metal and Ex-vivo ablation

V.3.5.1 Metal ablation

With a spot diameter of 3 μm , a transmitted pulse energy in the focus of about 60 nJ and a measured pulse duration of 1.5 ps on the distal side of the fiber, we were expecting a peak intensity of 0.5 $\text{GW}\cdot\text{cm}^{-2}$ in the center of the focal spot. Reported¹⁰⁶ threshold fluence for ablation in gold is 0.4 $\text{J}\cdot\text{cm}^{-2}$. In practice, we only managed to observe a hole through our gold-coated sample when using a pulse energy of 80 nJ, which corresponds to a peak irradiance close to 1 $\text{GW}\cdot\text{cm}^{-2}$. The minimum hole diameter was 1.2 μm , as measured with a confocal microscope.

This was nevertheless enough to proceed with ablation with a scanned beam using the amplitude correction we mentioned earlier, and which allowed us to ablate patterns of 120 μm by 120 μm in one single scan with a laser repetition rate of 1 kHz, 1 ps pulse duration, and a fluence of 0.64 $\text{J}\cdot\text{cm}^{-2}$.

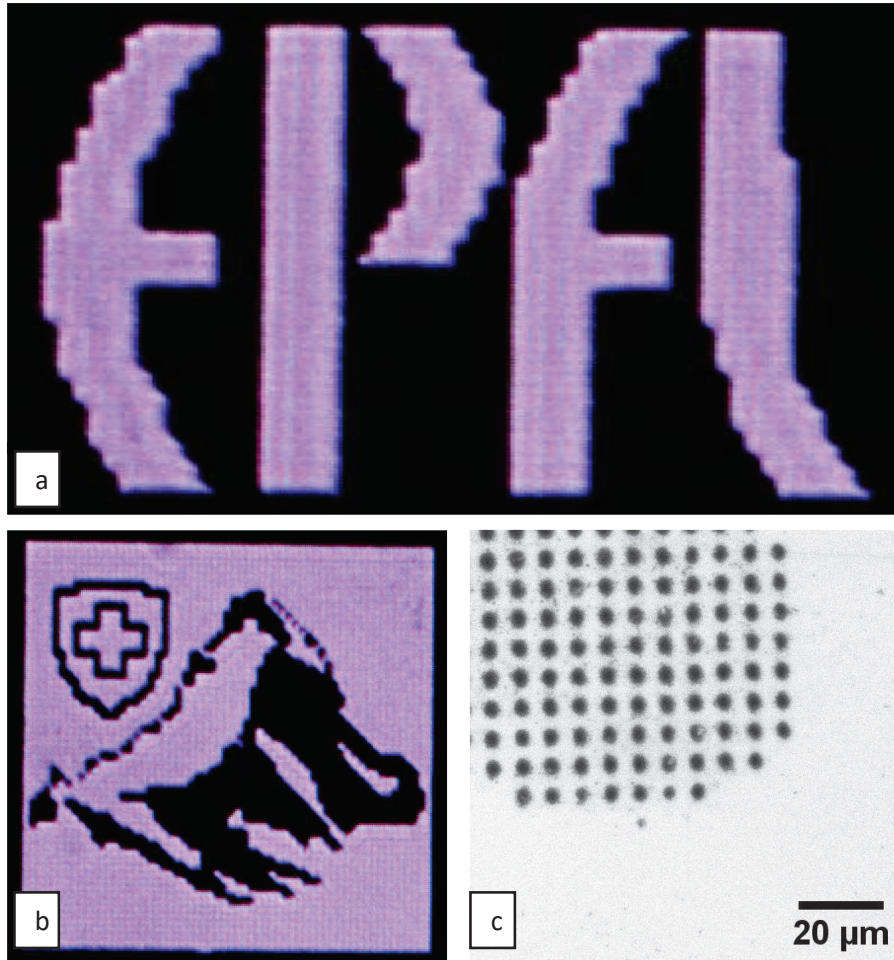


Figure V-9: (a) & (b): ablation of gold through the multicore fiber, after a point-by-point serie of focus spots generated using the transmission matrix. For (a), the EPFL logo was made using pulses of 0.9 μJ at the output of the fiber. For (b), the Matterhorn design was made using 0.64 J pulses. (c) ablation spots of between 1.2 and 3.2 μm in diameter, created with a fluence of 0.64 $\text{J}\cdot\text{cm}^{-2}$, observed with a confocal microscope in reflection.

V.3.5.2 Ex-vivo ablation

Considering the previous measurements we had conducted in tissue and via the multicore fiber, we tried to trigger LIOB at the surface of tissue. To maximize the intensity in the focus, we did several modifications to our setup:

- We changed the focusing lens at the input of the fiber from a 150 mm lens to a 125 mm lens, to decrease the demagnification of the SLM imaging on the proximal facet of the MCF, which allowed us to use 10000 cores instead of 6000. The corresponding new optimal focusing distance was 800 μm , which is in line with the analogy to a lens, for which a larger diameter gives us a longer working distance for an identical NA.
- We changed the objective at the distal end of the MCF from a 20x NA0.4 to a 40x NA0.65, which decrease the minimum spot size on the CMOS camera.
- We shortened the fiber to 4.5 cm, which should decrease the non-linear effects according to equation V-4.

We prepared a sample as defined earlier in this part, and placed it between the distal end of the fiber and the imaging objective. To get the best quality coupling and the highest peak energy, we did not use our amplitude correction and focused light directly 800 μm in front of the fiber. This new setup provided us with higher efficiency (about 20% of the light exiting the distal end to couple in the focus) without noticeable change for various distal power values between 60 mW and 400 mW, and limited pulse broadening. At the time of handing in this thesis, the characterization of this setup was not finished, but Figure V-10 shows the results obtained with it, demonstrating creation of bubbles in water, as well as ablation of glass and water. Based on the ablated material, the fluence for this irradiation was estimated to be above 4 $\mu\text{J}.\text{cm}^{-2}$, which is higher than what we were expecting to gain from the changes to this setup in term of diminution of self-modulation in the fiber cores. This shows there is more investigation to be done in this new method of wavefront shaping, and probably potential for even higher peak intensity transmission.

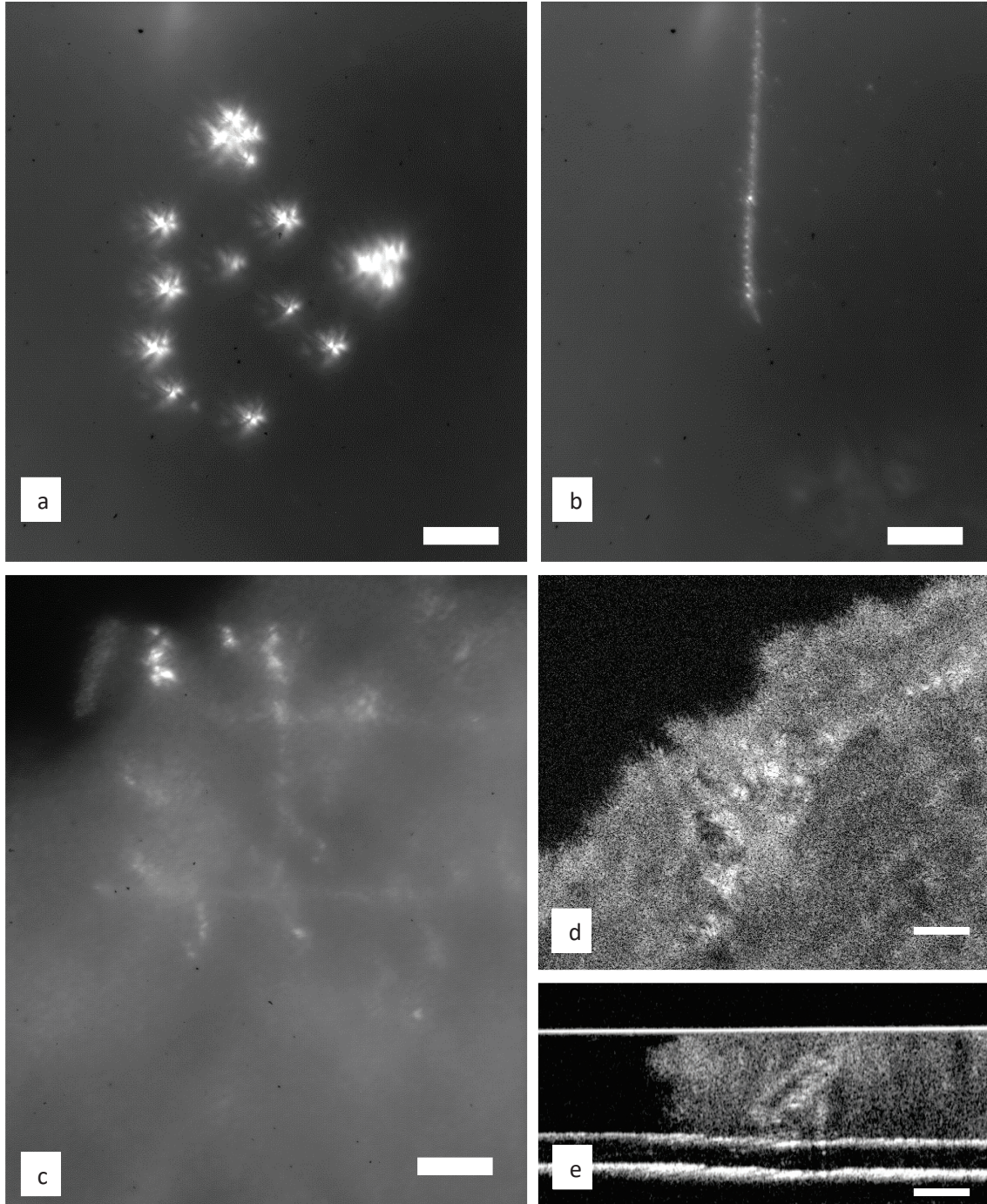


Figure V-10: Ablation of different material through a 4.5 cm long multicore fiber using wavefront shaping. (a), (b), and (c) were pictures taken using the CCD camera for recording of the TM. (a) Bubbles created in water (next to the chicken sample). (b) Line ablation in glass bulk (in the coverslip over the chicken sample). (c) Ablation of chicken breast sample along a pattern of four lines crossing to form a rectangle, scanned manually by moving the sample in front of the fiber. (d) Top view of the ablated chicken sample of image (c) imaged with the OCT. (e) OCT A-scan of the ablated chicken sample, along the red line shown on (d). Scale bars on the OCT images is 50 μm , scale bar on the CCD camera images is 20 μm .

V.3.6 Conclusion

In this last chapter, we have investigated two different approaches for performing ablation in a minimally invasive way. The use of a hollow-core fiber may be limited in that it only allows minimal pulse shaping, but its ability to deliver very high peak intensity pulses is still unmatched. On the other hand, although multicore fibers have shown sensitivity to non-linear effects during our experiments, we were able to demonstrate they offered the benefits of way more freedom in wavefront shaping, while being able to carry enough energy to trigger LIOB.

Further work in this domain would require more understanding of the non-linear effects in the cores of the multimode fiber, as well as developing a system to limit the current limitation on bending inherent to the transmission matrix approach. Progress in correction of linear and non-linear sources of phase-shift between the core would also be very beneficial to the use of MCF for transmission of high peak intensities, and could, on the long-run, strongly broaden the scope of their use in the field of biomedical applications.

Chapter VI: Conclusion

During the course of this thesis, we have investigated the concept of Laser-Induced Optical Breakdown from the perspective of a tool for biomedical applications. Our approach was mainly experimental, and we took steps to develop an extensive view of the effects of LIOB in soft biological samples, particularly arterial tissues. Although this approach was driven by the potential we foresaw in the use of LIOB for treatment of atherosclerosis, most of our work can find applications beyond this specific pathology and type of tissue. In particular, the observations made in biological phantoms, the study of cell reaction to LIOB in 3D environments, as well as the progress made in designing a catheter for optical microsurgery can be considered independently from biomedical applications in arteries.

We have discussed the process of LIOB, how it could be triggered in biological tissue and how it can have a direct impact on cells and living organisms. In particular, we have seen that it could selectively trigger the death of a cell directly exposed to a laser ablation beam. This can either happen in one of two ways. It can take place at low plasma intensity (up to 10^{21} electrons.cm⁻³), where free electrons created by the ionization of material in the focal volume can generate high quantities of Reactive Oxygen Species (ROS) inside the cytoplasm of a cell, and trigger its apoptosis. Selective cell destruction can also happen at higher plasma density (above up to 10^{21} electrons.cm⁻³), where a large enough cavitation bubble can be induced by LIOB, effectively killing a cell by overextending and rupturing its membrane. We were able to verify these two types of cellular cell death regimes in 2D and 3D cell cultures of endothelial cells. At even higher pulse energies, cellular damage can also be observed outside of the focal volume, mainly in the form of apoptotic cell death. This may be caused by large quantities of ROS being generated by the plasma and carried over distances of several tenths of micrometers by the expansion of the cavitation bubble, and long range mechanical damage may also be involved.

Hence, three regimes of cell deaths by LIOB were observed in-vitro on HCT116 cells in gels, dependent on the pulse energy used. One is the triggering of mostly apoptotic cell death at irradiance below 0.1 GW.cm⁻². The second one is mostly necrotic cell death without increase significant increase in apoptotic cell death, for irradiance between 0.1 GW.cm⁻² and 2 GW.cm⁻², around the LIOB threshold. The third one is mostly necrotic cell death in the volume scanned by the ablation focus, surrounded by apoptotic cell deaths, above 2 GW.cm⁻². These three regimes could present different interests depending on the type of cell death and structural damage favored for a biomedical application or another. Further steps in this in-vitro approach would include adapting the in-vivo experiments to create cellular models closer to arterial tissues, or other potential biological targets for LIOB. Cellular patterning may be an interesting approach to this problematic, as it could potentially enable to model the cell-to-cell short-range signaling. Another advantage would be the high cell density appropriate to finely analyze the special dependence of damage from ablation site.

We replicated our approach in ex-vivo and in-vivo rodent arteries. When exposed to a focused laser beam with peak intensities close to the LIOB threshold, these samples responded quantitatively similarly to phantoms and in-vitro cultures. These observations required establishing ablation setups and protocols to cope with challenges in isolating the effects of

ablation despite the samples being optically and mechanically inhomogeneous. We could observe creation and dynamics of relatively large bubbles by optical coherence tomography, both in healthy arterial tissues and atherosclerotic plaques, as well as finer damage patterns using a histological approach. Although necrosis was not assessed, a limited increase in the apoptotic signal was measured around the site of ablation during in-vivo experiments, in line with what was observed in-vitro. However, if we extensively characterized in-vivo ablation in arterial tissue, more ex-vivo experiments would be required to validate our results, ideally in animal atherosclerotic models.

Finally, we investigated the possibilities for designing and using an optical catheter for minimally invasive ablation of tissues. We demonstrated subsurface ablation of tissue through a 2 cm long catheter prototype using a Kagome type hollow-core fiber through a lens of less than 1 mm in diameter. We then considered a different approach for catheter design, by using wavefront shaping through a multicore fiber for lens-less ablation. We demonstrated ablation of metal, glass and biological tissue with scanning possibility, through 5 cm of a fiber with a diameter of 470 μm . This makes it one of the smallest ablation device with scanning possibility in the world. Although this approach is currently limited by bending and length constraints, there are promising approaches to cope with these in the future. The damage induced by LIOB are by essence very confined in space, and scanning of the beam is still one of the main challenges for miniaturized system taking advantage of multiphoton processes in general, so we think our research can have impact outside the field of research on LIOB.

In the frame of this thesis, we have thus developed a holistic approach to the use of LIOB in subsurface ablation of soft tissue, with a focus in the domain of cardiology. We have shown and discussed the benefits and limitations of this phenomenon at the cellular and tissue level, and presented concrete advances to delivering the high energy pulses needed for medical applications in living organisms.

Bibliographie:

1. Liu, X., Du, D. & Mourou, G. Laser ablation and micromachining with ultrashort laser pulses. *IEEE J. Quantum Electron.* **33**, 1706–1716 (1997).
2. Gabel, C. V. Femtosecond lasers in biology: nanoscale surgery with ultrafast optics. *Contemp. Phys.* **49**, 391–411 (2008).
3. Friedman, A., Gover, A., Kurizki, G., Ruschin, S. & Yariv, A. Spontaneous and stimulated emission from quasifree electrons. *Rev. Mod. Phys.* **60**, 471–535 (1988).
4. Sacchi, C. A. Laser-induced electric breakdown in water. *J. Opt. Soc. Am. B* **8**, 337 (1991).
5. Savolainen, J., Uhlig, F., Ahmed, S., Hamm, P. & Jungwirth, P. Direct observation of the collapse of the delocalized excess electron in water. *Nat. Chem.* **6**, 697–701 (2014).
6. Von der Linde, D. & Schüller, H. Breakdown threshold and plasma formation in femtosecond laser–solid interaction. *JOSA B* **13**, 216–222 (1996).
7. Noack, J. & Vogel, A. Laser-induced plasma formation in water at nanosecond to femtosecond time scales: calculation of thresholds, absorption coefficients, and energy density. *IEEE J. Quantum Electron.* **35**, 1156–1167 (1999).
8. Bloembergen, N. Laser-induced electric breakdown in solids. *IEEE J. Quantum Electron.* **10**, 375–386 (1974).
9. Kennedy, P. K. A first-order model for computation of laser-induced breakdown thresholds in ocular and aqueous media. I. Theory. *IEEE J. Quantum Electron.* **31**, 2241–2249 (1995).
10. Thiagarajan, M. & Thompson, S. Optical breakdown threshold investigation of 1064 nm laser induced air plasmas. *J. Appl. Phys.* **111**, 73302 (2012).
11. Rand, S. Inverse Bremsstrahlung with High-Intensity Radiation Fields. *Phys. Rev.* **136**, B231–B237 (1964).
12. Vogel, A., Noack, J., Hüttman, G. & Paltauf, G. Mechanisms of femtosecond laser nanosurgery of cells and tissues. *Appl. Phys. B* **81**, 1015–1047 (2005).
13. Docchio, F. Lifetimes of Plasmas Induced in Liquids and Ocular Media by Single Nd:YAG Laser Pulses of Different Duration. *EPL Europhys. Lett.* **6**, 407 (1988).
14. Assel, M., Laenen, R. & Laubereau, A. Retrapping and solvation dynamics after femtosecond UV excitation of the solvated electron in water. *J. Chem. Phys.* **111**, 6869–6874 (1999).
15. Zhang, S. *et al.* Laser-induced plasma temperature. *Spectrochim. Acta Part B At. Spectrosc.* **97**, 13–33 (2014).
16. Ansari, M. A., Erfanzadeh, M. & Mohajerani, E. Mechanisms of Laser-Tissue Interaction: II. Tissue Thermal Properties. *J. Lasers Med. Sci.* **4**, 99–106 (2013).
17. Paltauf, G. & Schmidt-Kloiber, H. Photoacoustic cavitation in spherical and cylindrical absorbers. *Appl. Phys. A* **68**, 525–531
18. Paltauf, G. & Schmidt-Kloiber, H. Microcavity dynamics during laser-induced spallation of liquids and gels. *Appl. Phys. A* **62**, 303–311
19. Kiselev, S. b. Kinetic boundary of metastable states in superheated and stretched liquids. *Phys. Stat. Mech. Its Appl.* **269**, 252–268 (1999).
20. Skripov, V. P. *et al.* Thermophysical properties of liquids in the metastable (superheated) state. (1988).
21. Fine, R. A. & Millero, F. J. Compressibility of water as a function of temperature and pressure. *J. Chem. Phys.* **59**, 5529–5536 (1973).
22. *Nonlinear Optics, Quantum Optics, and Ultrafast Phenomena with X-Rays.* (Springer US, 2003).
23. Couairon, A. & Mysyrowicz, A. Femtosecond filamentation in transparent media. *Phys. Rep.* **441**, 47–189 (2007).
24. Martin, C. & Ben-Yakar, A. Studying ultrafast laser parameters to deter self-focusing for deep tissue ablation. in **9740**, 97401I–97401I–8 (2016).

25. Volkova, E. A., Popov, A. M., Popovicheva, O. B. & Eftimiu, C. Dynamics of multiphoton ionization in a femtosecond laser pulse. *Sov. Phys. JETP* **75**, 263–268 (1992).
26. Vogel, A., Nahen, K., Theisen, D. & Noack, J. Plasma formation in water by picosecond and nanosecond Nd:YAG laser pulses. I. Optical breakdown at threshold and superthreshold irradiance. *IEEE J. Sel. Top. Quantum Electron.* **2**, 847–860 (1996).
27. Docchio, F., Regondi, P., Capon, M. R. C. & Mellerio, J. Study of the temporal and spatial dynamics of plasmas induced in liquids by nanosecond Nd:YAG laser pulses 2: Plasma luminescence and shielding. *Appl. Opt.* **27**, 3669 (1988).
28. Ultrafast optical Kerr effect in liquids and solids. *Science* **262**, 1386 (1993).
29. Kelley, P. L. Self-Focusing of Optical Beams. *Phys. Rev. Lett.* **15**, 1005–1008 (1965).
30. Couairon, A., Sudrie, L., Franco, M., Prade, B. & Mysyrowicz, A. Filamentation and damage in fused silica induced by tightly focused femtosecond laser pulses. *Phys. Rev. B* **71**, 125435 (2005).
31. Feit, M. D. & Jr, J. A. F. Effect of refraction on spot-size dependence of laser-induced breakdown. *Appl. Phys. Lett.* **24**, 169–172 (1974).
32. Rayner, D. M., Naumov, A. & Corkum, P. B. Ultrashort pulse non-linear optical absorption in transparent media. *Opt. Express* **13**, 3208 (2005).
33. Atkins, P. & Paula, J. de. *Atkins' Physical Chemistry*. (OUP Oxford, 2010).
34. Tay, K. A., Coudert, F.-X. & Boutin, A. Mechanism and kinetics of hydrated electron diffusion. *J. Chem. Phys.* **129**, 54505 (2008).
35. Martin, M. M. & Hynes, J. T. *Femtochemistry and Femtobiology: Ultrafast Events in Molecular Science*. (Elsevier, 2004).
36. Boudaïffa, B., Cloutier, P., Hunting, D., Huels, M. A. & Sanche, L. Resonant formation of DNA strand breaks by low-energy (3 to 20 eV) electrons. *Science* **287**, 1658–1660 (2000).
37. Hotop, H. in *Gaseous Dielectrics IX* (eds. Christophorou, L. G. & Olthoff, J. K.) 3–14 (Springer US, 2001).
38. Shen, N. *et al.* Ablation of cytoskeletal filaments and mitochondria in live cells using a femtosecond laser nanoscissor. *Mech. Chem. Biosyst. MCB* **2**, 17–25 (2005).
39. Garrett, B. C. *et al.* Role of water in electron-initiated processes and radical chemistry: issues and scientific advances. *Chem. Rev.* **105**, 355–390 (2005).
40. Foyer, C. H. & Mullineaux, P. M. *Causes of photooxidative stress and amelioration of defense systems in plants*. (CRC Press, 1994).
41. Fridovich, I. Fundamental Aspects of Reactive Oxygen Species, or What's the Matter with Oxygen? *Ann. N. Y. Acad. Sci.* **893**, 13–18 (1999).
42. Sharma, P., Jha, A. B., Dubey, R. S. & Pessarakli, M. Reactive Oxygen Species, Oxidative Damage, and Antioxidative Defense Mechanism in Plants under Stressful Conditions. *J. Bot.* **2012**, e217037 (2012).
43. Tirlapur, U. K. & König, K. Cell biology: Targeted transfection by femtosecond laser. *Nature* **418**, 290–291 (2002).
44. Leszczynski, D., Pitsillides, C. M., Pastila, R. K., Anderson, R. R. & Lin, C. P. Laser-Beam-Triggered Microcavitation: A Novel Method for Selective Cell Destruction. *Radiat. Res.* **156**, 399–407 (2001).
45. Dayton, P. A. *et al.* Optical and Acoustical Dynamics of Microbubble Contrast Agents inside Neutrophils. *Biophys. J.* **80**, 1547–1556 (2001).
46. Hongyu, Z. Molecular and biochemical studies of the hair bundle. (2012).
47. Ying, W. NAD⁺/NADH and NADP⁺/NADPH in cellular functions and cell death: regulation and biological consequences. *Antioxid. Redox Signal.* **10**, 179–206 (2008).
48. Karimi, A., Navidbakhsh, M., Shojaei, A. & Faghihi, S. Measurement of the uniaxial mechanical properties of healthy and atherosclerotic human coronary arteries. *Mater. Sci. Eng. C* **33**, 2550–2554 (2013).
49. Akhtar, R., Sherratt, M. J., Cruickshank, J. K. & Derby, B. Characterizing the elastic properties of tissues. *Mater. Today* **14**, 96–105 (2011).
50. Hall, T. J., Bilgen, M., Insana, M. F. & Krouskop, T. A. Phantom materials for elastography. *IEEE Trans. Ultrason. Ferroelectr. Freq. Control* **44**, 1355–1365 (1997).

51. Cubeddu, R., Pifferi, A., Taroni, P., Torricelli, A. & Valentini, G. A solid tissue phantom for photon migration studies. *Phys. Med. Biol.* **42**, 1971–1979 (1997).
52. Tracqui, P. *et al.* Mapping elasticity moduli of atherosclerotic plaque in situ via atomic force microscopy. *J. Struct. Biol.* **174**, 115–123 (2011).
53. Cai, D. K., Neyer, A., Kuckuk, R. & Heise, H. M. Optical absorption in transparent PDMS materials applied for multimode waveguides fabrication. *Opt. Mater.* **30**, 1157–1161 (2008).
54. Wang, Z., Volinsky, A. A. & Gallant, N. D. Crosslinking effect on polydimethylsiloxane elastic modulus measured by custom-built compression instrument. *J. Appl. Polym. Sci.* **131**, n/a-n/a (2014).
55. Ayers, F., Grant, A., Kuo, D., Cuccia, D. J. & Durkin, A. J. Fabrication and characterization of silicone-based tissue phantoms with tunable optical properties in the visible and near infrared domain. in **6870**, 687007-687007-9 (2008).
56. Goy, A. Imaging and microscopy in linear and nonlinear media using digital holography. (2013). doi:10.5075/epfl-thesis-5617, urn:nbn:ch:bel-epfl-thesis5617-6
57. Poumellec, B., Lancry, M., Chahid-Erriaji, A. & Kazansky, P. G. Modification thresholds in femtosecond laser processing of pure silica: review of dependencies on laser parameters [Invited]. *Opt. Mater. Express* **1**, 766–782 (2011).
58. Itoh, K., Watanabe, W., Nolte, S. & Schaffer, C. B. Ultrafast Processes for Bulk Modification of Transparent Materials. *MRS Bull.* **31**, 620–625 (2006).
59. Loeb, L. A., Springgate, C. F. & Battula, N. Errors in DNA Replication as a Basis of Malignant Changes. *Cancer Res.* **34**, 2311–2321 (1974).
60. Chinnery, P. F. in *GeneReviews*(®) (eds. Pagon, R. A. *et al.*) (University of Washington, Seattle, 1993).
61. Elmore, S. Apoptosis: A Review of Programmed Cell Death. *Toxicol. Pathol.* **35**, 495–516 (2007).
62. Calvino Fernández, M. & Parra Cid, T. H. pylori and mitochondrial changes in epithelial cells. The role of oxidative stress. *Rev. Espanola Enfermedades Dig. Organo Of. Soc. Espanola Patol. Dig.* **102**, 41–50 (2010).
63. Jarpe, M. B. *et al.* Anti-apoptotic versus pro-apoptotic signal transduction: checkpoints and stop signs along the road to death. *Oncogene* **17**, 1475–1482 (1998).
64. Alberts, B. *et al.* *Essential Cell Biology, Fourth Edition.* (Garland Science, 2013).
65. Kyrylova, K., Kyryachenko, S., Leid, M. & Kioussi, C. Detection of apoptosis by TUNEL assay. *Methods Mol. Biol. Clifton NJ* **887**, 41–47 (2012).
66. Cunningham, K. S. & Gotlieb, A. I. The role of shear stress in the pathogenesis of atherosclerosis. *Lab. Invest.* **85**, 9–23 (2004).
67. Goyal, T. *et al.* Current Concepts of the Role of Oxidized LDL Receptors in Atherosclerosis. *Curr. Atheroscler. Rep.* (2012). doi:10.1007/s11883-012-0228-1
68. Mata, P. *et al.* Effect of dietary fat saturation on LDL oxidation and monocyte adhesion to human endothelial cells in vitro. *Arterioscler. Thromb. Vasc. Biol.* **16**, 1347–1355 (1996).
69. Moore, K. J., Sheedy, F. J. & Fisher, E. A. Macrophages in atherosclerosis: a dynamic balance. *Nat. Rev. Immunol.* **13**, 709–721 (2013).
70. Yamamoto, K., Ikeda, U. & Shimada, K. Role of mechanical stress in monocytes/macrophages: implications for atherosclerosis. *Curr. Vasc. Pharmacol.* **1**, 315–319 (2003).
71. Tomkin, G. H. & Owens, D. LDL as a cause of atherosclerosis. *Open Atheroscler. Thromb. J.* **5**, 13–21 (2012).
72. Østerud, B. & Bjørklid, E. Role of Monocytes in Atherogenesis. *Physiol. Rev.* **83**, 1069–1112 (2003).
73. Mantovani, A., Garlanda, C. & Locati, M. Macrophage Diversity and Polarization in Atherosclerosis. *Arterioscler. Thromb. Vasc. Biol.* **29**, 1419–1423 (2009).
74. Yu, X.-H., Fu, Y.-C., Zhang, D.-W., Yin, K. & Tang, C.-K. Foam cells in atherosclerosis. *Clin. Chim. Acta Int. J. Clin. Chem.* **424**, 245–252 (2013).
75. Bobryshev, Y. V. Monocyte recruitment and foam cell formation in atherosclerosis. *Micron* **37**, 208–222 (2006).

76. Spann, N. J. *et al.* Regulated Accumulation of Desmosterol Integrates Macrophage Lipid Metabolism and Inflammatory Responses. *Cell* **151**, 138–152 (2012).
77. Kawano, H., Yano, T., Mizuguchi, K., Mochizuki, H. & Saito, Y. Changes in aspects such as the collagenous fiber density and foam cell size of atherosclerotic lesions composed of foam cells, smooth muscle cells and fibrous components in rabbits caused by all-cis-5, 8, 11, 14, 17-icosapentaenoic acid. *J. Atheroscler. Thromb.* **9**, 170–177 (2002).
78. Rekhter, M. D. Collagen synthesis in atherosclerosis: too much and not enough. *Cardiovasc. Res.* **41**, 376–384 (1999).
79. Jaeger, E. *et al.* Joint occurrence of collagen mRNA containing cells and macrophages in human atherosclerotic vessels. *Atherosclerosis* **86**, 55–68 (1991).
80. Greilberger, J., Schmut, O. & Jürgens, G. In Vitro Interactions of Oxidatively Modified LDL With Type I, II, III, IV, and V Collagen, Laminin, Fibronectin, and Poly-d-Lysine. *Arterioscler. Thromb. Vasc. Biol.* **17**, 2721–2728 (1997).
81. Wexler, L. *et al.* Coronary Artery Calcification: Pathophysiology, Epidemiology, Imaging Methods, and Clinical Implications. *Circulation* **94**, 1175–1192 (1996).
82. Risk Factors for Calcified Atherosclerotic Plaque. *Medscape* Available at: <http://www.medscape.com/viewarticle/560864>. (Accessed: 9th November 2016)
83. Waksman, R. & Saito, S. *Chronic Total Occlusions: A Guide to Recanalization*. (John Wiley & Sons, 2013).
84. Finegold, J. A., Asaria, P. & Francis, D. P. Mortality from ischaemic heart disease by country, region, and age: Statistics from World Health Organisation and United Nations. *Int. J. Cardiol.* **168**, 934–945 (2013).
85. Arroyo, L. H. & Lee, R. T. Mechanisms of plaque rupture. *Cardiovasc. Res.* **41**, 369–375 (1999).
86. Goy, J.-J. *et al.* 10-year follow-up of a prospective randomized trial comparing bare-metal stenting with internal mammary artery grafting for proximal, isolated de novo left anterior coronary artery stenosis the SIMA (Stenting versus Internal Mammary Artery grafting) trial. *J. Am. Coll. Cardiol.* **52**, 815–817 (2008).
87. Serruys, P. W. *et al.* A bioabsorbable everolimus-eluting coronary stent system (ABSORB): 2-year outcomes and results from multiple imaging methods. *The Lancet* **373**, 897–910 (2009).
88. Clemmons, D. R. Modifying IGF1 activity: an approach to treat endocrine disorders, atherosclerosis and cancer. *Nat. Rev. Drug Discov.* **6**, 821–833 (2007).
89. Kockx, M. M. & Herman, A. G. Apoptosis in atherosclerosis: beneficial or detrimental? *Cardiovasc. Res.* **45**, 736–746 (2000).
90. Tabas, I. Heart disease: Death-defying plaque cells. *Nature* **536**, 32–33 (2016).
91. Seimon, T. & Tabas, I. Mechanisms and consequences of macrophage apoptosis in atherosclerosis. *J. Lipid Res.* **50**, S382–S387 (2009).
92. Fredman, G. *et al.* Targeted nanoparticles containing the proresolving peptide Ac2-26 protect against advanced atherosclerosis in hypercholesterolemic mice. *Sci. Transl. Med.* **7**, 275ra20–275ra20 (2015).
93. Stocker, R. & Kearney, J. F. Role of Oxidative Modifications in Atherosclerosis. *Physiol. Rev.* **84**, 1381–1478 (2004).
94. Qian, Z. *et al.* Pulsetrain-burst mode, ultrafast-laser interactions with 3D viable cell cultures as a model for soft biological tissues. *Biomed. Opt. Express* **5**, 208–222 (2013).
95. Huang, D. *et al.* Optical Coherence Tomography. *Science* **254**, 1178–1181 (1991).
96. Yabushita, H. *et al.* Characterization of Human Atherosclerosis by Optical Coherence Tomography. *Circulation* **106**, 1640–1645 (2002).
97. Soofi, S. S., Last, J. A., Liliensiek, S. J., Nealey, P. F. & Murphy, C. J. The elastic modulus of Matrigel™ as determined by atomic force microscopy. *J. Struct. Biol.* **167**, 216–219 (2009).
98. Identification of programmed cell death in situ via specific labeling of nuclear DNA fragmentation. *J. Cell Biol.* **119**, 493–501 (1992).
99. Adams, J. C. Heavy metal intensification of DAB-based HRP reaction product. *J. Histochem. Cytochem.* **29**, 775–775 (1981).

100. Gu, H. *et al.* Gambogic acid mediates apoptosis as a p53 inducer through down-regulation of mdm2 in wild-type p53-expressing cancer cells. *Mol. Cancer Ther.* **7**, 3298–3305 (2008).
101. Owusu-Ansah, E., Yavari, A. & Banerjee, U. A protocol for in vivo detection of reactive oxygen species. *Protoc. Exch.* (2008). doi:10.1038/nprot.2008.23
102. Wang, X. *et al.* Imaging ROS signaling in cells and animals. *J. Mol. Med. Berl. Ger.* **91**, 917–927 (2013).
103. Tirlapur, U. K., König, K., Peuckert, C., Krieg, R. & Halbhauer, K. J. Femtosecond near-infrared laser pulses elicit generation of reactive oxygen species in mammalian cells leading to apoptosis-like death. *Exp. Cell Res.* **263**, 88–97 (2001).
104. Jacques, S. L. Optical properties of biological tissues: a review. *Phys. Med. Biol.* **58**, R37 (2013).
105. Sandell, J. L. & Zhu, T. C. A review of in-vivo optical properties of human tissues and its impact on PDT. *J. Biophotonics* **4**, 773–787 (2011).
106. Gamaly, E. G., Rode, A. V., Luther-Davies, B. & Tikhonchuk, V. T. Ablation of solids by femtosecond lasers: Ablation mechanism and ablation thresholds for metals and dielectrics. *Phys. Plasmas* 1994-Present **9**, 949–957 (2002).
107. Carmeliet, P., Moons, L. & Collen, D. Mouse models of angiogenesis, arterial stenosis, atherosclerosis and hemostasis. *Cardiovasc. Res.* **39**, 8–33 (1998).
108. Xu, C., Schmitt, J. M., Carlier, S. G. & Virmani, R. Characterization of atherosclerosis plaques by measuring both backscattering and attenuation coefficients in optical coherence tomography. *J. Biomed. Opt.* **13**, 34003-34003–8 (2008).
109. van der Meer, F. J. *et al.* Localized measurement of optical attenuation coefficients of atherosclerotic plaque constituents by quantitative optical coherence tomography. *IEEE Trans. Med. Imaging* **24**, 1369–1376 (2005).
110. Suhaimi, J. L. *et al.* Characterization of Cholesterol Crystals in Atherosclerotic Plaques Using Stimulated Raman Scattering and Second-Harmonic Generation Microscopy. *Biophys. J.* **102**, 1988–1995 (2012).
111. Koopman, R., Schaart, G. & Hesselink, M. K. Optimisation of oil red O staining permits combination with immunofluorescence and automated quantification of lipids. *Histochem. Cell Biol.* **116**, 63–68
112. Kammel, R., Ackermann, R., Tünnermann, A. & Nolte, S. Pump-probe investigation of fs-LIOB in water by simultaneous spatial and temporal focusing. in **8611**, 86110A–86110A–7 (2013).
113. Wisweh, H., Merkel, U., Hüller, A.-K., Lüerßen, K. & Lubatschowski, H. Optical coherence tomography monitoring of vocal fold femtosecond laser microsurgery. in **6632**, 663207-663207–7 (2007).
114. Hoy, C. L. *et al.* Towards endoscopic ultrafast laser microsurgery of vocal folds. *J. Biomed. Opt.* **17**, 38002 (2012).
115. Suh, W. M., Seto, A. H., Margey, R. J. P., Cruz-Gonzalez, I. & Jang, I.-K. Intravascular Detection of the Vulnerable Plaque. *Circ. Cardiovasc. Imaging* **4**, 169–178 (2011).
116. Wang, Y. *et al.* Hollow-core photonic crystal fibre for high power laser beam delivery. *High Power Laser Sci. Eng.* **1**, 17–28 (2013).
117. Wang, Y. Y. *et al.* Design and fabrication of hollow-core photonic crystal fibers for high-power ultrashort pulse transportation and pulse compression. *Opt. Lett.* **37**, 3111 (2012).
118. Ferhanoglu, O., Yildirim, M., Subramanian, K. & Ben-Yakar, A. A 5-mm piezo-scanning fiber device for high speed ultrafast laser microsurgery. *Biomed. Opt. Express* **5**, 2023 (2014).
119. Niemz, M. H. Threshold dependence of laser-induced optical breakdown on pulse duration. *Appl. Phys. Lett.* **66**, 1181–1183 (1995).
120. Lanvin, T. *et al.* Subsurface ablation of atherosclerotic plaque using ultrafast laser pulses. *Biomed. Opt. Express* **6**, 2552–2561 (2015).
121. Wang, Y.-X. *et al.* Increased aortic stiffness assessed by pulse wave velocity in apolipoprotein E-deficient mice. *Am. J. Physiol. - Heart Circ. Physiol.* **278**, H428–H434 (2000).

122. Kameyama, H. *et al.* Augmentation of pulse wave velocity precedes vascular structural changes of the aorta in rats treated with N(omega)-nitro-L-arginine methyl ester. *Hypertens. Res. Off. J. Jpn. Soc. Hypertens.* **28**, 439–445 (2005).
123. Stoneman, V. E. A. & Bennett, M. R. Role of apoptosis in atherosclerosis and its therapeutic implications. *Clin. Sci.* **107**, 343–354 (2004).
124. Majno, G. & Joris, I. Apoptosis, oncosis, and necrosis. An overview of cell death. *Am. J. Pathol.* **146**, 3–15 (1995).
125. Getz, G. S. & Reardon, C. A. Animal Models of Atherosclerosis. *Arterioscler. Thromb. Vasc. Biol.* **32**, 1104–1115 (2012).
126. Phinikaridou, A., Hallock, K. J., Qiao, Y. & Hamilton, J. A. A robust rabbit model of human atherosclerosis and atherothrombosis. *J. Lipid Res.* **50**, 787–797 (2009).
127. Johnson, W. D., Flemma, R. J., Lepley, D. & Ellison, E. H. Extended treatment of severe coronary artery disease: a total surgical approach. *Ann. Surg.* **170**, 460–470 (1969).
128. Kappetein, A. P. *et al.* Comparison of coronary bypass surgery with drug-eluting stenting for the treatment of left main and/or three-vessel disease: 3-year follow-up of the SYNTAX trial. *Eur. Heart J.* **32**, 2125–2134 (2011).
129. Furer, V., Fayad, Z. A., Farkouh, M. E., Rosenbaum, D. & Greenberg, J. D. Noninvasive atherosclerosis imaging modalities and their application to investigating cardiovascular drug effects in rheumatoid arthritis. *Drug Dev. Res.* **72**, 739–749 (2011).
130. Al-Moghairi, A. M. & Al-Amri, H. S. Management of Retained Intervention Guide-wire: A Literature Review. *Curr. Cardiol. Rev.* **9**, 260–266 (2013).
131. Davidson, C. J. Cardiovascular and Renal Toxicity of a Nonionic Radiographic Contrast Agent after Cardiac Catheterization: A Prospective Trial. *Ann. Intern. Med.* **110**, 119 (1989).
132. Sigwart, U., Puel, J., Mirkovitch, V., Joffre, F. & Kappenberger, L. Intravascular Stents to Prevent Occlusion and Re-Stenosis after Transluminal Angioplasty. *N. Engl. J. Med.* **316**, 701–706 (1987).
133. Akkus, N. I., Abdulbaki, A., Jimenez, E. & Tandon, N. Atherectomy devices: technology update. *Med. Devices Auckl. NZ* **8**, 1–10 (2014).
134. Buecker, A., Minko, P., Massmann, A. & Katoh, M. [Percutaneous mechanical atherectomy for treatment of peripheral arterial occlusive disease]. *Radiol.* **50**, 29–37 (2010).
135. Snitzer, E. Proposed Fiber Cavities for Optical Masers. *J. Appl. Phys.* **32**, 36–39 (1961).
136. Block, P., Fallon, J. & Elmer, D. Experimental angioplasty: lessons from the laboratory. *Am. J. Roentgenol.* **135**, 907–912 (1980).
137. Ginsburg, R., Wexler, L., Mitchell, R. S. & Profitt, D. Percutaneous transluminal laser angioplasty for treatment of peripheral vascular disease. Clinical experience with 16 patients. *Radiology* **156**, 619–624 (1985).
138. Bittl, J. A. *et al.* Clinical success, complications and restenosis rates with excimer laser coronary angioplasty. *Am. J. Cardiol.* **70**, 1533–1539 (1992).
139. Trokel, S. L., Srinivasan, R. & Braren, B. Excimer Laser Surgery of the Cornea. *Am. J. Ophthalmol.* **96**, 710–715 (1983).
140. Saponitis, J., Grantham, J. A. & Marso, S. P. Excimer laser atherectomy to overcome intraprocedural obstacles in chronic total occlusion percutaneous intervention: Case examples. *Catheter. Cardiovasc. Interv.* **85**, E83–E89 (2015).
141. Sangiorgi, G. & Colombo, A. Embolic protection devices. *Heart* **89**, 990–992 (2003).
142. Du, D., Liu, X., Korn, G., Squier, J. & Mourou, G. Laser-induced breakdown by impact ionization in SiO₂ with pulse widths from 7 ns to 150 fs. *Appl. Phys. Lett.* **64**, 3071–3073 (1994).
143. Benabid, F., Couny, F., Knight, J. C., Birks, T. A. & Russell, P. S. J. Compact, stable and efficient all-fibre gas cells using hollow-core photonic crystal fibres. *Nature* **434**, 488–491 (2005).
144. Gérôme, F., Cook, K., George, A. K., Wadsworth, W. J. & Knight, J. C. Delivery of sub-100fs pulses through 8m of hollow-core fiber using soliton compression. *Opt. Express* **15**, 7126 (2007).
145. Im, S.-J., Husakou, A. & Herrmann, J. Guiding properties and dispersion control of kagome lattice hollow-core photonic crystal fibers. *Opt. Express* **17**, 13050 (2009).

146. Pricking, S. *et al.* Hollow core fiber delivery of sub-ps pulses from a TruMicro 5000 Femto edition thin disk amplifier. in **9356**, 935602-935602-6 (2015).
147. Keeley, E. & Grines, C. L. Scraping of aortic debris by coronary guiding catheters A prospective evaluation of 1,000 cases. *J. Am. Coll. Cardiol.* **32**, 1861–1865 (1998).
148. Wolinsky, H. & Glagov, S. Comparison of Abdominal and Thoracic Aortic Medial Structure in Mammals. *Circ. Res.* **25**, 677–686 (1969).
149. Br  el, A. & Oxlund, H. Changes in biomechanical properties, composition of collagen and elastin, and advanced glycation endproducts of the rat aorta in relation to age. *Atherosclerosis* **127**, 155–165 (1996).
150. Fukui, S., Nawshiro, H., Wada, K., Shima, K. & Hallenbeck, J. M. A new method to catheterize a femoral artery in mice using a nylon suture as a ‘guide wire’. *Neurol. Res.* **23**, 655–656 (2001).
151. Bayrami  li, M.,   irino  lu, H. & Yal  in, D. A basic experimental model for end-to-end anastomosis of vessels with diameter discrepancy. *Microsurgery* **34**, 333–334 (2014).
152. Byrom, M. J., Bannon, P. G., White, G. H. & Ng, M. K. C. Animal models for the assessment of novel vascular conduits. *J. Vasc. Surg.* **52**, 176–195 (2010).
153. Th  roff, J. W., Hort, W. & Lichti, H. Diameter of coronary arteries in 36 species of mammalian from mouse to giraffe. *Basic Res. Cardiol.* **79**, 199–206 (1984).
154. Dodge, J. T., Brown, B. G., Bolson, E. L. & Dodge, H. T. Lumen diameter of normal human coronary arteries. Influence of age, sex, anatomic variation, and left ventricular hypertrophy or dilation. *Circulation* **86**, 232–246 (1992).
155. Hoy, C. L. *et al.* Towards endoscopic ultrafast laser microsurgery of vocal folds. *J. Biomed. Opt.* **17**, 38002 (2012).
156. Subramanian, K. *et al.* Kagome fiber based ultrafast laser microsurgery probe delivering micro-Joule pulse energies. *Biomed. Opt. Express* **7**, 4639 (2016).
157. Reichenbach, K. L. & Xu, C. Numerical analysis of light propagation in image fibers or coherent fiber bundles. *Opt. Express* **15**, 2151 (2007).
158. Loterie, D. *et al.* Digital confocal microscopy through a multimode fiber. *Opt. Express* **23**, 23845 (2015).
159. Loterie, D., Farahi, S., Psaltis, D. & Moser, C. Complex pattern projection through a multimode fiber. in (eds. Bifano, T. G., Kubby, J. & Gigan, S.) 93350I (2015). doi:10.1117/12.2077404
160. Kim, Y. *et al.* Adaptive Multiphoton Endomicroscope Incorporating a Polarization-Maintaining Multicore Optical Fibre. *IEEE J. Sel. Top. Quantum Electron.* **22**, 1–8 (2016).
161. Heyvaert, S., Debaes, C., Ottevaere, H. & Thienpont, H. Design of a novel multicore optical fibre for imaging and beam delivery in endoscopy. in **8429**, 84290Q–84290Q–13 (2012).
162. Fibich, G. & Gaeta, A. L. Critical power for self-focusing in bulk media and in hollow waveguides. *Opt. Lett.* **25**, 335 (2000).
163. Adair, R., Chase, L. L. & Payne, S. A. Nonlinear refractive-index measurements of glasses using three-wave frequency mixing. *J. Opt. Soc. Am. B* **4**, 875 (1987).
164.   i  m  r, T. & Dholakia, K. Shaping the light transmission through a multimode optical fibre: complex transformation analysis and applications in biophotonics. *Opt. Express* **19**, 18871 (2011).
165. Vellekoop, I. M. & Mosk, A. P. Focusing coherent light through opaque strongly scattering media. *Opt. Lett.* **32**, 2309 (2007).
166. Vellekoop, I. M., van Putten, E. G., Lagendijk, A. & Mosk, A. P. Demixing light paths inside disordered metamaterials. *Opt. Express* **16**, 67 (2008).
167. Conkey, D. B., Caravaca-Aguirre, A. M. & Piestun, R. High-speed scattering medium characterization with application to focusing light through turbid media. *Opt. Express* **20**, 1733 (2012).
168. Popoff, S. M., Lerosey, G., Fink, M., Boccara, A. C. & Gigan, S. Controlling light through optical disordered media: transmission matrix approach. *New J. Phys.* **13**, 123021 (2011).
169. Stasio, N., Conkey, D. B., Moser, C. & Psaltis, D. Light control in a multicore fiber using the memory effect. *Opt. Express* **23**, 30532–30544 (2015).

Appendix A: Making of the gels and phantoms

This Appendix presents an overview of the protocols using for making gels and phantoms.

Agar gels

Agar gels were used both as transparent phantoms of soft tissues and as culture medium for HCT 116. Here we will present the protocol for making gels containing cell cultures. To create phantoms which do not contain cells, skip all steps involving cells and replace the culture medium by PBS 1X. To create a scattering phantom, add intralipid at step 8.

- 1) Prepare the appropriate cell culture medium (for HCT116 cells, we used McCoy 5A medium with 10% BSA). Put pipette tips in an incubator at 37°C.
- 2) Trypsinize a cell culture to detach cells from their substrate. Add the same level of cell culture medium.
- 3) Count the number of cells in the solution, and calculate the dilution required to have a solution with 10x the cellular concentration you want in the final Agar gel.
- 4) Either dilute in the appropriate volume V_1 of cell culture medium, or concentrate the solution. To do this, centrifuge the cell suspension into a pellet, and then resuspend it in an appropriate volume of fresh culture media.
- 5) Prepare a volume V_2 of Agar gel by diluting the appropriate quantity of Agar in powder into the volume V_2 , considering the percentage in mass for a final volume of Agar gel $V_1 + V_2$, and put it in a becher. Stir the solution.
- 6) Add a magnetic stirrer into the Agar solution, cover the becher with aluminium foil, and put on a magnetic hot plate at medium speed.
- 7) Heat the Agar solution to 70°C, controlling the temperature by an optical thermometer or another mean. Keep the heating on until the Agar solution becomes completely transparent.
- 8) Remove the Agar solution from the hot plate, and wait for it to cool to about 50°C. Add in the cells in suspension.
- 9) Pipette in and out to homogenize the concentration of cells in solution.
- 10) Dispose the appropriate quantity of gels on the desired substrate using the warm pipettes tips.
- 11) For gels with less than 1% Agar, flip the gels over every thirty seconds for about 3 minutes, then put the cells in a fridge at 4°C for 3 minutes.
- 12) Store the gels in the incubator for 10 minutes. Add 2 times the volume of gel in culture medium.

PEG Hydrogel

PEG hydrogels were only used as cell culture scaffolds, and our protocol thus only covers it. We thank Dr.Nathalie Brandenburg for her help and guidance in the preparation of these gels and the

matrigels. This protocol was made to prepare 10 gels of 20 μL each, which requires preparation of a total volume of 200 μL of gel.

- 1) Prepare the appropriate cell culture medium (for HCT116 cells, we used McCoy 5A medium with 10% BSA).
- 2) Prepare a mix of 10% PEG solution.
- 3) Prepare a 10x Buffer with Tris(hydroxymethyl)aminomethane 50mM, 50mM Ca, and a adjusted pH 7.6.
- 4) Prepare 10 U.mL⁻¹ of FIIIa
- 5) Trypsinize a cell culture to detach cells from their substrate. Add the same level of cell culture medium.
- 6) Count the number of cells in the solution, and calculate the dilution required to have a solution with 10x the cellular concentration you want in the final Hydrogel. A concentration between 50000 and 100000 cells per millileter gave us relatively good results.
- 7) Either dilute in the appropriate volume V_1 of cell culture medium, or concentrate the solution. To do this, centrifuge the cell suspension into a pellet, and then resuspend it in an appropriate volume of fresh culture media.
- 8) Prepare an Eppendorf with a mix of
 - a. 120 μL culture medium
 - b. 30 μL of the prepared PEG mix
 - c. 20 μL of 10x Buffer solution
 - d. 20 μL of cells in suspension
- 9) Stir the solution prepared in step 8. Add in 10 μL of FXIIIa solution and stir some more for about 20 seconds.
- 10) Within 2 minutes, dispose the appropriate quantity of gels on the desired substrate and, if possible, turn the gels upside down regularly for the rest of this duration.
- 11) Put the hydrogels in incubator for 10 minutes. Add 2 times the volume of hydrogel in culture medium.

Matrigel

Matrigel were also only used as cell culture scaffolds, and our protocol thus only covers it. This protocol us made to prepare 10 gels of 20 μL each, which requires preparation of a total volume of 200 μL of gel.

- 1) Prepare the appropriate cell culture medium (for HCT116 cells, we used McCoy 5A medium with 10% BSA).
- 2) Trypsinize a cell culture to detach cells from their substrate. Add the same level of cell culture medium.
- 3) Count the number of cells in the solution, and calculate the dilution required to have a solution with 10x the cellular concentration you want in the final matrigel. A concentration between 50000 and 500000 cells per millileter gave us relatively good results.
- 4) Either dilute in the appropriate volume V_1 of cell culture medium, or concentrate the solution. To do this, centrifuge the cell suspension into a pellet, and then resuspend it in an appropriate volume of fresh culture media.

- 5) Unfreeze the matrigel slowly, for example by letting them warm up to above their melting temperature by laying them on ice for several minutes. Beware! The matrigel crosslinks at ambient temperature, so it is advised to prepare the gels as soon as they have reached their liquid state.
- 6) Prepare an Eppendorf with the desired volume of matrigel (in our case: 180 μL).
- 7) Add 20 μL of cells in suspension to the matrigel.
- 8) Stir the solution for about 20 seconds by pipetting in and out.
- 9) Within 2 minutes, dispose the appropriate quantity of gels on the desired substrate and, if possible, turn the gels upside down regularly for the rest of this duration.
- 10) Put the hydrogels in incubator for 10 minutes. Add 2 times the volume of matrigel in culture medium.

Appendix B: Monte Carlo simulation

The concept of Monte Carlo (MC) simulation is the following: the generation of a high number of individual events, whose overall behavior can be analysed to get a statistical approach to the behavior of a whole population. In the field of optics, it is often used to study the diffusion of light through scattering tissues.

We programmed a simulation of this type in the frame of our research, as we considered it could present valuable insights into not only the intensity and properties of light in the focal volume. But more importantly for us, it also provided information about the behavior of light in the surrounding volume, which could help in the prediction of damaging effect to surrounding cells. We have discussed in Chapter 2 that cells could be damaged by light intensities two order of magnitudes below the LIOB threshold, and we thought MC simulation could give inform us about where this could happen in the sample. Finally, by generating high quantities of photons with a stochastic behavior and generated with a Gaussian profile in time corresponding to the pulse duration progile, we wanted to evaluate the impact of the photon population reaching the focus on the plasma density and progression. Although very interesting and promising, this last approach was not conducted to its end due to shift in priorities toward the end of this thesis, but our code would not require major modification to be adapted to this.

It is based on Mie scattering theory and inspired by the work on Multi-Layered Monte Carlo simulation (MCML) of Lihong Wang and Steven Jacques¹⁰⁶, before the later released his *3D Monte Carlo simulation of heterogeneous tissues* in 2013.

In the following description, *rand* refers to a randomly generated number, whose value is comprised between 0 and 1.

The steps of the simulation go as follow.

- 1) We define a 3D space, mapped by an $m_1 \times m_2$ 3D mesh forming a space of voxels.
- 2) To each of these voxels, we attach a set of optical proprieties of the medium for the wavelength of photons we want to consider: refractive index n , scattering coefficient μ_s' , absorbtion coefficient μ_a , anisotropy g . This step is where we can define an inhomogeneous medium, such as circular artery containing fatty tissues or blood, for example.
- 3) We start a loop for simulating N photons. For better management of the memory of the computer, we segment this population in n photons being simulated for each one of the m batches of photons.
- 4) For each photon, we first proceed with an initialization step: initialization of the position and initial angle of a photon. The probability profile for these parameters depends on the expected field on the input surface from which generation of photons starts. In other words, for the study of a focusing beam corresponding to our experiments, it depends on the depth of focus z_{focus} relative to the plane of generation P_0 , and the NA of the focusing fiber considered in the simulation. By default, we spread the initial position of photons onto P_0 following a Gaussian profile. The initial angle α_0 and β_0 on the other hand qre the polqr coordinqtes angles corresponding to a photon directly aimed at the center of focus. We also estimate the absolute distance d_{abs_total} what will be traveled by the photon as a random variable generated by:

$$d_{abs_total} = -\log\left(\frac{rand}{\mu a}\right)$$

Every distance traveled by the photon will be remove from this “total lifetime” until it equals 0, when the photon disappears. We used to use a Poisson distribution for this, but this logarithmic law gave us better results compared to measurements. The distance traveled by the photon d_{trav} is set to 0.

5) The photon then enters a loop of simulations of collisions and scattering. It goes as follows:

a. A travel distance d_{step} is generated by:

$$d_{step} = -\log\left(\frac{rand}{\mu s'}\right)$$

b. We project the medium in which the photon will travel, taking into account the angle and the distance d_{step}/n . If the medium has homogeneous optical properties, and if $d_{trav} + d_{step} < d_{abs_total}$ we pursue a “normal” traveling step. If not, we account for the change in index by dividing a step in two consecutive steps in different index of refraction, which will influence the propagation angle and traveled distance of the photon.

c. We generate a deflection event by a scattering entity in the medium. This includes two angles of deflection: one in a random direction perpendicular to the axis of travel of the photon, γ , and one making an angle with this axis, Θ . γ is easily computed as

$$\gamma = rand * 2\pi$$

d. whereas Θ is defined according to Mie scattering model by its sinus and cosinus:

$$\cos \Theta = (1 + g^2 - (\frac{1 - g^2}{1 - g + rand})^2) \frac{1}{2g}$$

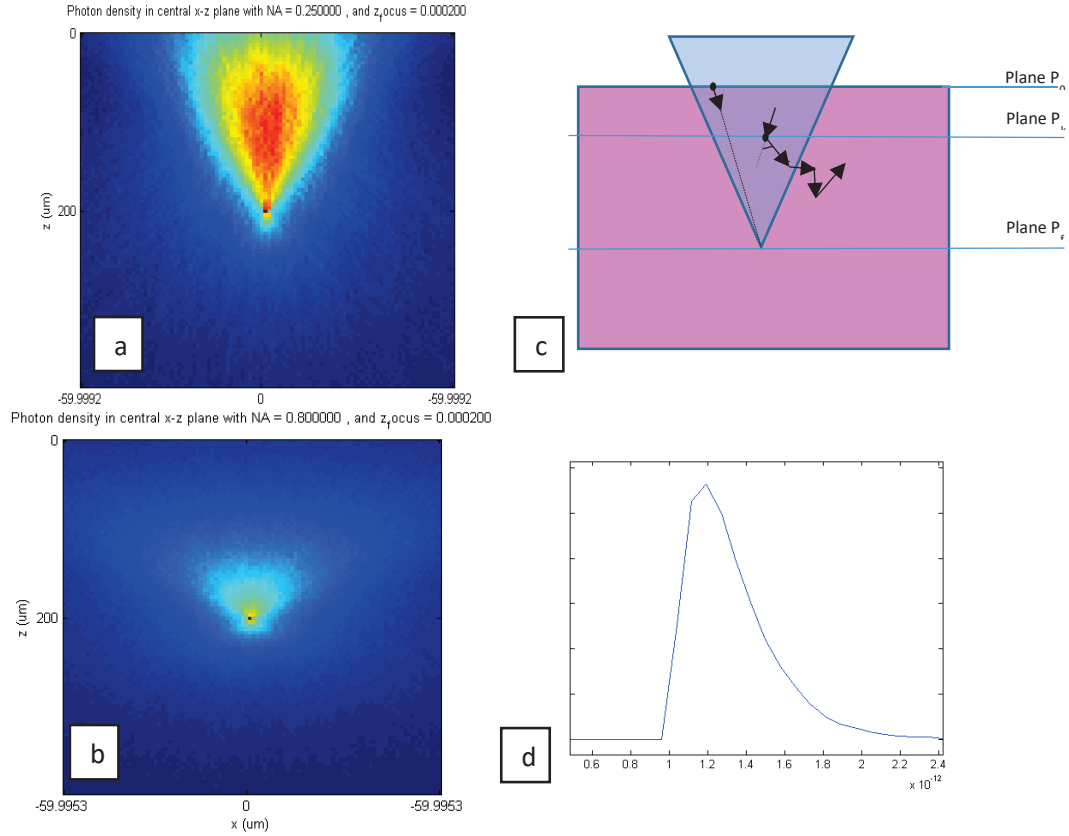
$$\sin \Theta = \text{sign}(0.5 + rand) \sqrt{1 - \cos^2 \Theta}$$

The new angle α_n and β_n in polar coordinated are computed based on addition of Θ and γ angles to the old angles α_{n-1} and β_{n-1} of the photon.

6) This loops repeats itself until $d_{trac} + d_{step} < d_{abs_total}$, at which point an estimate of the final position of the photon when it is absorbed is computed by propagating it a distance $d_{abs_total} - d_{trav}$ and its position is recorded before we start another loop with another photon.

During our simulation, we recorded the position of the photon at each collision, which allowed us to recompute its also trajectory, and calculating the precise optical intensity in each plane crossed by the photon. We also recorded its trajectory time at each position it occupied.

If we set the duration of collision to a certain value τ_{col} and know the exact trajectory and number of collisions of the photons, we can map precisely the time evolution of the intensity profile. We can also restrict our study to the intensity in a defined focal volume. For example, the study on the number of photons reaching the focal volume was made by restricting our measurement volume to a small disk in the center of the focal plane P_f and analyse the pathlength of the photons reaching this target.



Example results of the MC simulation. (a-b) Results of the Monte Carlo simulation for scattering through $200 \mu\text{m}$ for a value μ_s of 200 cm^{-1} with a NA0.25 objective, showing the intensity profile in a plane cutting through the focal folume in the center of the image. (a) and a NA0.8 objective (b) . (c)The Diagram of the Monte Carlo simulation we made for a focused beam propagating through a homogeneous or inhomogeneous medium. (d) Quantity of photons reaching the focal volume within a 1 ps timeframe; the first peak at 1.5 ps corresponds to the ballistic photons (in a.u).

Appendix C: Staining Protocols

In this appendix, we will present the three protocols we used most commonly during our research on apoptosis

Immunostaining of Caspase 3

Staining of caspase 3 was used both in gels and ex-vivo. The ex-vivo part was managed entirely by the HCF of EPFL, so this part will focus on the immunostaining of cells embedded in gels.

- 1) Prepare a solution of PBS 1X with 1% BSA and 0.1% Triton-X, and a solution of PBS 1X with 1% BSA and 0.3% Triton-X.
- 2) Remove the cell culture medium. Clean the gel by rinsing 3x (1 time quickly, 2 times 10 minutes) with PBS 1X.
- 3) Fix the gel with 3 times the gel volume of PFA 4% for 30 mins.
- 4) Wash 3 times (1 time quickly, 2 times 10 minutes) with PBS 1X.
- 5) Prevent unspecific binding by adding 3 times the volume of gel with PBS 1X with 1% BSA and 0.3% Triton-X.
- 6) Add in the primary antibody, freshly diluted at 1/200 in PBS 1X with 1% BSA and 0.1% Triton-X. Keep 48h at 4°C on a slowly moving stage.
- 7) Wash 4 times (1 time quickly, 3 times 10 minutes) with PBS 1X with 1% BSA and 0.1% Triton-X.
- 8) Add in the secondary antibody, freshly diluted at 1/800 in PBS 1X with 1% BSA and 0.1% Triton-X. Keep overnight at 4°C on a slowly moving stage.
- 9) Wash 4 times (1 time quickly, 3 times 10 minutes) with PBS 1X with 1% BSA and 0.1% Triton-X.
- 10) Wash 3 times (1 time quickly, 2 times 10 minutes) with PBS 1X.
- 11) Add DAPI diluted in PBS 1X at $2\mu\text{g}.\text{mL}^{-1}$, keep for 10 mins.
- 12) Wash 3 times (1 time quickly, 2 times 10 minutes) with PBS 1X.

TUNEL staining

Staining with TUNEL protocol is a multiple step process based on the binding of TdT to DNA fragments, and labelled dUTP binding to TdT. This protocol was used for staining ex-vivo slices fixed in paraffin and 2D cell cultures after fixation in PFA4% (skip step 6 in this case).

- 1) Prepare a TdT Buffer solution (1% Tris-HCL, 5% Codium Cacodylate, Cobalt Chloride 0.5%, 0.1% BSA in distilled water, pH adjusted to 6.6).
- 2) Prepare an enzyme reagent with 4% Terminal Transferase (TdT) (Roche 03333566001) in reaction buffer.
- 3) Prepare a label reagent mixture 0.4% Biotin-16-dUTP in TdT Reaction Buffer.
- 4) Prepare stop wash buffer by mixing 2% NaCl with 1% sodium citrate in distilled water.
- 5) Prepare anti-digoxigenin fluorescein solution 0.5% in maleic acid buffer.

- 6) Just before staining, prepare the TdT reaction mixture by mixing 10% enzyme reagent with 90% label reagent.
- 7) Deparaffinize sections by dipping them in xylene 2 times (5 minutes each), followed by 2 times 100% ethanol (3 minutes each) and one time in 95% ethanol (1 minute).
- 8) Pretreatment: use proteinase K digestion method.
- 9) Wash 3 times (1 time quickly, 2 times 10 minutes) with PBS-Tween 20.
- 10) Block endogeneous peroxidase activity by incubating the sample in 3% H₂O₂ in PBS for 10 minutes.
- 11) Wash 4 times (1 time quickly, 3 times 10 minutes) with PBS-Tween 20.
- 12) Incubate sections in TdT reaction mixture for 2h in a pre-warmed humidified chamber.
- 13) Stop the reaction by washing it in stop wash buffer for 10 mins.
- 14) Wash 3 times (1 time quickly, 2 times 10 minutes) with PBS-Tween 20.
- 15) Incubate samples with anti-digoxigenin fluorescein solution for 30 mins at room temperature.
- 16) Wash 3 times (1 time quickly, 2 times 10 minutes) with PBS-Tween 20.
- 17) Counterstain with Hoechst diluted at 1/200 for 10 minutes.
- 18) Wash 3 times (1 time quickly, 2 times 10 minutes) with PBS-Tween 20.

Annexin V staining

This protocol for staining with Annexin V was conducted on matrigel. The penetration of Annexin through the gel was severely limited, and optimization of this protocol may be possible. As opposed to the other protocols for staining apoptotic cells, this protocol does not require fixation, and is thus compatible with a different set of stains, such as Propidium Iodide for necrotic cells.

- 1) Remove the cell culture medium. Clean the gel by rinsing 3x (1 time quickly, 2 times 10 minutes) with PBS 1X.
- 2) Clean the gel three times in Annexin V buffer solution or HEPES solution.
- 3) Prepare Propidium Iodide 1 µg.mL⁻¹ from PI in powder.
- 4) Prepare Annexin V 2 µg.mL⁻¹ staining solution in HEPES or buffer solution, from stock Annexin V solution.
- 1) Add 2 times the volume of gel in Annexin V staining solution.
- 2) Add 1 time the volume of gel in PI staining solution.
- 3) Incubate for 12h on a moving stage in an incubator.
- 4) Wash 3 times (1 time quickly, 2 times 10 minutes) with PBS 1X.

Appendix D: Challenges in in-vivo manipulation experiments

While conducting in-vivo experiments in rats, several unexpected challenges arose which impacted the quality of light intensity at focus. We conducted ablation on 8 other rats for which the results are not included in the thesis, as the experiments involving them either showed strong technical limitations, or the control of ablation area was not properly managed.

Fogging

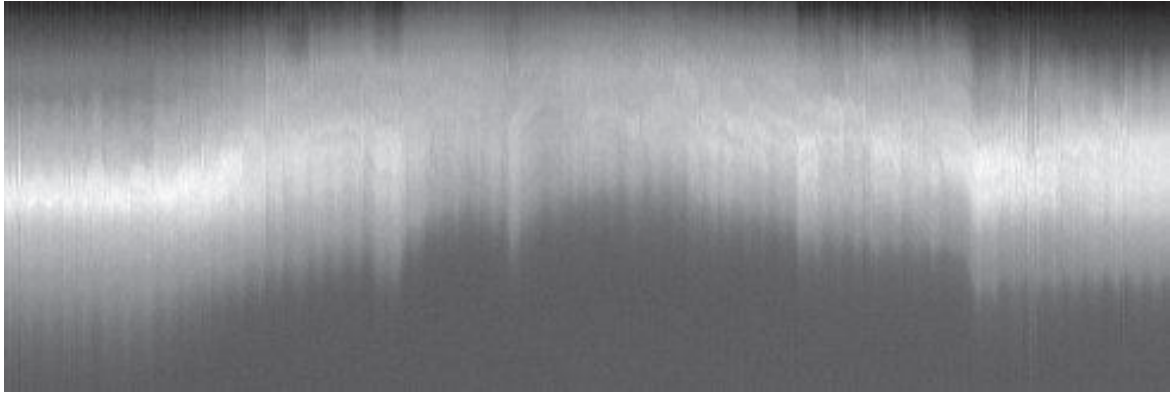
On three animals (rats 4, 6 and 9) for which ablation was made using the air OCT objective, a strong fogging of the objective outer lens would appear in less than a minute. For these experiments, we had to rise the microscope objective for about 30 seconds for the humidity on the objective to disappear, which prevented having a continuous ablation and increased our ablation time by a few extra minutes. Although this did not prevent ablation, it made each experiment significantly longer, homogeneity of the ablation over the whole experiment was reduced, and getting back to the location of ablation was not entirely precise.

Movement and hemorrhage

Another challenge to cope with is the need to control accurately the depth of ablation over the whole ablation area. A long depth of damage can destroy the artery from the endothelium to the adventitia in a series of consecutive shots, leading to a hemorrhage. This happened to us on separate animals: the first time (rat 5) as we increased the pulse repetition rate from 1 kHz to 10 kHz while having a focusing depth close to the adventitia and a pulse energy of 10uJ; the laser essentially “drilled” from the surface of the adventitia down to the endothelium, leading to an instantaneous leak in the arterial wall and flooding of the surrounding tissues in blood. The second time (rat 8) as an unfortunate small shock to the platform slightly offset the ablation to the side of the artery, leading to the rectangular ablation area to cut through the whole artery and causing another blood leak. In both cases, our experienced surgeon managed to limit the blood loss and stop the bleeding, but this somehow damaged the artery (flattening it and reducing blood flow).

Limitation of anesthesia protocol

Although most of the rats we used had a weight comprised between 340 g and 400 g, our last rat (rat 12, or B) had a weigh of 510 g, which corresponded to an animal bigger than what was within the tolerance of our anesthesia and life maintenance system. In consequence, the animal had died before we extracted the artery, but according to the post-ablation OCT recording (where the heartbeat can be observed) it was still alive at the time of intra-artery ablation. This experiment was done in less than 50 minutes between initial surgery and final extraction, and should be considered a limit in terms of animal size with the current system.



Side view of an averaged post-ablation OCT recording on rat 12 artery. The heartbeat variation can still be observed as a periodic oscillation along the width of this image.

The ablation along the artery lasted between 10 and 30 minutes depending on whether or not unexpected events such as fogging or hemorrhage took place. To estimate the duration of the full experiment, one has to add the time required for the surgery and the removal of connective tissue on the artery (15 to 25 minutes) as well as the time for extraction of the artery (5 minutes).

Appendix E: Simultaneous control of ablation scan and OCT imaging

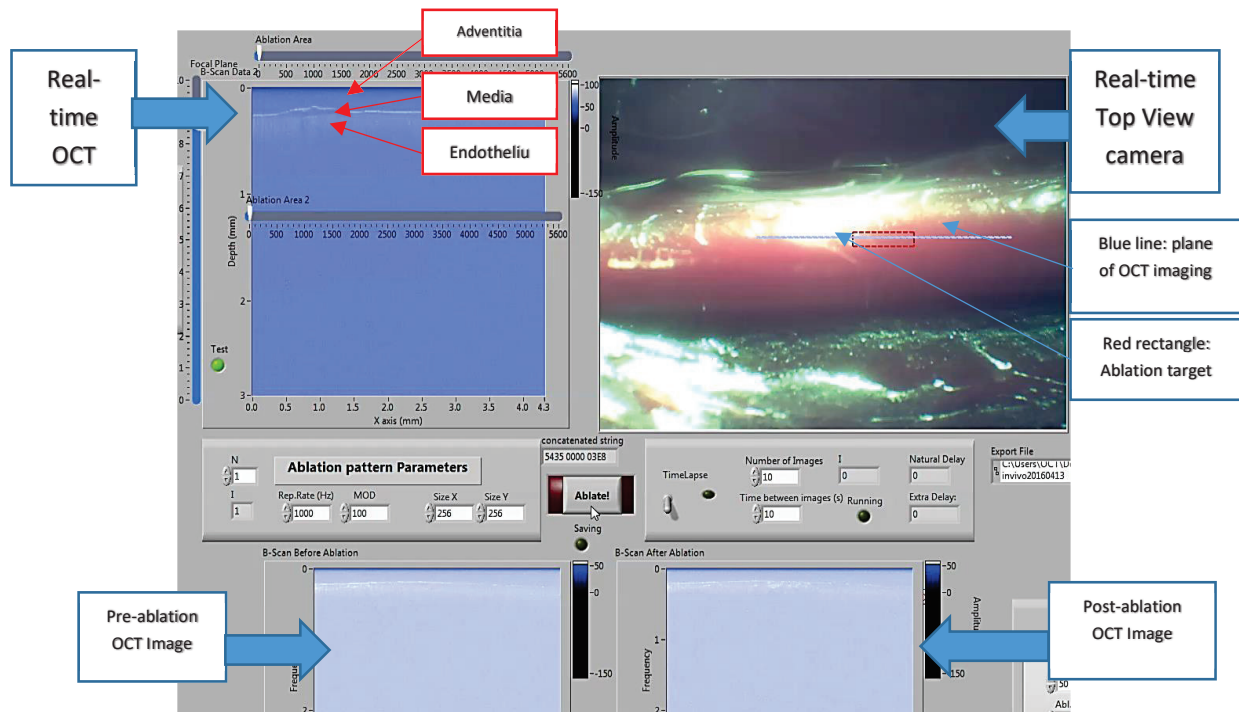
In particular for in-vivo experiments, but also for proper imaging of the bubble dynamics, rapid control of the ablation and monitoring was critical. For this purpose, we programmed a software for simultaneously control the ablation scan and the OCT imaging, using the LabView programming software.

For this software to be useable, one needs to consider the setup presented in Chapter II Part 4, including the integration of the OCT for scanning the ablation beam. For this, we needed to have control over the following parameters:

- The internal shutter of the fiber laser (a).
- The repetition rate and power modulation of the fiber laser (b)
- The scanning and recording controls of the OCT (c)
- The direct control over the galvanometric mirrors in the OCT head (d)

(a) and (b) were controlled using a direct RS232 connection to the Satsuma fiber laser using a set of input commands provided by Amplitude System. (c) and (d) were controlled using an integrated LabView library (*SpectralRadar.Ilb*) provided by Thorlabs OCT division.

We will not present the core of the code here, but it can be shared upon request.



Interface of our program for the simultaneous control of the ablation beam and OCT imaging, in the example of triggering and observation of LIOB in-vivo in a rat artery. The red arrows indicate different parts of the arterial wall identified on the A-scan.

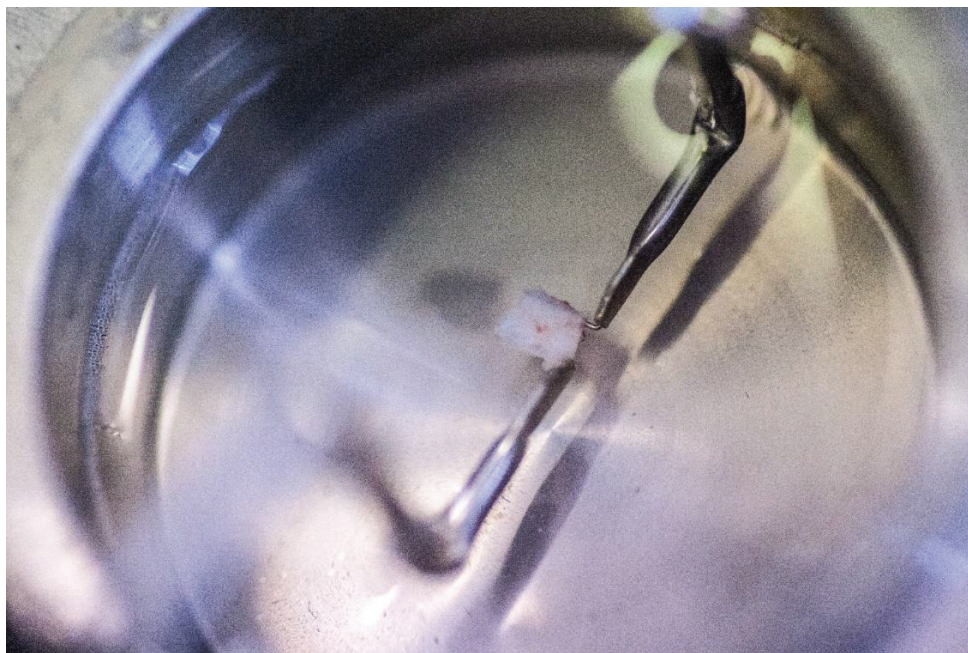
In details, we have access to the following:

- The top right panel shows an image of the sample (the artery can be seen as a red tube going left to right), the blue dotted line represents the line along which an OCT A-scan is measured, and the red dotted rectangle represents the target area for ablation scan.
- The top left panel continuously displays an image of the OCT A-scan, apart from the time when ablation scan is taking place.
- The bottom left and bottom right images are respectively recordings of the A-scan just before and just after ablation is made, and both images are saved on the hard drive.
- The central horizontal panel on the left controls the repetition rate of the laser, its power modulation, and the number of times the pattern must be repeated on one same location.
- The central horizontal panel on the right allows the recording of OCT images in a timelapse after ablation, for measurement of the bubble size decrease.

Another panels are not represented here, but allowed the user to control the position and size of the A-scan plane and of the ablation pattern. One last panel was used to change the scaling coefficients of scanning for OCT imaging and ablation when we were switching between the NA0.2 OCT objective and the NA0.8 40x objective, since they did not display the same field of view.

Appendix F: Complementary experiments in-vivo

Samples which were extracted for functionality tests were transferred from the artery to a vial filled with PBS, and placed in a myograph. We would like to thanks Dr. Manish Jain for this experiment. In the myograph, they were attached to two hook electrodes and immersed in a physiological solution for the duration of the experiment, typically a few hours.



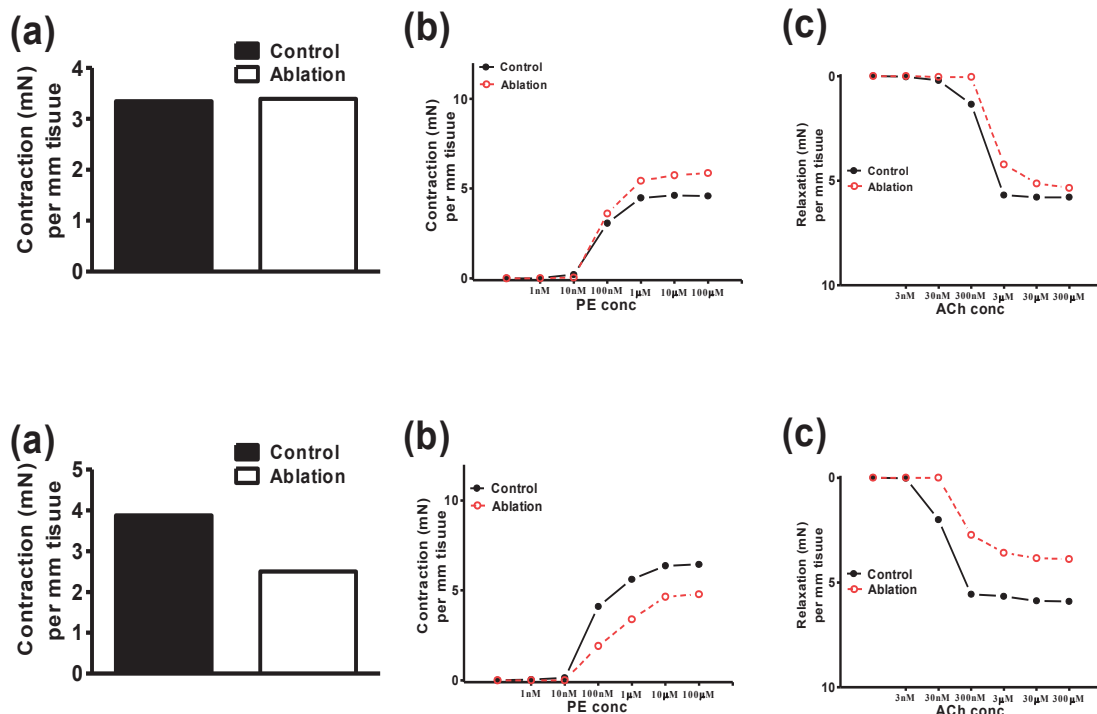
Sample or rat artery in the myograph, held by two electrodes.

Samples which were extracted for ROS staining were prepared for histology directly after extraction to maximize the observation of short-lived ROS-dependent effects. Depending on whether they were to be sliced by paraffin histology (rats 11 and 12) or cryocut (all the other animals), they were respectively fixed in PFA4% for 1h or frozen in cryomatrix. The samples fixed in PFA were then embedded in paraffin following a normal procedure. Independently of the way they were prepared for histology, the samples were then sliced to 8um, and staining with H&E and ROS stain, alternatively.

Samples which were extracted for TUNEL staining were maintained in physiological medium at 37°C and controlled CO₂ concentration in an incubator for an overnight incubation. This long incubation time was decided to allow the expression of the externally triggered apoptosis cascade, which results in the DNA-fragmentation and increase presence of dUTPs targeted by the TUNEL staining. They were then prepared for histology either by cryocut or paraffin slicing, as described above. The samples were then sliced to 8um, and staining with H&E and TUNEL stain, alternatively.

Functionality tests:

Considering both myogram measurements and TUNEL staining required maintaining the sample in physiological tissue, we decided to pursue apoptotic staining by TUNEL on several of the samples which had undergone myogram measurements (rat 2,3,4 & 12). All experiments were always performed on both an ablated sample and a negative control located next to it on the same animal.

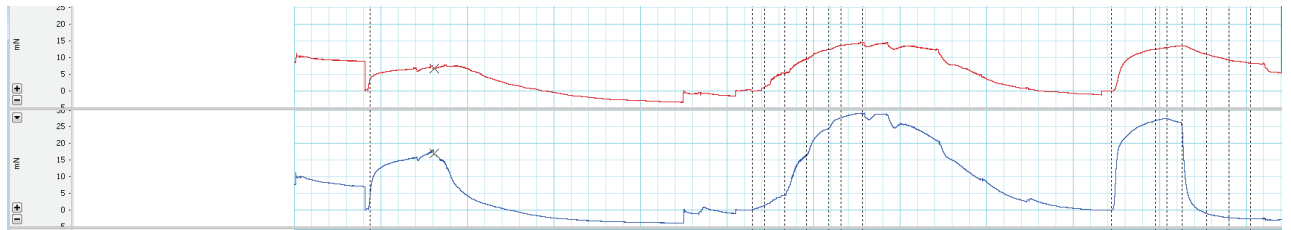


Results of arterial functionality tests performed by Manish Jain at UniFr. The upper set of a, b and c figures corresponds to rat 2 (ablation performed with about 6uJ pulse energy, and most of the ablation was probably done in the adventitia due to misalignment of the laser) and the second set of figures corresponds to rat 3 (ablation performed with 9.5uJ pulse energy and NA0.2 OCT objective).

It appears there has been a significant decrease (about 25%) in the contraction and relaxation capabilities of the ablated artery in rat 3 in comparison to its control.

Regarding the measurement on rat 12 (called rat B in Chapter 4, and where ablation was also performed at a pulse energy of 9.5uJ, but with the NA0.8 objective as opposed to the NA0.2 objective in the rat 3 experiment), the calculations and graph was not made yet, however the raw data (presented here) seem to show that contractions and relaxation capabilities were reduced by

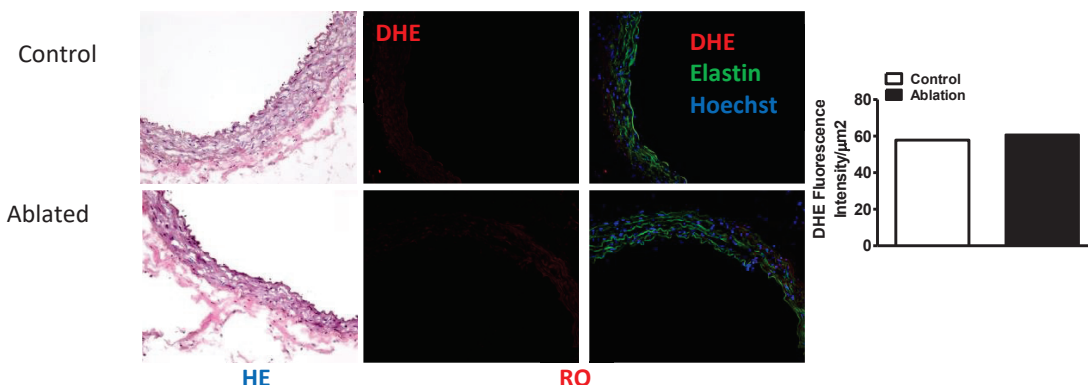
approximately 50 % in the ablated groups compared to healthy control. To conclusively say that this is due to ablation, proper control (tissue exposed for the same duration with all sham conditions) is missing.



Raw data of the myogram measurement for rat B. Each curve represents the strength applied by the sample between the electrodes following different stimuli. The red line corresponds to the ablated sample, the blue line corresponds to the control sample. Each rise and falls corresponds to a different stimuli: the 1st rise is due to injection of KCL 80 mm and denotes total tissue contractility (viability, independently from specific receptors). 2nd dose measures dependent on phentlephrine induced contraction (alpha receptor mediated, present on SMCs). 3rd indicates relaxation by acetylcholine (endothelium dependent). From this single experiment made with the best ablation parameters we have tried, we can observe a decrease in the overall functionality of the ablated sample. This is shown in particular by the longer relaxation period to the third stimuli, and denotes lower viability of cells in the endothelium.

Reactive Oxidizing Species (ROS) staining:

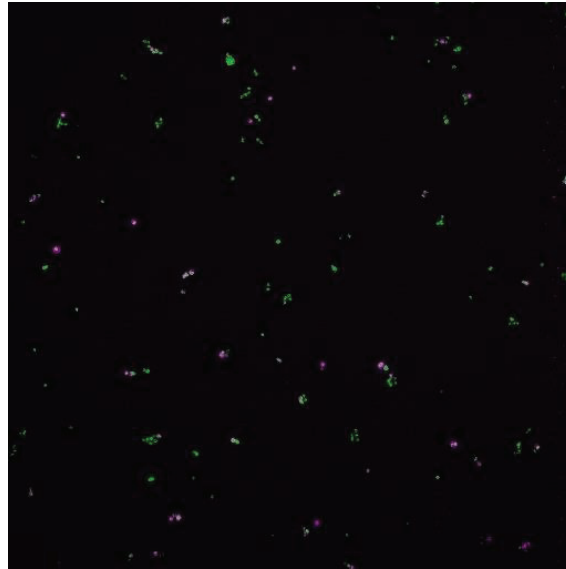
Samples from arteries from rats 2, 3, 4 and 12 were stained with Dihydroethidium (DHE) to detect presence of ROS close and away from the ablated area. Considering the short lifetime of ROS, the staining was conducted right after ablation (about 30 minutes). Since we were encountering issues in the localization of ablation holes, which was our main objective on these samples, we did not conduct a full analysis on the ROS signal. However, we never observed a significant increase in DHE signal



Staining with H&E, DHE and Hoechst for mice samples ablated at 7 μJ and 1 kHz by a NAO.2 OCT objective. No difference could be observed between ablated and control samples.

between the ablated samples and controls, let alone a localized increase around the target area.

The signal from DHE is weak in both control and ablated samples of the artery. We proceeded with a similar experiment in-vitro, by measured DHE and Caspase 3 (following the protocol defined in Chapter 3) on HCT 113 cells in PEG Hydrogels. There too, the DHE signal was very weak in both control and ablated samples. Pushing the detector gain, we could still detect a DHE signal, and compared it with the localization of caspase 3 activity: the colocalisation between DHE and Caspase 3 immunostaining signal are very low. This undermines the idea that apoptosis may be dependant on long-range ROS effects.



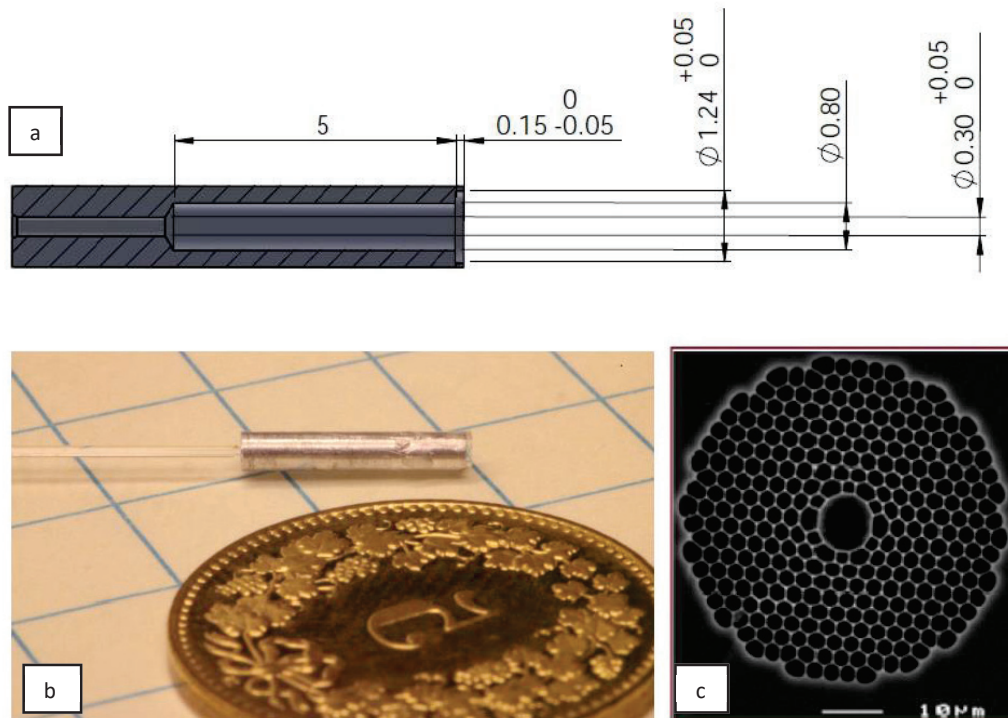
Imaging of HCT cells in a PEG Hydrogel, stained by Caspase 3 immunostaining (green) and DHE staining (purple).

However, a critical approach to this protocol presents two limitations in the interpretation of results on DHE staining. First, DHE is not a very stable component, as it can get oxidized easily. It can get oxidized if it is not stocked or manipulated properly, or if PH-stabilizing components left from the cell-culture medium, react with DHE. Secondly, the fluorescent signal of DHE is dependant on its oxidation reaction with $^1\text{O}_2$ and other ROS reacting with it may not give the expected fluorescent signal.

Appendix G: Design of catheters

Appart from the experiments conducted on the optical design of a catheter, we also investigated practical implementation of the fiber and lens systems in an assembled catheter. We discuss the size limitations for insertion in different arteries in Chapter 5. Here, we consider relatively larger protootypes aimed at diameters in the order of 2 mm, and without constraints on the length of the catheters. These models are essentially “scaled up” versions of what should be made for applications inside arteries, and are thus not made to be inserted in biological samples. In consequence, the choice of material was not made following a biomaterial approach and the prototypes have more sharp edges than what should be expected from practical biomedical devices.

The first design for a catheter able to trigger ablation was based on a HCF-800 Hollow Core Fiber from NKT Photonics, and a NA 0.6 lens with a diameter of 0.8 mm (LightPath Technologies, 355070). They were well to each other using a micromanufactured aluminium sheath produced at the EPFL microfabrication workshop. Both lens and fiber were put in the proper relative position and glued with epoxy glass.

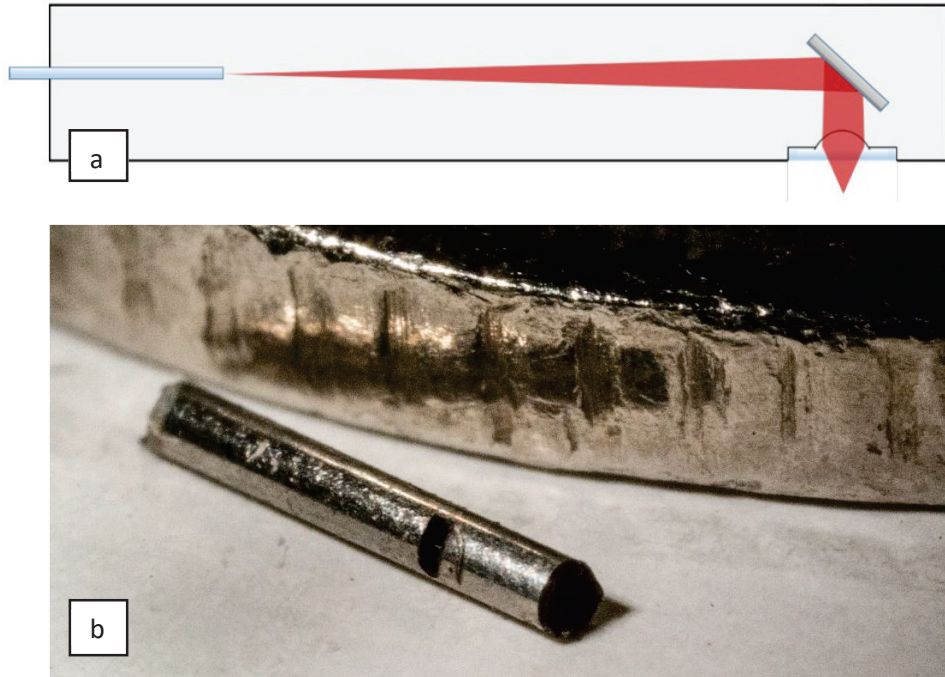


Design of the first catheter prototype. (a) Dimensions of the catheter probe. (b) Picture of the first prototype with the HC-800 Hollow Core Fiber. (c) SEM image of the profile of the HC-800 fiber, image credits to NKT Photonics.

We did not use the full diameter of the focusing lens, and the measured spot diameter of $1.0 \mu\text{m}$ for an input laser at wavelength of 1030 nm indicates we were rather using it as a NA0.5 lens. The light

transmitted through this fiber and focused by this lens did not prove to be intense enough to trigger LIOB. We thus modified the set-up to replace the HCF-800 fiber by a Kagome type fiber from GLO photonics, and this is the set-up whose results are presented in the first part of Chapter V.

A second prototype for single-mode optical fiber was devised but not carried through to testing. It consisted in replicating the first prototype, with the addition of a prism at the output to produce side ablation. This system would be closer to an actual device for subsurface ablation of the arterial wall or other cavities.



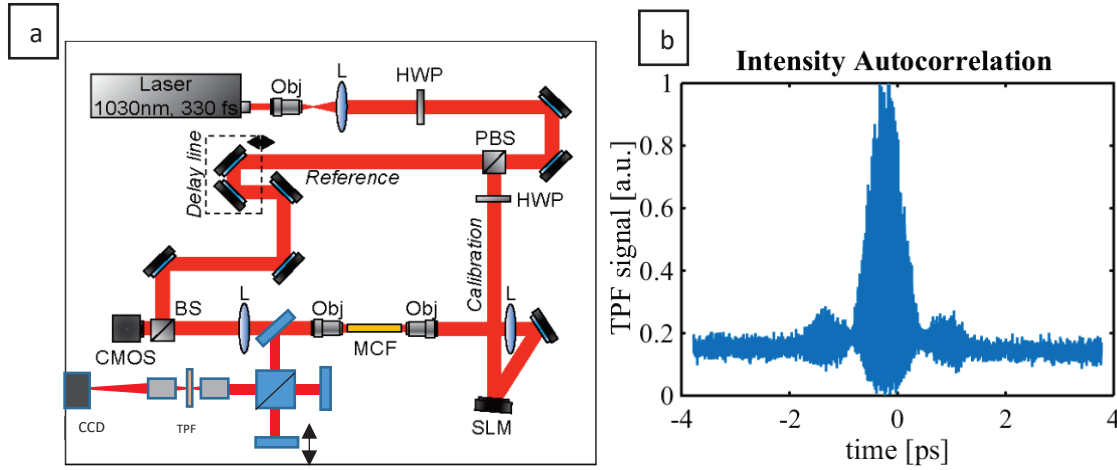
Design of the second catheter prototype. (a) initial design of a second generation of catheter. In practice, the tilted mirror was purchased as an assembly held to a similar 0.8 mm diameter lens as we had in the first prototype. (b) Prototype sheath for a catheter for side ablation. The hole on the side of the catheter was the window for the ablation beam to exit.

We fabricated a 1 mm sheath from a thin diameter tube from the mechanical workshop of EPFL, with 1 mm outside diameter and 0.8 inside diameter. The tube was cut to a length of 1 cm using our fiber-based ablation set-up with a NA of 0.3. A window for side exit of the fiber was also created using our ablation set-up, and the ablation was monitored in real-time using the OCT.

We conducted some initial tries of ablation through the lens and prism assembly. Unfortunately, the glue holding the lens and prism together was damaged during these tests (polymer have a LIOB threshold in the order of 0.1 GW.cm^{-1}). Considering this and the progress we were making in using the multicore fibers in parallel to this research, we did not pursue assembly of this prototype or other single-mode fiber catheter prototypes.

Appendix H: Autocorrelator for pulse duration measurement

For measuring the duration of pulses at the end of the multicore fiber, we set up an autocorrelator based on two-photon fluorescence of Rhodamine 6G. Rhodamine 6G has a relatively high two-photon cross-section around 1030 nm, about 45 GM according to the library of Cornell University on this subject. To do this, we added a flip-mirror between the objective at the output of the fiber and the lens imaging the output facet onto the CMOS camera. The beam was redirected toward a beamsplitter dividing the beam in two beams of same power, forming a Michaelson interferometer. The moving mirror of the interferometer was mounted on an automated one-axis stage. At the output of the Michaelson interferometer, a NA0.5 20x objective focused the beam on a glass slide coated with Rhodamine 6G. The fluorescence signal of this fluorophore was collected using a second NA0.5 objective, which imaged the plane of the fluorophores onto a CCD camera.



(a) Diagram of the MCF wavefront shaping setup from Chapter 5, with the addition of the TPF autocorrelator. (b) profile from the autocorrelator measurement for the pulse broadening of a 500 fs pulse to 840 fs for a transmitted power of 50 mW through the fiber.

When the two beams from the Michaelson interferometer are travel the same distance, the power of the beams interact at the same time with the Rhodamine. As long as there is an overlap between them, the two-photon fluorescence signal is proportional to the square of the sum of their intensities, $(I_1 + I_2)^2$.

Hence, scanning the length one of the two arms of the autocorrelator while measuring the two-photon fluorescence intensity on the CCD camera gives us a direct measurement of the pulse length, which can be directly converted into the pulse duration by dividing it by the velocity of light in the medium.

Curriculum Vitae

Thomas LANVIN

Born June, 22nd 1987 - French citizen
68 rue Rotchschild, 1202 Genève
Switzerland
thomas.lanvin@epfl.ch - +41/76 615 26 98



Education

2011 – 2016 PhD in Optics, EPFL Optics and Photonics Doctoral School (EDPO) - Ecole Polytechnique Fédérale de Lausanne (EPFL), Switzerland
Supervisor : Prof. Demetri Psaltis

2006 – 2011 Bsc and Master Degrees in Microengineering - Ecole Polytechnique Fédérale de Lausanne (EPFL), Switzerland

International Research Experience

Feb – Sep. 2011 – **University of California San Diego, USA**

Supervisor Prof. Yeshayau Fainman, United States.

Master Thesis. Design of microsystem and fabrication in a cleanroom. Independent work of microelectronics in an essentially optics lab.

May – Aug. 2009 - **Institute of Biotechnologies and Nanotechnologies (IBN) , Singapore**
Research Internship.

Experience in private sector

June to August 2010 **SCL-sensor Tech. Vienna, Austria.**
Internship

Languages and Technical skills

Languages: French (mother tongue), English (fluent), Spanish (Intermediate, B1), German (Basic, A2)

Technical skill: Biomedical devices, Laser manufacturing, Data Processing, Cell Biology and Physiology, Microprocessors programming and microfabrication.

Other interests

Photography (teaching in workshops, organization and participation in competitions), long-distance running.

Peer-reviewed publications and conference talks

Rachel Grange, Thomas Lanvin, Chia-Lung Hsieh, Ye Pu, and Demetri Psaltis, "*Imaging with second-harmonic radiation probes in living tissue*," Biomed. Opt. Express 2, 2532-2539 (2011)

R. Grange, T. Lanvin, C. Hsieh, Y. Pu, and D. Psaltis, "Second-Harmonic Nanoparticles for Deep Tissue In Vivo Imaging," in *CLEO/Europe and QEC 2011 Conference Digest*, OSA Technical Digest (CD) (Optical Society of America, 2011), paper CLEB2_2.

C. Hsieh, T. Lanvin, R. Grange, Y. Pu, and D. Psaltis, "In vivo Imaging Using Second-Harmonic Nanoparticles," in *CLEO:2011 - Laser Applications to Photonic Applications*, OSA Technical Digest (CD) (Optical Society of America, 2011), paper CThF3.

Thomas Lanvin, Donald B. Conkey, Aurelien Frobert, Jeremy Valentin, Jean-Jacques Goy, Stéphane Cook, Marie-Noelle Giraud, and Demetri Psaltis, "*Subsurface ablation of atherosclerotic plaque using ultrafast laser pulses*," Biomed. Opt. Express, (2015)

Thomas Lanvin ; Donald B. Conkey ; Laurent Descoux ; Aurelien Frobert ; Jeremy Valentin ; Jean-Jacques Goy ; Stéphane Cook ; Marie-Noelle Giraud ; Demetri Psaltis; "*Ultrafast laser ablation for targeted atherosclerotic plaque removal*" . Proc. SPIE , ECBO, (July 15, 2015);

